Non-Linear Terahertz Spectroscopy of Quantum Materials

Thomas Barnaby Gill, MEng

Submitted in accordance with the requirements for the degree of
Doctor of Philosophy

University of Leeds

School of Electronic and Electrical Engineering
Pollard Institute

January 2022

Acknowledgements

Firstly to my project supervisors, Dr. Joshua Freeman and Dr. Paul Dean–your knowledge, understanding and patience have been paramount to my project progression. Thank you both for the amazing support–I would not have anywhere near the skills and knowledge required for a PhD without your help. Also, thank you to the extended supervisory team: Prof. Edmund Linfield, Prof. Giles Davies, Prof. John Cunningham and Dr. Andrew Burnett. Your constant insight and wisdom has proved invaluable to this project and has helped me to push myself.

To Dr. David Bacon, firstly, thank you for your wonderful emitters, but much more importantly, for the practical skills, knowledge and enjoyment you bestowed upon me from our time together in the lab.

To Dr. Aniela Dunn, your understanding of amplified lasers and physics in general have been vital to this project, but I thank you most for the friendship and comradery that only working together for many hours in the amplified lab could bring.

To my good friends (and hopefully soon to be Drs.) Connor Kidd, Jac Richards and Eleanor Nuttall–I thank you all for the good times we've had together both in and outside the fourth floor labs. It would not be anywhere near as enjoyable being in the lab without you all and having people to talk to about the trials and tribulations of being a PhD student.

To the rest of the current and former members of the Terahertz research group including: Calum Towler, Dr. Alex Valavanis, Dr. Mark Rosamond, Dr. Chris Wood, Dr. Michael Horbury, Dr. Reshma Mohandas, Dr. Jay Keeley, Dr. Nicholas Peters, Dr. Nicholas Greenall and Susan Hobson to name a few–thanks for all the great experiences I have had during my time as a PhD student thanks to you lovely lot.

To my parents, sister, grandparents, extended family, and friends, thank you for supporting me in multitudes of ways, in particular over these past few years.

Finally, a special thanks to my amazing fiancée who without her love, support and motivation, the last few years would have been so much harder, as life outside the lab would not be filled with as much joy.

In short, thank you to all the wonderful, brilliant people who have helped me throughout my time as a PhD student. Also, thank you, dear reader, for taking your time to read this work, I hope it provides some useful insight to you.

Also, a special thanks to my writing buddy, Henry 🐾.

Abstract

Linear Terahertz (THz) spectroscopy has become well developed in recent years, utilising techniques such as Fourier-Transform Infrared Spectroscopy (FTIR) spectroscopy and Time-Domain Spectroscopy (TDS) to acquire material characteristics and study physical phenomena. Recently, owing to advances in high field THz sources, nonlinear responses in materials can now be studied, such as coherent and incoherent material processes, transport dynamics in graphene and biological processes. These measurements are often performed using a Free-Electron Laser (FEL) as they generate monochromatic radiation, tuneable between 1–100 THz with fields in the region of 100 MV cm^{-1}. These are exclusively contained in large, costly facilities, restricting the availability and practicality of the technology. There is therefore much appeal in the development of tabletop systems to perform these experiments, improving accessibility.

In this thesis, the development of a 2D THz TDS experimental system utilising a tabletop amplified laser as the source is discussed. The system can generate fields greater than 100 kV cm^{-1}, sufficient for inducing nonlinear effects within certain samples. This field is spread over a broad bandwidth (∼0.1–5 THz), allowing for multiple spectral features to be acquired simultaneously. The system uses both photoconductive arrays and electro-optic crystals to generate the high field, broad bandwidth pulses and investigations of both types of sources are presented in this thesis.

Also presented in this work are measurements of two samples using the system developed, the first being a doped semiconductor impurity centre (germanium doped with arsenic) and the other being a semiconductor quantum well structure designed to exhibit the self-induced-transparency effect. These measurements obtained values of the transition polarisation lifetimes (T_2) directly on the few ps timescales. Knowledge of this lifetime is important for performing coherent control experiments and is difficult to measure with other spectroscopy techniques.

Publications

Peer-Reviewed Journals

- K. Meng, S. J. Park, A. D. Burnett, **T. Gill**, C. D. Wood, M. Rosamond, L. H. Li, L. Chen, D. R. Bacon, J. R. Freeman, P. Dean, Y. H. Ahn, E. H. Linfield, A. G. Davies, and J. E. Cunningham.
  "Increasing the sensitivity of terahertz split ring resonator metamaterials for dielectric sensing by localized substrate etching".
  Optics Express, vol. *27*, no. *16*, p. *23164-23172*, August 2019.
- D. R. Bacon, **T. B. Gill**, M. Rosamond, A. D. Burnett, A. Dunn, L. Li, E. H. Linfield, A. G. Davies, P. Dean, and J. R. Freeman.
  "Photoconductive arrays on insulating substrates for high-field terahertz generation".
  Optics Express, vol. *28*, no. *12*, p. *17219-17231*, June 2020.
- N. Chudpooti, N. Duangrit, A. D. Burnett, J. R. Freeman, **T. B Gill**, C. Phongcharoenpanich, U.Imberg, D. Torrungrueng, P. Akkaraekthalin, I. D. Robertson and N. Somjit.
  "Wideband dielectric properties of silicon and glass substrates for terahertz integrated circuits and microsystems".
  Materials Research Express, vol. *8*, no. *5*, p. *056201*, May 2021.

Conference Proceedings

- D. R. Bacon, M. Rosamond, **T. Gill**, A. D. Burnett, L. Li, J. Cunningham, E. H. Linfield, A. G. Davies, P. Dean and J. R. Freeman.
  "Photoconductive Arrays for High-Field Terahertz Generation".
  44th Internation Conference on Infrared, Millimeter, and Terahertz Waves (IRMMW-THz) 2019.

- S. J. Park, K. Meng, A. D. Burnett, **T. Gill**, C. D. Wood, M. Rosamond, L. H. Li, L. Chen, D. R. Bacon, J. R. Freeman, P. Dean, Y. H. Ahn, E. H. Linfield, A. G. Davies and J. E. Cunningham.
  "Increasing the sensitivity of terahertz metamaterials for dielectric sensing by substrate etching ".
  45th Internation Conference on Infrared, Millimeter, and Terahertz Waves (IRMMW-THz) 2020.

- A. Dunn, D. R. Bacon, **T. B. Gill**, J. R. Freeman, L. H. Li, P. Dean, E. H. Linfield, A. G. Davies and A. D. Burnett.
  "Development of a Broadband Multidimensional THz Spectrometer".
  45th Internation Conference on Infrared, Millimeter, and Terahertz Waves (IRMMW-THz) 2020.

- **T. B. Gill**, D. R. Bacon, P. Dean, A. D. Burnett, A. Dunn, E. H. Linfield, A. G. Davies and J. R. Freeman.
  "Broadband Nonlinear Spectroscopy of Hydrogen-Like Levels in Ge:As".
  45th Internation Conference on Infrared, Millimeter, and Terahertz Waves (IRMMW-THz) 2020.

Contents

List of Figures

List of Tables

List of Acronyms

LiNbO$_3$ Lithium Niobate
1D One-Dimensional
2D Two-Dimensional
3D Three-Dimensional

AC Alternating-Current

BBO β-Barium Borate
BCB Benzocyclobutene
BK7 Borosilicate Glass
BNA *N*-Benzyl-2-Methyl-4-Nitroaniline
BSI Backside-Illumination

CCD Charge-Coupled-Device
CI Confidence Interval
CPA Chirped Pulse Amplification
CW Continuous Wave

DAC Digital-to-Analog Converter
DAST Diethylaminosulfur Trifluoride
DC Direct-Current
DFG Difference Frequency Generation
DQW Double Quantum Well
DSP Double Side Polished

EFL Effective Focal Length
EM Electromagnetic
EO Electro-Optic

FEL Free-Electron Laser
FFT Fast Fourier Transform
FTIR Fourier-Transform Infrared Spectroscopy
FTP File Transfer Protocol
FWHM Full Width at Half Maximum
FWM Four-Wave-Mixing

Ge:As Germanium doped with Arsenic
GVM Group Velocity Mismatch

HF Hydrofluoric Acid
HRR Horizontal Retro-Reflector

IR Infrared

LIA Lock-In Amplifier
LPF Low-Pass Filter
LT-GaAs Low-Temperature-Grown GaAs

MBE Molecular-Beam Epitaxy
MNA 2-Methyl-4-Nitroaniline
MQW Multiple-Quantum-Well

ND Neutral Density
Nd:YAG Neodymium-doped Yttrium Aluminum Garnet
NMR Nuclear Magnetic Resonance

OPA Optical Parametric Amplifier

PCA Photoconductive Array
PCS Photoconductive Switch
PE Potential Energy
PTFE Polytetrafluoroethylene

QCL Quantum Cascade Laser

RMSE Root-Mean-Square Error

SFG Sum-Frequency Generation

SH Second-Harmonic
SI-GaAs Semi-Insulating GaAs
SIT Self-Induced-Transparency
SNR Signal-To-Noise Ratio
SVEA Slow Varying Envolope Approximation

TDS Time-Domain Spectroscopy
THz Terahertz
Ti:Sapphire Titanium-Sapphire
TO Transvere-Optical
TPX Polymethylpentene

UV Ultraviolet

VCO Voltage-Controlled Oscillator
VRR Vertical Retro-Reflector

Chapter 1

Introduction

The Terahertz (THz) region is a band of the Electromagnetic (EM) spectrum between the microwave and infra-red regions, often defined from 0.1–10 THz. Owing to the difficulty in making suitable THz emitters and detectors, the region remains relatively unexplored when compared to other parts of the EM spectrum [1]. In recent years, there has been significant developments in THz sources, allowing for experimental systems capable of generating high-field THz radiation, opening new avenues for research into nonlinear material responses (material responses induced in samples other than weak light-matter interactions of absorption and emission).

1.1 Project Motivation

Nonlinear THz spectroscopy has been shown already to be a useful tool for investigating coherent and incoherent material processes [2], transport dynamics in graphene [3], plasmas in semiconductors [4] and biological processes [5,6], as well having application for coherent control of quantum states [7]. Free-Electron Laser (FEL) based systems are most commonly used for these measurements as they are capable of producing the large fields necessary to induce nonlinear effects (up to $\sim 100\,\mathrm{MV\,cm^{-1}}$). These beams are monochromatic and tunable between 1–100 THz, dependent on the facility [1]. The main disadvantage of these systems are that they are large, costly facilities, restricting the availability and practicality of the technology. There is therefore much interest in developing tabletop systems which can perform these measurements in a typical lab setting. The advent of Chirped Pulse Amplification (CPA) [8], where an ultrafast (fs) pulse is stretched and then recompressed has allowed for relatively compact laser systems with large pulse energies (greater than 10 mJ) and small pulse widths (< 50 fs) [9], enabling THz spectroscopy systems on a tabletop scale.

This project aims to develop an experimental system capable of performing Two-Dimensional (2D) THz Time-Domain Spectroscopy (TDS) of quantum materials with narrow transitions such as doped semiconductor impurity centres and electronically confined systems, such as quantum well and dots. To do this, the system must be able to generate THz pulses with fields in the $\sim$10–100 kV cm^{-1} range over a broad bandwidth (3 THz) to allow for a wide variety of samples to be investigated. The developed system will then be used to investigate samples of technological interest using 2D THz TDS.

1.2 Thesis Structure

The thesis begins with Chapter 2 where background theory relevant to this work is presented. Basic laser theory is introduced first, with more detail provided about techniques for producing ultra-short and intense pulses. A brief review of methods used to generate and detect THz pulses relevant to this work is then provided, with the chapter ending with an introduction to THz TDS in one and two dimensions.

Chapter 3 discusses in detail the Photoconductive Array (PCA) emitters developed for this work. A short literature review on PCA technology is presented before a summary of the fabrication technique developed. After this, the methods used to characterising these emitters are presented alongside results from some of the devices measured.

Chapter 4 summarises the 2D THz TDS system development process, providing information on the instruments used and how data acquired from the system is processed to acquired information from a sample. The first attempt at creating a system using a single PCA to generate two THz pulse is discussed first, highlighting the problems with the system that led to the development of the final system which utilises two emitters which is in turn discussed at the latter end of the chapter. The next two Chapters (5 and 6) present measurements performed with the experimental system.

The sample measured in Chapter 5 is a doped semiconductor impurity centre (Germanium doped with Arsenic (Ge:As)), so basic semiconductor and impurity theory is presented first before the measurement results. Three different measurements are discussed here: first a low field, linear TDS measurement using a high repetition rate laser system; then a “saturation” measurement, where multiple measurements are performed at different THz field strengths to acquire the field required to saturate the transition of interest and induce nonlinearities; and finally a 2D TDS measurement. Within the examination of the 2D TDS results, more detail is provided on how the data is processed.

The sample measured in Chapter 6 is a semiconductor quantum well structure, designed to exhibit the Self-Induced-Transparency (SIT) effect. Some background theory on quantum well systems and SIT is provided before the sample measurements are reviewed. Similarly to the measurements in the previous chapter, linear TDS, saturation and 2D TDS are performed sequentially, however, the linear and saturation measurements are performed twice as two different methods were attempted to couple the THz pulses into the quantum well structure (namely 45° incident facets and diffraction gratings).

The thesis concludes with Chapter 7, where the findings of this work are summarised, alongside a discussion of what further work could be done to improve the system and the findings from the experimental results.

Chapter 2

Introduction to High-Field Terahertz

2.1 Amplified Lasers

Advances in tabletop laser sources capable of generating ultrashort (fs), high power pulses, in particular, those utilising the Nobel prize winning technique of CPA [8], have allowed for the generation of high field THz pulses. This first section will discuss the operating principles of lasers and how ultrashort, high power pulses are generated.

2.1.1 Principles of Lasers

In a simple two-level energy system, photon emission is possible when an electron transitions from the higher energy state E_2, to the lower energy state E_1, with the frequency of the emitted photon being determined by the following equation:

$$f = \frac{E_2 - E_1}{h}. \tag{2.1}$$

If the electron transition occurs randomly, the photon is emitted with a random phase in a random direction. This is known as spontaneous emission (see Figure 2.1a). The change in number density of electrons in the lower state over a given period of time can be obtained with the following formula:

$$\frac{dn_1}{dt} = A_{21} n_2, \tag{2.2}$$

where n_i is the number density in state i and A_{21} is the Einstein coefficient, which is the probability per unit of time that an electron in the upper state will spontaneously decay to the lower state.

If a photon with the same energy as the gap E_{21} passes through the system whilst there is an electron in state E_2, the photon emitted by the electron transition will have the same frequency, phase and direction of the incident photon. This is known as stimulated emission (see Figure 2.1b). The change in number density of electrons in the lower state per unit time due to this process can be obtained with the following formula:

$$\frac{dn_1}{dt} = B_{21} n_2 \rho(\nu), \tag{2.3}$$

where $\rho(\nu)$ is the energy of the photons, per unit frequency bandwidth at the transition frequency and B_{21} is the Einstein coefficient, which is the probability per unit time, per unit of spectral radiance that an electron in the upper state will decay to the lower state.

If the electron is in state E_1 when a photon passes through the system, the photon is absorbed and the electron transitions from E_1 to E_2 (see Figure 2.1c). The change in number density of electrons in the lower state per unit time due to this process can be obtained with the following formula:

$$\frac{dn_1}{dt} = B_{12} n_1 \rho(\nu), \tag{2.4}$$

where B_{12} is the Einstein coefficient, which is the probability per unit time, per unit of spectral radiance that an electron in the lower state will absorb a photon and become excited to the higher state.

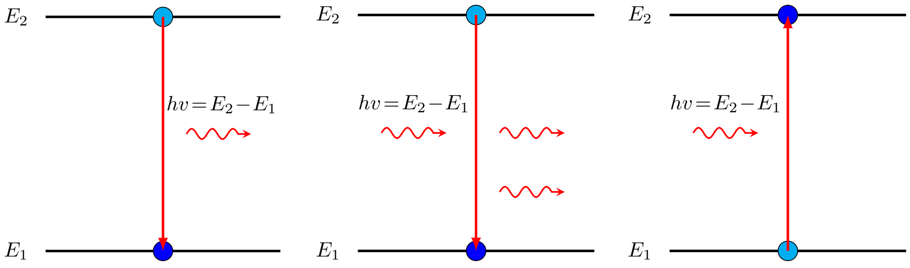

(a) Spontaneous Emission (b) Stimulated Emission (c) Absorption

Figure 2.1: Energy level diagrams illustrating the possible interactions between electrons and photons in a two-level system

In a system where there are more electrons in E_2 than E_1, known as a population inversion, and we have an energy matched incident photon, it is possible to have a net gain in the number of outgoing photons, as more photons will be emitted than absorbed. This is the principle of light amplification (see Figure 2.1b). To create a population inversion, a system with at least three energy levels is required, as due to the ratio between Einstein coefficients in a two level system, a photon used to 'pump' electrons into the upper state has the same probability of stimulating emission in electrons already in the upper state.

In a three-level system, electrons start at the ground state E_1 and are excited up to the E_3 state with either pump photons or via electrical discharge. E_3 has a short state lifetime so the electrons quickly transition down to E_2, which has a much longer lifetime, allowing a population inversion between E_2 and E_1 to build. Eventually an electron in state E_2 will spontaneously decay and cause a stimulated emission of further photons. Figure 2.2 illustrates this three level system.

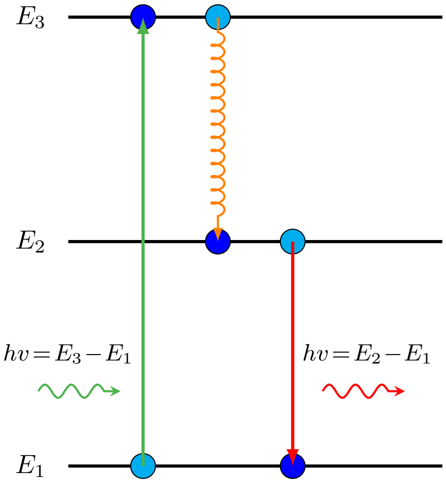

Figure 2.2: Energy level diagram illustrating a three-level system used for lasing.

This process allows for photon amplification and is known as a 'LASER' (Light Amplification by Stimulated Emission of Radiation), whilst the material in which the light amplification occurs is known as the gain medium. To increase the intensity of the output beam, the gain medium is integrated between two mirrors, forming a laser oscillator (shown in Figure 2.3). One mirror has a $\sim 100\,\%$ reflectivity whilst the other is partially transmitting (e.g. $\sim 99\,\%$ reflectivity), increasing the degree of collimation of the emitted beam and increasing the gain intensity, as photons can be reused to perform stimulated emission. The reflectivity of the mirrors in the oscillator cavity must be designed so that the round-trip laser gain is greater than the losses from the mirrors or the intensity of a pulse will decay after a few round trips. The length of the laser oscillator cavity must also be optimised to be of length $n\lambda/2$, where n is an integer and λ is the wavelength of the emitted photons, to avoid deconstructive interference of the target wavelength. The mirrors on either side of the cavity cause the photons to form standing waves of discrete frequencies, dependent on the gain bandwidth and length of the cavity:

$$\text{No. of Modes} = \frac{2BL}{c}, \tag{2.5}$$

where B is the gain bandwidth and L is the cavity length. [10,11]

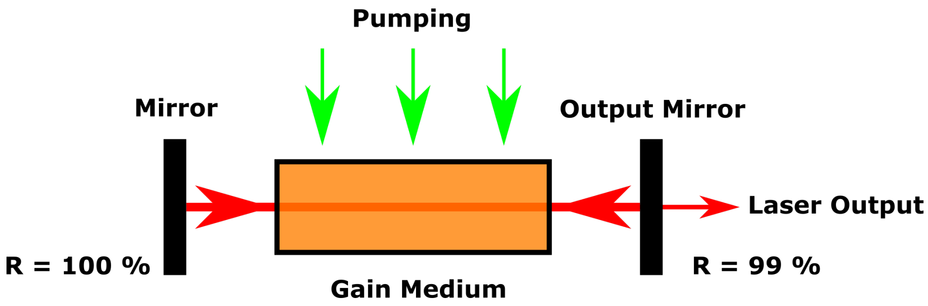

Figure 2.3: Optical diagram of a simple laser oscillator cavity.

This aforementioned technique of utilising a three-level system to create a population inversion and engineering the gain cavity were first used in 1960 to create the first laser, utilising a ruby crystal as the gain medium and a flash tube to generate the pump photons [12].

Many modern lasers utilise a four-level system to achieve lasing (see Figure 2.4). Electrons from E_1 are optically pumped into E_4 where they rapidly decay to E_3, which has a longer lifetime. The E_4 to E_3 transition is often radiationless, with the transition occurring due to material vibrations, known as phonons. After some time, electrons in E_3 then begin to spontaneously decay to E_2, causing stimulated emission of further electrons. This transition causes the photon emission for this laser system. Electrons in E_2 then rapidly decay with another radiationless transition back to E_1. The fast decay of E_2 to E_1 means that there is a greater population inversion between E_3 and E_2, making the system more efficient than a three-level system, as fewer electrons need to be pumped for lasing to occur.

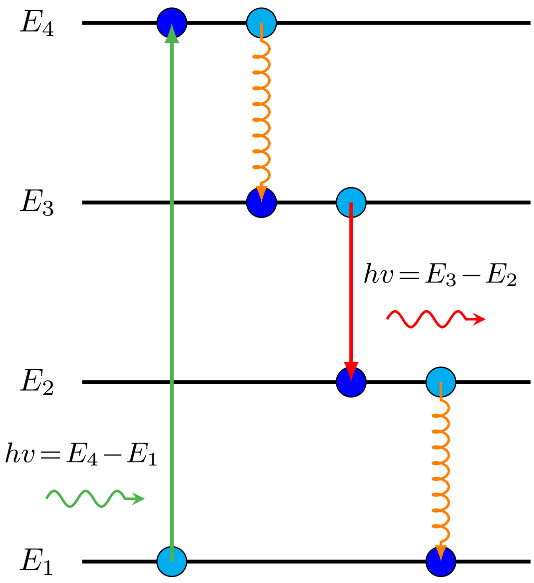

Figure 2.4: Energy level diagram illustrating a four-level system used for lasing.

2.1.1.1 Titanium-Sapphire Lasing

Titanium-Sapphire (Ti:Sapphire) (Ti^{3+}:Al_2O_3) crystals can be used as a four-level laser system (see Figure 2.5), capable of emitting photons with a wavelength of 650–1200 nm, generating most efficiently around 800 nm. The gain bandwidth of a Ti:Sapphire is 128 THz [13]. There are two energy level continua in the crystal used to create a four-level system; one above E_1 and the other above E_3. E_4 is contained within the continuum above the first excited state, E_3 is the first excited state, E_2 is contained within the continuum above the ground state and E_1 is the ground state. The $E_4 - E_3$ and $E_2 - E_1$ transitions occur due to vibrations within the crystal and have a lifetime on the order of 1×10^{-13} s, whilst the radiative transition $E_3 - E_2$ has a lifetime around 3.8 µs [13].

Ti:Sapphire crystals strongly absorb photons with wavelengths between 400–600 nm, but are most efficient when pumped using 510–530 nm. The short lifetime of the lasing state (3.2 µs) and high saturation power means that it is difficult to pump using non-coherent sources. Strongly focused solid-state lasers (e.g. Frequency doubled Neodymium-doped Yttrium Aluminum Garnet (Nd:YAG)) and diode lasers which generate radiation around 530 nm are the most common pump lasers for Ti:Sapphire lasers [13].

A pump laser with a wavelength of 530 nm has sufficient energy (2.35 eV) to excite electrons from E_1 into the continuum above the first excited state, E_4, where they will rapidly decay into E_3, creating a population inversion. After 3.8 µs, electrons in E_3 will spontaneously decay to the continuum above the ground state, E_2, causing stimulated emission of further electrons in E_3. The electrons in E_2 will then rapidly decay back to E_1 [13].

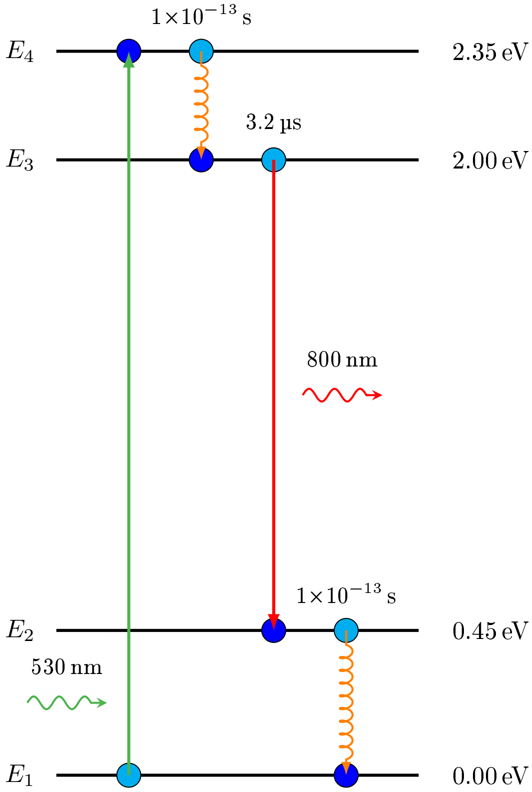

Figure 2.5: Energy level diagram of the four-level system of a Ti:Sapphire laser.

2.1.2 Q-Switched Lasers

Whilst the previously discussed techniques can be used to develop lasers capable of emitting a constant stream of single frequency photons, known as Continuous Wave (CW) lasers, more complex techniques are required for producing short bursts of intense light.

Q-switching is a technique that can be applied to a laser system to produce pulses on the nanosecond timescale by adding a ‘Q-Switch’ inside the laser cavity. Initially, the Q-Switch is ‘off’, causing the losses in the cavity to be kept high, preventing lasing and allowing the pump to build up energy in the gain medium. The Q-Switch is then turned ‘on’, reducing cavity losses, allowing for lasing to begin and the beam to make multiple trips inside the cavity to amplify the pulse. The energy stored in the gain medium is quickly depleted, creating a short pulse with high intensity. The Q-Switch is then turned back ‘off’, and the process is repeated. [14]

2.1.3 Mode-Locked Lasers

To produce ultrashort (sub-picosecond) pulses, techniques other than Q-switching are required. The technique of 'mode-locked' lasing will be described here, as it is the most common technique used for femtosecond laser oscillators in bench-top systems.

As mentioned in Section 2.1.1, laser cavities contain multiple standing waves or 'modes' of light. Normally, these modes will have a random phase, causing multiple frequencies to be emitted at a relatively stable output intensity. If the phases of these modes are manipulated however, it is possibly to cause interference within the cavity, leading to an ultrashort pulse with a greater peak intensity. An example of this effect using ten modes is displayed in Figure 2.6.

Each round trip of the cavity causes a single pulse to be emitted, allowing for the repetition rate to be calculated using the following formula:

$$f_{\text{Rep}} = \frac{2L}{c}, \tag{2.6}$$

where L is the cavity length [15]. The minimum pulse duration that can be obtained from a given laser system is given by the following equation:

$$\Delta t = \frac{\text{TBP}}{N\Delta\nu}, \tag{2.7}$$

where TBP is the time-bandwidth product, N is the number of modes, $\Delta\nu$ is the frequency separation between the modes, which when multiplied together are the gain bandwidth of the laser. The value of the TBP depends on the temporal pulse shape with Gaussian pulses have a TBP of 0.441, whilst sech^2 pulses have a TBP of 0.315. From this, we can estimate that a Ti:Sapphire laser, which has a gain bandwidth of 128 THz, would have a minimum pulse duration of approximately 3.4 fs. Currently, the smallest pulse width observed from a Ti:Sapphire laser is approximately 5 fs [16].

Owing to most of the energy being contained within a small packet of photons, the peak power is often several magnitudes greater than the average power. The peak power can be calculated using the following equation:

$$P_{\text{Peak}} = \frac{P_{\text{Avg}}}{\Delta t f_{\text{Rep}}}, \tag{2.8}$$

where P_{Peak} is the peak power, P_{Avg} is the average power, Δt is the pulse width and f_{Rep} is the repetition rate of the laser.

Mode-locking can be achieved both passively and actively. Passive mode-locking allows for much shorter pulses as the phase modulation occurs much faster than electronically activated modulation. An example of active mode-locking is the use of an electro-optic modulator within the cavity. The modulator is periodically activated, synchronised with the round-trip of the pulse in

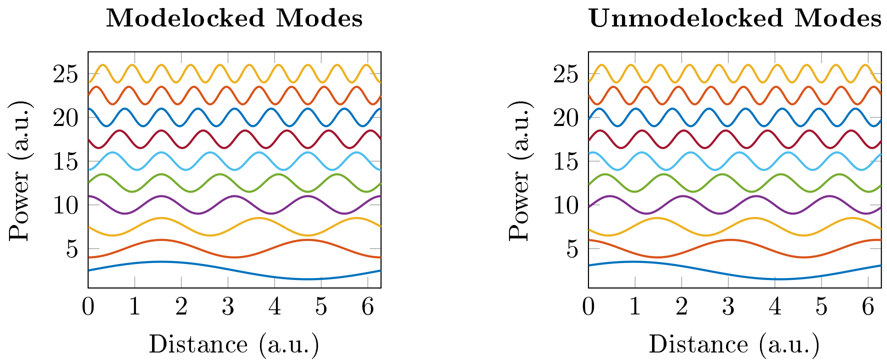

Modelocked Modes

Unmodelocked Modes

(a) Simulation of a cavity with 10 modelocked modes ($\sin(nx + \pi(n-1)/2)$). Modes are offset to improve readability.

(b) Simulation of a cavity with 10 randomly phased modes ($\sin(nx + \text{Rand})$). Modes are offset to improve readability.

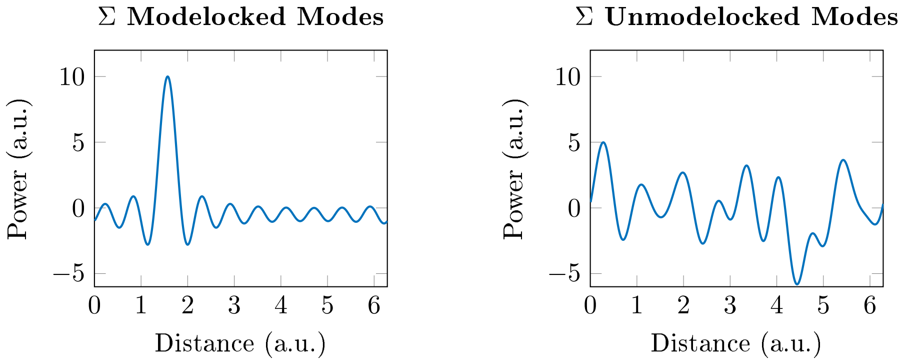

Σ Modelocked Modes

Σ Unmodelocked Modes

(c) Sum of modes in Figure 2.6a.

(d) Sum of modes in Figure 2.6b.

Figure 2.6: Simulation of a cavity with 10 modes, with and without modelocking. Figure 2.6c shows that the sum of modes in a modelocked cavity produces a short, intense burst.

the cavity. When activated, a voltage is applied to the modulator, causing the refractive index of the modulator to change, altering the phase of the modes inside the cavity. An example of passive mode-locking is the use of a saturable absorber. When the pulse in the cavity hits the saturable absorber, the absorption becomes saturated, causing a brief reduction in the loss through it. This causes low-intensity CW light to be absorbed, whilst high-intensity pulses will be transmitted. Kerr-lens mode-locking is another passive mode-locking technique. It utilises the Kerr effect, which is nonlinear effect where the refractive index of the medium is dependent of the field strength of the incident pulse. As the power density in a laser resonator is Gaussian, introducing a Kerr medium into the resonator causes the higher power regions at the centre of the beam to become focused, changing their path inside the resonator cavity. This allows for the higher power centre of the beam to be diverted out of the cavity over the edges, causing a reduction in pulse width.

When femtosecond lasers with greater peak powers are required, such as for systems performing nonlinear spectroscopy, complex techniques must be performed other than simply sending the pulse through an increased amount of gain media. The large peak powers from the ultrashort duration of the pulses quickly becomes much greater than the optical damage threshold for many optical components, which would lead to lasers with short operational lifetimes.

2.1.4 Chirped Pulse Amplification

Developed in 1985 [8], the nobel prize winning technique of CPA provides a method to amplify ultrashort laser pulses. Firstly, the incoming ultrashort laser pulse is stretched in time in the 'Stretcher', reducing the peak power of the pulse, preventing the pulses from overcoming the gain medium's damage threshold when it is amplified. After being stretched, the pulse is amplified in the 'Amplifier' and then the pulse is compressed in time, back into being ultrashort using the 'Compressor'. A block diagram of this is shown in Figure 2.7.

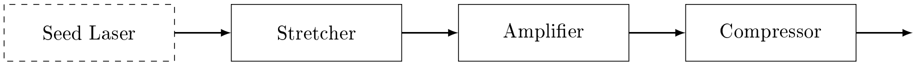

Figure 2.7: Block diagram of a CPA

2.1.4.1 Stretcher

Pulse stretching is achieved when the incident pulse undergoes chromatic dispersion, where the different wavelength components of the incident pulse are delayed with respect to each other. In free space systems this is normally achieved by either using dispersive prism pairs or diffraction gratings, however for powerful CPA systems, owing to the large amount of dispersion required to stretch the pulses to a safe enough peak power, diffraction gratings are much more common. When pulses reflect off, or pass through a diffraction grating they are dispersed spatially, allowing for the path lengths of each wavelength component to be altered. For a grating based pulse stretcher, the longer wavelength components are sent over a longer path than the shorter wavelength components before being recombined. The difference in path length stretches the pulse in time, thus reducing the peak power, as the average power is unchanged (disregarding losses). The recombination is performed with the split components passing through or reflecting off another grating, although this can also be performed using a single grating with two passes. [17]

2.1.4.2 Compressor

Pulse compression works inversely to pulse stretching, therefore it is possible to perform compression with the same optical components as a stretcher, such as prisms and gratings. Whilst stretchers increase the path lengths of longer wavelengths components, compressors increase the path lengths of the shorter wavelengths before they are recombined.

2.1.4.3 Amplification Geometries

The amplification step within a CPA system uses similar gain mediums to mode-locked laser oscillators, such as Ti:Sapphire for 800 nm wavelength systems. To prevent distortions of the resulting pulse's bandwidth, the gain medium must have a gain bandwidth greater or equal to the incident pulse's bandwidth [15].

The most simple geometry for performing amplification is to have the incident beam make a single pass through the gain medium (see Figure 2.8), however, this is not the most efficient geometry. A single pass gain stage only has a gain factor between two to five, but CPA systems often amplify the pulse by several orders of magnitude, meaning that many single pass gain stages would be required.

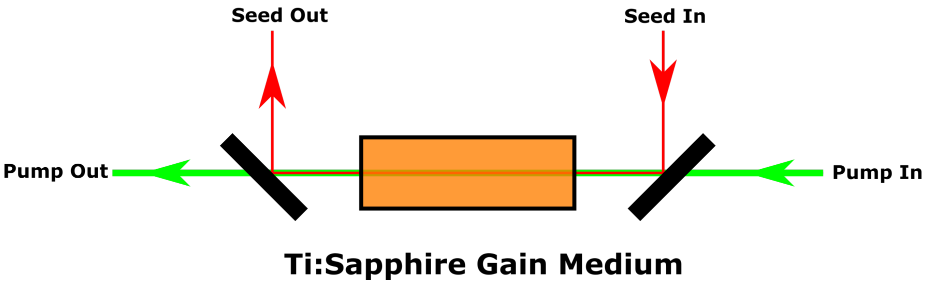

Figure 2.8: Optical diagram of a single pass amplification stage.

One alternative is to use a 'multi-pass' geometry (see Figure 2.9), in which multiple mirror pairs are placed either side of the gain medium's facets, allowing for the incident pulse to pass through the gain medium multiple times. This geometry does have a limit to the amount of gain that can be applied, as each extra pass through the gain medium must be carefully aligned to overlap with the pumped area.

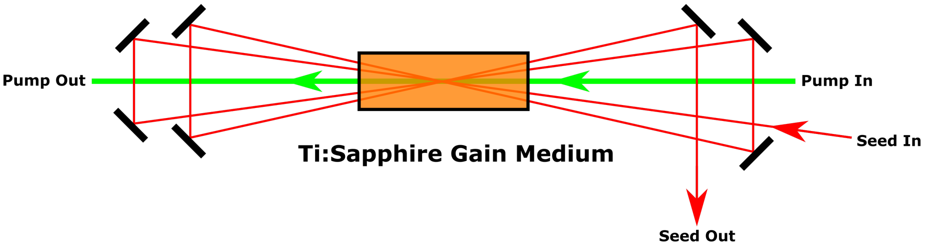

Figure 2.9: Optical diagram of a multi-pass amplification stage.

Another alternative is to use a 'regenerative' geometry (see Figure 2.10), in which the pulse is reflected an arbitrary number of times in an electrically controlled cavity. The pulses entering a regenerative cavity begin vertically polarised, but are reflected off a polariser into a quarter-wave plate ($\lambda/4$) and a Pockels cell, before being reflected back through the Pockels cell and quarter wave plate, towards the polariser. Pockels cells are electronically controllable polarisers, therefore it is possible to change the polarisation of the beam to become horizontally polarised before the beam is reflected back to the polariser, allowing it to pass through it and into the gain medium. To keep the pulse inside the cavity so it can pass through the gain medium multiple times, the Pockels cell polarisation is changed to keep the pulse horizontally polarised. After the pulse has passed through the gain medium a set number of times, the Pockels cell polarisation is then changed so that the pulse will be vertically polarised again, allowing for it to be reflected off the polariser, out of the cavity.

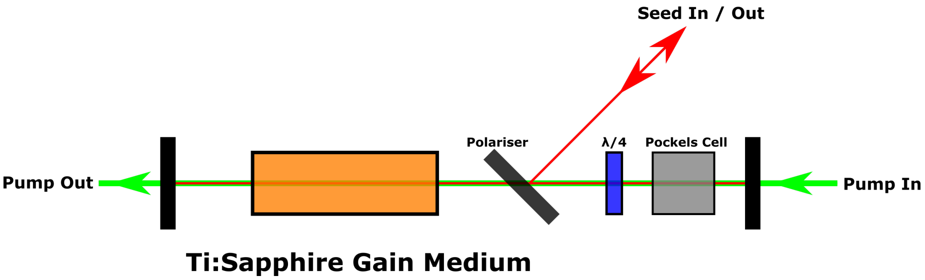

Figure 2.10: Optical diagram of a regenerative amplification stage.

2.1.5 Spitfire Ace PA Amplified Laser

The amplified laser used for this project was a Spitfire Ace PA (*Spectra-Physics*) [9]. It is a regenerative amplifier with an extra power amplifier section, capable of generating 800 nm pulses with a 40 fs width and 13 W average power, at a repetition rate of 1 kHz. A block diagram of the laser is shown in Figure 2.11, whilst a full optical diagram is shown in Figure 2.12. The following sections will describe the optical path of a pulse in the amplification cavity, referencing components shown in the full optical diagram.

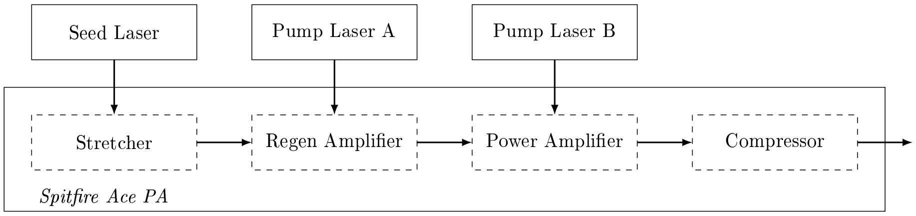

Figure 2.11: Block Diagram of the Spitfire Ace PA amplified laser used during this project.

2.1.5.1 Seed and Pump Lasers

The seed laser is a mode-locked Ti:Sapphire laser (*Spectra Physics Element*), emitting radiation with a wavelength of 800 nm with a pulse width of 20 fs at a repetition rate of 80 MHz. Rearranging Equation 2.7, the number of modes can be estimated as 276000, substituting $\Delta t = 20\,\mathrm{fs}$ and $\Delta v = 80\,\mathrm{MHz}$.

The pump lasers for both amplification stages are Q-switched, diode-pumped, frequency doubled Nd:YAG lasers (*Spectra Physics Ascend*), emitting radiation with a wavelength of 527 nm and an average power of 35 W at a repetition rate of 1 kHz.

Seed pulses first enter the amplifier and pass into a Faraday isolator (*F1*), preventing any reflected pulses from re-entering the seed laser, as the amplified pulses can cause significant damage to the seed laser's internal components. The Faraday isolator works by vertically polarising the seed pulse, then polarising by 45° using a Faraday rotator, and then finally polarising by another 45° using an analyser. The seed pulse will now be horizontally polarised. Any reflected pulses will not be able to pass through the Faraday isolator as it will be polarised by 45° in one direction by the analyser and then 45° in the other direction by the Faraday rotator, causing no net change in polarisation. The pulse being horizontally polarised will therefore not be able to pass through the input vertical polariser. [9,17]

2.1.5.2 Stretcher

After the Faraday isolator, the pulse then passes through a *Vertical Retro-Reflector (VRR)* and into the stretcher grating which splits different wavelengths in the pulse spatially. This allows for the longer wavelengths of the pulse to travel a longer path than the shorter wavelengths, stretching the pulse in time, reducing the pulse's peak power. The pulse is then reflected off a concave mirror (*M1*) to a normal mirror (*M2*), back to *M1* and then back through the stretching grating, recombining the pulse in space. The pulse then reflects off the *VRRs*, making a second pass through the stretcher. After this, the pulse is

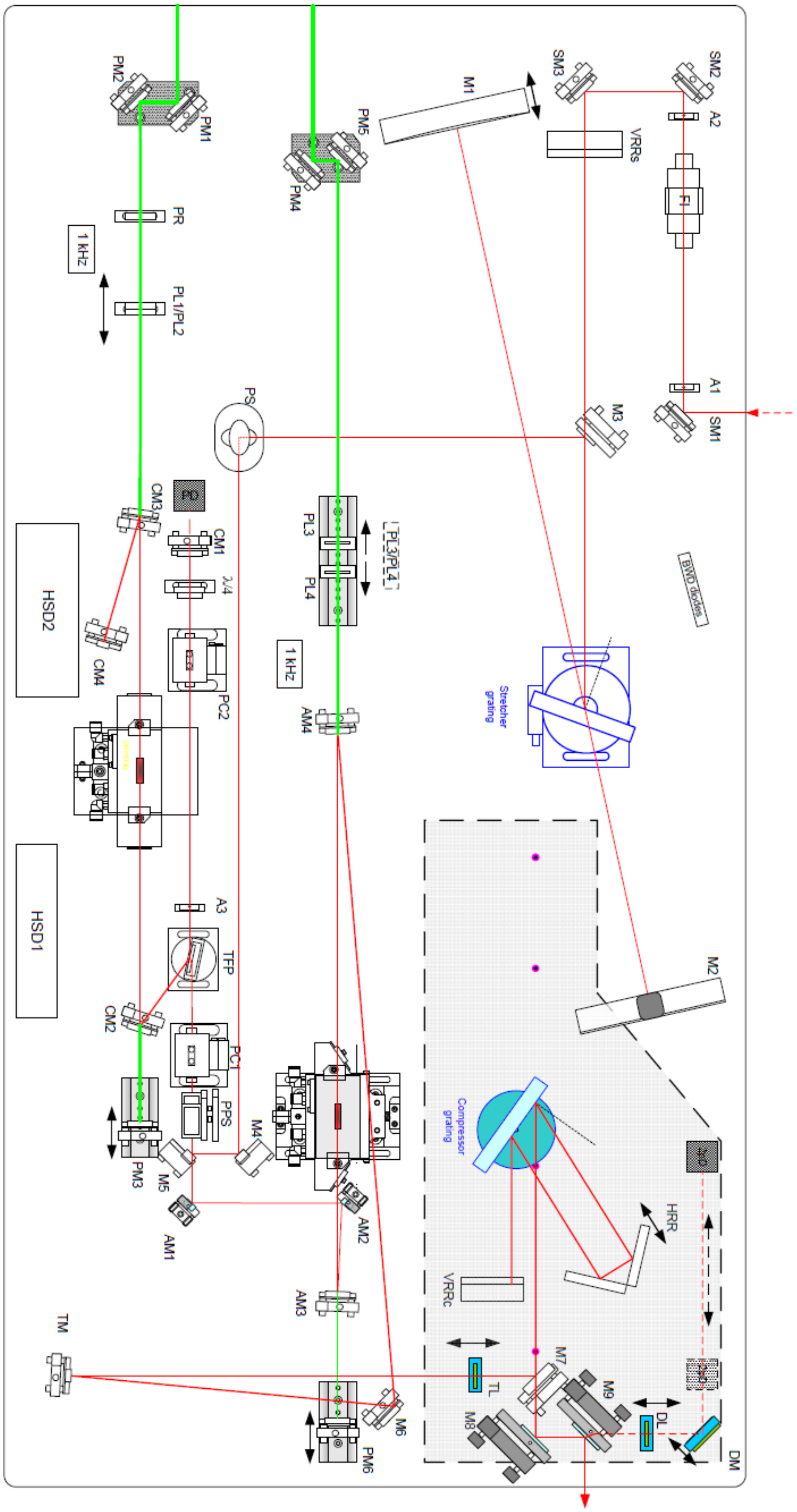

Figure 2.12: Optical Diagram of the Spitfire Ace PA (Provided by Spectra Physics) [9]

passed through a polarisation rotation periscope (*PS*) and reflected off *M4* and *M5* into the regenerative amplification section. [9,17]

2.1.5.3 Regenerative Amplifier

The beam's height is reduced by the polarising periscope *PPS* and then enters the Pockels cell *PC1*. If *PC1* is off, the vertically polarised pulse will pass through the cell without a change in polarisation, reflecting off the polariser *TFP* into a beam shield (not pictured). If *PC1* is on, the vertically polarised pulses undergo a 90° change in polarisation, allowing it to pass through *TFP*, into the second Pockels cell *PC2*.

If *PC2* is on, the horizontally polarised pulse will undergo a 45° change in polarisation, pass through the $\lambda/4$ waveplate, rotating the polarisation by another 45°, reflect off *CM1*, passing through the $\lambda/4$ waveplate and *PC2* again, leading to a net rotation of 180°. As the pulse is now horizontally polarised, it will pass through *TFP* and continue to the power amplifier section, unamplified.

If *PC2* is off, the horizontally polarised pulse will pass through the $\lambda/4$ waveplate, rotating the polarisation by 45°, reflect off *CM1* and pass through the $\lambda/4$ waveplate again, leading to a net rotation of 90°. As the pulse is now vertically polarised, it will reflect off *TFP*, onto *CM2* and then pass through the Ti:sapphire crystal, which is pumped by a Q-switched pump laser, creating a population inversion. This causes the optical pulse to increase in gain. The pulse is then reflected off *CM3* to *CM4*, then back to *CM3*, which reflects the pulse back through the Ti:sapphire crystal, performing the second gain pass. The pulse then reflects off *CM2* and *TFP* back into *PC2*.

If *PC2* is still switched off, the vertically polarised pulse will undergo the aforementioned 90° phase shift from the two passes through the $\lambda/4$ waveplate, causing the now horizontally polarised beam to pass through *TFP* and continue to the power amplifier section, amplified.

If *PC2* is switched on before the amplified pulse reaches it, it will undergo a 180° phase shift, owing to the two passes through the $\lambda/4$ waveplate and the Pockels cell, maintaining the vertical polarisation. This will cause the pulse to be trapped inside the cavity, as *TFP* will reflect the pulse back towards the Ti:sapphire crystal, increasing the pulse's gain with each subsequent pass until a threshold where saturation will begin to occur as the pumped state will become depleted until the next pump pulse travels through the crystal. The gain of an optical pulse coming out of this section can therefore be selected by carefully switching off *PC2*, just before the pulse with the requested gain reaches *PC2*.

The timing of both Pockels cells is synced to the 1 kHz repetition rate of the pump lasers and allows for just enough passes of the pulse through the crystal for gain saturation to occur, as this helps keep the output power stable.

As the pulse leaves the regenerative amplifier section for the power amplifier, it passes through *PPS*, increasing the height of the beam, allowing it to pass over *M5*, onto *AM1*. [9]

2.1.5.4 Power Amplifier

After the pulse reaches *AM1*, it is reflected off *AM2* and *AM3* and through the second Ti:Sapphire crystal, which is optically pumped by pump laser B. This second amplification stage is required to increase the pulse energy further, as the Ti:Sapphire crystal in the previous regenerative stage becomes depleted, reducing the population inversion between E_3 and E_2 and therefore the amount of gain which can be applied. Only one pass through the crystal in the power amplifier section is performed.

After the pulse passes through the second Ti:Sapphire crystal, it reflects off *AM4*, then off *M6* and into the telescope optics *TM* and *TL*, where it enters the compressor. [9]

2.1.5.5 Compressor

The pulses are directed onto the compressor grating by *M7*. The compressor grating splits different wavelengths of the pulse spatially, but causes the shorter wavelengths to travel a longer path, reducing the temporal stretching and increasing the pulse's peak power. The pulse is then reflected onto a *Horizontal Retro-Reflector (HRR)*, which can be adjusted to optimise the temporal compression, thus optimising the peak power. After reflecting off the *HRR*, it passes through the compression grating, into a *VRR*, reflecting it back into the compression grating, reversing any stretching effects. The amplified pulse then passes over *M7* onto the alignment optics, *M8* and *M9*, after which the pulse leaves the system. [9, 17]

2.2 Sources

This section summarises some of the sources used to generate high-field THz radiation, in particular, focusing on those driven by amplified lasers.

2.2.1 Photoconductive Emission

First described in 1984 [18], a Photoconductive Switch (PCS) (also known as a photoconductive antenna) is a device commonly used in free-space THz systems for both emission and detection. These devices consist of a semiconductor (commonly Low-Temperature-Grown GaAs (LT-GaAs) [19] or InGaAs [20]) on a host substrate (e.g. quartz [19] or Semi-Insulating GaAs (SI-GaAs) [21]), coated with metal contacts to form a small gap (usually 10–1000 µm in size). Figure 2.13 shows a schematic diagram of a PCS.

When these devices are electrically biased and have a femtosecond pulse of light incident on the semiconductor in the gap (band-matched to the semiconductor material), electron-hole pairs are produced. The bias then accelerates the excited carriers, causing a transient photocurrent, with the rise-time being proportional to the pulse width of the excitation pulse. The photocurrent then reaches a maxima and begins to decay, at a rate dependent on the electrical

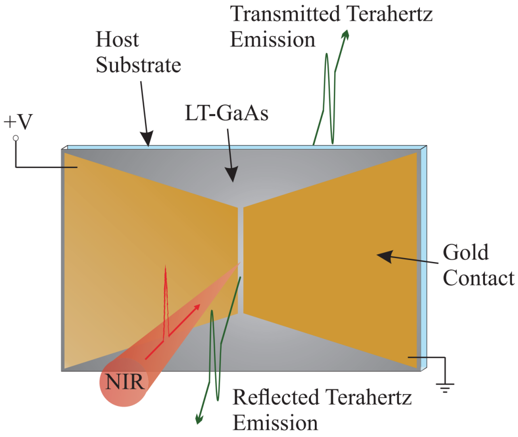

Figure 2.13: Schematic diagram of a PCS. Image taken from [22].

properties of the device (which will be discussed later in the section) [23]. This transient photocurrent generates a single cycle THz EM pulse, with a bandwidth usually covering 0.1–5 THz, although this is dependent on the pulse width of the excitation pulse and the electrical properties of the device. The field of the generated THz pulses are proportional to the change in the photocurrent over time and scale with the square of the applied bias [24]:

$$E_{\mathrm{THz}} \propto \frac{dI_{\mathrm{PC}}(t)}{dt}, \tag{2.9}$$

$$E_{\mathrm{THz}} \propto V^2. \tag{2.10}$$

When designing a PCS, there are certain device parameters which can be optimised to improve the emitted power, bandwidth and Signal-To-Noise Ratio (SNR). An optimal choice for the device's semiconductor material would have: a short carrier lifetime, as this would shorten the transient photocurrent, increasing the bandwidth of the emitted pulse; a high carrier mobility, as this would increase the strength of the generated photocurrent; a high dark resistivity, as this would reduce heating within the device from the applied bias; a large breakdown voltage, as this would allow for greater biases to be applied to the device without risking damage to the device; and a direct bandgap matched to the excitation beam's wavelength, as indirect bandgap materials have a longer recombination time, owing to the involvement of a phonon in the recombination process. When exciting at 800 nm, LT-GaAs is commonly used as the semiconductor material, owing to it having a direct band gap at ∼870 nm, a short carrier lifetime (∼300 fs), high breakdown field (∼500 kV cm^{-1}), reasonably good mobility (∼200 cm^2 V^{-1} s^{-1}) and a high dark resistance [25, 26]. When using LT-GaAs as the semiconductor material, SI-GaAs is commonly used as the substrate material [21], as it has suitable material properties for

THz generation and is needed to grow LT-GaAs using Molecular-Beam Epitaxy (MBE). It has a high carrier mobility ($\sim$8000 $\mathrm{cm^2\,V^{-1}\,s^{-1}}$) and a reasonable breakdown voltage (10–100 $\mathrm{kV\,cm^{-1}}$) [27]. SI-GaAs does however suffer from low resistivity and long carrier lifetimes ($\sim$100 ps [28]) which creates long lasting, parasitic current channels, causing excess heating, reducing the generation efficiency [29–31]. Z-cut quartz has been shown to be a promising alternative to SI-GaAs as a substrate [19] as it has a much greater dark resistivity, allowing for larger biases to be applied [32], whilst also preventing parasitic current channels. Quartz also has a lower refractive index at THz frequencies (~ 1.9 [33]) than SI-GaAs (~ 3.6 [34]), reducing the magnitude of the THz pulse being reflected back into the device at the substrate-air interface. Being optically transparent, the quartz substrate also allows for ‘through-substrate excitation’, where the excitation beam passes through the substrate before interacting with the semiconductor. This reduces the attenuation and broadening of the generated THz pulse, leading to a pulse of greater magnitude. LT-GaAs can be bonded to the quartz substrate after growth via Van der Waals bonding [19] or using Benzocyclobutene (BCB) [35]. Bonding via BCB is described in Section 3.1.

The design of the device’s electrodes also alters the performance of the device. Device efficiency has been shown to be inversely proportional to the gap size [31], with small gap devices (<100 µm) being more efficient for generating THz radiation, particularly at higher frequencies [29]. The shape of the electrodes has also been shown to affect the emission spectrum, with sharp edged electrodes increasing the emission bandwidth [29] and bow-tie shaped electrode increasing the device’s efficiency [26]. For larger gap devices (>1 mm), the electrode shape has a negligible effect [29]. The width of the device’s anode has also been shown to increase the efficiency of the device linearly owing to plasmonic oscillations caused by electrons arriving at the anode [36,37]. The cathode width was shown to have no effect on the generation efficiency. Figure 2.14 shows some of the more commonly used antenna designs [22].

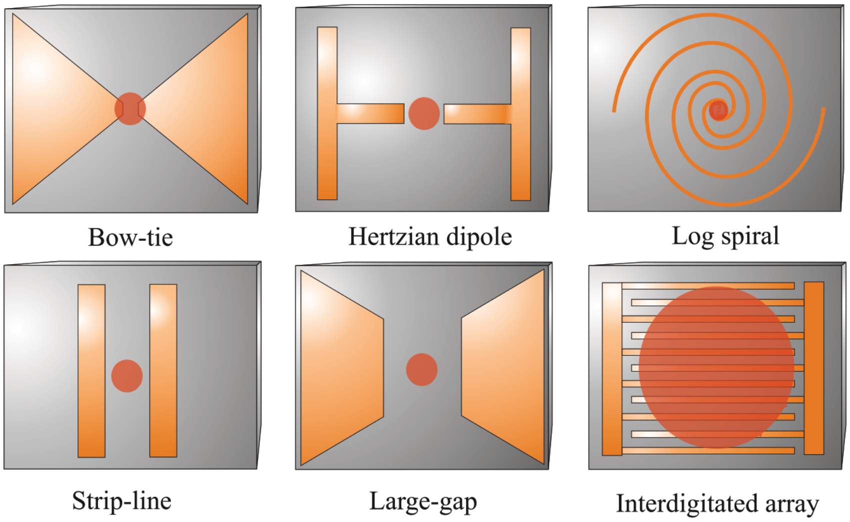

Figure 2.14: Various PCS antenna designs. Diagram taken from [22].

2.2.1.1 High Power Considerations

When using PCS to generate large THz fields (>50 kV cm^{-1}) there are certain design criteria that must be considered. Firstly, adequate thermal capacity is required to dissipate the large amounts of heat produced by the incident high power optical beam to prevent efficiency reduction or damage to the device. It is therefore practical to use the host substrate as a heatsink, making materials with a high thermal conductivity preferable. Large voltages are also required, making large gap devices and devices with a greater breakdown voltage most suitable. Using a PCS in an array configuration, known as a PCA is one solution and has certain benefits over single gap devices. These are discussed in detail in Chapter 3.

2.2.2 Electro-Optic Emission

Electro-Optic (EO) crystals are a popular choice for generating broadband and narrowband THz pulses, especially in high power pulsed systems, such as amplified laser systems. This is owing to their relatively high optical damage threshold, when compared with other devices, such as PCS.

In linear optical materials, the polarisation of light passing through the material can be determined using the following formula [1, 24, 38]:

$$P = \chi(E)E, \tag{2.11}$$

where $\chi(E)$ is the electrical susceptibility and E is the electric field. However, in EO crystals which are nonlinear, the polarisation is dependant on a series of terms, increasing in order:

$$P = (\chi_1 + \chi_2 E + \chi_3 E^2 + \chi_4 E^3 + \ldots)E. \tag{2.12}$$

As the main methods of generating THz radiation are second order effects, we only consider the second order term:

$$P_2 = \chi_2 E^2. \tag{2.13}$$

The following two sections discuss the main methods used to generate THz radiation: Difference Frequency Generation (DFG) and optical rectification.

2.2.2.1 Difference Frequency Generation

When two oscillating optical fields are incident on an EO crystal with differing frequencies of $E_1 = E_0 cos(\omega_1 t)$ and $E_2 = E_0 cos(\omega_2 t)$, the second order term becomes the following:

$$P_2 = \chi_2 E_1 E_2 = \chi_2 \frac{E_0^2}{2}[cos((\omega_1 - \omega_2)t) + cos((\omega_1 + \omega_2)t)]. \tag{2.14}$$

This causes the polarisation to oscillate at both the sum and difference frequencies, allowing for CW THz radiation to be generated. In practice, THz generation is often performed with the difference frequency interaction, with the technique referred to as DFG. [1, 24, 38]

2.2.2.2 Optical Rectification

When femtosecond pulses are incident on the EO crystal, the DFG occurs, with a mixing of all the frequencies within the pulse's bandwidth occurring. This causes a polarisation to occur within the crystal, proportional to the envelope of the incident pulse, with the emitted pulse's bandwidth being the inverse of the incident pulse's duration. As the optical pulse can be described in the time domain as:

$$E(t) = E_0 e^{(i\omega_0 t)} e^{(-at^2)}, \tag{2.15}$$

the time dependence in the polarisation can be said to be:

$$|P| \propto E_0^2 e^{-2at^2}. \tag{2.16}$$

This technique is used for generating broadband THz pulses.

To solve the polarisation in multiple dimensions, the multidimensional second-order susceptibility tensor χ^2_{ijk} is required. It requires 27 elements to be solved, however, owing to crystal symmetry, this often reduces to 18 or less, owing to many elements being zero. The element tensor can be written as a *d*-matrix:

$$d_{il} = \frac{1}{2}\chi^{(2)}_{ijk} \tag{2.17}$$

Equation 2.12 thus becomes:

$$\begin{pmatrix} P_x \\ P_y \\ P_z \end{pmatrix} = 2E \begin{pmatrix} d_{11} & d_{12} & d_{13} & d_{14} & d_{15} & d_{16} \\ d_{21} & d_{22} & d_{23} & d_{24} & d_{25} & d_{26} \\ d_{31} & d_{32} & d_{33} & d_{34} & d_{35} & d_{36} \end{pmatrix} \begin{pmatrix} E_x^2 \\ E_y^2 \\ E_z^2 \\ 2E_yE_z \\ 2E_xE_z \\ 2E_xE_y \end{pmatrix}. \tag{2.18}$$

Matrices for different crystal structures are discussed in section 2.2.2.6. [24,38, 39]

2.2.2.3 Coherence Length

Photons at different frequencies propagate through the crystal at different velocities, leading to deconstructive interference and pulse broadening. The coherence length is then the propagation length at which the coherence at a given frequency reduces significantly and can be described by the following equation:

$$l_c = \frac{c\tau_p}{n_T - n_O}, \tag{2.19}$$

where l_C is the coherence length, τ_p is the duration of the ultrashort optical pulse, n_T is the refractive index at THz frequencies and n_O is the refractive index at optical frequencies. The larger l_c is, the more efficient the generation becomes as the optical pulse will interact with a longer length of the crystal, increasing the generated field.

A metric related to the coherence length is the Group Velocity Mismatch (GVM), often quoted in units of $\mathrm{ps\,mm^{-1}}$ and is the difference in time that two pulses through a medium per unit length, with a lower number being better for EO generation.

2.2.2.4 Phase Matching

Improving the phase matching between the optical and THz pulses can allow for the coherence length to be increased as the destructive interference will be reduced. A common method of performing phase matching is to tilt the crystal to an angle determined by the following equation:

$$\theta_c = cos^{-1}(\frac{n_O}{n_{\mathrm{THz}}}). \tag{2.20}$$

Phase matching by this method has been shown to produce high pulse powers, however, the bandwidth is not as large as other techniques [24].

2.2.2.5 Optical Damage Threshold

An important property of EO crystals to consider, especially for high optical power systems, is the optical damage threshold. This threshold dictates the maximum optical power which can be incident on the crystal before it becomes irreversibly damaged. As greater optical powers generate higher field THz pulses, crystals with higher damage thresholds are preferred. Crystals with damage thresholds far away from the optical power often suffer from low conversion efficiency, so it is beneficial to have the damage threshold close to the operating power, although this can reduce the crystal's lifetime [40]. The optical damage threshold is dependant on the incident pulse's frequency, pulse width and repetition rate and differs from crystal to crystal. Typical values range from a few tens of $\mathrm{MW\,cm^{-2}}$ to a few hundred $\mathrm{GW\,cm^{-2}}$ [41–43].

2.2.2.6 Commonly Used Electro-Optic Crystals

This section will discuss some of the more commonly used EO crystals in systems using a 800 nm excitation beam. The important information is also summarised on Table 2.2.2.6.

ZnTe is potentially the most commonly used crystal for THz generation, owing to it being phased matched at 800 nm to 1.6±1.0 THz emission at and having a good EO coefficient of $3.9\,\mathrm{pm\,V^{-1}}$ [44]. The major limitation of ZnTe is that it has a relatively small bandwidth owing to its first Transvere-Optical (TO) phonon being at 5.3 THz [45]. TO phonons in EO crystals cause a massive reduction in emission and detection frequencies at their resonant frequencies, causing dips in the emitted or detected spectra. Being a zincblende crystal the d matrix takes the following form:

$$\begin{pmatrix} 0 & 0 & 0 & d_{14} & 0 & 0 \\ 0 & 0 & 0 & 0 & d_{14} & 0 \\ 0 & 0 & 0 & 0 & 0 & d_{14} \end{pmatrix}. \tag{2.21}$$

GaP is a common alternative to ZnTe owing to it also not requiring any awkward phase matching techniques at 800 nm. The first TO phonon does not appear until 8 THz [46], allowing for a greater bandwidth in emission and detection, however, it has a much smaller EO coefficient (d_{14}) of $0.97\,\mathrm{pm\,V^{-1}}$ [47], reducing the magnitude of the generated or detected pulse. GaP has a zincblende structure and therefore the same d matrix as ZnTe.

GaSe is another alternative to ZnTe as it has a slightly higher frequency TO phonon at 6.4 THz [48], a much larger EO coefficient of $14.4\,\mathrm{pm\,V^{-1}}$ [49] and is usually quoted with having a larger damage threshold than ZnTe [42], however, it must be phase matched by being tilting around the horizontal axis. Different tilting angles have been shown to alter the magnitudes of different parts of the emission and generation spectra [50, 51]. This tilt based phase matching has been shown useful for generation of tunable narrowband THz emission, where the emission frequency is set by the tilt of the crystal. [52]. GaSe has a hexagonal structure and is therefore birefringent, meaning that it has only one optical axis. Its d matrix is as follows:

$$\begin{pmatrix} 0 & 0 & 0 & 0 & 0 & d_{16} \\ d_{16} & -d_{16} & 0 & 0 & 0 & 0 \\ 0 & 0 & 0 & 0 & 0 & 0 \end{pmatrix}. \tag{2.22}$$

When looking at only the EO coefficient and first phonon frequency, Lithium Niobate ($LiNbO_3$) appears to be an ideal crystal for THz generation, with values of $27\,\mathrm{pm\,V^{-1}}$ [1] and 7.7 THz [53] respectively. However, it suffers from a large mismatch between the optical and THz phase velocities, making it ineffective for collinear generation. This phase mismatch can be resolved by tilting the optical pulses as discussed in Section 2.2.2.4, with a phase matching angle of $\sim 64°$ [1]. The tilt of the optical pulse is induced by reflecting the pulse off a diffraction grating, after which the beam is collimated and then focused through the crystal. The resulting THz radiation is emitted at $\sim$64° from the incident beam. Systems using $LiNbO_3$ often employ cooling of the crystal, as most of the generated THz radiation is absorbed by the optical phonon decaying into two acoustic phonons, but this is reduced at lower temperatures [1]. The bandwidth from pulses generated using $LiNbO_3$ are rarely greater than ~ 2 THz however. $LiNbO_3$ has a trigonal structure and thus, the d matrix takes the following form:

$$\begin{pmatrix} 0 & 0 & 0 & 0 & d_{31} & -d_{22} \\ -d_{22} & d_{22} & 0 & d_{31} & 0 & 0 \\ d_{31} & d_{31} & d_{33} & 0 & 0 & 0 \end{pmatrix}. \tag{2.23}$$

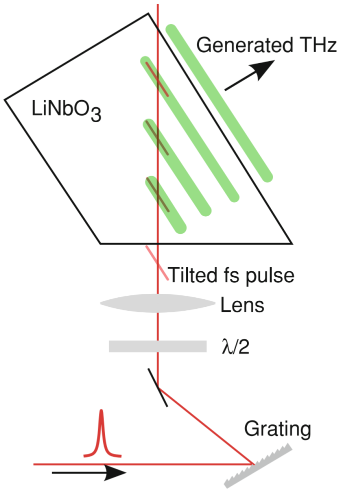

Figure 2.15: Optical path of THz generation using a $LiNbO_3$ crystal, using a grating to tilt the incident pulse front. Image taken from [24].

First synthesised in 1989 [54], Diethylaminosulfur Trifluoride (DAST) is the most widely used organic crystal for THz generation. It has a large EO coefficient at 800 nm of $160\,\mathrm{pm\,V^{-1}}$ [44], but is limited at lower frequencies owing to two TO phonons at 1.1 THz and 3 THz [55]. It has a similar GVM to ZnTe and does not require any phase matching techniques.

Another organic crystal comparable with DAST is N-Benzyl-2-Methyl-4-Nitroaniline (BNA). It was first developed as a derivative from another organic crystal, 2-Methyl-4-Nitroaniline (MNA), known for being difficult to grow effectively [56, 57]. It has a large EO at 800 nm of $\sim 234\,\mathrm{pm\,V^{-1}}$ [58] at 800 nm and despite having a phonon at 2.3 THz [38], it is capable of generating with a bandwidth of 15 THz [58]. Similarly to ZnTe, it does not require any phase matching techniques to be used, owing to the optical refractive index matching the THz refractive index.

Crystal	EO Coeff (pm/V)	1st Phonon Frequency (THz)	Crystal Class	GVM (ps/mm)	Structure	Material Type
BNA	234	2.3	$mm2$	0.2	Monoclinic	Organic Crystal
DAST	160	1.1	m	1.22	Monoclinic	Organic Crystal
GaP	0.97	11	$\bar{4}3m$	-	Zincblende	Semiconductor
GaSe	14.4	6.4	$\bar{6}2m$	0.1	Hexagonal	Semiconductor
$LiNbO_3$	27	7.7	$3m$	14.1	Trigonal	Inorganic Crystal
ZnTe	3.9	5.3	$\bar{4}3m$	1.1	Zincblende	Semiconductor

Table 2.1: Properties of commonly used EO crystals at 800 nm excitation wavelength.

2.2.3 Plasma Emission

Generation of THz radiation from air plasma was first established in 1993 [59], with the plasma being generated by focused, high power femtosecond laser pulses. The THz radiation is created by the acceleration of charged particles in the inhomogeneous EM field within the air plasma, known as the ponderomotive force. Further experiments attempting to improve air plasma generation found that adding a parallel Second-Harmonic (SH) pulse at double the frequency of the main pulse greatly improved the generation efficiency, as the SH pulse applies a transverse bias to the plasma [60]. The SH generation is often performed by a type-I β-Barium Borate (BBO) crystal placed after the focusing lens (see Figure 2.16). Other methods of improving the THz generation include applying a bias to the plasma, which causes a linear increase [61]; shortening the laser pulse's duration, which increases the magnitude and bandwidth [62]; using a gas with a greater breakdown voltage (such as Nitrogen) and increasing the pressure of the gas [63]. As this method of generation is not limited by damage threshold, the maximum THz field possible with plasmas is limited by the excitation beam power, allowing for fields in the $\mathrm{MV\,cm^{-1}}$ range to be obtained, however, this requires very large pulse energies.

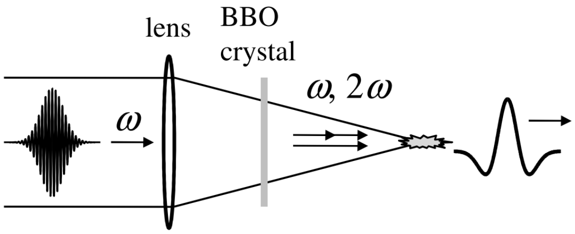

Figure 2.16: Optical path of plasma generation using a BBO crystal. Image taken from [1].

2.3 Detectors

This section summarises some of the detection schemes used in THz spectroscopy systems, focusing on laser driven detectors, capable of performing coherent detection (where amplitude and phase of the electric field are acquired). To perform 2D spectroscopy, phase and amplitude information of the electric field is critical for acquiring 2D Fourier transforms (see Section 2.4.3).

2.3.1 Photoconductive Detection

To use a PCS for detection of THz radiation, an additional femtosecond 'sampling' pulse is required. When the probe pulse is focused onto the PCS gap, electron-hole pairs are generated in the device's semiconductor material. Incident THz radiation then causes these charges to become accelerated owing to the electrical field of the radiation, generating a current in the gap, proportional to the field of the THz pulse. The instantaneous current can be calculated using the following equation:

$$J(t) = \int_{-\infty}^{t} E_{\mathrm{THz}}(t')\sigma(t-t')dt', \tag{2.24}$$

where E_{THz} is the energy of the THz pulse and $\sigma(t)$ is the conductivity induced by the femtosecond pulse. In the frequency domain, the relationship can be seen to be:

$$\tilde{J}(v) = \tilde{\sigma}(v)\tilde{E}_{\mathrm{THz}}(v), \tag{2.25}$$

where $\tilde{J}(v)$, $\tilde{\sigma}(v)$ and $\tilde{E}_{\mathrm{THz}}(v)$ are the Fourier transforms of $J(t)$, $\sigma(t)$ and $E_{\mathrm{THz}}(t)$ respectively. This shows that a slower recapture time will reduce the detectable bandwidth, as a faster recapture time will lead to a greater change of $\sigma(t)$. [24]

The induced photocurrent is often fed into a transimpedance amplifier, allowing for the small current to be converted proportionally into a voltage. As the generated photocurrents are small, it is preferable to use a semiconductor with a high dark resistivity, as the dark current will be a source of noise [64].

Although PCSes work well as detectors for high repetition rate systems as multiple measurements of the small generated currents can be performed quickly, however, they are not ideal candidates for low repetition rate systems, such as ones using amplified lasers.

2.3.2 Electro-Optic Detection

EO crystals may also be used for detection of THz radiation, by use of the Pockels effect. The Pockels effect occurs when a static electric field is applied to an EO crystal, causing the polarisation of any incident radiation to change, proportional to the strength of the electric field. This effect is also utilised in Pockels cells, as described in Section 2.1.4.3. In Pockels cells, the electric field is generated by a controllable power source, however in EO detection, the field of incident THz pulse is used. The THz pulse that is to be detected is focused onto a spot on the EO crystal's surface and a femtosecond pulse is also focused onto the same spot. The incident femtosecond pulse is short compared to the THz pulse, therefore, the resulting change in polarisation becomes proportional to the instantaneous strength of the THz field. The phase of the incident femtosecond pulse is also dependent on the THz pulse with the following relation:

$$\Gamma \propto \frac{1}{\lambda} L n_0^3 d_{41} E_{\mathrm{THz}}, \tag{2.26}$$

where λ is the wavelength of the incident pulse, L is the crystal thickness, d_{41} is the electro-optic coefficient and n_0 is the refractive index of the crystal at the incident pulse's frequency.

After the femtosecond pulse passes through the EO crystal, it then travels through a quarter-wave plater, causing the beam to be split into uneven X and Y components, owing to its elliptical polarisation. The X and Y components are then separated into two pulses using a Wollaston prism. The difference in intensity between each component is then detected using balanced photodiodes (see Figure 2.17). The field of the detected THz pulse can then be calculated using the following equation:

$$I_s = I_y - I_x = \frac{I_0 \omega L}{c} n_0^3 d_{41} E_{\mathrm{THz}}, \tag{2.27}$$

where I_x and I_y are the intensities of the X and Y components, I_0 is the beam intensity without an incident THz field and ω is the angular frequency. It should be noted that equation is only valid in the linear regime. To acquire a more accurate value of the detected field, further corrections can be added to this equation which are discussed in Appendix 8.1.

Owing to the nature of this detection method requiring the interaction between THz pulses and femtosecond pulses which have different wavelengths, the coherence length of the EO crystal (described in section 2.2.2.3) must be taken into account. This causes thinner crystals to have a larger detection bandwidth, but a decreased sensitivity. [22]

Crystal phonons must also be considered when choosing a detection crystal, as the phonons cause gaps in the detection bandwidth at their resonant frequency, making it hard to resolve information at those frequencies. ZnTe, GaP, GaSe and $LiNbO_3$ are commonly used crystals for detection. For this project, a thin (150 µm) GaP crystal was used for characterising emitters (see Section 3.3) due to the larger detection bandwidth, but for sample measurements, a thicker (1 mm) ZnTe crystal was used due to the better SNR and because the reflections of the THz pulse are pushed back further in time, increasing spectral resolution (see Section 2.4.1).

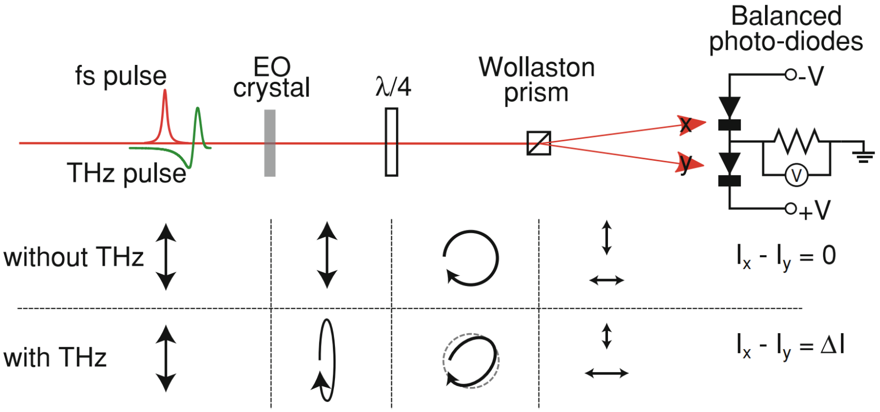

Figure 2.17: Optical path of EO detection. Arrows below diagram denote the polarisation of the femtosecond pulse, with and without THz radiation incident on the detection crystal. Image taken from [24].

2.3.3 Noise Reduction Instruments

This section describes some of the instruments used in detection schemes to reduce noise.

2.3.3.1 Lock-In Amplifier

A Lock-In Amplifier (LIA) is a instrument commonly used in THz detection systems to acquire a signal obscured by large background noise. The input signal to the LIA ($V_{\mathrm{In}}(t)$) can be represented using the following equation [65]:

$$V_{\mathrm{In}}(t) = V_0 \sin(\omega_0 t + \theta_0) + V_{\mathrm{N}}(t), \tag{2.28}$$

where $V_{\mathrm{N}}(t)$ is the noise and V_0, ω_0 and θ_0 are the amplitude, angular frequency and phase of the input signal respectively. V_0 and θ_0 are the components of the signal to be extracted. A reference signal (which will be used to modulate the input signal) is fed into the LIA, wherein a sine wave of frequency ω_{R}, matching the frequency of the reference signal, is generated by a Voltage-Controlled Oscillator (VCO), producing the internal reference signal ($V_{\mathrm{Ref}}(t)$):

$$V_{\mathrm{Ref}}(t) = V_{\mathrm{R}} \sin(\omega_{\mathrm{R}} t + \theta_{\mathrm{R}}), \tag{2.29}$$

where V_{R} and θ_{R} are the amplitude and phase of the reference signal respectively. The input signal and the internal reference signal are then mixed together:

$$\begin{aligned} V_{\mathrm{Mix}}(t) = V_{\mathrm{In}}(t)V_{\mathrm{Ref}}(t) = &\frac{1}{2}V_0 V_{\mathrm{R}} \cos([\omega_0 - \omega_{\mathrm{R}}]t + \theta_0 + \theta_{\mathrm{R}}) \\ &- \frac{1}{2}V_0 V_{\mathrm{R}} \cos([\omega_0 + \omega_{\mathrm{R}}]t + \theta_0 + \theta_{\mathrm{R}}) \\ &+ V_{\mathrm{N}}(t) V_{\mathrm{R}} \sin(\omega_{\mathrm{R}} t + \theta_{\mathrm{R}}). \end{aligned} \tag{2.30}$$

The mixed signal is then passed through a Low-Pass Filter (LPF), blocking all Alternating-Current (AC) signals. If ω_0 is set to the same frequency as ω_{R}, the difference frequency component of $V_{\mathrm{Mix}}(t)$ becomes a Direct-Current (DC) signal:

$$V_{\mathrm{LPF}}(t) = \frac{1}{2}V_0 V_{\mathrm{R}} \cos(\theta_0 - \theta_{\mathrm{R}}). \tag{2.31}$$

As V_{R} and θ_{R} are known, V_0 and θ_0 can be acquired without noise signal $V_{\mathrm{N}}(t)$ present in the input signal (Equation 2.28).

2.3.3.2 Boxcar Averager

A boxcar averager, also known as a boxcar integrator, is another method of reducing noise in systems, particularly when the signal of interest has a relatively short period when compared to the background, such as ultrashort pulses from low repetition rate laser systems. For the amplified laser used in this project, the pulses are 40 fs every 1 ms which in turn causing a response on the photodiodes with a period of ~3 µs giving a very low duty cycle of 0.003.

An ideal boxcar can be imagined as a periodic box function with an amplitude of 1 and width equal to the peak of interest being multiplied with the periodic input signal. The signal in the box function is then integrated to acquire the resulting in a digitised value. Any noise outside of the pulse of interest is then suppressed as it is multiplied by 0 from the box function. To improve the SNR further, the result of each period of the boxcar signal can be averaged. The SNR can be approximated using the following formula [66]:

$$\mathrm{SNR}_{\mathrm{Out}} = \mathrm{SNR}_{\mathrm{In}} \sqrt{n}, \tag{2.32}$$

where n is the number of averages.

2.4 Time Domain Spectroscopy

Whilst other methods of spectroscopy measure directly in the frequency domain or using light intensity, TDS acquires spectral features by measuring the electric field of a pulse in the time-domain and later performing a Fourier transform to it. Unlike intensity based measurements (e.g. bolometer based measurements), THz-TDS measurements can also retrieve phase information, by sampling the electric field directly, allowing for information to be acquired directly from the sample, such as real and complex dielectric properties, the refractive index and absorptions. THz-TDS has become a common technique in the field of THz spectroscopy as it is a coherent form of detection that can be performed in free space systems and can have a high SNR without requiring a cryogenically cooled emitter or detector. THz-TDS systems use femtosecond lasers (such as fibre or Ti:Sapphire lasers) to drive both emission and detection, allowing for broadband spectroscopy to be performed. [67]

2.4.1 One Dimensional Spectroscopy

In One-Dimensional (1D) THz-TDS systems (see Figure 2.18), a time-domain pulse is built up over multiple measurements using two femtosecond pulses which will be referred to as the 'sampling' pulse and the 'probe' pulse. The 'probe' pulse is used to activate the emitter (such as a PCS or a EO crystal), generating the broadband THz pulse, meanwhile the 'sampling' pulse activates the broadband THz detector. When the detector is illuminated by the 'sampling' pulse and the broadband THz pulse produced by the emitter, an instantaneous reading is taken of the THz pulse, as the period of the femtosecond pulse is much smaller than the THz pulse, which is normally several picoseconds. To build up the full measurement of the THz pulse in the time domain, the delay between the 'probe' and 'sampling' beams is changed, allowing for a sample of a different point in time to be acquired. This delay in usually achieved by use of a mirror attached to a moveable stage, particularly in systems where only one femtosecond laser is used to generate the 'probe' and 'sampling' pulses. As the detector is only active when both the sampling and THz pulses hit it simultaneously, a high SNR can be achieved [67].

Once a time-domain signal is obtained, it can be fourier transformed to obtain frequency information. The resolution of the resulting fourier transform is proportional to the time range of time of the time-domain signal. This length is normally limited by reflections in the system rather than the length of the delay stage, as these reflection cause pulses to appear in the time domain data. When EM radiation passes through an interface of differing refractive indexes, part of the signal is reflected back, with the delay between the reflection calculated using the following equation:

$$t = \frac{2nL}{c}, \tag{2.33}$$

where n is the refractive index and L is the length of the sample. The reflections cause oscillations to appear in the frequency domain, making it difficult to

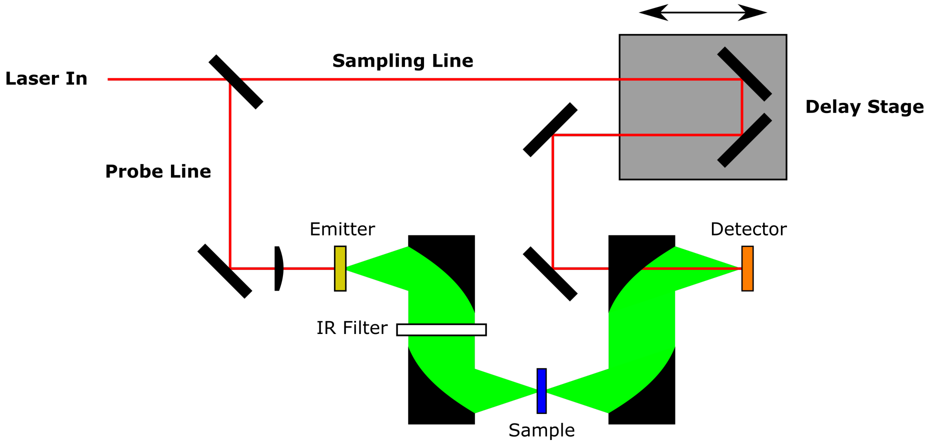

Figure 2.18: Example of a 1D THz TDS system using transmission geometry.

resolve spectrally narrow features [68]. To remove these features, the scan data is often windowed in post-processing to just before the first reflection. The most common causes of reflections are from the emitter, detector and sample. Adding a thin metal subsurface layer to the emitter [69] or an anti-reflective coating to the detector [68] has shown to greatly reduce the magnitude of these reflections, however this comes at the cost of reducing the emitted or detected THz signal.

An example of data obtained using TDS and the resulting Fast Fourier Transform (FFT) is shown in Figure 2.19.

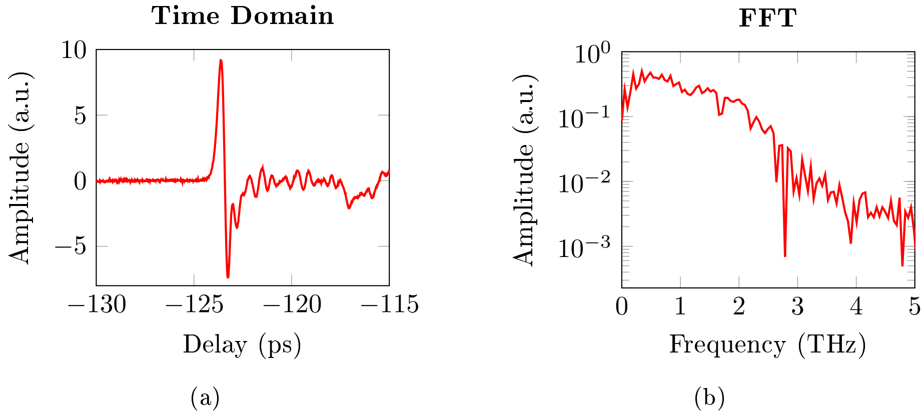

(a) (b)

Figure 2.19: Example of data from a TDS measurement and its resulting FFT.

To improve SNR further, signal processing hardware or software is often used, the most common being a LIA (see Section 2.3.3.1). Systems using a LIA require the probe pulses to be modulated on and off at a set frequency, with this frequency used as a reference in the LIA. This modulation is usually performed with either a mechanical chopper which periodically blocks the ‘probe’ beam, or via electrical modulation when using a PCS. The LIA is also setup with a ‘time constant’ which averages the received signal over a given time period, also increasing SNR at the expense of scan time. Measurements are also normally performed in a purged air environment to prevent absorption of the THz radiation from the water vapour in the air.

To obtain information about a given material, measurements are performed on a sample and then compared to a reference [1, 24]. A time domain THz pulse after being Fourier transformed into the frequency domain can be represented as:

$$E(\omega) = \int_{-\infty}^{\infty} E(t) e^{i\omega t} dt, \tag{2.34}$$

where $E(t)$ is the electric field of the pulse. The complex refractive index of a material is defined as:

$$N = n + ik, \tag{2.35}$$

where n is the real refractive index and k is known as the extinction coefficient. n represents the time delay in the light travelling through the medium, whilst k represents the attenuation of the electric field travelling through the medium and can be obtained using:

$$k = \frac{c\alpha}{2\omega}, \tag{2.36}$$

where α is the absorption coefficient of the medium. This in turn is defined as the inverse of the distance where the intensity of an incident pulse is reduced to $1/e$ of its original intensity. For homogeneous samples, the Beer-Lambert law can be used:

$$I = I_0 e^{-\alpha d}, \tag{2.37}$$

where I is the measured electric field intensity, I_0 is the initial electric field intensity and d is the distance the electric field has propagated into the sample, usually the thickness of the sample. To acquire the real refractive index (n), of a sample of a known thickness (d), the following equation can be used:

$$n_{\mathrm{S}} = n_{\mathrm{R}} + \frac{\delta t c}{d}, \tag{2.38}$$

where n_{S} and n_{R} are the real refractive indexes of the sample and reference respectively and δt is the time difference between the sample and reference pulses arriving at the detector. This complex refractive index also relates to the complex dielectric constant with the following relation:

$$\epsilon_r = N^2. \tag{2.39}$$

The transmission coefficient as a function of frequency can be obtained by dividing the Fourier transform of the sample signal by the reference signal:

$$T(\omega) = \frac{E_{\mathrm{S}}(\omega)}{E_{\mathrm{R}}(\omega)}. \tag{2.40}$$

The above equations only provide an estimate of the complex refractive index. Further processing involving transfer functions are required to obtain a more accurate value [70].

The most common sample set-up for a THz-TDS system is a ‘transmission’ configuration, in which the THz radiation is focused onto a sample using parabolic mirrors and is then collected at the other side of the sample by a separate mirror and focused onto the detector. Reference measurements are performed by simply having no sample in the set-up, or using a substrate material when thin layer samples are being measured.

While most THz-TDS systems have a ‘transmission’ based set-up (i.e. the THz radiation passes through the sample and is measured on the other side), it is in some cases impractical to perform measurements this way if a material is too reflective in the THz region, as not enough signal will be detected by the receiver. It is still possible to perform THz-TDS measurements with these materials, but it requires a slightly different experimental set-up. In a reflection TDS system, the THz radiation is focused onto the sample and then reflected off and gathered by a parabolic mirror, to be focused onto the detector. In most cases, to obtain a reference sample, a material with close to 100% reflectivity in the THz region is used, such as a metal mirror. If the sample has a high reflectivity however, a reference must be taken using a material with low reflectivity (e.g. silicon). [71–73]

2.4.2 Pump-Probe Spectroscopy

In pump-probe TDS systems, a third beam is added into the system, known as the pump pulse. This pump pulse may be broadband or narrowband and may be in the THz frequency range or otherwise. The probe pulse however is in the THz range, and relatively weak in field to prevent nonlinear interactions with a given sample. The pump pulse is used to excite samples, creating responses that would otherwise not appear without it, for example, exciting a specific electron transition. The probe beam can then investigate how that transition interacts with the rest of the sample. If the pump beam is pulsed and can be delayed in time, then time resolved pump-probe spectroscopy is possible, wherein the delay between the pump and probe is changed, allowing for the evolution of the response over time to be measured.

When acquiring a pump-probe response from a sample, the probe signal measurement with and without the pump beam incident must be acquired. This is usually done by chopping the pump and ‘probe’ beams at different frequencies or at the same frequency but out of phase with each other. The response induced by the pump is then acquired with the following equation:

$$E_{\text{Response}}(\omega) = \frac{E_{\text{Probe+Pump}}(\omega)}{E_{\text{Probe}}(\omega)}. \tag{2.41}$$

Optical pump, THz probe measurements are the most commonly used THz TDS pump-probe technique and have been shown to be able to investigate carrier dynamics in semiconductors [74, 75] and nanoparticles [76], as well as vibrational spectroscopy in condensed matter systems [77,78]. THz pump, THz probe measurements have been shown to be able to investigate the gain recovery time in Quantum Cascade Lasers (QCLs) [79].

2.4.3 Two Dimensional Spectroscopy

Broadband 2D TDS systems are similar in design to broadband pump-probe systems with both systems utilising two broadband THz pulses, the main difference being that in 2D systems, both excitation pulses are powerful enough to induce nonlinear responses within the sample. 2D spectroscopy is a well defined technique for Infrared (IR) spectroscopy [80], but is still a relatively new technique for THz spectroscopy [81]. In IR 2D spectroscopy, 'photon echo' experiments utilising three, non-collinear excitation pulses are the most commonly used [80]. The first pulse causes the sample to become coherently polarised and then shortly after, at a delay time of τ, the second pulse excites the sample. After another delay of T, the third pulse interacts with the sample, generating the nonlinear signals. To acquire phase and amplitude information of the nonlinear signal, a fourth, low power pulse heterodynes with this signal, acting as a local oscillator [80,82]. This technique is analogous to Nuclear Magnetic Resonance (NMR) [83]. As these pulses are non-collinear, the different nonlinear signals generated are separated in space on the detector. In 2D THz TDS, only two excitation pulses are required to generate the nonlinear signal (E_{NL}) as the amplitude and phase of both excitation pulses are acquired as a function of time when performing TDS. To acquire the nonlinear response, all possible combinations of the pulses incident on the sample are required; E_{A} (only signal 'A' on the sample), E_{B} (only signal 'B' on the sample) and E_{AB} (signals 'A' and 'B' on the sample simultaneously). The following equation acquires the nonlinear response:

$$E_{\mathrm{NL}}(t,\tau) = E_{\mathrm{AB}}(t,\tau) - E_{\mathrm{A}}(t) - E_{\mathrm{B}}(t,\tau), \tag{2.42}$$

where τ is the delay between the two pulses and t is the delay of the sampling beam. The nonlinear response only occurs when both beams 'A' and 'B' are incident on the sample (E_{AB}), therefore when there is no nonlinear response in a material, $E_{\mathrm{AB}} = E_{\mathrm{A}} + E_{\mathrm{B}}$. The four states can be acquired by chopping pulses A and B at the same frequency but 90° out of phase. Figure 2.20 shows an example of a system with no nonlinear response compared with a fictitious nonlinear response. In this example, obvious pulse broadening can be seen in E_{AB} when the nonlinear response is present, however in reality, the nonlinear response is often more subtle (e.g. the nonlinear signal having a peak field of $\sim 25\,\mathrm{V\,cm^{-1}}$ with a pump field of $\sim 11\,\mathrm{kV\,cm^{-1}}$ [84]). Delays t and τ are altered throughout the measurement, allowing for a 2D time domain nonlinear signal to be acquired. This can then be transformed into the frequency domain in terms of t and τ by performing a 2D FFT, allowing for the nonlinear signal to be interpreted.

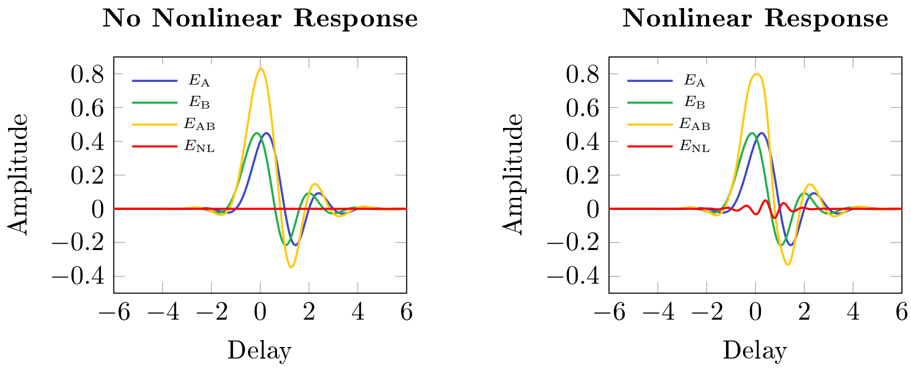

(a) Simulation where E_AB does not induce a nonlinear response.

(b) Simulation where E_AB does induce a nonlinear response.

Figure 2.20: Simulation of time-domain pulses in a 2D THz TDS system and the resulting nonlinear response.

There are two possible beam geometries for 2D spectroscopy setups; collinear (see Figure 2.21) and non-collinear (see Figure 2.22). In a collinear setup, both pulses are combined using a beamsplitter before being focusing onto a sample. This beam combination can either be done for the excitation beams, meaning that only a single emitter is required to generate both intense pulses, or for the intense THz pulses, using a THz beamsplitter such as a Si wafer or a pellicle beamsplitter. In non-collinear setups, the pulses are only combined in space on the sample, usually achieved by having the beams reflecting off different areas on the parabolic mirror used to focus the pulses onto the sample. Collinear setups have the advantage of being much simpler to align, making them more reliable for combining both beams onto the same point on the sample, however this comes at the cost of reducing the peak field that can be applied to the sample. For two emitter collinear systems, this is owing to a proportion of the THz beam being lost at the beamsplitter, whilst for single emitter systems, this is from the optical power of both excitation beams combined being less than the damage threshold of the emitter. Non-collinear systems, despite having a potential for generating greater fields, also suffer from a reduction in the detected nonlinear response from the phase mismatch, owing to the limited spatial interaction of both pulses on the sample. This also limits the thickness of samples that non-collinear measurements can be performed on [81].

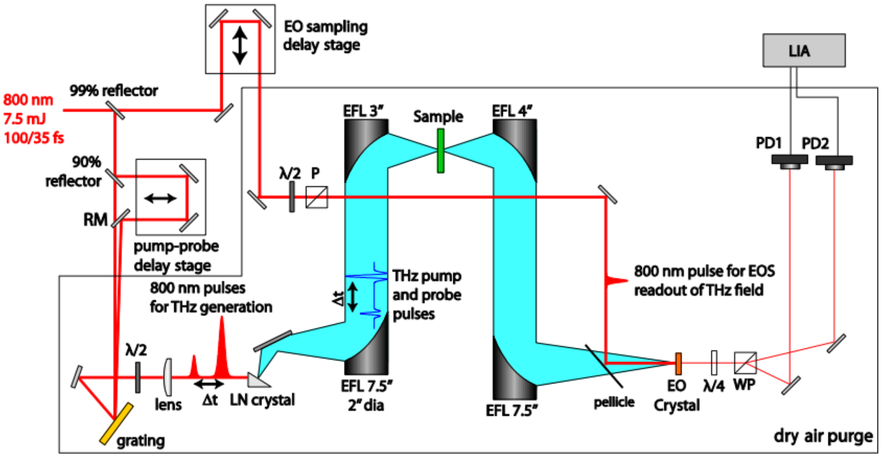

Figure 2.21: Example of a 2D THz TDS system using a collinear geometry. Image taken from [85].

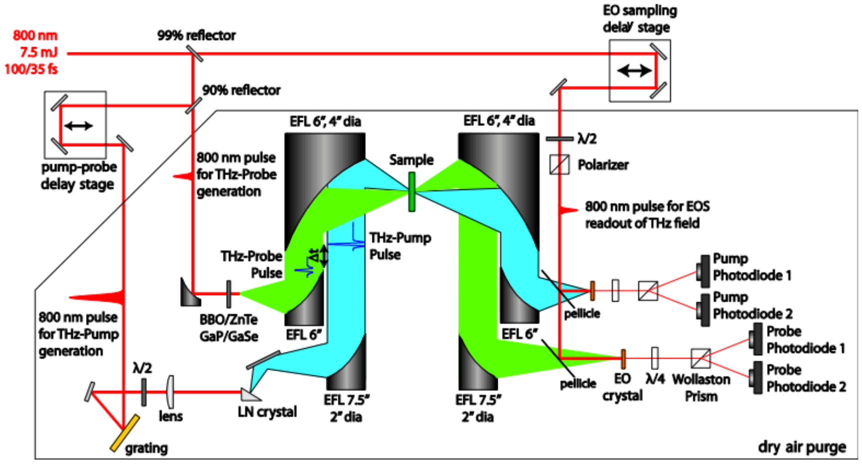

Figure 2.22: Example of a 2D THz TDS system using a non-collinear geometry. Image taken from [85].

As 2D-TDS measurements are often performed using a collinear beam geometry (see Figure 2.21), all nonlinear responses to appear in the 2D FFT of E_{NL}, separated in frequency as defined in Table 2.2 [81, 82, 84, 86]. The locations of the nonlinear signals can be interpreted as a chain of wavevectors $\vec{k}_{\mathrm{A}}$ and $\vec{k}_{\mathrm{B}}$, corresponding to a Liouville pathway. The wavevector $\vec{k}_{\mathrm{A}}$ is a purely horizontal vector of size $(\pm\nu_0, 0)$, whilst $\overrightarrow{k}_{\mathrm{B}}$ is 45° to $\overrightarrow{k}_{\mathrm{A}}$, with size $(\pm\nu_0, \pm\nu_0)$. Figure 2.23 shows examples of the wavevectors in the nonlinear 2D FFT (left side of the diagram) compared with the double-sided Feynman diagram (right side of the diagram). The various nonlinear responses can then be isolated and viewed in the time domain by performing an inverse 2D FFT on a given region (see Figure 2.24), allowing for information about the specific response to be obtained [81, 82, 84, 86].

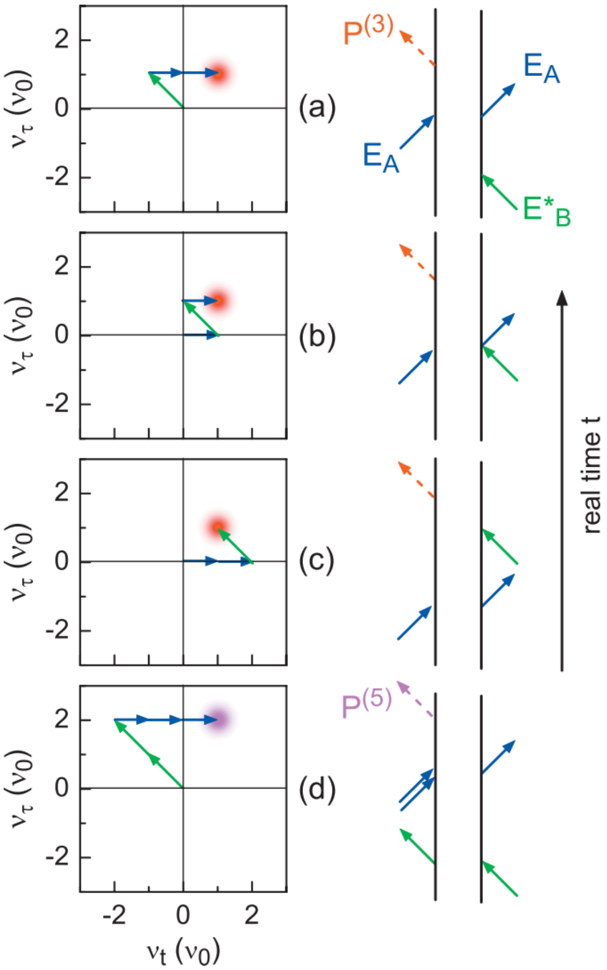

Figure 2.23: Various wavevector combinations and corresponding Liouville pathways. (a)-(c) are the pathways contributing to the FWM signal, whilst (d) is a single pathway contributing to the six-wave mixing signal. Image taken from [81].

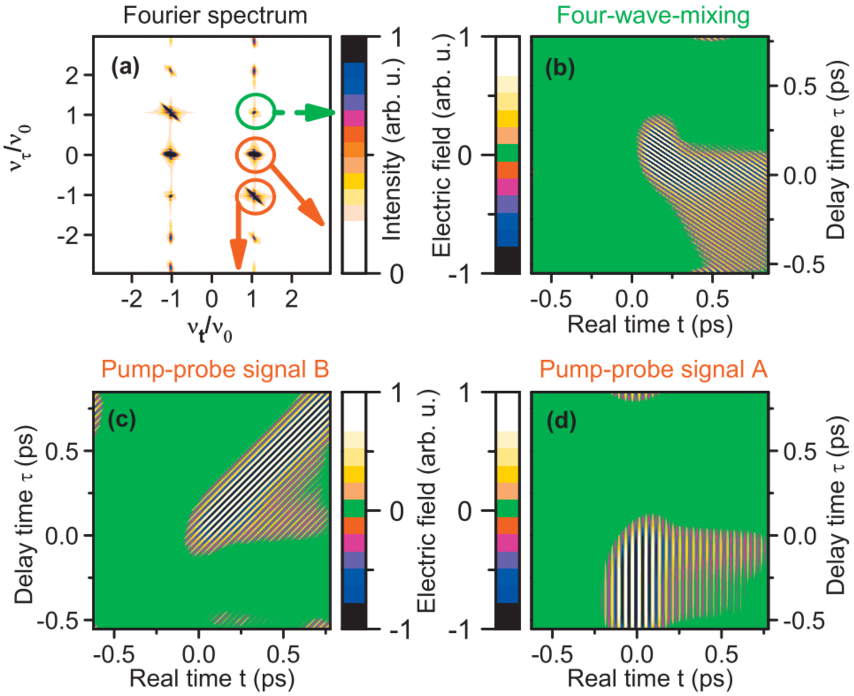

Figure 2.24: Inverse 2D FFT of a nonlinear signal, separating out the two ‘pump-probe’ signals, and one of the FWM signals. Image taken from [81].

	Wavevector Space	**Frequency Space** (ν_t, ν_τ)
	$\chi^{(3)}$ Effects	
Pump-Probe Signal	$(\vec{k}_{\mathrm{A}} - \vec{k}_{\mathrm{A}} + \vec{k}_{\mathrm{B}}) = \vec{k}_{\mathrm{B}}$	$(\nu_0, -\nu_0)$
	$(\vec{k}_{\mathrm{B}} - \vec{k}_{\mathrm{B}} + \vec{k}_{\mathrm{A}}) = \vec{k}_{\mathrm{A}}$	$(\nu_0, 0)$
Four-Wave Mixing	$2\vec{k}_{\mathrm{A}} - \vec{k}_{\mathrm{B}}$	(ν_0, ν_0)
	$2\vec{k}_{\mathrm{B}} - \vec{k}_{\mathrm{A}}$	$(\nu_0, -2\nu_0)$
Third Harmonic	$3\vec{k}_{\mathrm{A}}$	$(3\nu_0, 0)$
	$2\vec{k}_{\mathrm{A}} + \vec{k}_{\mathrm{B}}$	$(3\nu_0, -\nu_0)$
	$\vec{k}_{\mathrm{A}} + 2\vec{k}_{\mathrm{B}}$	$(3\nu_0, -2\nu_0)$
	$3\vec{k}_{\mathrm{B}}$	$(3\nu_0, -3\nu_0)$
	$\chi^{(5)}$ Effects	
Six-Wave Mixing	$3\vec{k}_{\mathrm{A}} - 2\vec{k}_{\mathrm{B}}$	$(\nu_0, 2\nu_0)$
	$3\vec{k}_{\mathrm{B}} - 2\vec{k}_{\mathrm{A}}$	$(\nu_0, -3\nu_0)$

Table 2.2: Mapping of different nonlinear responses in wavevector and frequency space [81].

The technique of 2D THz TDS has been shown to be able to resolve multilevel dynamics in quantum well systems [81, 82], including intersubband saturable absorbers [2, 84] and QCLs [86], graphene [82], cyclotron resonances in 2D electron gases [87], rotational spectroscopy of gas phase molecules [88] and vibrational spectroscopy of semiconductor phonons [89, 90]. The most common generation method used for these experiments have been EO rectification (see Section 2.2.2.2), with $\mathrm{LiNbO_3}$ being a popular choice as the generation crystal, owing to its large damage threshold and good EO coefficient, allowing for fields greater than $1\,\mathrm{MV\,cm^{-1}}$ to be generated [91]. As discussed in Section 2.2.2.6, generation using $\mathrm{LiNbO_3}$ does have drawbacks, namely that complex phase matching is required involving reflective gratings and also the bandwidth is usually limited to ~2 THz.

Chapter 3

Photoconductive Arrays

A Photoconductive Array (PCA) is a Photoconductive Switch (PCS) design constructed of multiple interdigitated electrode finger pairs connected to a single anode or cathode, separated by semiconductor strips, creating multiple PCSes in a parallel configuration, allowing for constructive interference of the THz pulses emitted from each PCS. Due to their design, they allow for a much larger area to be optically excited, reducing the incident optical density and local heating of the device [92], therefore reducing the likelihood of damaging the device. Having a large area device consisting of multiple smaller PCSes also has the added benefit of not requiring as great a bias voltage to apply the same electric field strength across the semiconductor.

PCAs are typically fabricated similarly to single gap PCSes (a semiconductor on a host substrate with metal electrodes on the top), but with the electrode structure consisting of multiple interdigitated pairs, allowing for multiple semiconductor strips to be illuminated. This design requires an optical mask to be deposited on every other gap to prevent deconstructive interference of the emitted THz pulse, as every other gap is inversely biased which would result in an equal but oppositely polarised THz pulse to be emitted [92]. Alternatively, every other semiconductor gap can be removed during the fabrication process, making the optical mask unnecessary [93, 94].

The design of the PCAs electrodes has been shown to have an impact of the generation efficiency. For a fixed area of illumination, it can be estimated using the following formula [37]:

$$E_{\mathrm{THz}}(\mathrm{a.u.}) \propto k_1 \frac{a}{p(1+a/L)} + k_2 \frac{b}{p}, \tag{3.1}$$

$$p = a + b + c + d, \tag{3.2}$$

where k_1 is the THz emission efficiency due to the antenna effect on the metallic anode, k_2 is the emission efficiency due to the acceleration of carriers within the semiconductor, a is the width of the anode fingers, b is the width of the bright gap (where the semiconductor is illuminated), c is the width of the cathode, d is the width of the dark gap (where there is no semiconductor or where the semiconductor is not illuminated) and L is 'saturation length' [37]. This is the length at which the THz field stops scaling linearly with the width of the anode. For a Au electrode on a GaAs substrate, L is ~40 µm [36]. Figure 3.1 shows a, b, c and d on a schematic diagram. From equation 3.1, it can be seen that the efficiency of the device can be improved by minimising both the width of the cathode, and the width of the dark gap. The increased efficiency from increasing the anode size can be attributed to plasmonic oscillations created by the photoexcited electrons arriving at the anode [36]. It should be noted however that this study was only performed on small gap devices $< 50\,\mu m$ and these equations may not be accurate for large gap devices.

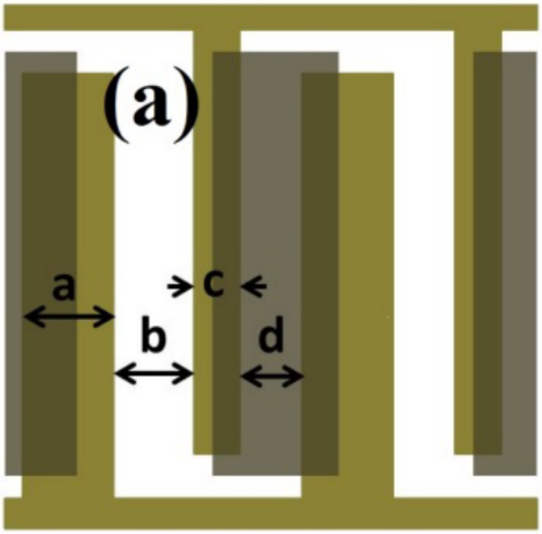

Figure 3.1: Schematic diagram of a PCA, highlighting lengths a, b, c and d used in Equations 3.1 and 3.2. Image taken from [37].

Certain PCA designs have also been shown to be capable of generating THz pulses with precise control of both the amplitude and polarisation [95, 96]. The device is split into multiple smaller PCA 'pixels', with half of them emitting horizontally polarised radiation and the other half emitting vertically polarised radiation. The amplitude and polarisation can then be controlled by changing the magnitude and ratio of the voltage applied to the horizontal and vertical 'pixels'.

3.1 Fabrication Technique

The fabrication technique for the PCAs used in this project was developed by Dr. David Bacon [94] and is summarised in this section. Devices used in this project were provided by Dr. David Bacon and Connor Kidd. Figure 3.2 shows a simplified version of fabrication process as a visual aid.

The semiconductor material used for these devices is 2 µm thick LT-GaAs, grown at ~290 °C using MBE on a SI-GaAs substrate with a 400 nm $Al_{0.7}Ga_{0.3}As$ sacrificial layer. The wafer is first scribed into the desired size and then annealed at 550 °C for 15 minutes to increase resistivity [97]. Next, a 300 nm thick layer of BCB thinned with mesitylene (2:1 by weight) is spun onto an insulating substrate (sapphire or z-cut quartz), after which, the LT-GaAs wafer is placed onto the insulating substrate where they are then bonded, heated and under vacuum, in a wafer bonder. When using a sapphire substrate, bonding is performed at 250 °C for one hour, whilst for a quartz substrate, this is performed at a lower temperature for a longer duration due to the thermal expansion coefficient mismatch between the quartz and LT-GaAs. BCB is used as the bonding adhesive as it is optically transparent and ensures effective heat transfer between the wafer and the insulating substrate [98]. After bonding, the SI-GaAs substrate is chemically-mechanically polished until it is ~30 µm thick and then the remainder is removed using citric acid (5:1 ratio). The AlGaAs is removed afterwards with buffered Hydrofluoric Acid (HF). The LT-GaAs is then patterned with a positive photoresist and etched in dilute sulphuric acid (H_2SO_4:H_2O_2:H_2O, 1:8:800 volume ratio), removing the alternate LT-GaAs strips, preventing deconstructive THz emission. To form the electrodes, a thin layer (15/200 nm) of Ti/Au is first deposited over the entirety of the device, followed by another positive photoresist. Potassium iodide and buffered HF are then used to etch through the gold and titanium respectively, creating the interdigitated electrodes.

The first devices produced using this method had electrodes with squared ends (see Figure 3.3a), but after some devices failed under prolonged use at higher applied biases, it was concluded that the sharp edges were creating a concentrated localised electric field. In subsequent devices, the electrode ends were rounded (see Figure 3.3b) to reduce the concentration of the localised electric field, improving the longevity of the devices.

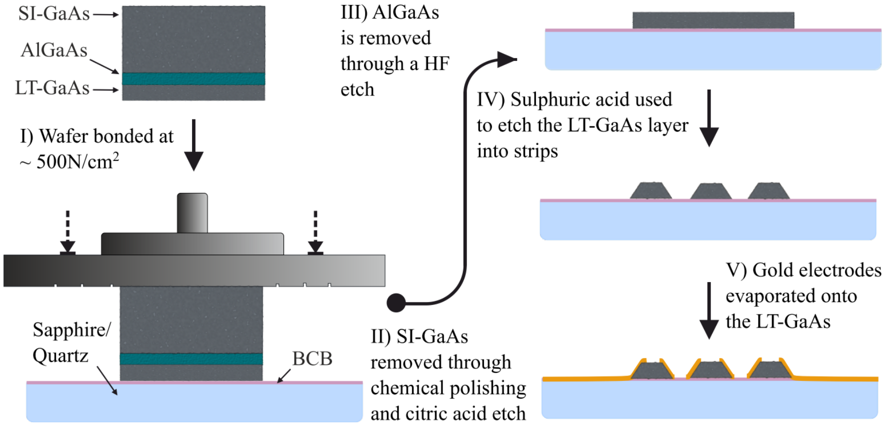

Figure 3.2: Diagram showing the simplified process for fabricating a PCA. Image taken from [94].

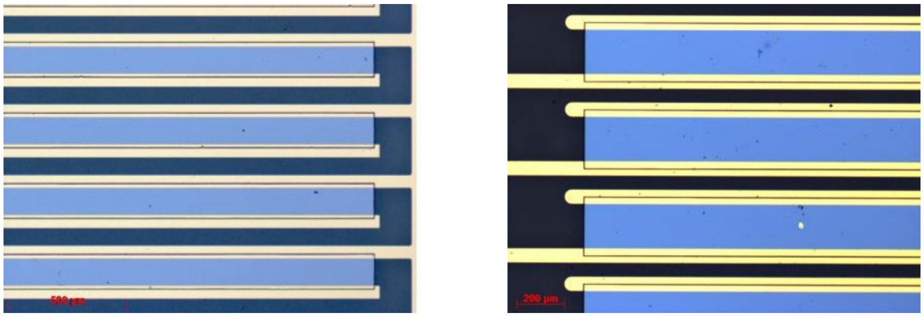

(a) PCA with squared electrodes

(b) PCA with rounded electrodes

Figure 3.3: Microscope image of two PCAs. Yellow areas are the Ti/Au electrodes, light blue areas are LT-GaAs and dark areas are the quartz/sapphire substrate.

3.2 Experimental Setup

This section describes the experimental setup used to characterise the PCAs used in this project.

3.2.1 Optical Setup

Figures 3.4a to 3.4c show a simplified optical diagram of the system used to characterise the PCAs. It is a 1D TDS system, with the emitter in a collimated configuration, utilising a reflective telescope to expand the size of the excitation beam to fully illuminate larger devices. For devices smaller than the size of the expanded beam, this also the provides less intensity variation across the active region, preventing the centre of the device becoming saturated before the edges, reducing the risk of damage at the cost of optical efficiency. Due to the transparent nature of the emitter substrate, Backside-Illumination (BSI) is used to generate the THz pulse. Here, the excitation beam travels through the transparent substrate (quartz/sapphire) before illuminating the active region, preventing attenuation and broadening of the generated THz pulse, leading to a pulse of greater magnitude.

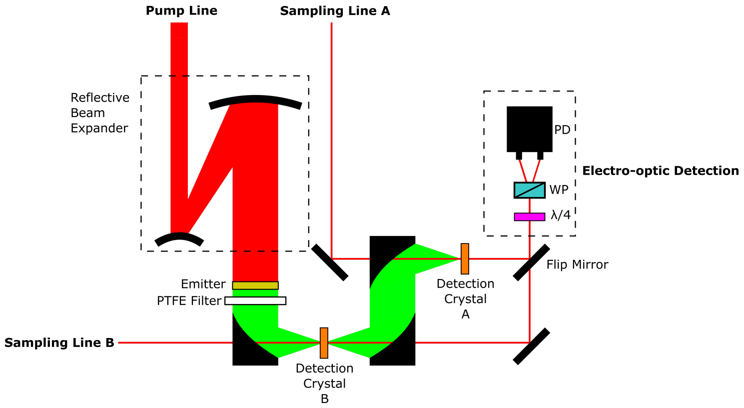

(a) Full System Setup.

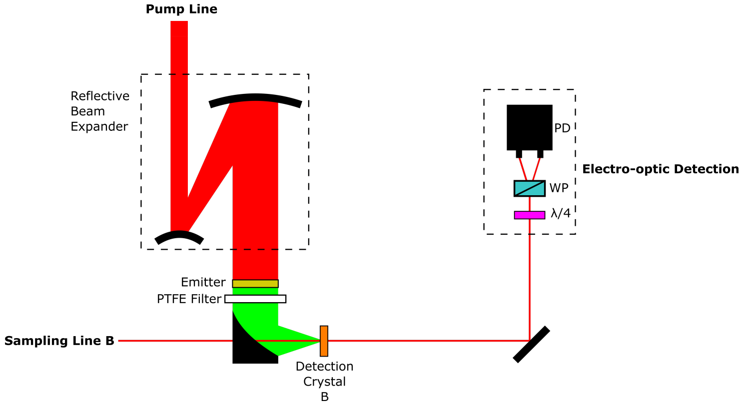

(b) Sample Space Detection.

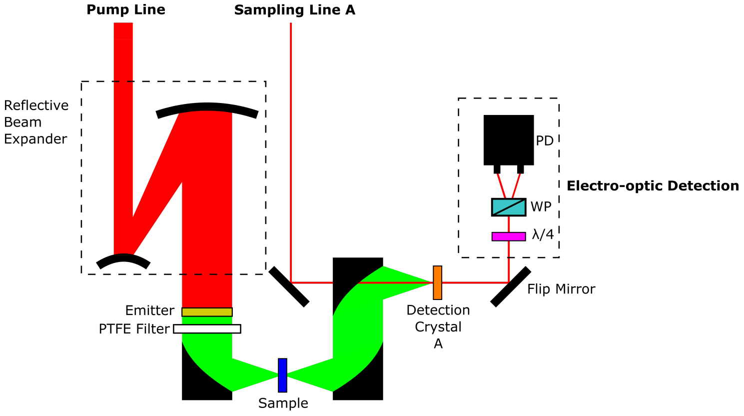

(c) Sample Measurement Detection.

Figure 3.4: Optical diagrams of the experimental system configurations used to characterise PCAs. The system can be configured to detect the pulses at either the sample space or in the detection space. Measuring the field at the sample space can provide more accurate values for fields incident on a sample and aid with alignment.

The spot size of a Gaussian beam being focused from a lens can be found using the following equation:

$$2w_0 = \frac{4\lambda F M^2}{\pi D}, \tag{3.3}$$

where w_0 is the beam waist, λ is the wavelength of the beam, F is the focal length of the lens, D beam diameter at the lens and M^2 is the Gaussian beam propagation factor. For an ideal beam, M^2 is assumed to be 1. From this equation it can be seen that the spot size is proportional to the focal length of the lens and as a smaller spot size beam would create a larger electric field. As higher fields are required to perform nonlinear spectroscopy, it is therefore critical to use a parabolic mirror with as short a focal length as is feasible to still allow for a sample to be measured. To allow for ample room for a large cryostat, 2 " parabolic mirrors with a 4 " Effective Focal Length (EFL) were used, giving a total sample space of approximately 6 " (the two parabolic mirrors in the sample space take up 1 " each from the total 8 " length).

The system was designed in such a way to allow for the THz field to be measured at the sample space (after the first parabolic mirror), as well as after the final parabolic mirror. This was done to provide a more accurate measurement of the THz field incident on a sample for calculation of saturation fields, as well as to aid with the alignment of the system. Simplified optical diagrams with unused optics removed for sample space and measurement configurations are shown below in Figures 3.4b and 3.4c respectively.

Both expanded Polytetrafluoroethylene (PTFE) and a Si wafer were tested as potential IR filters for the system, but PTFE was ultimately chosen. Si does have the benefit of attenuating the signal at higher frequencies to a lesser degree and allows for a greater bandwidth to be applied to a sample (see Figure 3.5), however, at higher optical powers, the absorption of the IR beam generates carriers within the wafer which cause the signal to be attenuated. PTFE does suffer from a phonon at ~2.5 THz, reducing the SNR around that frequency. PTFE also does not attenuate IR to the same degree as Si, so at very high incident optical powers, enough light will pass through to be detectable on the detection photodiodes.

Earlier iterations of the system utilised a transmissive, focus-through configuration (shown in Figure 3.6), where the emitter is placed between the focusing lens and the sample focal point. THz beams produced from large PCSes have been shown to follow the path of the IR excitation beam well [99, 100], making this setup much simpler to align and acquire large fields as short focal length lenses were used, however, some problems were found when using it. To expand the beam to a large diameter and then focus it with a short focal length lens with transmissive optics requires relatively thick optics. This causes the excitation beam to travel through a large and varying amount of glass, leading to variation across the beam [101]. The pulse broadening can be compensated to some degree by altering the compression of the amplified laser (see Section 2.1.5), but due to the variation across the beam, it can never be optimally compressed. The placement of the emitter after the focusing lens also vastly reduced the amount of room available for a cryostat when performing sample measurements.

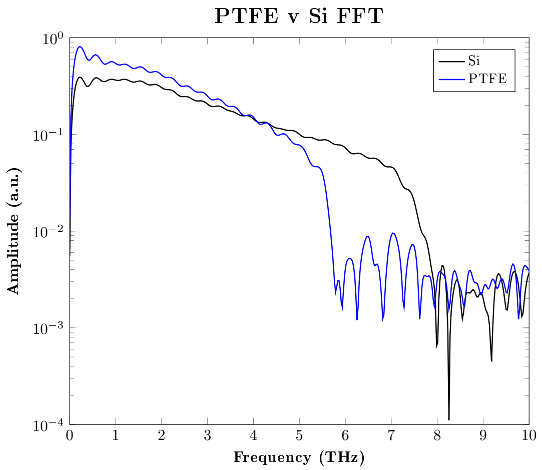

Figure 3.5: Bandwidth comparison of using PTFE and Si as an IR filter. The emitter used was a 15×15 mm PCA biased at 400 V, excited with an optical fluence of ~5 µJ mm^{-2}. A 150 µm GaP crystal was used for detection.

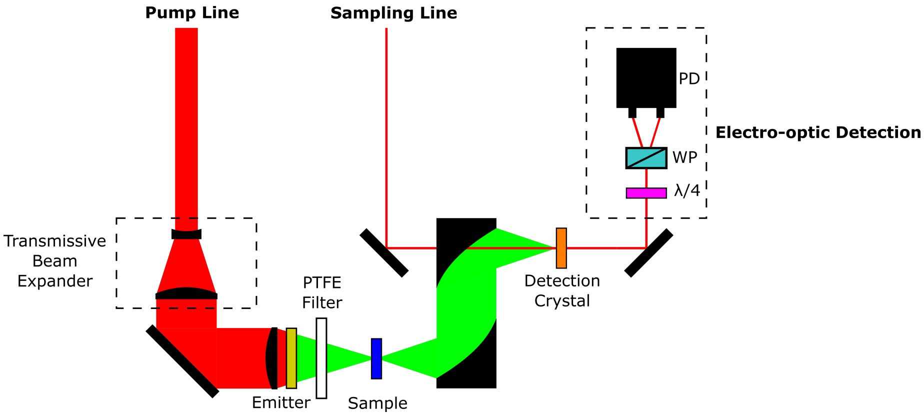

Figure 3.6: Focus-through 1D TDS system, utilising a transmissive telescope to expand the beam size.

3.2.2 Instrument Setup

This section will summarise the setup of the instruments used in the system to acquire data for both reference modulation techniques; electrically chopping the emitter and optically chopping the excitation IR beam.

3.2.2.1 1D Spectroscopy Setup (Electrical Chopping Reference)

Figure 3.7 shows a block diagram of the instruments used to acquire 1D-TDS signals from the system, electrically modulating the emitter as a reference for the LIA. The amplified laser (*Spitfire Ace PA*) provides a master 1 kHz reference derived from the 80 MHz repetition rate of the seed laser, synced to the laser pulse output. The reference is used to generate a 125 Hz signal by the pulse generator (*Agilent 33500B*) which is in turn used as the gate signal for the pulse generator (*DEI PVX-4150*). The pulse generator takes a high voltage DC input from the voltage supply (*Keithley 2410*) and converts it into a square wave, chopping the DC input using the gate input as a reference. This high-voltage chopped signal is then applied to a PCA, which generates the THz pulses. Using EO sampling (see Section 2.3.2), the THz field drives a pair of balanced photodiodes (*Newport Nirvana 2007*), which is fed into a boxcar averager (*SRS SR250*) and then a LIA (*AMETEK 7265*) to reduce noise before the resulting signal is acquired using a LabView program on a PC. The boxcar averager removes the 'laser off' noise from each pulse, as it uses the 1 kHz reference from the amplifier. A boxcar amplifier is used here, as the signal of interest (where the laser is on) has a relatively low duty cycle. Figure 3.8 shows the boxcar window used compared to the response from the photodiodes when a THz pulse is present and absent on the detection crystal. From testing multiple window sizes and positions, it was found that the ~2 µs window shown provided the best SNR. The output from the boxcar when a PCA chopped at 500 Hz is used as the source is shown in Figure 3.9. Here it can be seen that a quantized 500 Hz square wave is produced from the small photodiode responses. The LIA operates on pulse trains of 8 pulses (4 with the emitter on, 4 with the emitter off), using the 125 Hz reference from the pulse generator. It allows for a reduction of the 'laser on' noise by extracting the THz signal of interest, which is being modulated at 125 Hz by the emitter being turned on/off periodically. 125 Hz was chosen as the emitter modulation frequency as it allows for the signal to be averaged over 4 pulses, helping to reduce noise created by the difference in optical power between laser pulses.

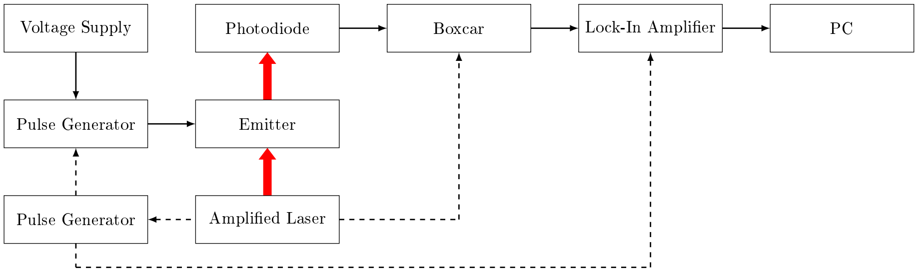

Figure 3.7: Block Diagram of Experimental System when set up for 1D spectroscopy, using electrical modulation for the LIA reference. Dotted lines denote a trigger connection, thick red lines denote an optical connection, other lines denote an electrical connection.

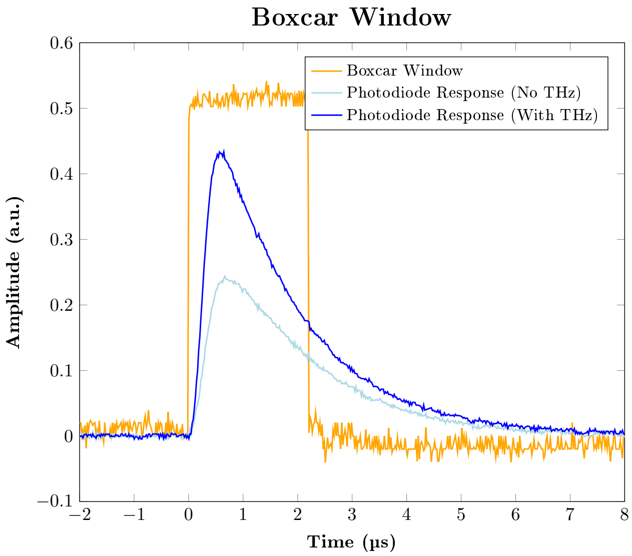

Figure 3.8: Window of the boxcar compared to the photodiode response with and without a THz pulse present on the detection crystal.

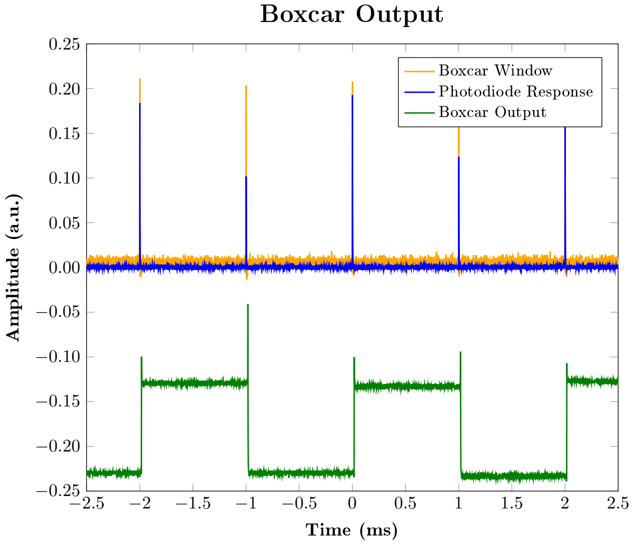

Figure 3.9: Output of the boxcar compared to the photodiode response. Emitter is operated at 500 Hz.

3.2.2.2 1D Spectroscopy Setup (Optical Chopping Reference)

Figure 3.10 shows a block diagram of the instruments used to acquire 1D-TDS signals from the system, optically modulating the emitter as a reference for the LIA. The setup is similar to when the emitter is electrically chopped, but with the emitter biased directly from the high voltage DC supply (*Keithley 2410*), and an optical chopper (*ThorLabs MC2000B*) operating at 125 Hz, phased locked to the 1 kHz reference from the amplified laser, being placed in the optical path before the emitter. The 125 Hz chopping signal is the used as the reference signal for the LIA.

The main advantages of optically chopping the emitter instead of electrically chopping is that it is simpler to implement as a pulse generator is not required, as well it increasing the emitter lifetime, as the number of amplified pulses incident on the device over a given period of time is halved, reducing the chance of the device becoming damaged. The main disadvantages are that owing to the large beam diameter, the phase of the optical chopper must be set precisely to avoid the excitation beam being clipped and that the chopping phase does shift with respect to the 1 kHz reference owing to the mechanical nature of the chopping.

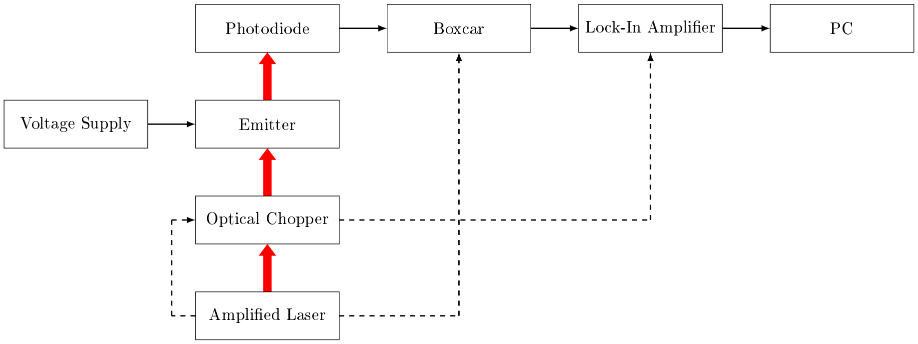

Figure 3.10: Block Diagram of Experimental System when set up for 1D spectroscopy, using optical modulation for the LIA reference. Dotted lines denote a trigger connection, thick red lines denote an optical connection, other lines denote an electrical connection.

3.3 Characterisation

Emitter characterisation is an important part of creating an experimental system as it provides crucial information required to interpret data acquired from sample measurements, such as the bandwidth and field strength that was applied. Characterisation is also an important part of developing novel emitters, as it allows for areas of improvement to be identified for the next design iteration. This informed the change of electrode design shown in Figure 3.3 for example. This section discusses the techniques performed to characterise the PCAs used in this work.

3.3.1 Optical Characterisation

To optically characterise the PCAs, multiple time-domain scans are recorded, with the optical power applied to the device changing with each scan (the bias remains constant). To vary the optical power applied to the device, a series of two optical filter wheels containing Neutral Density (ND) filters are situated in both pump beam lines, allowing for 36 possible optical powers to be incident upon the device. The ND filters were all chosen to be of the same thickness and to be as thin as possible to prevent broadening of the pump beam. A 150 µm thick GaP crystal is used as the detection crystal for most measurements. The detection crystal used for the scans is either a 150 µm thick GaP crystal or a 1 mm thick ZnTe crystal. The GaP crystal is preferred due it being able to detect a much larger bandwidth than the ZnTe crystal, however for devices which do not produce large fields, the ZnTe crystal is used, owing to the better SNR.

Figure 3.11 shows an example of the relation between the peak THz field observed, against the applied optical power. For lower optical excitation beam powers, the field of the emitted THz pulse increases linearly, but for greater optical powers, saturation begins to occur. When performing this measurement, the optical power applied to the device is carefully increased until saturation is observed. If the optical power is increased much further after saturation is observed, the risk of damaging the device increases dramatically. Saturation in PCS occurs due to screening caused by the generation of local fields created by the separation of carriers in the semiconductor [102], particularly in smaller gap devices [103].

For these measurements, the value of the THz field was obtained by EO detection using Equation 8.1 with some correction factors added (see Appendix 8.1). These values were later verified using a calibrated THz power meter (see Section 3.3.4).

Although Figure 3.11 shows data from emitters of three different areas, it should be noted that the responses cannot be directly compared, as each set of data was taken using a different optical configuration. The data for the 7×7 mm array was taken with an optical setup similar to Figure 3.6. The data for the 18×18 mm array was taken with an optical setup similar to Figure 3.4c, but with the emitter placed after the first parabolic mirror, allowing for a focus-through setup. The data for the 15×15 mm array was taken with an optical setup similar to Figure 3.4a. The optical density data from this array has also corrected by a factor of 0.43 to account for only part of the expanded Gaussian beam illuminating the device. This factor can be estimated using the following equation:

$$\text{Power Factor Through Iris} = 1 - e^{\frac{-2\times\text{Iris Diameter}^2}{\text{Beam FWHM}^2}}. \tag{3.4}$$

As the beam expander expands the beam by a factor of four, the incident beam

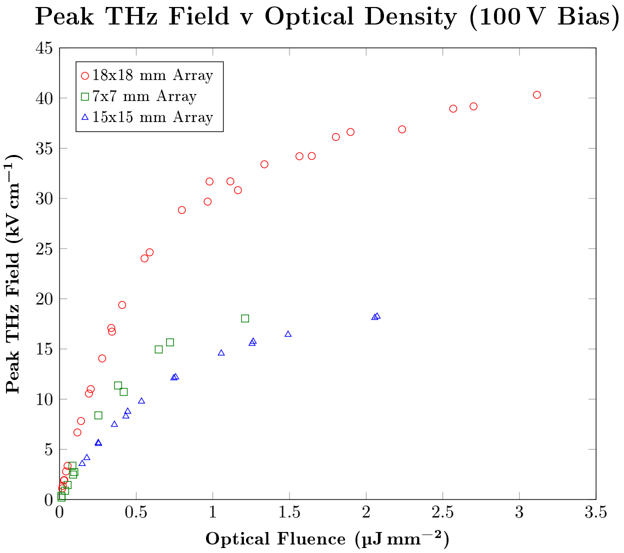

Figure 3.11: Optical characterisation data from three emitters of different sizes, each biased with 400 V. Field estimated from EO detection using a 150 µm thick GaP crystal. Data for each emitter was taken on different optical setups. Field values determined using EO sampling.

with a Full Width at Half Maximum (FWHM) of 8 mm becomes 32 mm. Equation 3.4 presumes a circular iris, however, the active area of the PCA is a 15×15 mm square, so to acquire the diameter of a circle of equivalent area, the following equation is used:

$$d = 2\sqrt{\frac{\text{Area of Active Region}}{\pi}}. \tag{3.5}$$

Substituting Equation 3.5 into Equation 3.4 obtains the correction factor of 0.43.

3.3.1.1 Noise Suppression

As well as producing a greater output field, using a higher powered optical excitation beam has the additional benefit of suppressing pulse-to-pulse noise common in low repetition rate amplified systems caused by the optical power changing between pulses [104]. This was tested by recording 100 time-domain scans using an optical power in both the linear and saturated regions of the PCA's optical response. From this data, the signal peaks were recorded for each scan and the standard deviation was acquired. As seen in Figure 3.12, the scans in the linear regime had a standard deviation of 3 % of the mean, whilst the scan in the saturation regime had a smaller standard deviation of 1.4 % of the mean [94].

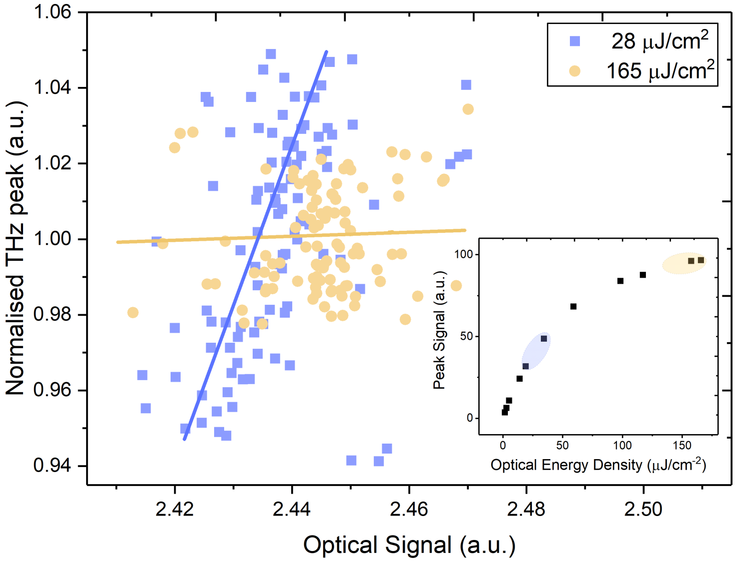

Figure 3.12: Plot of the peak THz field of 100 scans against the optical power of the excitation beam for a PCA in the linear and saturation regime of its optical response. The peaks of the THz pulses in the saturation regime have a lower standard deviation than those of the linear regime (1.4 % v 3 %). This suggests that operating a PCA in the saturation regime aids in suppressing optical noise created by the amplified laser. Data was acquired using an emitter biased at 400 V. Image taken from [94].

3.3.2 Voltage Characterisation

To perform a voltage characterisation, multiple time domain scans are recorded, with the bias applied to the device changing with each scan (the optical power remains constant). As seen in Figure 3.13, increasing the applied bias to the device causes a linear increase in the field of the emitted THz pulse [19], with the maximum bias being limited by the breakdown voltages of the semiconductor ($\sim$300 kV cm^{-1} for LT-GaAs [26]) and the atmosphere the device is operated in ($\sim$30 kV cm^{-1} for air [105]). To prevent breakdown of air occurring, the maximum fields applied to the devices was $\sim$20 kV cm^{-1}, which corresponds to $\sim$400 V for a device with a gap size of $\sim$200 µm. Figure 3.14 shows the frequency response of an emitter as a function of bias for a 12×12 mm PCA measured with a 150 µm GaP crystal where it can be seen that the shape of the response does not alter as the device bias changes within a bandwidth of 5 THz. The differences in response at frequencies greater than 5 THz are from the low SNR at higher frequencies.

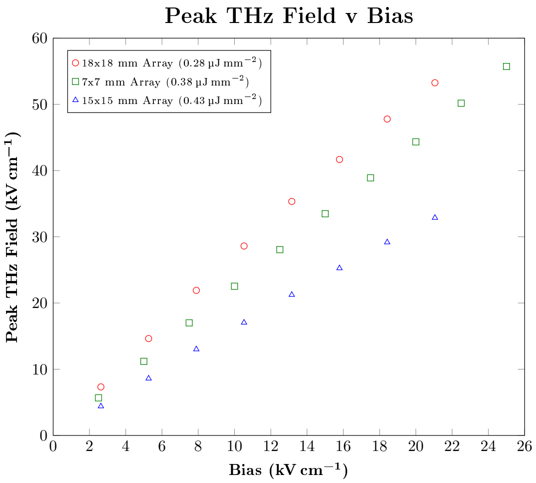

Figure 3.13: Voltage characterisation data from three emitters of different sizes. Data for each emitter was taken on different optical setups. Field values determined using EO sampling.

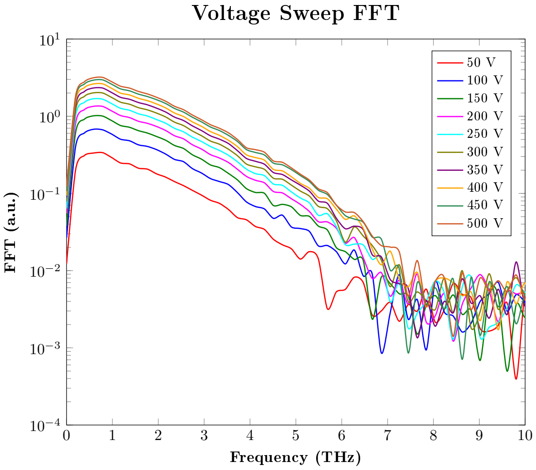

Figure 3.14: Frequency response of a 12×12 mm PCA at different biases. An optical fluence of 1.5 µJ mm^{-2} was used to excite the emitter. A 150 µm GaP crystal was used for detection.

3.3.3 Spot Size Measurement

Knowledge of the spot size is important as it can be used to estimate the power of the THz pulse incident on a sample from the measured field and indicate if the system is well aligned, because the experimental value will be close to the diffraction limit (calculated using Equation 3.6).

3.3.3.1 Experimental Details

To acquire the spot size of an emitter, a knife edge is placed perpendicularly in the focus of the beam and moved systematically to block gradually more of the beam. At each knife position, a THz time domain signal is recorded, with the peak of the signal decreasing as more of the knife blocks the beam. For a 2D profile of the beam at a given position, the measurements are repeated with the knife rotated by 90° and for a Three-Dimensional (3D) profile of the beam, the knife is translated in the plane of the beam either side of the focus.

The THz spot size can also be acquired by capturing an image using a THz camera with a known pixel size, as seen in Figure 3.15.

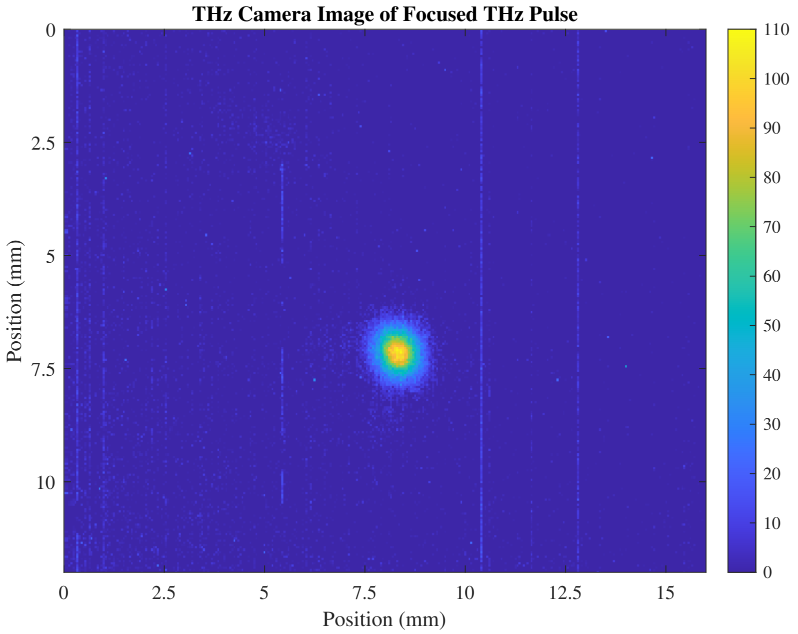

Figure 3.15: Image of a focused THz pulse generated by a 12×12 mm PCA taken by a THz camera (*Photonic Solutions TZCam*). False colour applied to image for clarity. Each pixel is 50×50 µm in size.

3.3.3.2 Data Processing

To acquire the spot size for a given position, a magnitude metric (such as the signal peak) is found from the time domain trace recorded at each knife position. The resulting magnitude metrics are then fitted to the error function, the integral of the Gaussian function, because the beam has a Gaussian power distribution. From the fit, the knife positions where 90 % and 10 % of the maximum signal are acquired, with these positions then being used to estimate the spot size ($1/e^2$) using the following formula [106]:

$$\text{Spot Size} = 0.7803 \times |\text{Knife}_{90\%} - \text{Knife}_{10\%}|, \tag{3.6}$$

where $\text{Knife}_{90\%}$ and $\text{Knife}_{10\%}$ are the knife positions where 90 % and 10 % of the maximum signal is found respectively [107]. Figure 3.16 shows an example of data from a knife-edge experiment being fitted to an error function, using the peak-to-peak of the time domain scans as the magnitude metric. Using the peak or peak-to-peak as the magnitude metric acquires the spot size across all frequencies of the broadband THz pulse, however, it is possible to acquire the spot size across a given frequency band by using bounded integrals of the Fourier transforms of the time domain pulses as the magnitude metric.

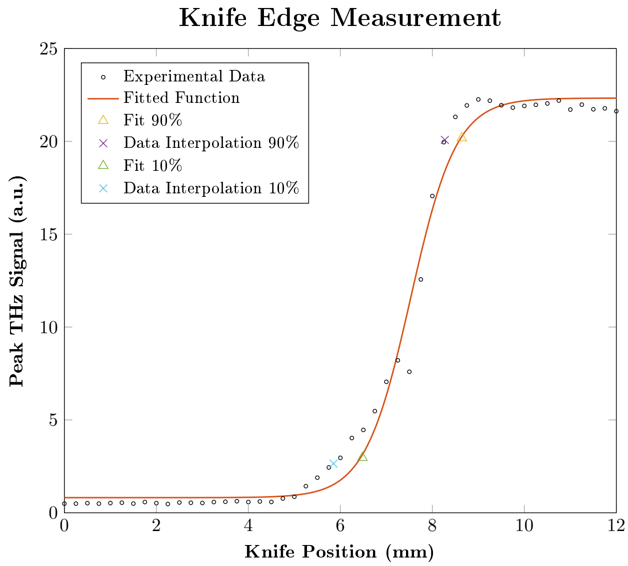

Figure 3.16: Experimental data showing the fitted error function against the experimental data points of a knife edge measurement. Using the 90% and 10% values of the fitted data results in a spot size of 1.69 mm, whilst using the 90% and 10% values of the interpolated data results in a spot size of 1.89 mm (see Equation 3.6).

Figure 3.17 shows the results of a series of knife-edge measurements of a 18×18 mm array, giving a minimum spot size of ~640±35 µm. The spot size of this device was later acquired using a THz camera (*Photonic Solutions TZCam*), producing images as seen in Figure 3.15. The measurements from the camera resulted in a spot size of ~740±60 µm. These values agree somewhat with the theoretical value of the spot size, which can be estimated using Equation 3.6. The peak of the frequency response of the emitter is ~0.8 THz, so a $\lambda = 375$ µm is used with $F = 10$ cm and $D = 32$ mm, resulting in a value of ~746 µm.

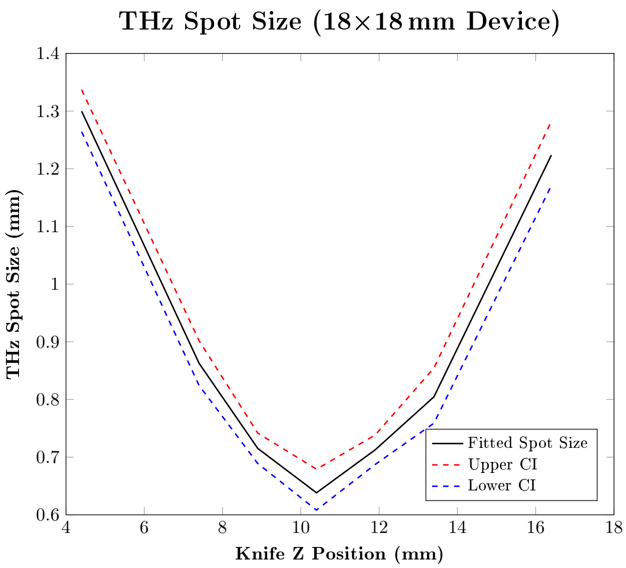

Figure 3.17: Spot size of a 18×18 mm device acquired using error function fitting. 90% upper and lower Confidence Interval (CI) also shown.

3.3.4 Power Measurements

To measure the power of the generated THz pulses and verify the estimated field values, a calibrated pyroelectric power meter (*OPHIR RM9-THz*) placed in the sample space was used. In certain crystals, changes in temperature cause the crystal's atoms to shift, giving rise to a voltage across the crystal, known as the pyroelectric effect. When THz radiation is incident on these crystals, it is absorbed, causing a small change in temperate, inducing a voltage which can be measured. As this measurement is sensitive to other heating sources, the power reading for a PCA is acquired by averaging the measured power over a period of a few minutes with the emitter both biased and unbiased. The resulting power is obtained by subtracting the average power when the emitter is unbiased from the average power acquired when the emitter is biased. For a 18×18 mm device, the pulse energy measured was 113 nJ when biased to 20 kV cm^{-1}. To convert the measured energy into a field, the following equation is used:

$$E_{\mathrm{THz}} = \sqrt{\frac{4W}{c\varepsilon_0 d^2 \pi t}}, \tag{3.7}$$

where W is the THz pulse energy, d is the spot size and t is the duration of the pulse. For the measured device, the spot size was measured as 640 µm and the pulse width (obtained from a time domain scan) was ~1.2 ps, acquiring a field value of 120 kV cm^{-1}. This matched well with the estimated value obtained using EO sampling (see Section 2.3.2). Due to the sensitivity of this detector, it was unable to detect lower power THz pulses. To acquire the power for these pulses, the field estimate from EO sampling is used instead. For accurate field values, measurements using a power meter are preferred, because when measuring the field using EO detection, lots of correction factors are required (see Appendix 8.1), which if are assumed incorrectly, will provide an inaccurate field value. Measurements using a power meter are therefore more accurate, presuming that an accurate value for the spot size has been obtained and that the signal is strong enough to be detected.

3.4 Conclusion

In conclusion, large area LT-GaAs PCAs with transparent substrates have been developed and tested, with the work presented here being published in Ref [94]. It has been shown that these emitters are capable of generating the largest recorded fields from PCAs of $\sim 120\,\mathrm{kV\,cm^{-1}}$, with a broad bandwidth ($> 5\,\mathrm{THz}$) without spectral holes, common to pulses created by EO generation. Being able to control the pulse field strength with the device bias is also advantageous as it means that extra optics do not need to be introduced to attenuate the excitation beam which may cause the time the pulse arrives at the device to be altered slightly, owing to different ND filter glass thicknesses for example. Controlling the device with biasing also means that the emitter does not need to be chopped using a mechanical chopper as it can be done by applying a square wave instead of a DC bias. As this is not a mechanical process, it is more resilient to phase jitter, thus improving the accuracy of measurements.

Chapter 4

Multi-Beam Experimental Setup

This chapter discusses the development of the 2D spectroscopy system created during this project. It is split into two sections, with the first discussing the initial attempt at creating a 2D TDS using a single PCA to produce both pulses (Section 4.1) and the other section discussing the final system developed using two emitters (Section 4.2).

4.1 Single Emitter Setup

The first system developed was designed to be simple to set up, requiring little change from the system described in Section 3.2, using a single PCA as the source for both pulses. A single PCA was chosen over using a single EO crystal because the field generated from a PCAs is sublinear with applied optical power, therefore using optical powers at half the damage threshold does not mean a halving of the output field.

4.1.1 Optical Setup

Figure 4.1 shows a simplified optical diagram of the first iteration of the experimental system developed for this work capable of 1D, pump-probe and 2D spectroscopy in a collinear configuration. The setup is mostly unchanged from the setup described in Section 3.2, with the only difference being a 50:50 beamsplitter being added in the pump beam path to combine two separate pump beams. To prevent destructive interference of the two pump beams, a $\lambda/2$ waveplate was added to one of the lines, rotating its polarisation by 90°. The rotation of polarisation does not affect that of the generated THz pulse, as the output polarisation of a PCA is dependent on the direction of the bias field [18]. Combining two IR beams was chosen over other techniques for producing two pulses as it greatly reduces the complexity of both the optical and instrumentation setup, as only one emitter is needed to produce both pulses. The collimation of both beams is critical for performing pump-probe and 2D spectroscopy, as they need to be aligned at the same point in space on the sample to generate a nonlinear response. Combining both beams in the IR region helps considerably with this, as there are many more easily accessible methods of detecting and measuring the spacial profile of IR beams than THz ones (e.g. IR Charge-Coupled-Device (CCD) arrays and handheld IR-optical viewers). The main disadvantage of system like this where only one emitter is used is that the peak THz field available for each pulse is reduced, as the optical power of both pump beams combined cannot exceed the damage threshold of the emitter.

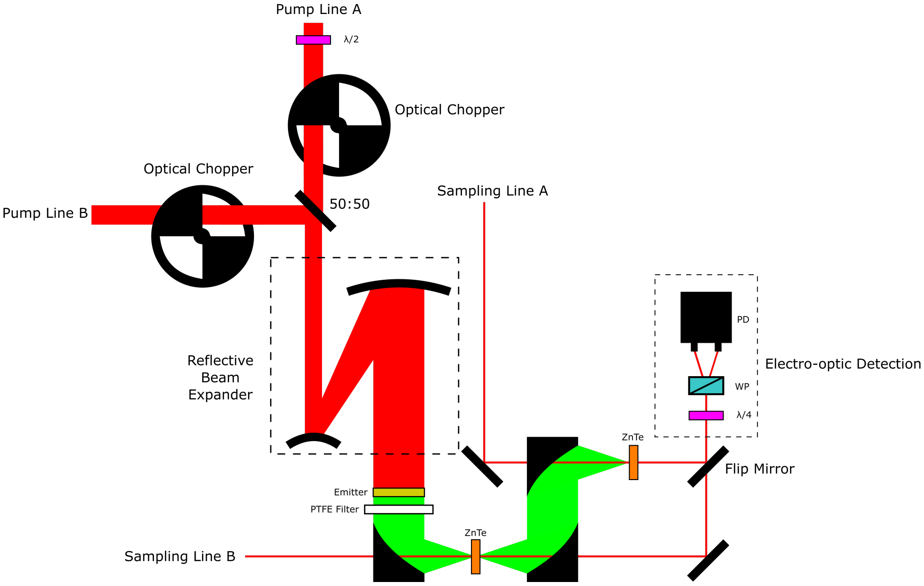

Figure 4.1: Simplified optical diagram of the single emitter 2D TDS system developed.

4.1.2 Instrument Setup

Figure 4.2 shows a block diagram of the instruments used to acquire 2D-TDS and pump-probe TDS signals from the system. Two separate IR beams are acquired from the amplified laser using a beamsplitter, with each passing through an optical chopper (*ThorLabs MC2000B* with an *MC1F2* wheel) then being recombined on another beamsplitter before the emitter. Both choppers are operated at 125 Hz with a 90° phase difference between them. Chopper A is phase-locked to the 1 kHz amplified laser reference whilst Chopper B is phase-locked to Chopper A. This is done to improve phase stability between the choppers. A DC bias is applied to the emitter using the high voltage supply (*Keithley 2410*), allowing for THz pulses to be generated at any point in time when either optical

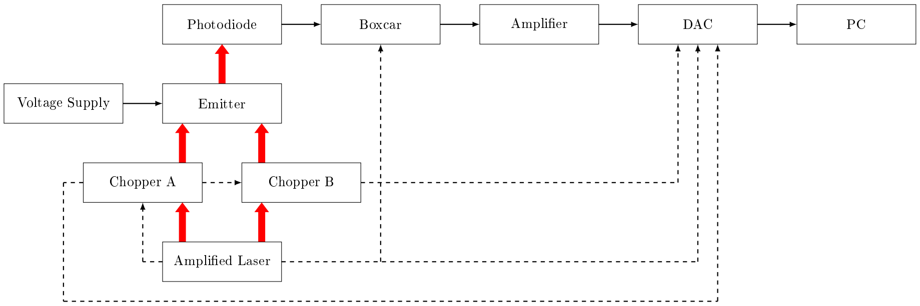

Figure 4.2: Block diagram of the experimental system when set up for pump-probe or 2D spectroscopy. Dotted lines denote a trigger connection, thick red lines denote an optical connection, other lines denote an electrical connection.

pulse passes through it. The resulting THz pulses are acquired using a balanced photodiode pair (*Newport Nirvana 2007*) with a boxcar averager to reduce the noise (*SRS SR250*), but instead of being fed into a LIA, the signal is amplified (*SR560*) and then sent into a Digital-to-Analog Converter (DAC) (built into the delay stage controller *Newport XPS-Q8*). The amplification stage is performed to utilise the full signal range of the DAC, improving the resolution, whilst also having the added benefit of filtering out the high-frequency 'spikes' which occur between boxcar samples. Removal of the LIA was done to reduce the time taken to perform scans, allowing for more repeat scans for averaging to increase the SNR. This is done because large SNR are often required for 2D TDS measurements, as the fields of the nonlinear signals acquired are often very small in comparison to the fields of the pump pulses [84]. The sampling delay stage is also set to move at a constant rate throughout the measurement to reduce the time taken to perform the measurement. The two chopper reference signals are also fed into the DAC, with data acquisition being triggered by a 1 kHz amplified laser reference. Due to the phasing of the choppers, every eight pulses, all possible combinations of the two input beams will occur (*Blocked (∅), A, B, AB*) (see Figure 4.3), with each state containing two pulses due to the chopping frequency (125 Hz). The data received from a single scan thus appears as a combination of four time domain scans (see Figure 4.4a), as the signal state being detected changes as function of the sampling delay, owing to the constant movement of the stage. By recording the state of both choppers, it is possible to separate which data points belong to which state in post-processing, allowing the four signals to be acquired (example is shown in Figure 4.4b). To acquire data points evenly spaced in time for each state, the received data is also interpolated.

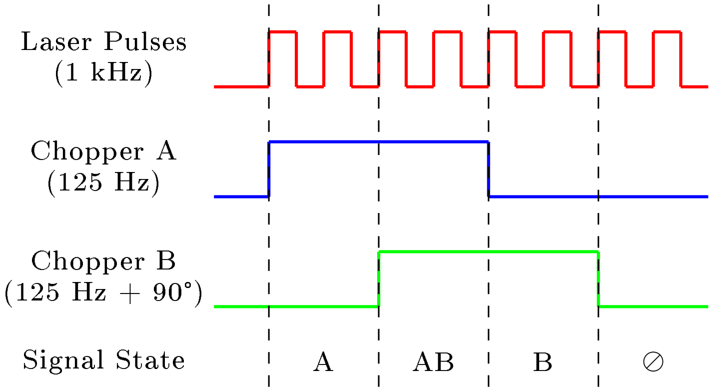

Figure 4.3: Diagram showing the signal state resulting from the choppers position.

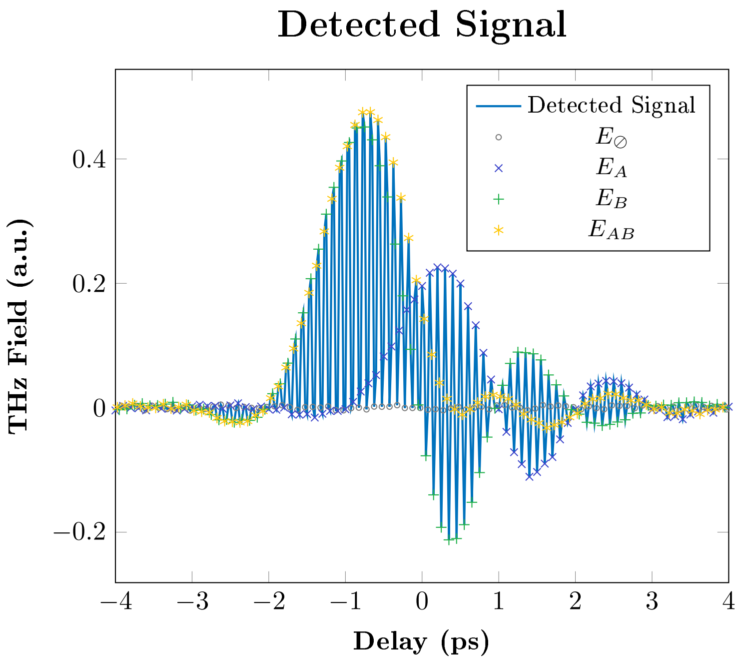

(a) Example of the signal detected by the DAC. Marks added to highlight the different signal states embedded in the signal.

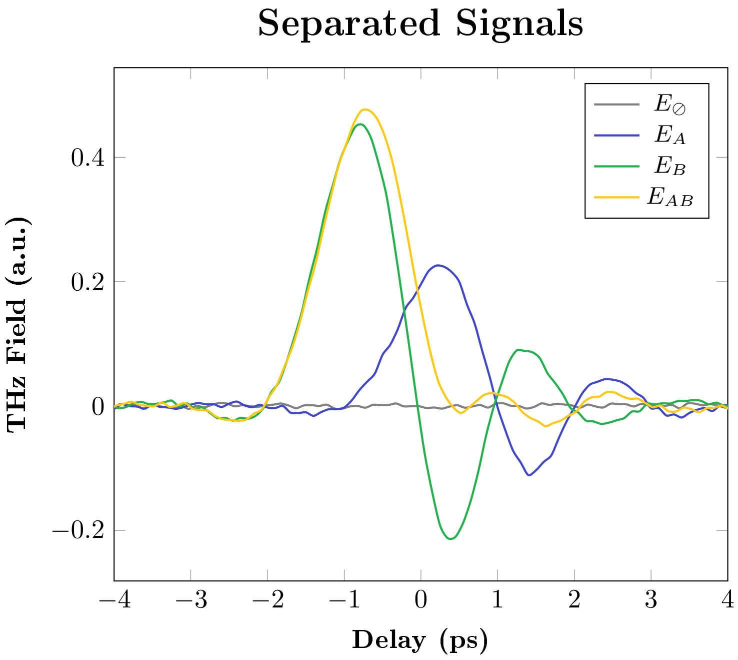

(b) Signal from Figure 4.4a separated into states and interpolated.

Figure 4.4: Example of data acquired during a scan and the resulting interpolated signals.

4.1.3 Data Processing

Data is obtained using a LabView data acquisition program developed by myself and Dr. Joshua Freeman. The raw data is stored in internal memory on the delay stage controller and copied across to the program using File Transfer Protocol (FTP). This was done to reduce scan times to allow for more averaging, as the default data acquisition protocol is significantly slower. Throughout a measurement, the program creates multiple text files, one for each τ delay (A-B delay), with each file containing the four state signals obtained from each repeat measurement. The files are then loaded into MATLAB and are checked for any state mismatches in the data for any series of scans, which are then fixed. State mismatches occur due to instabilities in the chopper phase with respect to the data acquisition trigger. Data spikes are also removed here. After this is done, the nonlinear signal is acquired for each scan, using a modified version of Equation 2.4.3:

$$E_{\mathrm{NL}} = (E_{\mathrm{AB}} - E_{\oslash}) - (E_{\mathrm{A}} - E_{\oslash}) - (E_{\mathrm{B}} - E_{\oslash}) \equiv E_{\mathrm{AB}} - E_{\mathrm{A}} - E_{\mathrm{B}} + E_{\oslash}, \quad (4.1)$$

where $E_{\oslash}$ is the signal when no THz pulses are incident on the sample. $E_{\oslash}$ is removed from each signal to reduce the effect of the background noise. After the nonlinear signal for each scan is acquired, nonlinear signals of the same τ delay are then averaged together to improve the SNR. The nonlinear signal for each scan is acquired first to reduce the effects of noise which is only present in a single scan (e.g. a brief increase in laser power or data 'spikes' caused by vibrations in the lab). After the nonlinear signal has been acquired for each τ delay, they are arranged into a 2D time domain configuration, with t (sampling delay) and τ as the x and y axis and the nonlinear signal amplitude as the z axis. Figure 4.5 shows an example of the nonlinear 2D time domain signal.

The nonlinear 2D time domain signal is then Fourier transformed with respect to t and τ, producing the 2D nonlinear frequency response, from which information about the sample can be interpreted (see Section 2.4.3). Figure 4.6 the shows an example of the nonlinear 2D time domain signal.

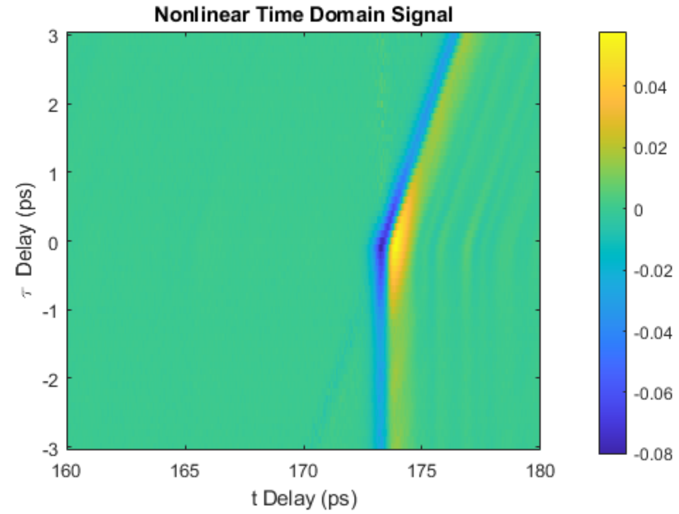

Figure 4.5: Example of the 2D nonlinear time domain signal.

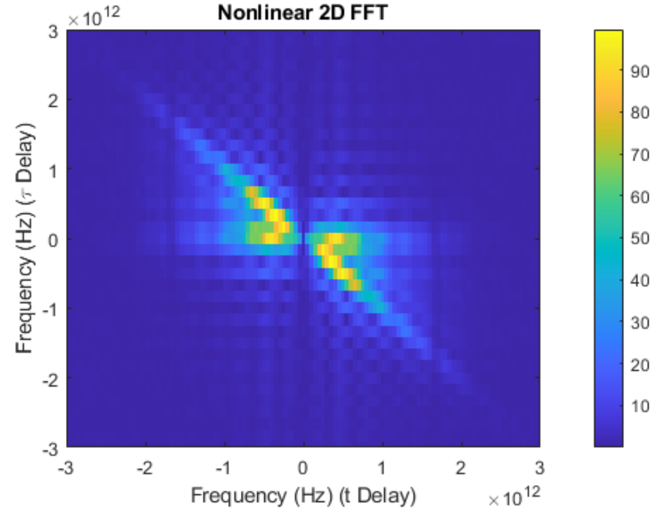

Figure 4.6: 2D Fourier transform of the nonlinear signal in Figure 4.5.

4.1.4 Efficiency Correction

Initial testing of the system revealed that using a single PCA with two excitation pulses required further processing to acquire the nonlinear signal, as a false nonlinear signal would be present, even without a sample being present as $E_{\mathrm{AB}} - E_{\mathrm{A}} - E_{\mathrm{B}} \neq 0$. These can be attributed to a combination of the optical response, recovery time and heating of the PCA. As shown in Figure 4.7 and highlighted in Section 3.3.1, the optical response of a PCA is sublinear at greater optical fluencies. This creates a false nonlinear response at $\tau = 0$. The generated electron-hole pairs from the first pulse creates a screening field opposing the applied bias, leading to a reduced applied bias, reducing the strength of the generated field from the second excitation pulse. On short τ timescales ($|{\sim}1\,\mathrm{ps}|$ [22]), the carrier lifetime of the LT-GaAs is also a factor of the false nonlinear response. On these short timescales, the carriers used to generate the THz pulse from the first excitation pulse have not returned to their resting position, so when the second excitation pulse is incident on the device, fewer carriers are available to generate a photocurrent, thus reducing the magnitude of the generated THz field. For LT-GaAs, the carrier lifetime is $\sim 0.4\,\mathrm{ps}$ [19]. Previous measurements of the recovery time of LT-GaAs emitters at lower pulse energies provided a similar response, including the sharp oscillation [22].

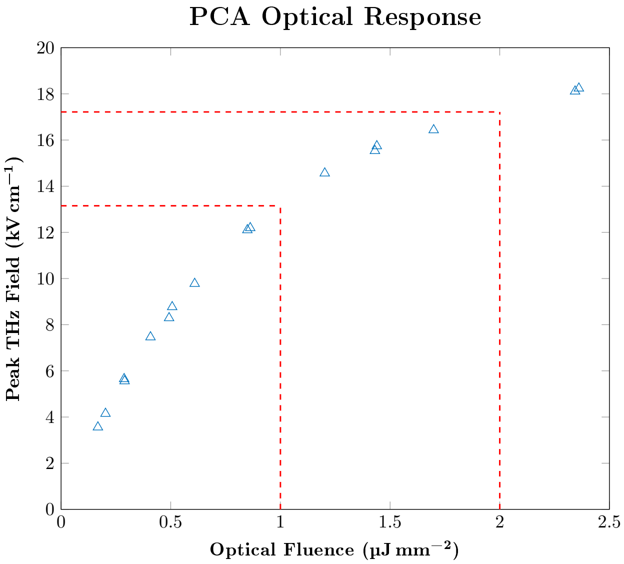

Figure 4.7: Optical response of a PCA. Here it can be seen that a doubling of the optical fluence on the device does not create a doubling of the emitted THz field.

To correct for these effects, a series of scans were taken across a range of τ delays without a sample present in the system, allowing for the four signal states to be acquired. For each τ delay, an 'Efficiency Factor' (ϵ) is applied to E_{A} and E_{B} so that:

$$E_{\mathrm{AB}} - \epsilon_{\mathrm{A}} E_{\mathrm{A}} - \epsilon_{\mathrm{B}} E_{\mathrm{B}} + E_{\oslash} = 0. \tag{4.2}$$

ϵ_{A} and ϵ_{B} are acquired for each τ delay by systematically varying each between 0 and 1 to minimise the resulting nonlinear signal. Figure 4.8 shows an example of the efficiency correction factor as a function of τ, whilst Figure 4.9 shows a comparison of the false nonlinear signal with and without ϵ_{A} and ϵ_{B} applied. The efficiency factor as a function of τ can be used to estimate the carrier lifetime by fitting the response of the pulse that is incident on the device last (E_{B} for $\tau < 0$ or E_{A} for $\tau > 0$) to the following equation [22, 108]:

$$\epsilon_n = A\exp(\frac{\tau}{t_{\mathrm{CL}}}) + c, \tag{4.3}$$

where t_{CL} is the carrier lifetime. Performing this fit in MATLAB using th ϵ_{B} response where $\tau < 0$, a value of $0.459 \pm 0.019\,\mathrm{ps}$ is obtained for t_{CL}, in good agreement with other measurements performed on LT-GaAs grown at similar temperatures [22, 108].

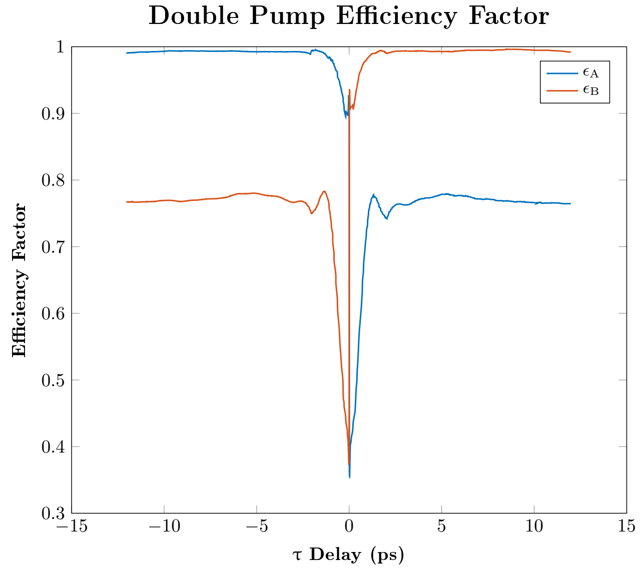

Figure 4.8: Efficiency correction factor for 15×15 mm PCA using two excitation beams of equal intensity.

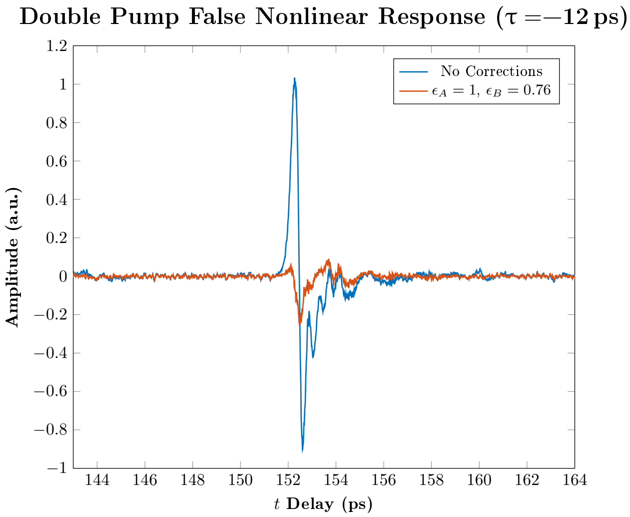

Figure 4.9: False nonlinear signal with and without the efficiency correction factor applied. Without corrections, the nonlinear signal magnitude is ~23 % of E_A and E_B. With corrections, the magnitude is ~6 %.

It can be seen in Figure 4.9 that although the magnitude of the false nonlinear signal is reduced by a factor of ~ 4, it is still significant enough to obscure any nonlinear signal generated from a sample interaction. As the THz field strength is proportional to the change in photocurrent over time (see Equation 2.9), the residual signal is likely caused by there being a different change in current in the device when both pulses are present on the sample than the single pulse case, making it impossible to match using a linear combination of the two single pulse cases.

To simplify the data processing at the expense of alignment simplicity, the system was therefore redesigned to use two THz emitters to prevent the false nonlinear signal.

4.2 Two Emitter Setup

This section describes the final version of the setup developed for this thesis.

4.2.1 Optical Setup

Figure 4.10 shows a simplified optical diagram of the final iteration of the experimental system. The system is still collinear like the system described in Section 4.1.1, however, the two THz pulses are generated by two emitters and are then combined in the THz regime using a Si wafer, acting as a beamsplitter. As well as the aforementioned reduction in data processing complexity, using two emitters also has the added benefit of being able to mix emitters, allowing for the potential to use broadband and narrowband sources, possibly allowing for a greater spectral resolution, however, this was not performed during this work. Using a THz beamsplitter does also come with the disadvantage that a proportion of the generated THz pulses will be lost due to transmitting or reflecting off the Si wafer away from the sample, reducing the maximum field that can be applied to a sample. This problem is unavoidable without switching to a non-collinear geometry, which comes with its own complexities (see Section 2.4.3). Due to space constraints, the magnification factor of the reflective beam expander was reduced from 4× to 3×. PTFE was placed after each emitter to block the excess IR pulses from exciting carriers in the Si wafer. If this is not done, a false nonlinear signal is produced, as whichever pulse hits the wafer first will reduce the magnitude of the second pulse, when both beams are unblocked by the chopper wheels. The newly added beamline did not include a beam expander because EO crystals roughly the size of the unexpanded beam would be used for emission.

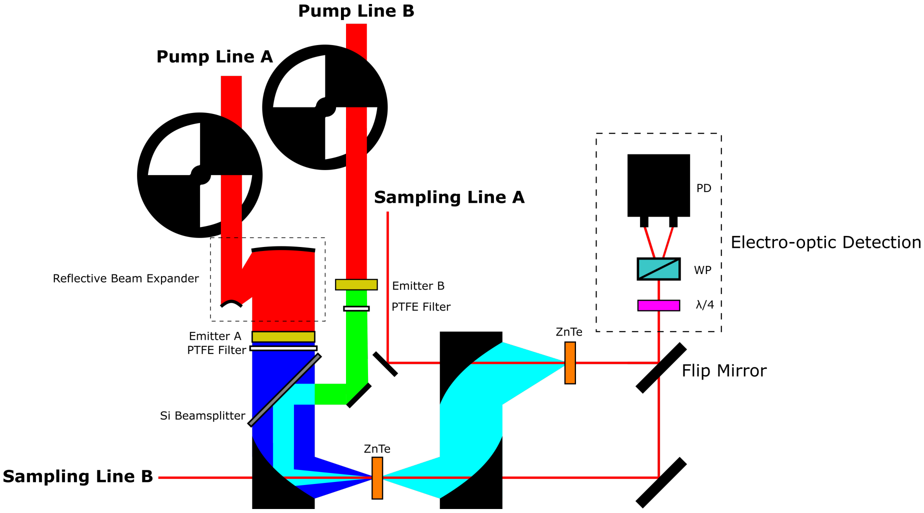

Figure 4.10: Simplified optical diagram of the two emitter 2D TDS system developed.

4.2.2 BNA Emission Crystal

For the second emitter in the system, it was decided that a BNA crystal mounted to a sapphire substrate (*Terahertz Innovations*) would be used as it is well phase matched at 800 nm, has a large EO coefficient, large damage threshold and emits over a broad bandwidth of ~11 THz (see Section 2.2.2), allowing for it to generate large fields with a collinear beam geometry. The crystal is mounted to a high thermal conductivity sapphire substrate as it has been shown to increase the damage threshold by a factor of three, allowing for a ~ 2.4× increase in the generated field [109]. Due to the relatively low melting point of BNA (103 °C), it is believed that the damage threshold is impacted significantly by the repetition rate of the laser system, as the faster repetition rate systems do not allow for the crystal to cool down significantly, increasing the chance of melting. For an unmounted crystal, the damage threshold was found to be 6 mJ cm^{-2} with a 100 Hz repetition rate system using 50 fs 800 nm pulses [110], for a 500 Hz repetition rate system using 100 fs 800 nm pulses, the damage threshold was found to be 4 mJ cm^{-2}, dropping to 2 mJ cm^{-2} when the repetition rate was doubled to 1 kHz [109]. Adding the crystal substrate increases the damage threshold to between 11–15.4 mJ cm^{-2} (using a 500 Hz repetition rate system) [109]. As the system used for this project is a 40 fs 800 nm system with a repetition rate of 1 kHz, a damage threshold for the crystal in this system was estimated by extrapolating the aforementioned values to be 2 mJ cm^{-2} (including the 3× increase in damage threshold from the sapphire substrate).

The BNA was first optically characterised using a range of optical powers below the damage threshold of the crystal in an unexpanded beam (see Figure 4.11), resulting in a peak detected field of 232 kV cm^{-1} when using a Si wafer as the IR filter. It was expected that the optical response would be linear, however the sublinearity seen can be explained by the excess IR beam generating carriers in the Si, screening the emitted THz pulse. This is confirmed when a PTFE filter is used instead of the Si, as the response become linear (see in Figure 4.12).

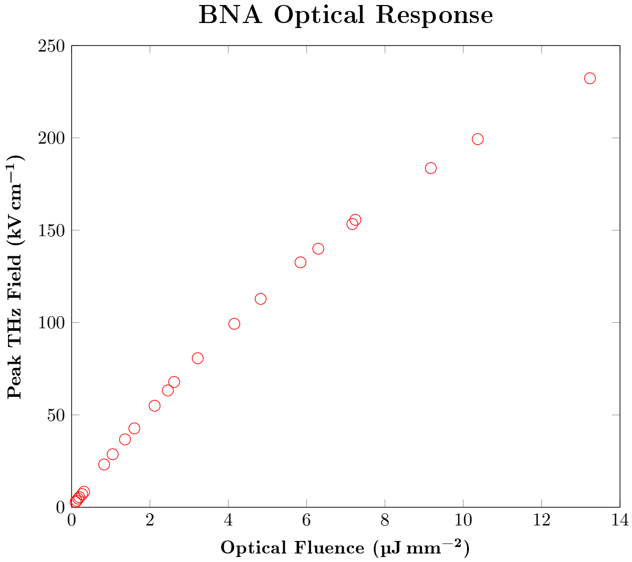

Figure 4.11: Optical response of the BNA crystal. Sublinear response is due to the use of a Si filter (see Figure 4.12).

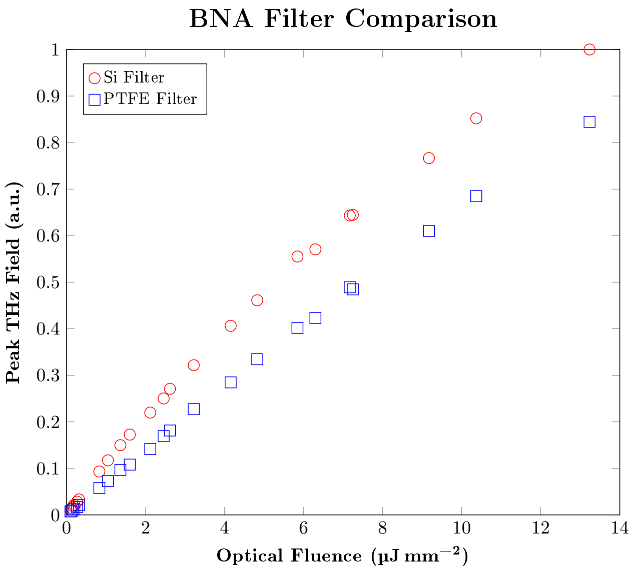

Figure 4.12: Optical response of the BNA crystal using a Si wafer and PTFE as a filter. The optical response can be seen to become linear when using the PTFE.

Comparing the BNA at its maximum output to a 15×15 mm PCA using the same system configuration (no beam expansion with a Si filter), it can be seen that the BNA is capable of generating peak fields $\sim \times 4.6$ greater in magnitude (see Figure 4.13a), over a greater bandwidth (see Figure 4.13b).

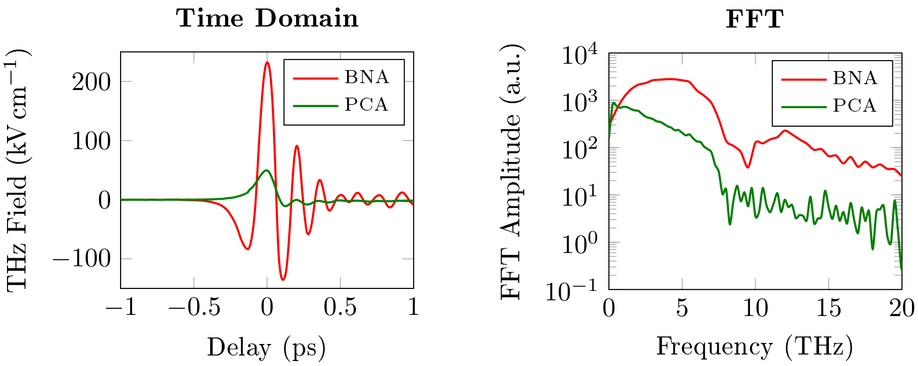

(a) Time domain responses.

(b) Fourier transform of Figure 4.13a.

Figure 4.13: Comparison of the BNA crystal and a 15×15 mm PCA and peak operating fields. Both measurements were performed using the same setup shown in Figure 4.10 without the reflective beam expander. Both emitters were placed in a collimated excitation beam in the position of 'Emitter A'. Time domain scans were obtained using a 150 µm GaP detection crystal. An Si filter was used to block excess any of the excess IR excitation beam after the emitters. The delay of both pulses have been centred on the peak of the response. The PCA was biased with an electric field of 22 kV cm^{-1} and excited with an optical power of 380 mW. The BNA was excited with an optical power of 2 W.

In the system described in Section 4.2.1, the BNA crystal will be used as 'Emitter B' for 2D measurements, as the incident beam size is comparable to the crystal and because the from testing, it was found that the Si beamsplitter is not 50:50 and more of the THz pulse is transmitted than reflected. This meant that for both pulses to reach the emitter with a large field, the strongest emitter would have to be placed in the Emitter B position to compensate for the transmission losses. For 1D saturation measurements where larger fields are required than the PCA can generate, the BNA is used in the 'Emitter A' position.

4.3 Conclusion

Figure 4.14 shows the false nonlinear response of the single emitter system compared with that of the two emitter system. From this it can be seen that the false nonlinear signal of the two emitter system is indistinguishable from noise, unlike the single emitter system which has a definite response. This shows that this system is a definite improvement over the first developed.

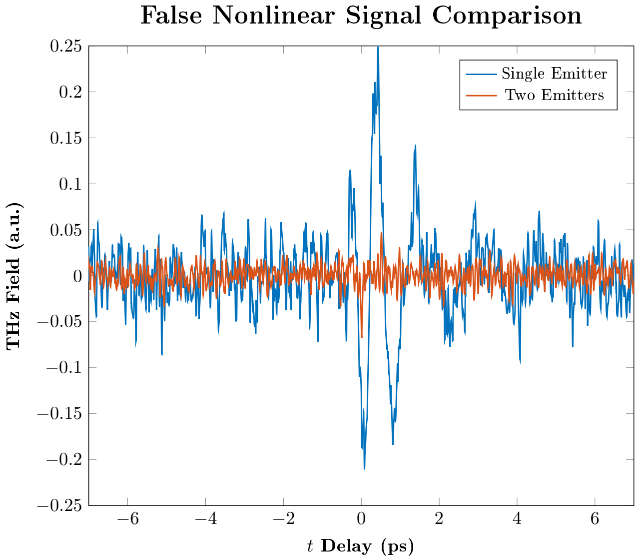

Figure 4.14: Comparison of the false nonlinear signal of the single and two emitter systems. Signals have been normalised to the peak field of E_{AB} and t delay has been centred to the peak of E_{AB}. The false nonlinear response for the single emitter system has efficiency factors applied. Both scans were taken at $\tau = 0\,\mathrm{ps}$.

In summary, a 2D THz TDS using two emitters has been developed. Both excitation beamlines have a maximum pulse energy of 3 mJ, sufficient for PCAs and EO crystals to be operated close to their damage threshold, providing the maximum field.

Owing to the design of the system, the THz field at the sample space can be measured. This has proved to be incredibly useful when aligning the system, as the overlap of both pulses can be measured at the sample space and the detection space. For 2D TDS measurements to be performed successfully, both pulses must be overlapped on the sample in space for the same region to be excited, allowing for nonlinear responses to be induced. Field detection at the sample space also proved useful for calibrating 'saturation' measurements which are discussed in the following chapters (Sections 5.4, 6.3.2 and 6.4.2), where TDS measurements are performed at multiple field strengths to extract the field required to saturate an absorption within a sample.

A BNA EO crystal has been tested with the system and shown to be able to generate peak fields $> 200\,\mathrm{kV\,cm^{-1}}$ over a broad bandwidth ($> 6\,\mathrm{THz}$) without the need of any phase matching as required with other EO crystals, such as $\mathrm{LiNbO_3}$. This allows for BNA crystals and PCAs to be used interchangeably within the system.

The system has also been designed for possible future measurements. Using two separate emitters allows for the possibility of using a narrowband THz emitter combined with a broadband THz emitter (instead of the two broadband emitter approach currently used). This may be useful for 'pump-probe' measurements (see Section 2.4.2), where a narrow transition is to be excited, with the dynamics of the multiple relaxation paths are measured.

Chapter 5

2D Spectroscopy of Ge:As

This chapter details the first sample measured using the experimental setups described in the previous chapters. The sample itself is a semiconductor wafer (Ge) doped with impurities (As). The chapter is split into three sections, with some background semiconductor physics theory being introduced first (Section 5.1), followed by a more detailed summary of the sample (Section 5.2), finishing with a summary of the measurements performed on the sample and findings (Sections 5.3 to 5.6). It should be noted that the measurements performed on this sample occurred throughout the three-year duration of this PhD, thus there are differences in the experimental setup used between experiments. A summary of the specific experimental system used is provided at the start of each experimental section.

In the THz region, applications of impurity centre transitions include development of impurity state lasers [111], THz detectors for space telescopes [112] and coherent control of quantum phenomena [7], which has applications in quantum computing for control of spin orbitals. Impurity centres operating outside the THz region (specifically Si:P) have been shown to be able to perform quantum computing operations [113, 114].

This sample was chosen due to the strong transitions in the 1–3 THz range, well within the detectable bandwidth of a 1 mm ZnTe detection crystal. Performing broadband 2D THz TDS measurements on the sample gives access to multi-level dynamics and for T_1 and T_2 lifetimes to be measured in a lab based system, rather than a FEL. Using a FEL, the T_1 value can be acquired using pump-probe measurements [115] whilst the T_2 value can be acquired using photon-echo measurements [7]. With 2D THz TDS, both of these values can be acquired simultaneously from the nonlinear signal [84].

5.1 Theory

This section will introduce the theory of semiconductors, in particular, doped semiconductors and impurity centre theory.

5.1.1 Introduction to Semiconductors

Electrons orbit atoms in shells which can be described by two quantum numbers, n and l, which are the principal and orbital angular momentum quantum numbers respectively. Both numbers are integers, increasing by one for each shell ($n = 1, 2, 3\ldots$ and $l = 0, 1, 2\ldots$), with the maximum number of electrons in a given shell given by $2(2l + 1)$ [11]. Table 5.1 shows the maximum number of electrons per shell and subshell. Using Ge as an example, it has an atomic number of 32 so the electrons in the subshells $n = 1 \rightarrow 3$ will all be filled and at $n = 4$, the s subshell will be filled and the p subshell will contain two electrons. This is commonly written in the form $1s^2 2s^2 2p^6 3s^2 3s^6 3d^{10} 4s^2 4p^2$ with the superscript denoting the number of electrons in the given state. The sum of electrons in the atom equal its atomic number.

		Subshell			
		$l = 0$	1	2	3
n	Shell	s	p	d	f
1	K	2			
2	L	2	6		
3	M	2	6	10	
4	N	2	6	10	14

Table 5.1: Maximum number of electrons per shell and subshell of an atom.

Subshells are grouped into pairs of electrons with opposite spin and when a given subshell is filled, no more electrons can be accepted into that state. When groups of atoms are brought together, electrons in the outermost unfilled subshell interact with each other, allowing for them to become bonded. In a structure with N atoms, the energy levels overlap, forming energy bands. Within these bands, the probability of finding an electron at a given energy level (E) can be obtained using the Fermi function:

$$f(E) = \frac{1}{1 + \exp(\frac{E - E_F}{kT})}, \tag{5.1}$$

where k is the Boltzmann constant, T is the temperature and E_F is the Fermi energy of the material, which is the energy level that electrons will fill up to at 0 K. In metals (e.g. Cu and Au), the bands overlap, producing a single, continuous energy band, forming a ‘sea’ of free electrons available for conduction. The region of fully filled electron states is known as the valence band, whilst the region with unfilled states is known as the conduction band. This can be represented using an energy band diagram, shown in Figure 5.1.

In semiconductors (e.g. Si and Ge), the bands do not overlap, but are separated by an energy gap (E_G), meaning that at 0 K, they act as insulators, but electrons in the valence band can undergo thermal or photo excitation into the conduction band. The fermi energy for an intrinsic semiconductor is found

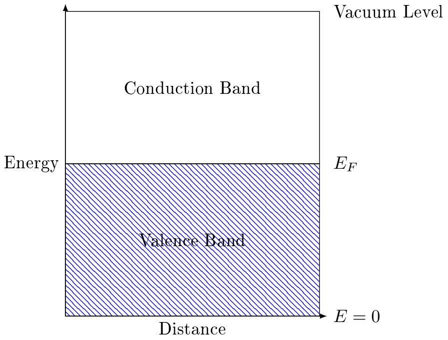

Figure 5.1: Bandstructure diagram of a metal.

in the middle of E_G. Figure 5.2a shows an energy bandstructure diagram of an intrinsic semiconductor.

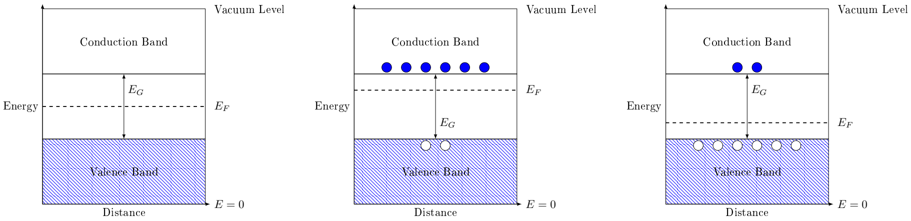

(a) Intrinsic semiconductor. (b) n-type semiconductor. (c) p-type semiconductor.

Figure 5.2: Bandstructure diagrams of differently doped semiconductors at low temperature. Impurity donor electrons are shown as blue circles. Impurity acceptor holes are shown in white.

Semiconductors may also have impurities embedded into the crystal structure in a process know as 'doping'. This is done to introduce carriers into the material, either as electrons in the conduction band (n-type doping), or as holes in the valence band (p-type doping). This increases the fermi energy of the crystal in the case of n-type doping, whilst decreasing the fermi energy for p-type doping. Figures 5.2b and 5.2c show the energy bandstructures of an n and p doped semiconductor respectively. The amount of dopant added to the crystal is often very small (1 dopant atom per 10^5 intrinsic atoms), but can cause a drastic increase in conductivity ($\sim 1000\times$ increase in magnitude), leaving the crystal structure mostly unchanged.

5.1.2 Impurity Centres

At low temperatures, the extra carrier introduced by a donor atom becomes bound to the donor atom itself, whilst still being affected by the forces from the surrounding crystal structure. Under these effects, the donor atoms behave like hydrogen atoms and are known as impurity centres [116, 117].

For a hydrogen atom, the frequency of a transition can be obtained using the Rydberg equation:

$$f = cR_H(\frac{1}{n_1^2} - \frac{1}{n_2^2}), \tag{5.2}$$

where n_1 is the principal quantum number of the base energy transition level, n_2 is the principal quantum number of the excited energy transition level and R_H is the Rydberg constant, which is $\sim 1.097 \times 10^7\,\mathrm{m}^{-1}$. For an impurity centre, the forces from the surrounding crystal structure decrease the energy of these transitions, acting as a scaling factor, allowing for the transition frequencies to be obtained using the following formula:

$$f = cR_H(\frac{1}{n_1^2} - \frac{1}{n_2^2})(\frac{m^*}{\varepsilon_r^2}), \tag{5.3}$$

where m^* and ε_r are the effective electron mass and dielectric constant of the bulk semiconductor respectively. The main impact of this factor is how the transition wavelengths become shifted into different spectral regions. For $n_1 = 1$ in hydrogen, the transitions occur in the Ultraviolet (UV) region, whilst for an impurity centre in a Ge crystal, the transition will be in the THz region ($m^* = 0.22$ and $\varepsilon_r = 16.2$).

5.1.2.1 Transition Relaxation Times

The relaxation times of transitions of impurity centres have historically been estimated using indirect methods, such as measuring the detection bandwidth [118] and the dependence between temperature and hole mobility [119], however, this led to values ranging from picoseconds [120] to microseconds [121], depending strongly on the doping concentration. The advent of the FEL and pump-probe techniques have allowed for direct and therefore more precise measurements to be performed, enabling relaxation times on the nanosecond [122] and even ~100 ps [123, 124] to be measured. Measurements using FELs do however suffer from limited time resolution of ~50 ps [125].

5.2 Sample Details

The sample tested was a Double Side Polished (DSP) 10×10×3 mm Ge:As wafer, with a doping concentration of $9\times10^{14}\,\mathrm{cm}^{-3}$, giving a resistivity of $1.7\,\Omega\,\mathrm{cm}$. The sample was provided by Dr. Sergey Pavlov, DLR, Berlin. The As dopant causes the wafer to become n-type doped, as an extra electron is embedded into the structure. Table 5.2 shows the energy levels of the As impurity centre, from which it can be seen that the s states split into two separate states; $Ns(A_1)$ and $Ns(T_2)$. This is due to ‘chemical splitting’ and occurs at all states of the impurity centre, but only causes significant splitting on the s states. Owing to the states having non-spherical symmetry, the p states lose their degeneracy, splitting into a singlet (p_0) and double ($p_\pm$) state. The combination of these perturbations in the sample relaxes the selection rules compared to the atomic structure, allowing for $s \rightarrow s$ and $p \rightarrow p$ transitions in some circumstances. [117]

State	Energy (meV)	Frequency (THz)
$1s(A_1)$	-14.18	3.42
$1s(T_2)$	-9.94	2.40
$2p_0$	-4.74	1.14
$2s(A_1)$	-4.10	0.99
$2s(T_2)$	-3.59	0.87
$3p_0$	-2.57	0.62
$3s(A_1)$	-2.32	0.56
$3s(T_2)$	-2.14	0.52
$2p\pm$	-1.74	0.42
$3p\pm$	-1.03	0.25

Table 5.2: Energy levels of Ge:As [117]. Diagram of these level shown in Figure 5.3.

Initial linear spectroscopy was performed by Dr. Sergey Pavlov and the research team at the DLR using Fourier-Transform Infrared Spectroscopy (FTIR), producing the data seen in Figure 5.4 (dark purple line). From the data, it can be seen that as well as the expected absorptions from the As impurities, there were other, lower frequency absorptions. These were determined to be unintended Sb impurities which embedded into the wafer during the doping process.

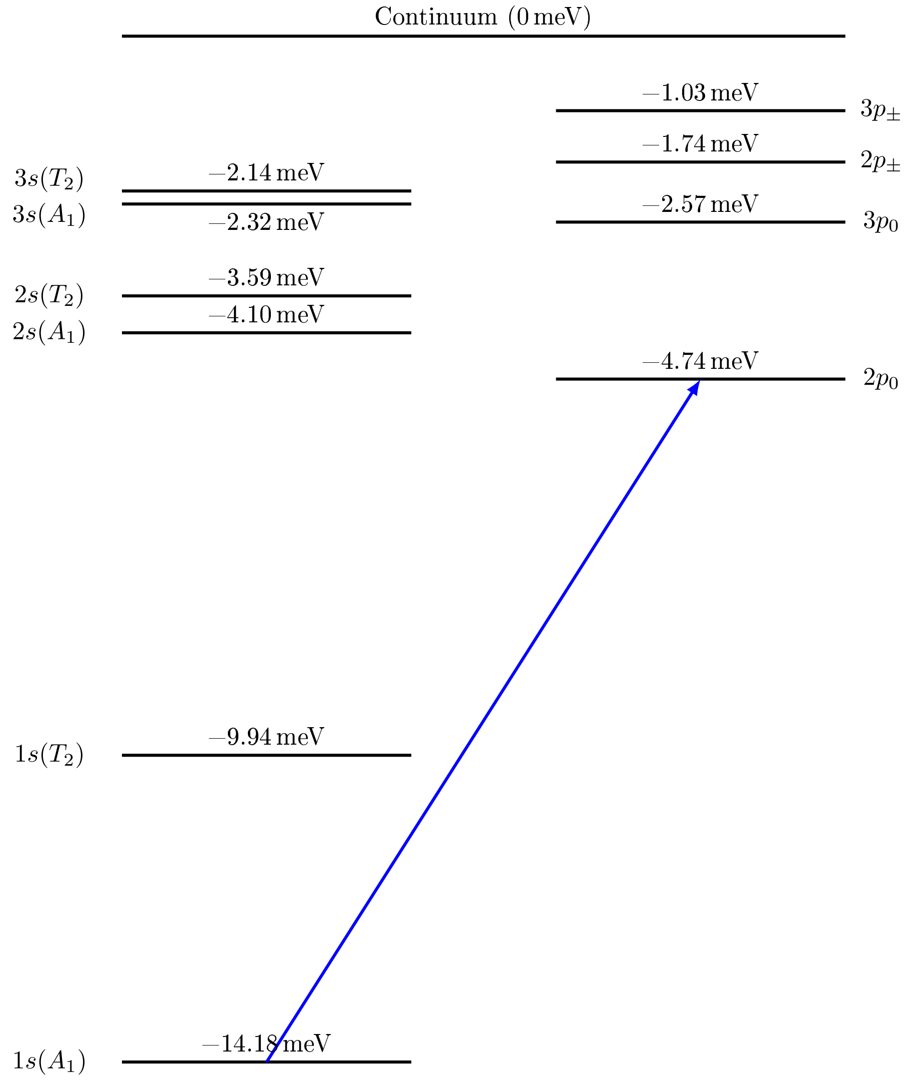

Figure 5.3: Energy level diagram of the Ge:As [117]. The blue arrow represents the main transition under investigation ($1s(A_1) \rightarrow 2p_0$) which has frequency of 2.28 THz.

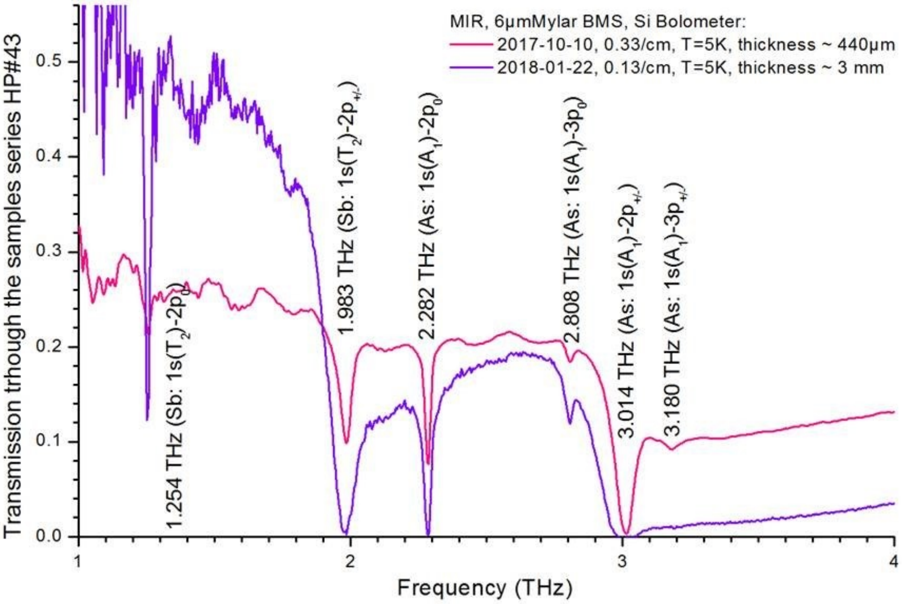

Figure 5.4: FTIR transmission through the Ge:As sample. Dark purple line is the 3 mm thick sample measured. The light purple line is a thinner (440 µm) sample not discussed. Data provided by Dr. Sergey Pavlov (DLR, Berlin).

5.3 Linear Spectroscopy

To confirm that the transitions were visible using TDS, the sample was measured in a low power TDS system [126]. The system uses a Ti:Sapphire laser oscillator (*Coherent Vitatra-HP*) with a 80 MHz repetition rate and <20 fs pulse duration with single-gap PCS for emission and detection [19]. The emitter and detector are both mounted on thick quartz substrates, allowing for a long time range before the first reflection to improve the frequency resolution [19]. The use of a PCS as a detector allows for a detectable bandwidth >5 THz and due to it being an high repetition rate oscillator system, it is easier to obtain a high SNR when compared with a low repetition rate amplified system.

The sample was clamped on the cold finger of a cryostat (*Oxford Instruments Microstat*) with Polymethylpentene (TPX) windows using two copper plates with 3 mm diameter holes cut into each plate to allow for light to be coupled in and out of the sample. For the experiment, the Ge:As was first measured at a temperature cold enough for the free electron from each As impurities to settle into quantised, hydrogen-like states (<10 K) and then the measurement was repeated at a higher temperature where the electrons become thermally distributed, so no hydrogen-like states will be observed. The higher temperature measurement was performed to act as a reference to normalise the data when post-processing. For the remainder of this chapter, the low temperature measurement will be referred to as the 'sample' measurement, whilst the higher temperature measurement will be referred to as the 'reference' measurement. For this experiment, the temperature of the sample and reference measurements were 4.8 K and 50 K respectively. The system is also purged with dry air to prevent the excitation pulse being absorbed by water molecules in the air, increasing the strength of the THz pulse and producing a cleaner spectrum [127].

Figure 5.5a shows the obtained time domain data. The measured scan range ended before the first system reflection so no windowing was performed on the data. Figure 5.5b shows the resulting frequency domain data, obtained by performing a FFT on the time domain data. After the FFT is acquired, the transmission through the sample as a function of frequency is then acquired by dividing the sample FFT by the reference FFT. This normalises the sample frequency domain data, suppressing unrelated absorptions present in the system. Figure 5.6 shows the resulting transmission of the sample. From this, the $1s(T_2) \rightarrow 2p_0$ of the Sb (1.25 THz) and the $1s(T_2) \rightarrow 2p_\pm$ of the Sb (1.98 THz) can be seen quite clearly, whilst the absorptions around 3 THz have become obscured into a single, broad absorption. The feature of main interest ($1s(A_1) \rightarrow 2p_0$ of the As) at 2.28 THz is unfortunately not as clear to distinguish from the transmission data, but can be seen more clearly in Figure 5.5b. This was attributed to the temperature of the reference measurement not being warm enough for all of the higher frequency states to be fully ionised ($kT/h = f \approx 1\,\mathrm{THz}$). The greater transmission seen at lower frequencies is attributed to the electrons in the sample no longer screening the THz pulse when the sample is cooled. The shape of the graph is quite different to that of FTIR data (Figure 5.4) because the length of scan used was relatively short, obscuring the narrow transitions, but it could also be because the sample was not cooled enough to depopulate all the states. This measurement still however confirmed that the transitions could be seen using THz TDS.

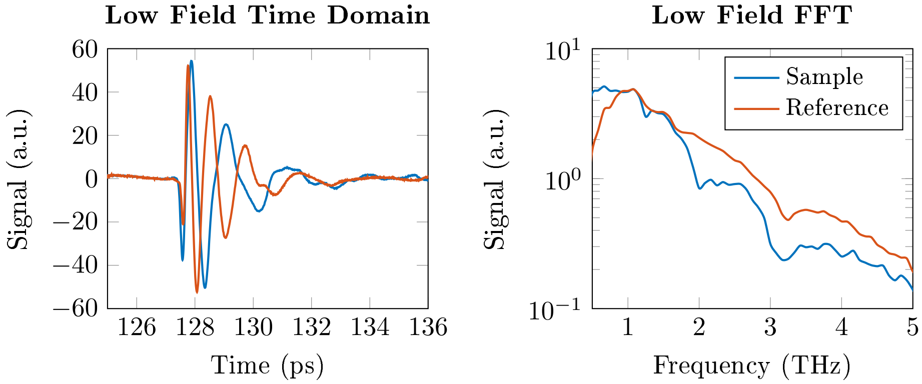

(a) Measured time domain data.

(b) Fourier transform of Figure 5.5a.

Figure 5.5: Data from the linear spectroscopy measurement of the Ge:As wafer. Blue data is the 'sample' measurement of the wafer cooled to 4.8 K and the red data is a 'reference' measurement of the same wafer at 50 K. A PCS was used as the detector.

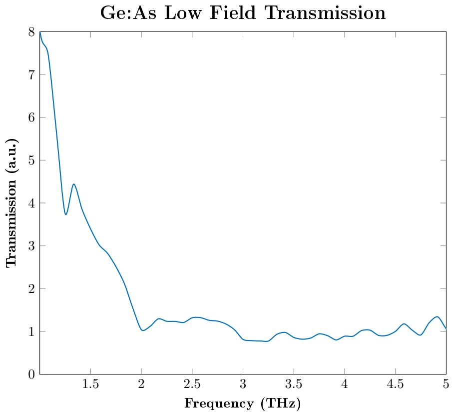

Figure 5.6: Transmission through the Ge:As at low excitation fields. Transmission response obtained by dividing the response of the 'sample' measurement (taken of the Ge:As wafer at 4.8 K) by that of the 'reference' measurement (taken of the same sample at 50 K) shown in Figure 5.5b.

5.4 Saturation Measurement

The next measurement to be performed was a ‘saturation’ measurement, wherein multiple 1D-TDS measurements are made, with the peak THz excitation field being altered after each series of measurements. This is done to acquire an estimate for the excitation field required to saturate a specific transition within the sample. This information is crucial when performing 2D-TDS measurements, as if the transition is not saturated, certain nonlinear effects may not occur.

5.4.1 Saturation Field Estimation

First, an estimate is made of the field required to saturation the transition, for which, we need the dipole moment of the transition, which can be estimated by using the Bohr radius, the radius between and electron in the ground state and the nucleus. For hydrogen, this radius, a_0 is well known as ~52.9 pm. Because the sample can be viewed as hydrogen-like, we can apply a scaling factor to account for the surrounding Ge crystal field to estimate the Bohr radius of the sample using the following equation:

$$a_d = a_0(\frac{\varepsilon_r}{m^*}), \tag{5.4}$$

where ε_r is the dielectric constant and m^* is the effective electron mass; for Ge, these values are 16.2 and 0.22 respectively, acquiring $a_d \approx 73.64a_0$. The Bohr radius can then be used to estimate the distance between the transitions of interest, as the radius of a transition can be acquired using:

$$r = n^2 a_d, \tag{5.5}$$

where n is the quantum number of the transition. As the transition of interest is a $1s \rightarrow 2p$ transition, the distance between the states can be estimated as ~11.7 nm. This is then the dipole moment when multiplied by the unit charge ($d = q\Delta r = q11.7\,\text{nm}$). Finally, we can estimate the field required to induce a full Rabi oscillation (explained in detail in Section 6.1.2) using:

$$E_{\text{THz}} = \frac{\Omega_{\text{Rabi}}\hbar}{|d|}, \tag{5.6}$$

where Ω_{Rabi} is the Rabi frequency, which for this transition is $2\pi \times 2.28\,\text{THz}$. Substituting in the dipole moment estimate, a narrowband saturation field of ~$8\,\text{kV}\,\text{cm}^{-1}$ is acquired. Because the system can produce peak broadband fields greater than $100\,\text{kV}\,\text{cm}^{-1}$, it should be possible to saturate the transition.

5.4.2 Experimental Information

For this measurement, a setup similar to the system shown in Figure 3.6 was used, with a 10×10 mm PCA being used as the emitter. The 800 nm excitation beam width was doubled using a transmissive beam expander and then focused onto the emitter and subsequently the sample using a 50 mm focal length lens. The emitter was placed 5 mm away from the focusing lens. A 2 mm sheet of expanded PTFE was placed between the emitter and the sample to block any excess IR from exciting the sample. This configuration allowed for fields greater than 100 kV cm^{-1} to be obtained. A 1 mm thick ZnTe crystal was used as the EO detection crystal. This crystal was chosen as the features of interest were all below the maximum detectable bandwidth of the crystal (~3 THz) and to maximise strength of the detected signal and the time range available before the first reflection. The sample was mounted in a cryostat the same way as described in Section 5.3. The sample and reference temperatures used were 10 K and 100 K respectively. The excitation field strength was altered throughout the measurement by varying the bias applied to the PCA. PCAs are ideal for this style of measurement, as the emitted THz field is linearly proportional to the applied bias [18]. In a system using EO crystals for generation, the THz field strength would need to be altered by changing the power of the excitation beam which is commonly done using a series of ND filters. These ND filters potentially induce a difference in path length between different configurations due to slight changes in the thickness of glass, causing issues when comparing scans at different excitation powers. All measurements were performed in a dry air environment.

5.4.3 Data Analysis

To process the data, the acquired time domain traces were first windowed to remove reflections which may obscure the transition of interest in the frequency domain. Figure 5.7a shows the time domain trace before and after windowing and Figure 5.7b shows the resulting Fourier transforms. It can be seen in Figure 5.7b that the oscillations in the trace are suppressed, allowing for a cleaner trace to be obtained, showing a definite absorption at 2.28 THz, relating to the $1s(A_1) \rightarrow 2p_0$ transition.

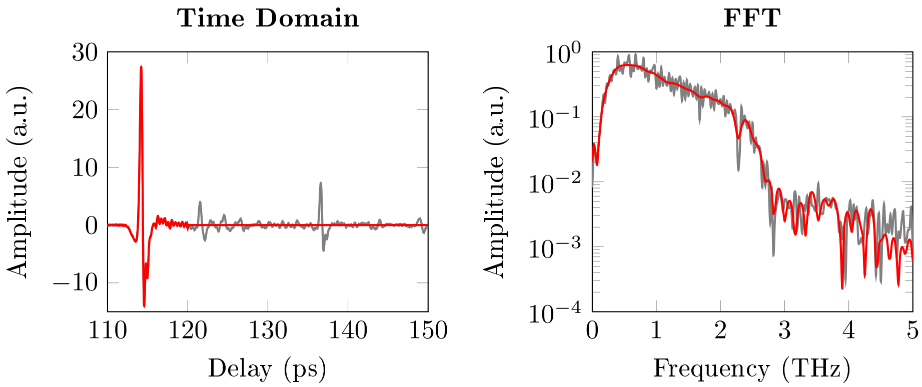

(a) Measured time domain data. (b) Fourier transform of Figure 5.7a.

Figure 5.7: Measured data of the Ge:As at 10 K with an applied field of 14 kV cm^{-1}. Red traces are the windowed data whilst grey traces are unwindowed data. The reflection at ∼121 ps is from the PCA substrate. The reflection at ∼136 ps is from the detection crystal. A 1 mm thick ZnTe crystal was used as the detection crystal.

From the windowed data, it can be seen that the absorption at 2.28 THz narrows and strengthens when unwindowed, suggesting that the lifetime of the transition is longer that the window used. When plotting the strength of the absorption as a function of window size, if the window size reaches the transition lifetime, the absorption would reach a constant amplitude. Figure 5.8 shows that with the data taken, even unwindowed, this has not occurred, suggesting that the lifetime larger than 40 ps.

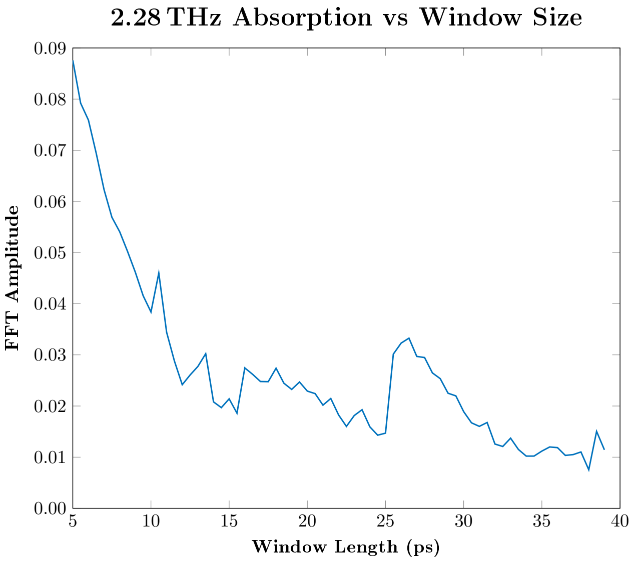

Figure 5.8: Absorption at 2.28 THz of the Ge:As sample cooled to 10 K with an applied THz field of 14 kV cm^{-1} as a function of window size. The data being windowed is shown in Figure 5.7a. Window starts at the same position (Delay = 110 ps) for all window sizes evaluated. Data is windowed in the time domain and then Fourier transformed to obtain the FFT amplitude for each window size evaluated.

Figure 5.9 shows the sample and reference data for the same applied THz field after being windowed. From Figure 5.9a, it can be seen that the strength of the detected reference signal is much lower than the sample signal. This is because at higher temperature, the electrons in the wafer are in an excited state, screening the incident THz radiation. The shift in time of the signal is attributed to the refractive index of Ge changing as a function of temperature [128].

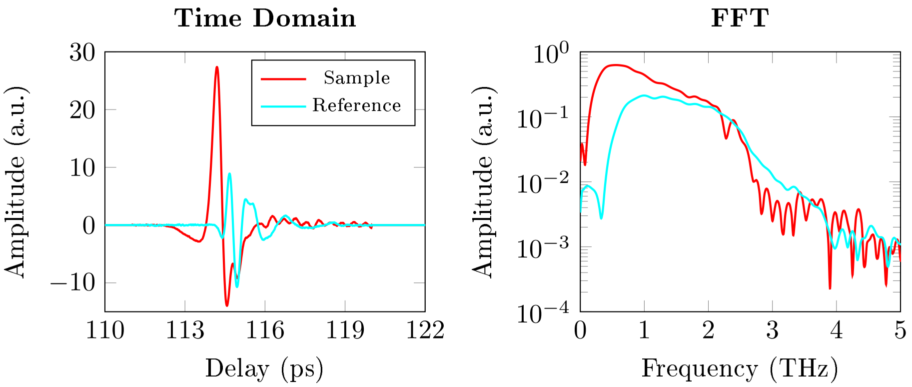

(a) Measured time domain data.

(b) Fourier transform of Figure 5.9a.

Figure 5.9: Sample and reference measurement of the Ge:As wafer with an applied field of 14 kV cm^{-1}. Red data is the 'sample' measurement of the wafer measured at 10 K and the cyan data is a 'reference' measurement of the same wafer at 100 K. A 1 mm thick ZnTe crystal was used as the detection crystal.

After the data is windowed and Fourier transformed, the transmission as a function of frequency is acquired by dividing the sample frequency domain data by the reference frequency domain data. This normalises the sample frequency domain data, suppressing unrelated absorptions present in the system. Figure 5.11 shows the resulting transmission response of the sample. From this, it can be seen that there is a strong absorption at 2.28 THz present with all excitation fields as expected, but there is also a strong absorption at ∼2.6 THz, only at present at the strongest applied field. After further investigation, the unexpected absorption was determined to be an artefact caused by the photodiode signal saturating the boxcar, causing the signal to become clipped. The other traces were checked and no clipping was found. This is more pronounced when comparing the Fourier transforms of the sample data at the highest field, shown in Figure 5.10, where a low frequency oscillation, characteristic of squared waveforms, can be observed in the response that is absent from the lower field measurements.

From the calculated transmission, the peak absorption at a given frequency can be obtained using the following formula:

$$A(f) = -\log_{10}(T(f)), \tag{5.7}$$

where $T(f)$ is the transmission through the sample as a function of frequency.

To acquire the field required to saturate the transition of interest, a frequency slice at the transition frequency (2.28 THz) is acquired and plotted as a function of intensity. The square of the applied THz field is used as the unit of intensity because $I \propto V^2$. As the measured transitions of the As dopants are interacting with the non-uniform field of the surrounding Ge crystal structure, it is expected

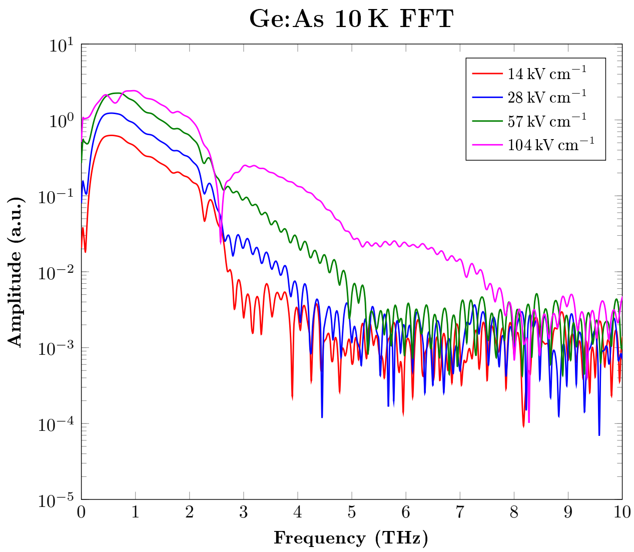

Figure 5.10: Frequency response of the Ge:As wafer measured at 10 K at various applied THz field strengths. Differing field strengths obtained by changing the bias applied to the PCA emitter. A 1 mm thick ZnTe crystal was used as the detection crystal.

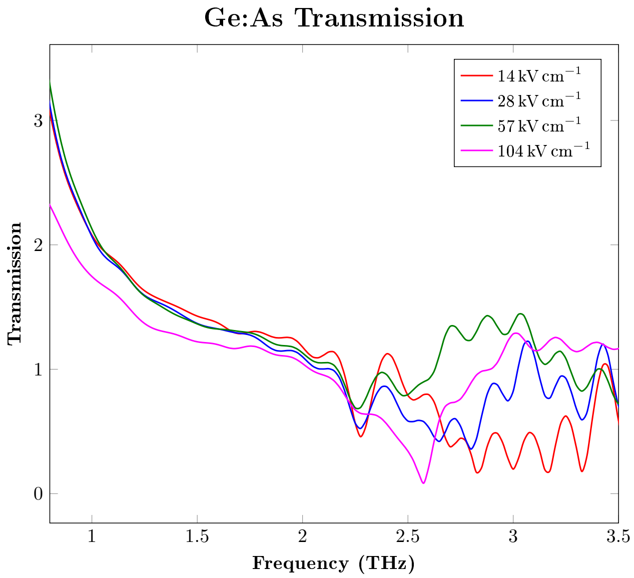

Figure 5.11: Transmission through the Ge:As wafer at different THz field strengths as a function of frequency at low temperature (10 K) when compared to the same sample at a higher temperature (100 K).

that the linewidth of the transition will be inhomogeneously broadened [117]. For inhomogeneously broadened transitions, the absorption response can be fitted to:

$$A_{\mathrm{I}}(I) = \frac{1}{\sqrt{1+\dfrac{I}{I_s}}}, \tag{5.8}$$

where I is the intensity and I_s is the saturation intensity. An attempt to fit the absorption response to a homogeneously broadened transition is also made:

$$A_{\mathrm{H}}(I) = \frac{1}{1+\dfrac{I}{I_s}}. \tag{5.9}$$

This is done to aid the validity of the analysis, as if the absorption response was homogeneous, it would indicate that another transition is being measured.

Figure 5.12 shows the calculated absorption data with four fits. From this, it can be seen that the data is a closer fit to an inhomogeneously broadened transition, with a saturation field 15–20 kV cm^{-1}. The data point from the highest field does not entirely fit within the expected line, however this may be owing to the aforementioned clipping. This range of saturation fields is well within the range that can be generated by the system, meaning that it should be possible to generate nonlinear effects within the sample using 2D-TDS.

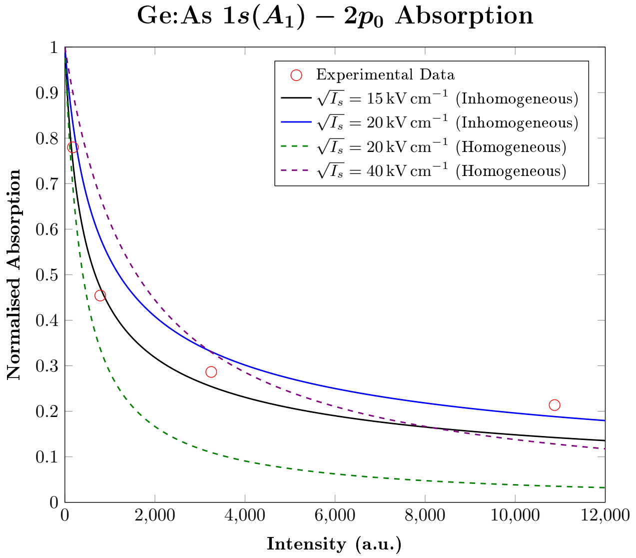

Figure 5.12: Absorption of the $1s(A_1) - 2p_0$ transition (2.28 THz) of the Ge:As wafer as a function of estimated intensity. Normalised absorption values acquired from the transmission at low temperature (10 K) when compared with a higher temperature (100 K), seen in Figure 5.11.

5.5 Two-Dimensional Spectroscopy

The previous measurements indicated that the $1s(A_1) \rightarrow 2p_0$ transition could be saturated with THz fields in the 15–20 kV cm^{-1} region so a 2D-TDS measurement was performed on the sample using the two emitter setup described in Section 4.2.

5.5.1 Experimental Information

A 15×15 mm PCA and a BNA crystal (described in Section 4.2.2) were used as the emitters, combining on a Si beamsplitter. Expanded PTFE filters were placed after each emitter to block any excess IR. With this configuration, both emitters are capable of generating peak fields of ∼60 kV cm^{-1}. The peak fields of both devices were used for this experiment. For the remainder of this section, the pulses generated from the PCA will be referred to as 'A' pulses, whilst pulses generated from the BNA will be referred to as 'B' pulses. A 1 mm thick ZnTe crystal was used for detection, identical to the one used for the saturation measurements in Section 5.4. The sample was again mounted in a cryostat, as described in Section 5.3. The sample was cooled to 6 K for the measurement. All measurements were performed in a dry air environment.

A sampling delay (t) range of 18 ps with a step size of 0.01 ps was used, giving a Fourier transform range and resolution of 100 THz and 56 GHz respectively. The delay range between E_A and E_B (τ) was −5–1 ps with a step size of 0.05 ps, giving a Fourier transform range and resolution of 20 THz and 167 GHz respectively. It was initially planned for a larger τ range with a smaller step size to be used, however, this was impractical owing to the time constraints on performing the experiment. This dataset took ∼ 10 hours to obtain and requires the sample to be cooled to < 10 K using a continuous flow He dewar. Performing the measurements over longer timescales would require the sample to be left cooling unsupervised overnight which could cause temperature instabilities or at worst, a potential safety hazard. Time domain traces of all four signal states were acquired for each τ delay 100 times to improve the SNR.

5.5.2 Data Analysis

The following sections summarise the data analysis techniques performed on the dataset and the results acquired.

5.5.2.1 Initial Processing

After all the data is acquired from the experiment, the τ delay of each measurement is corrected before any other processing takes place, as the initial τ delay is only an estimate. This is done by acquiring the difference in t delay between the peak signals of E_A and E_B for each estimated τ delay and calculating the difference from the estimated τ delay:

$$\tau_{\text{Correction}} = \tau_{\text{Estimate}} - \left[t_{(\text{Peak } E_\text{B})} - t_{(\text{Peak } E_\text{A})}\right]. \tag{5.10}$$

The mean $\tau_{\text{Correction}}$ is then calculated using $\tau_{\text{Correction}}$ from every τ delay and then added to τ. For this measurement, $\tau_{\text{Correction}} = -0.31\,\text{ps}$. To make the data easier to read, the t delay for the data is centred to the t delay where the peak field of E_{A} is found as well. Next, the time domain traces are converted from arbitrary units to estimated field using Equation 8.1. As a 1 mm ZnTe crystal is the detection crystal, $r_{41} = 3.9\,\text{pm}\,\text{V}^{-1}$ [44], $L = 1\,\text{mm}$ and $n_0 = 2.85$ [129].

5.5.2.2 Excitation Pulse Analysis

Figures 5.13a and 5.13b show the time and frequency domain responses of the excitation pulses E_{A} and E_{B} at $\tau \approx 0$ after passing through the sample. From this, it can be seen that E_{A} has more power at lower frequencies (<1 THz), whilst E_{B} has more power at higher frequencies, centred around ~1.7 THz. The frequency domain plots for both pulses appear to show an absorption around the $1s(A_1) \rightarrow 2p_0$ transition frequency (2.28 THz), indicating that both pulses are inducing the transition in the sample as expected. Figures 5.14 and 5.15 show the signals in the time and frequency domains respectively as a function of t and τ.

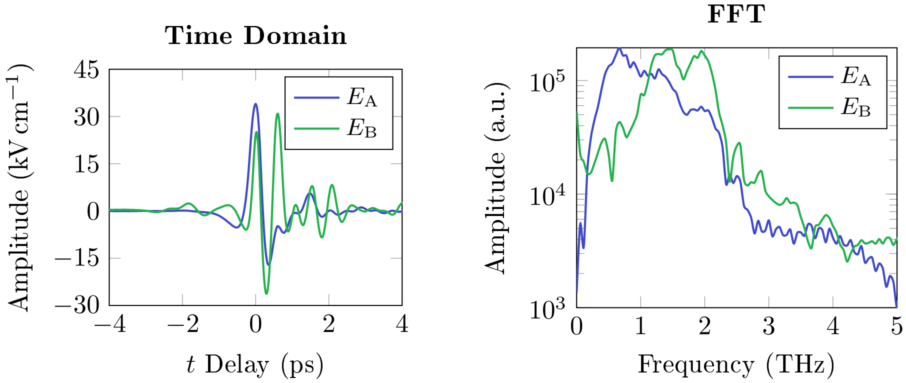

(a) Measured time domain data.

(b) Fourier transform of Figure 5.13a.

Figure 5.13: Time and frequency domain response of E_{A} and E_{B} at $\tau = 0.01\,\text{ps}$ after passing through the Ge:As sample cooled to <10 K. E_{A} is generated by a PCA with a peak field of $60\,\text{kV}\,\text{cm}^{-1}$. E_{B} is generated by a BNA crystal with a peak field of $60\,\text{kV}\,\text{cm}^{-1}$.

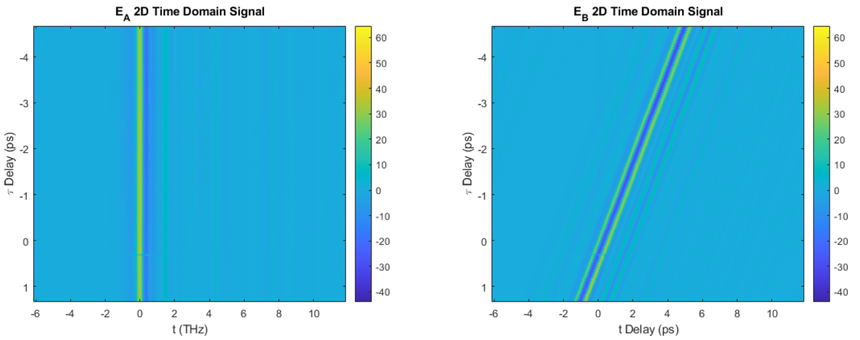

Figure 5.14: Time domain responses of E_A and E_B as a function of t and τ delay. E_A is generated by a PCA with a peak field of $60\,\mathrm{kV\,cm^{-1}}$. E_B is generated by a BNA crystal with a peak field of $60\,\mathrm{kV\,cm^{-1}}$.

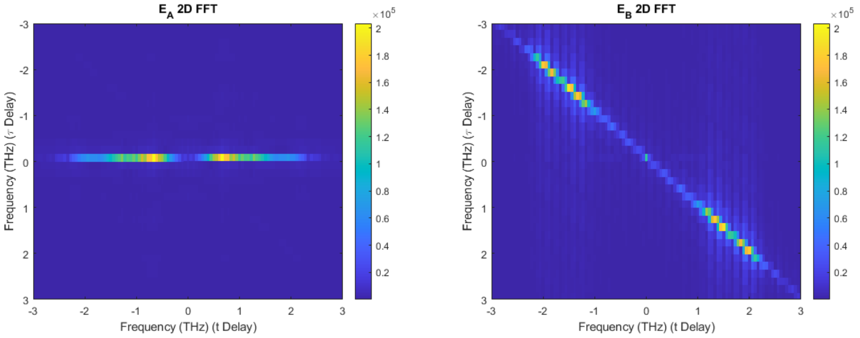

Figure 5.15: 2D FFT of the signals in Figure 5.14.

To see if any nonlinear effects are induced in the sample when both pulses are present on the sample simultaneously, the E_AB and $E_\mathrm{A} + E_\mathrm{B}$ signals can be compared in the 2D time and frequency domains. It should be noted that this type of comparison may not always indicate nonlinearities if the nonlinear effects are small, relative to the strength of the input pulses. Figures 5.16 and 5.17 show the 2D time domain and corresponding 2D FFT respectively. Only small differences can be observed between the time domain plots around $t = \tau = 0$, however, in the frequency domain, features can be seen faintly at $\tau < 0,\ t > 0$, indicating that some nonlinear effects have been induced in the sample.

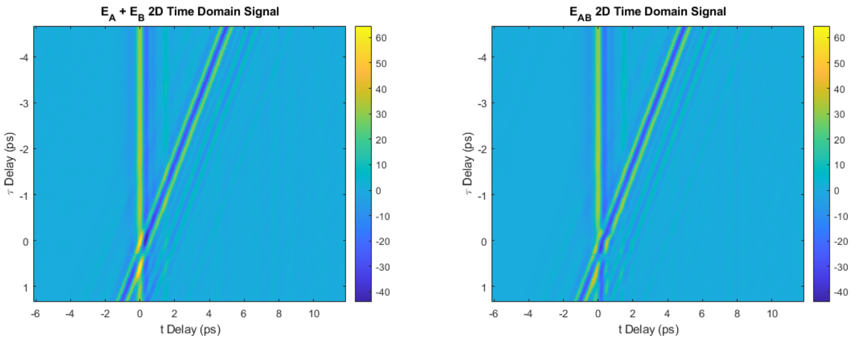

Figure 5.16: Time domain responses of $E_{\mathrm{A}} + E_{\mathrm{B}}$ and E_{AB} as a function of t and τ delay. E_{AB} is a measured signal whilst $E_{\mathrm{A}} + E_{\mathrm{B}}$ is calculated. If no nonlinear response is induced, $E_{\mathrm{AB}} = E_{\mathrm{A}} + E_{\mathrm{B}}$.

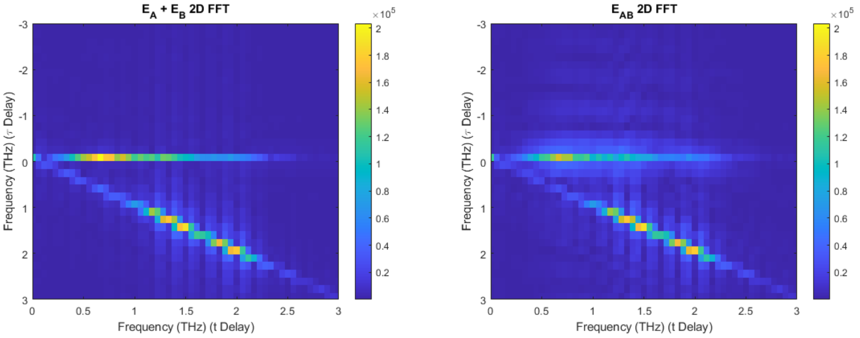

Figure 5.17: 2D FFT of the signals in Figure 5.16.

5.5.2.3 Nonlinear Signal Analysis

Although a small nonlinear effect can be seen in Figure 5.17, it is obscured by the strong excitation signals. Using Equation 4.1.3 allows for the nonlinear signal to be isolated in post-processing. This section discusses how the nonlinear signal is acquired from the measurement and how it can be analysed.

The nonlinear signal for each repeat measurement at each τ delay is first acquired, giving a signal as seen in Figure 5.18. The nonlinear signals from each of the 100 repeat measurements are then averaged together to improve the SNR (see Figure 5.19). In this example, the peak SNR is increased from ∼12 dB to ∼30 dB. A subset of the final nonlinear signals are shown in Figure 5.20, offset to improve readability. From this, it can be seen that the largest nonlinear response occurs when E_{A} and E_{B} overlap at $\tau \approx 0\,\mathrm{ps}$, which is when the sample is excited by the greatest field ($\sim 120\,\mathrm{kV\,cm^{-1}}$). For $\tau \leq 0$, the nonlinear response appears at $t = 0$ due to pulse B exciting the sample initially, then pulse A, which is fixed at $t = 0$, further exciting the sample, inducing the nonlinear response. For $\tau > 0$, the nonlinear response appears to move in time with respect to t due to pulses A and B swapping roles. The nonlinear response at $\tau = 1\,\mathrm{ps}$ is different to that of $\tau = -1\,\mathrm{ps}$ as $E_\mathrm{A} \neq E_\mathrm{B}$, meaning that the sample experiences a different excitation depending on pulse order, leading to a different nonlinear response. The greater nonlinear response seen at $\tau > 0$ is likely due to E_A having more amplitude at low frequencies ($< 1\,\mathrm{THz}$) (see Figure 5.13b).

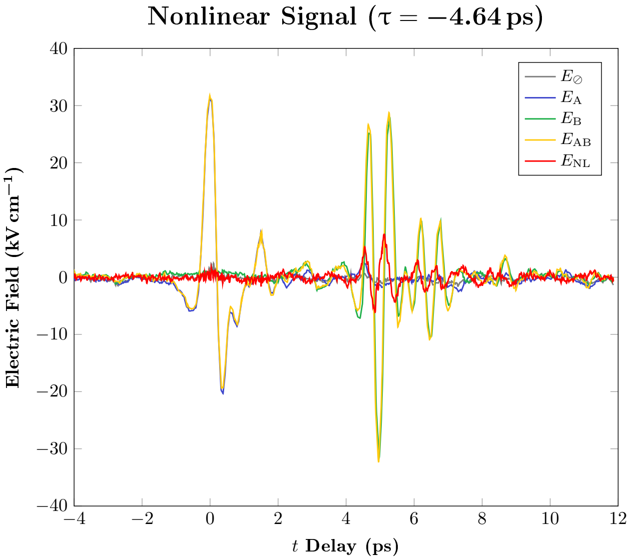

Figure 5.18: Time domain signals of each of the four states obtained with a single scan of the Ge:As wafer and the resulting nonlinear signal. E_A is generated by a PCA with a peak field of $60\,\mathrm{kV\,cm^{-1}}$. E_B is generated by a BNA crystal with a peak field of $60\,\mathrm{kV\,cm^{-1}}$.

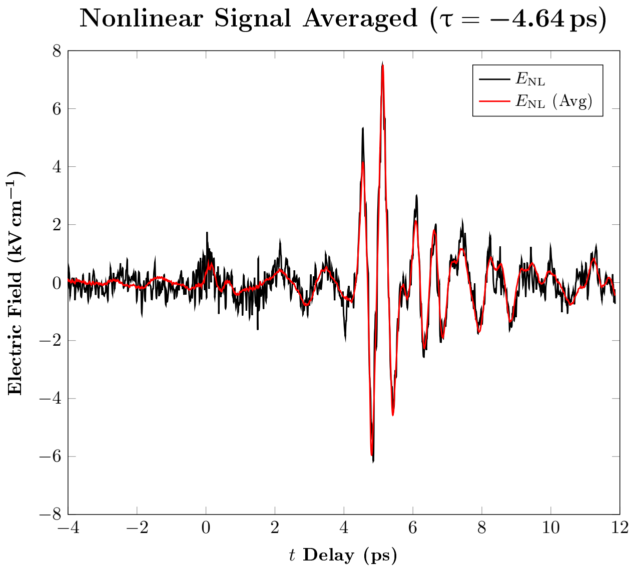

Figure 5.19: Comparison of the Ge:As wafer's nonlinear signal at $\tau = -4.64$ ps acquired from a single scan and the result after 100 scan repeats. This averaging increases the SNR from 25 dB to 58 dB.

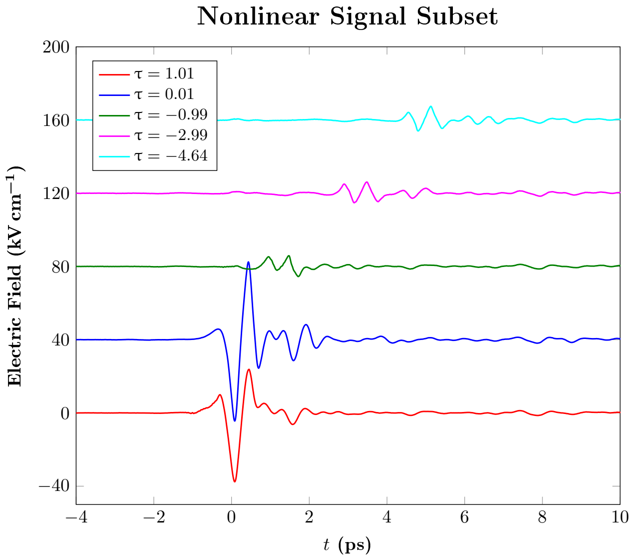

Figure 5.20: A subset of nonlinear signals at different τ delays induced in the Ge:As wafer. Signals are offset to improve readability.

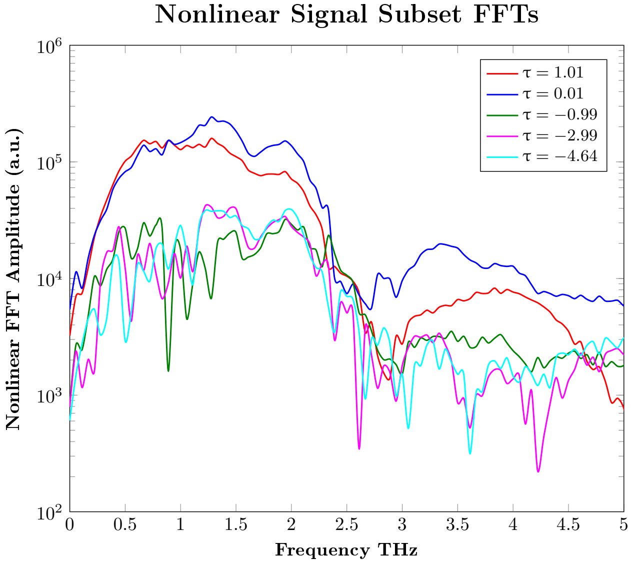

Figure 5.21: Fourier transform of the nonlinear signals shown in Figure 5.20.

A 2D plot of the nonlinear signal as a function of t and τ delay is then produced, shown in Figure 5.22. Performing a 2D Fourier transform on this produces the 2D frequency domain response, shown in Figure 5.23.

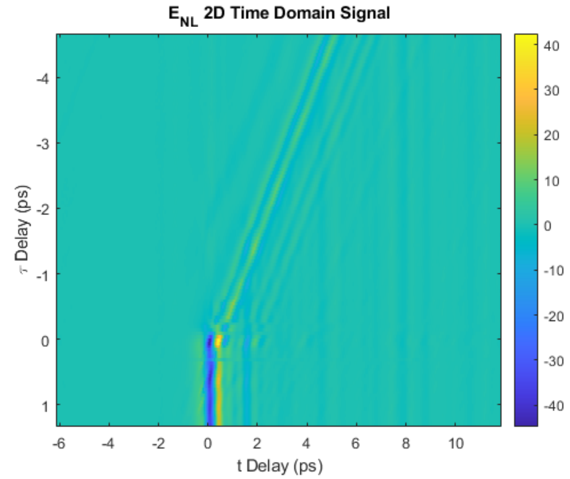

Figure 5.22: 2D nonlinear signal of the Ge:As sample. Nonlinear signal induced by a PCA with a peak field of $60\,\mathrm{kV\,cm^{-1}}$ (E_{A}) and a BNA crystal with a peak field of $60\,\mathrm{kV\,cm^{-1}}$ (E_{B}).

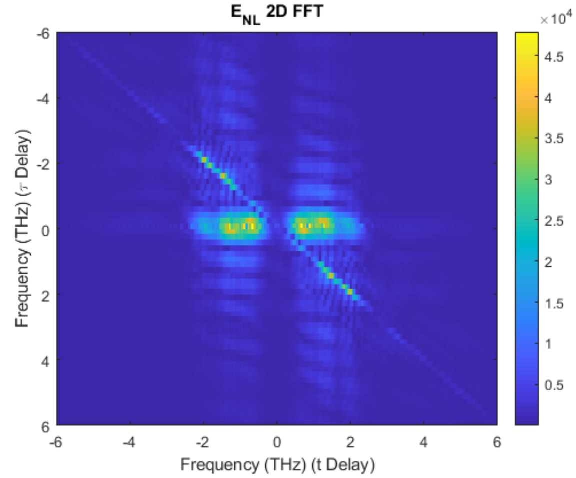

Figure 5.23: 2D Fourier transform of 5.22.

As discussed in Section 2.4.3, different regions of the nonlinear 2D FFT correspond to different nonlinear responses (e.g. third harmonic and Four-Wave-Mixing (FWM)). These regions can be inverse Fourier transformed to allow for that effect to be isolated in the time domain [81,82]. Figure 5.24 shows the nonlinear 2D FFT with the different third-order regions labelled and Figures 5.25a to 5.25d show the resulting time domain signals after the inverse FFT is performed. These regions were decided upon using the frequency space rules shown in Table 2.2 with $\nu_0 = 2.28\,\mathrm{THz}$. To improve readability of this section, 'pump-probe' signals will be denoted using P and p, where P represents the 'pump' pulse, p represents the 'probe' pulse. The pump pulse refers to the pulse initially exciting the sample, whilst the probe pulse identifies the pulse which then further excites the sample. It should be noted that this response is not referring a classical pump-probe experiment, as the probe pulse in such an experiment is set to be low in power so as not to induce nonlinear effects.

Both $P_\mathrm{A}p_\mathrm{B}$ and $P_\mathrm{B}p_\mathrm{A}$ both appear as expected, with the response of $P_\mathrm{A}p_\mathrm{B}$ appearing at a constant t delay and then dissipating at $\tau < 0$, where E_B switches to becoming the probe pulse. Meanwhile, the response of $P_\mathrm{B}p_\mathrm{A}$ appears when $\tau < 0$ and is strongest at $t \approx \tau$. It does not appear at exactly $t = \tau$ as the 'zero' position of E_B is defined as the first peak of the time domain response, which has a slightly lower field than the second peak (see Figure 5.13a).

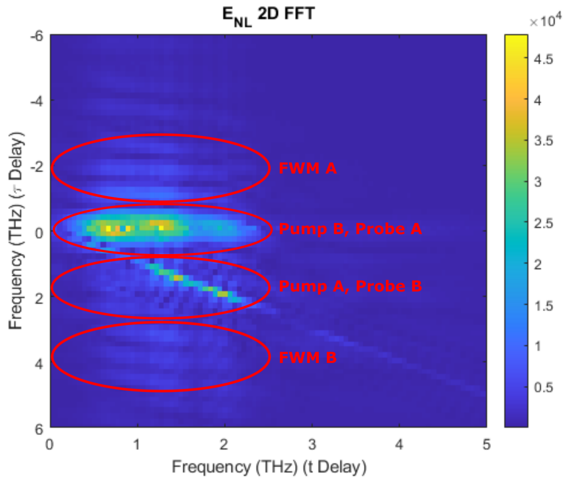

Figure 5.24: Zoomed area of Figure 5.23, highlighting the suspected third-order signal regions. $P_\mathrm{B}p_\mathrm{A}$ found at $(0 \to 3, 0)$ THz, $P_\mathrm{A}p_\mathrm{B}$ found at $(0 \to 3, \sim 2)$ THz, FWM A found at $(0 \to 3, \sim -2)$ THz and FWM B found at $(0 \to 3, \sim 4)$ THz.

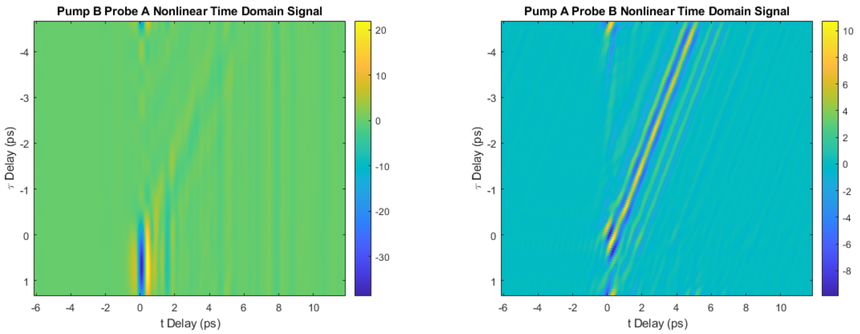

(a) Pump B, Probe A Response (b) Pump A, Probe B Response

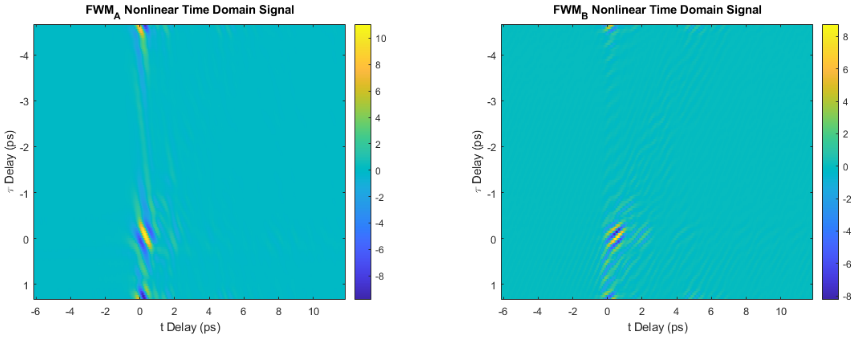

(c) FWM A Response (d) FWM B Response

Figure 5.25: Inverse 2D FFT of the nonlinear responses highlighted in Figure 5.24.

The FWM responses can be used to determine if the transition is homogeneously or inhomogeneously broadened by comparing where their centre points in time are found when compared with E_{A} and E_{B} [81]. The time centre of a pulse is obtained using the following equation:

$$t_c = \frac{\int tE(t)^2 dt}{\int E(t)^2 dt}. \tag{5.11}$$

For a homogeneously broadened transition, t_c of the FWM response would appear at a constant delay after the second pulse excites the sample, whilst for an inhomogeneously broadened transition, t_c would appear at a delay of τ after the second excitation pulse [81]. Figure 5.26 shows the comparison between t_c of both FWM responses compared with E_{A} and E_{B} and where the expected response of the FWM should be for an inhomogeneously and homogeneously broadened transition. It should be noted that an arbitrary delay of 1 ps was used for the homogeneously broadened response. From this, it can be seen that neither FWM responses follow the expected t_c of either an inhomogeneously or homogeneously broadened transition.

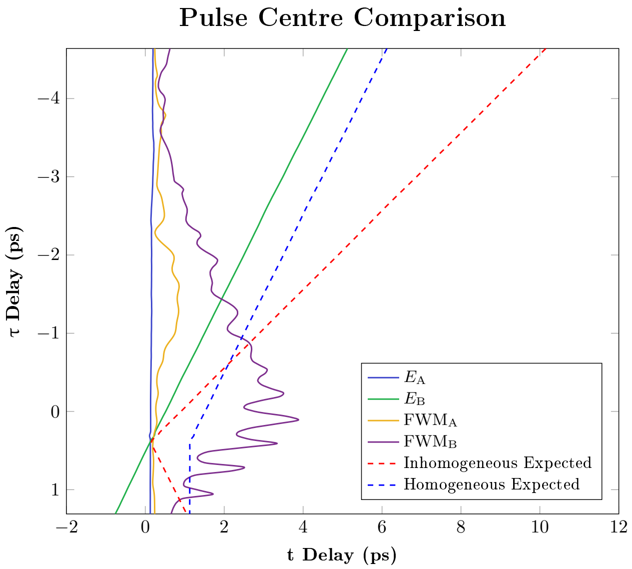

Figure 5.26: The t_c of the FWM responses seen in Figure 5.25 compared with E_A and E_B.

The 2D nonlinear time domain response can also be directly investigated to obtain the T_1 and T_2 values of the transition by fitting a slice of τ at a set t delay using the following equation [84]:

$$E_\mathrm{NL}(\tau) = A_1 \exp(-\frac{\tau}{T_1}) + A_2 \sin(\omega\tau) \exp(-\frac{\tau}{T_2}). \tag{5.12}$$

Figure 5.27 shows the 2D nonlinear time domain signal with the chosen delay slice to be fitted at $t = 0.5$ ps highlighted.

The T_1 for the sample is expected to be large when compared with the delay range of the data (∼ ns [130]), meaning that $A_1 \exp(-\frac{\tau}{T_1}) \approx A_1$. This removes a term from the fit, improving the chance of acquiring an accurate fit for T_2. As the main transition expected to be excited occurs at 2.28 THz, $\omega = 2.28 \times 2\pi$. The equation used for the first attempt of the fit was then:

$$E_\mathrm{NL}(\tau) = A_1 + A_2 \sin(2.28 \times 2\pi\tau) \exp(-\frac{\tau}{T_2}). \tag{5.13}$$

Using MATLAB's fitting toolbox, the data slice shown in Figure 5.27 was fitted using Equation 5.13, creating the fit shown in Figure 5.28a. From this, it can immediately be seen that Equation 5.13 is not a good fit, with a Root-Mean-Square Error (RMSE) of 2.906. This fit acquires T_2 as 0.2251±0.1867 ps. As the nonlinear signal may be being generated from a three-level system rather than a two-level system, Equation 5.13 was further modified, adding a second

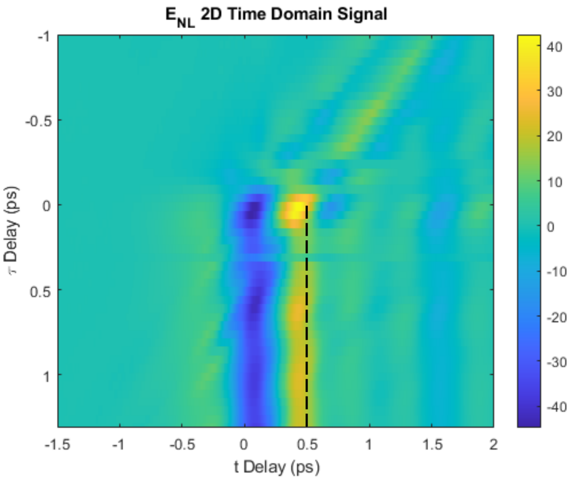

Figure 5.27: Zoomed region of the 2D nonlinear signal shown in Figure 5.22. The dotted line denotes the slice used for fitting Equation 5.12.

exponentially decaying sine wave to the fit, leading to the following equation:

$$E_{\mathrm{NL}}(\tau) = A_1 + A_2 \sin(2.28 \times 2\pi\tau)\exp(-\frac{\tau}{T_{2A}}) + A_3 \sin(f_B \times 2\pi\tau)\exp(-\frac{\tau}{T_{2B}}), \tag{5.14}$$

where f_B is the frequency of the second transition, T_{2A} is the T_2 value of the primary transition (occurring at 2.28 THz) and T_{2B} is the T_2 value of the secondary transition (occurring at f_B). The most likely secondary transition from the $2p_0$ state is to $2p_\pm$ so f_B was set to ~ 0.7 THz. Figure 5.28b shows the resulting fit, with the two frequency components separated, so their contributions to the final fitting functions can be seen. This fit acquires $T_{2A} = 5.829{\pm}4.311$ ps and $T_{2B} = 0.1340{\pm}0.0518$ ps with a RMSE of 1.6. This fit can still be improved further by ignoring the outlying data point, leading to the fit shown in Figure 5.28c. This acquires $T_{2A} = 0.8656{\pm}1.7214$ ps and $T_{2B} = 0.1268{\pm}0.0179$ ps with a RMSE of 0.6297. The two frequency fits with and without the outlier included give a similar value T_{2B} value of ~ 0.13 ps, however the value of T_{2A} varies wildly. This is likely owing to the value of T_{2A} being much larger than the provided delay range, making it difficult to accurately fit to the data. This is indicated by the large uncertainty of T_{2A}, however, the lower uncertainty of T_{2B} makes it more likely to be an accurate fit. The measured T_2 value of $1s(T_2) \rightarrow 2p_0$ is much smaller than that of the same transition in Si:P, measured as 160±20 ps using a FEL in Ref [7], which does raise some doubt about the value acquired for the Ge:As.

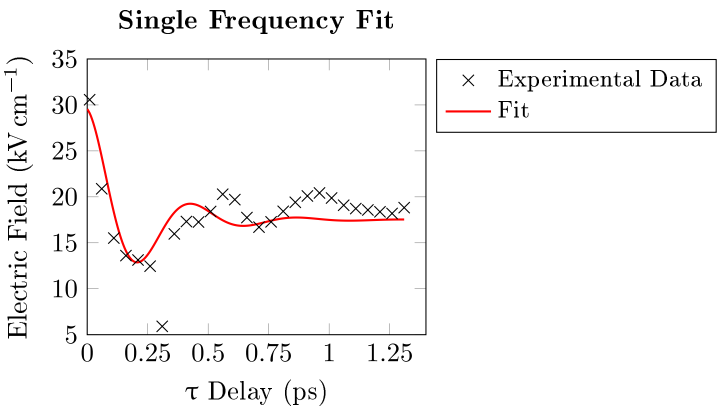

(a) Single frequency fit.

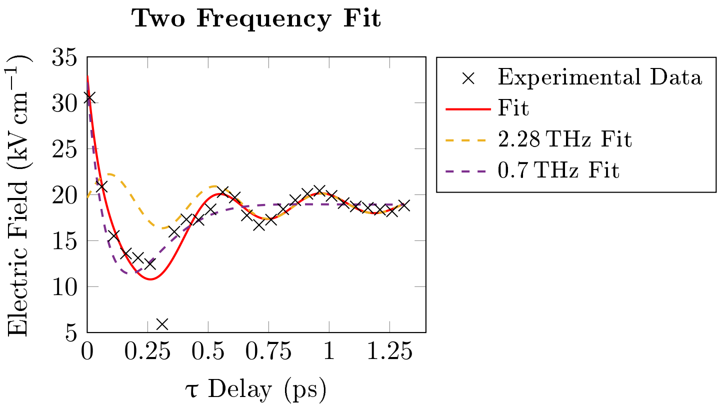

(b) Two frequency fit.

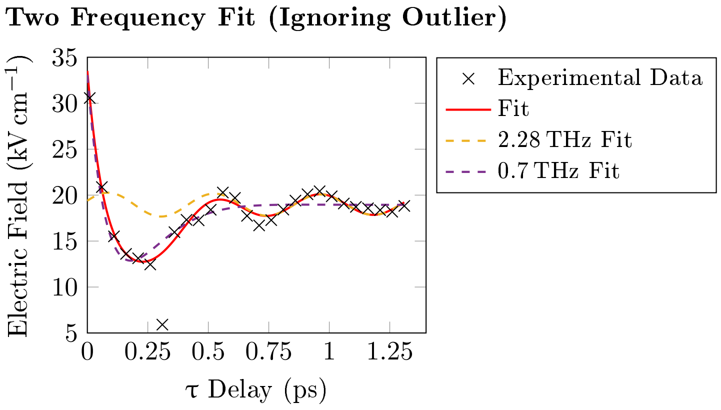

(c) Two frequency fit, ignoring the outlier.

Figure 5.28: Results of fitting Equations 5.13 and 5.14 to the nonlinear response slice shown in Figure 5.27. Fitting reveals that there are two frequency components in the nonlinear response, relating to the primary transition $1s(A_1) \rightarrow 2p_0$ (2.28 THz and a secondary transition at 0.7 THz, possibly the $2p_0 \rightarrow 2p_{\pm}/3s(A_1)$ transition.

5.5.2.4 Pump-Probe Analysis

The data can also be interpreted using a 'pump-probe' style analysis where the response induced in the sample when both pulses are incident on the sample can be obtained using the following equation:

$$E_{Pp}(t,\tau) = \begin{cases} E_{AB}(t,\tau) - E_A(t,\tau) & \tau < 0, \\ E_{AB}(t,\tau) - E_B(t,\tau) & \tau > 0, \end{cases} \tag{5.15}$$

$$E_p(t,\tau) = \begin{cases} E_B(t,\tau) & \tau < 0, \\ E_A(t,\tau) & \tau > 0, \end{cases} \tag{5.16}$$

$$\nu_R(\omega_t,\omega_\tau) = \frac{\nu_{Pp}(\omega_t,\omega_\tau)}{\nu_p(\omega_t,\omega_\tau)}, \tag{5.17}$$

where E_{Pp} is the time domain response through the sample when both pulses are incident with the 'pump' signal removed, E_p is the 'probe' signal, ν_{Pp} is the 2D FFT of E_{Pp} and ν_p is the 2D FFT of E_p. It should be noted however that this is not a true pump-probe measurement, as the probe pulse is intense enough to cause nonlinear effects within the sample. Figure 5.29 shows a time domain and corresponding FFT obtained using the above equation at $\tau = -0.99$ ps. Although the difference between E_{Pp} and E_p is quite subtle in the time domain (Figure 5.29a), it is more pronounced in the frequency domain (Figure 5.29b), where an absorption can be seen between ~0.6–0.8 THz, whilst an increase in signal can be seen between ~2.2–2.8 THz. This could be interpreted as that when both pulses are incident on the sample, the first pulse has saturated the $1s(A_1) \rightarrow 2p_0$ transition (leading to the observed increase in transmission around 2.28 THz), allowing for the second pulse to excite the $2p_0 \rightarrow 2p_\pm$ or $2p_0 \rightarrow 3s(A_1)$ transitions (leading to the reduction in transmission between ~0.6–0.8 THz). Due to the lack of spectral resolution, it is difficult to resolve if the drop in transmission at ~0.6–0.8 THz is caused by a single transition or from two or more transitions as the $2p_0 \rightarrow 2p_\pm$ and $2p_0 \rightarrow 3s(A_1)$ transitions occur within the region (0.72 THz and 0.58 THz respectively). Figure 5.30 shows the full response of ν_R as a function of τ, where the aforementioned features can be seen to oscillate as a function of τ. Taking a frequency slice as a function of τ at these frequencies show that the response is an exponentially decaying sine wave.

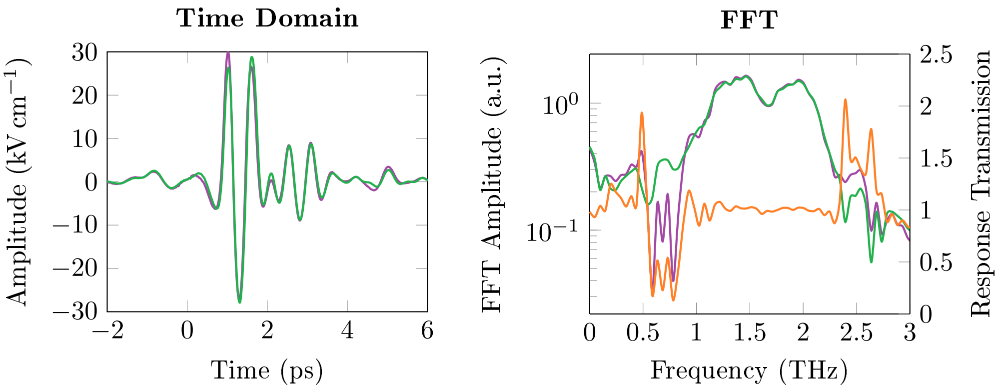

(a)

(b)

Figure 5.29: Time domain and FFT of the 'pump-probe' signal compared with the 'probe' at $\tau = -0.99\,\mathrm{ps}$. $E_\mathrm{p} \equiv E_\mathrm{B}$ is shown in green, $E_\mathrm{Pp} \equiv E_\mathrm{AB} - E_\mathrm{A}$ is shown in purple and $\nu_R \equiv \nu_\mathrm{Pp}/\nu_\mathrm{p}$ is shown in orange.

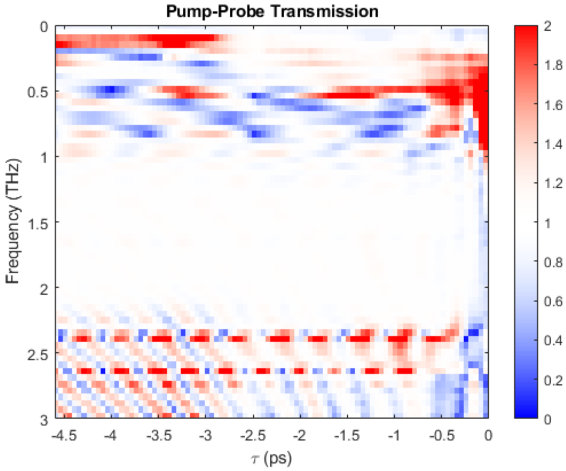

Figure 5.30: Pump-probe frequency response ($\nu_R \equiv \nu_\mathrm{Pp}/\nu_\mathrm{p}$) of the Ge:As wafer as a function of τ delay.

5.6 Experimental Conclusions

In conclusion, the data suggests that the main transition ($1s(A_1) \rightarrow 2p_0$) can be saturated by the experimental setup with a field of $\sim 20\,\mathrm{kV\,cm^{-1}}$. There is also data to suggest that with a two pulse experiment, the $2p_0$ state can be excited into higher states (possibly $2p_\pm$ or $3s(A_1)$) as the absorption at 0.7 THz is not seen in the linear spectroscopy data. The 2D TDS measurement allowed for the T_2 values of both transitions to be obtained simultaneously; $\sim$0.87 ps for the $1s(A_1) \rightarrow 2p_0$ transition and $\sim$0.13 ps for the $2p_0 \rightarrow 2p_\pm/3s(A_1)$ transition. A 2D TDS measurement with a larger τ range would allow for a more accurate measurement of T_2 of the transitions in the sample, whilst performing the experiment at a range of excitation fields would allow for it to be tested if one of the transitions is undergoing Rabi flopping [84]. Confirmation of this would allow for further experiments to be planned to perform coherent control on the transition [7]. Performing a 'reference' 2D-TDS measurement with the sample at room temperature would also improve the validity of the results, because at higher temperatures, the sample should not show any nonlinearities, thus any nonlinearities seen will be caused by other factors in the system (e.g. phase mismatch between the excitation pulses or interactions with the cryostat windows).

Chapter 6

2D Spectroscopy of Self-Induced-Transparency Structures

This chapter details the second sample measured for this work. The sample is a GaAs quantum well structure designed to exhibit the SIT effect for potential applications in mode-locking QCLs. Owing to the ultrashort recovery time of QCLs (∼1–50 ps [79]), mode-locking has proved difficult to achieve, with only active mode-locking techniques being employed [131–133], allowing for 3 ps pulses to be obtained with mid-IR QCLs [132] and 5 ps pulses with THz QCLs [134].

Mode-locking using SIT is not limited by the gain recovery time, making it an ideal candidate for performing mode-locking of QCLs. SIT absorbers can be engineered using quantum wells structures, so it is also possible for them to be integrated within the QCL structure, alternating between gain and absorbing layers [135]. Simulations of this design suggest that it is possible to achieve 100 fs pulses for mid-IR QCLs [135].

The SIT absorbing layers need to be precisely engineered to operate as intended so the saturation dynamics of the structures must be investigated. Investigations of T_1 and T_2 lifetimes in quantum well structures have been shown to be possible using 2D-TDS, allowing for short lifetimes (<5 ps) to be measured [2, 84, 86].

The chapter is formatted similarly to the previous chapter, with background theory being introduced first (Section 6.1), followed by a detailed summary of the sample (Section 6.2), finishing with a summary of the measurements and findings (Sections 6.3 to 6.6). As mentioned in the previous chapter introduction, the measurements were performed throughout the duration of the PhD so differences in the experimental setup are provided at the start of each experimental section.

6.1 Theory

This section will introduce the background theory of quantum well structures.

6.1.1 Quantum Wells

When electrons are confined in a narrow region of low Potential Energy (PE) by two regions of high PE, such as in a semiconductor heterostructure, the allowed energies becomes quantised. These systems are known as quantum wells.

6.1.1.1 Infinite Quantum Well

In a quantum well of length L bounded by infinitely high PE regions, the energy of the system can be calculated using the time-independent Schrödinger equation [11, 136–138]:

$$H\Psi_n = E_n\Psi_n, \tag{6.1}$$

where E_n is the energy of the electron, Ψ_n is the wavefunction of the electron and H is the total energy of the system, which is the sum of the kinetic and potential energy of the system. As $V(z) = 0$ in the low PE region and $V(z) = \infty$ in the high PE region, the total PE of the system will be 0, therefore H is equal to the kinetic energy only:

$$H = \frac{\rho^2}{2m}, \tag{6.2}$$

where m is the mass of an electron and ρ is the electron momentum operator:

$$\rho = -i\hbar\nabla \tag{6.3}$$

and ∇ is the gradient operator. As the quantum well is a one dimensional system, ∇ can be replaced with d/dz, leading to the full Schrödinger equation:

$$-\frac{\hbar^2}{2m}\frac{d^2}{dz^2}\Psi(z) = E\Psi(z), \tag{6.4}$$

As $\Psi(z)$ must be a function equal to itself with a negative multiplication factor after being differentiated twice and be 0 at the boundary regions $z = 0$ and $z = L$, $\Psi(z) = A\sin(kz)$, with kz being equal to an integer multiple of π:

$$\Psi(x) = A\sin(\frac{n\pi z}{L}). \tag{6.5}$$

Substituting Equation 6.5 into Equation 6.4:

$$\frac{\hbar^2}{2m}(\frac{n^2\pi^2}{L^2})(A\sin(\frac{n\pi z}{L})) = E(A\sin(\frac{n\pi z}{L})), \tag{6.6}$$

$$\therefore E = \frac{\hbar^2}{2m}(\frac{n^2\pi^2}{L^2}). \tag{6.7}$$

From this, we can see that the energy difference between the bands in the well can be engineered by changing the length of the quantum well. The probability of finding an electron at a given energy level must be equal to one, thus the condition of normalisation is:

$$\int_0^L \Psi^*(z)\Psi(z)dz = 1. \tag{6.8}$$

Solving this allows for A from Equation 6.5 to be obtained as $A = \sqrt{2/L}$, meaning that the full wavefunction is:

$$\Psi(z) = \sqrt{\frac{2}{L}}\sin(\frac{\pi n z}{L}). \tag{6.9}$$

Figure 6.1 shows a 200 Å GaAs infinite quantum well (using an effective electron mass of $m^* = 0.067m_e$) and its first three wavefunctions at their respective energy levels.

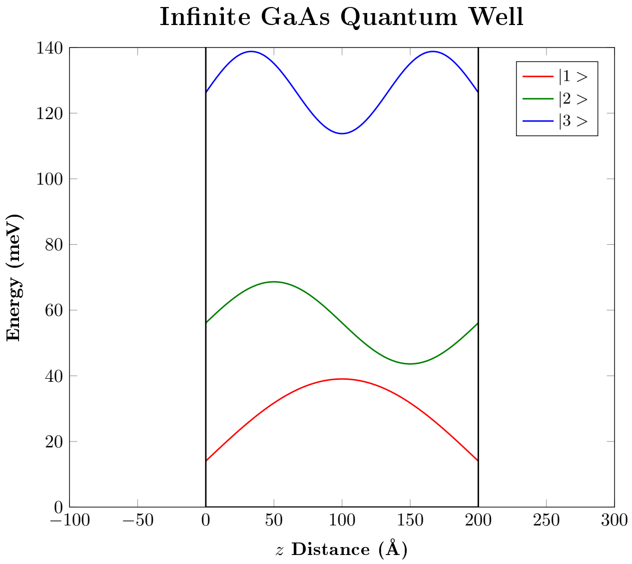

Figure 6.1: Diagram of an infinite quantum well, showing the first three wavefunctions. Simulated using QWWAD simulation tools [137].

6.1.1.2 Finite Quantum Well

In real systems, the potential barrier between the low and high energy regions are finite, changing the electron wavefunction. Considering a low PE region of length L, symmetric around $z = 0$, so that the potential barriers are at $z = \pm L/2$ and have an energy of V, the Schrödinger equation in each region will be the following [11,136–138]:

$$-\frac{\hbar^2}{2m}\frac{d^2}{dz^2}\Psi(z)+V\Psi(z)=E\Psi(z), \qquad z\leq-\frac{L}{2}, \tag{6.10}$$

$$-\frac{\hbar^2}{2m}\frac{d^2}{dz^2}\Psi(z)=E\Psi(z), \qquad -\frac{L}{2}\leq z\leq\frac{L}{2}, \tag{6.11}$$

$$-\frac{\hbar^2}{2m}\frac{d^2}{dz^2}\Psi(z)+V\Psi(z)=E\Psi(z), \qquad \frac{L}{2}\leq z. \tag{6.12}$$

In the well ($-L/2 \leq z \leq L/2$), the wavefunction may now be either a cosine or sine function, dependent on the parity. Parity is referred to as either 'even' when the function is symmetric ($\Psi(z)=\Psi(-z)$) or 'odd' when the function is antisymmetric ($\Psi(z)=-\Psi(-z)$).

Inside the right barrier ($z\leq -L/2$), by rearranging Equation 6.12:

$$\frac{\hbar^2}{2m}\frac{d^2}{dz^2}\Psi(z)=(V-E)\Psi(z), \tag{6.13}$$

it can be seen that the wavefunction must equal itself when differentiated twice, meaning that $B\exp(\pm\kappa z)$ would fit. As z tends towards $\pm\infty$, $\Psi(z)$ tends towards zero, this leads to the following wavefunctions when the states have an even parity:

$$\Psi(z)=B\exp(\kappa z), \qquad z\leq-\frac{L}{2}, \tag{6.14}$$

$$\Psi(z)=A\cos(kz), \qquad -\frac{L}{2}\leq z\leq\frac{L}{2}, \tag{6.15}$$

$$\Psi(z)=B\exp(-\kappa z), \qquad \frac{L}{2}\leq z. \tag{6.16}$$

where

$$k=\frac{\sqrt{2mE}}{\hbar}, \quad \text{and} \quad \kappa=\frac{\sqrt{2m(V-E)}}{\hbar}. \tag{6.17}$$

Equation 6.16 equals Equation 6.15 at $z=L/2$, for an even parity wavefunction, thus:

$$k\tan(\frac{kL}{2})-\kappa=0. \tag{6.18}$$

For an odd parity wavefunction (where Equation 6.15 is substituted with $\Psi(z)=A\sin(k)$):

$$k\cot(\frac{kL}{2})+\kappa=0. \tag{6.19}$$

The allowed energy levels can then be acquired either graphically [139] or numerically, using techniques such as Newton-Raphson iteration [137]. Figure 6.2 shows a 200 Å finite GaAs quantum well surrounded by two $\mathrm{Al_{0.12}Ga_{0.88}As}$ barriers and its first three wavefunctions at their respective energy levels. An effective electron mass of $m^*=0.067m_e$ and a barrier height of 100 meV was used.

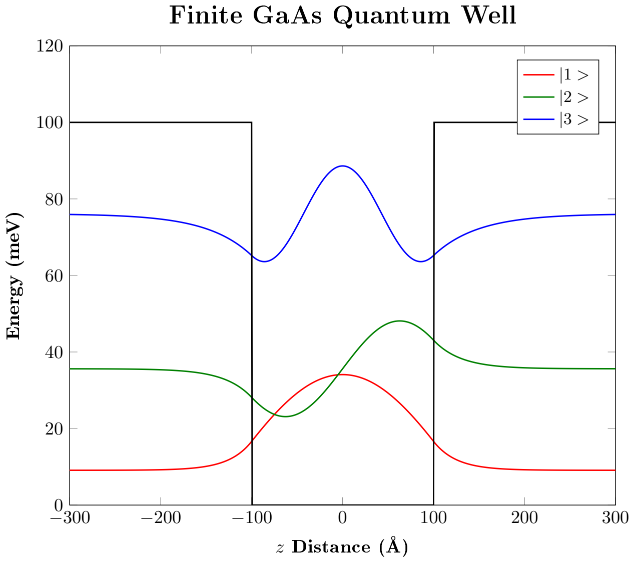

Figure 6.2: Diagram of a GaAs finite quantum well surrounded by two $Al_{0.12}Ga_{0.88}As$ barriers, showing the first three wavefunctions. Simulated using QWWAD simulation tools [137].

6.1.1.3 Multiple Quantum Well Systems

It can be seen that there is a small probability in a finite quantum well for an electron to be outside the well. This effect is known as quantum tunnelling [11]. Due to this tunnelling effect, when multiple quantum wells are placed in close succession, separated by a thin potential barrier, the wavefunctions become coupled between the wells. This is known as ‘hybridisation’ and can be seen in Figure 6.3 which shows two GaAs wells (the same as shown in Figure 6.2), separated by a 17 Å $Al_{0.12}Ga_{0.88}As$ high PE region. In superlattices of many repeated quantum well structures, wavefunctions with the same quantum number hybridise, forming minibands, with the width dependent on the strength of the coupling between wells [138]. Applying a bias to these structures cause a potential gradient to be applied across the wells, causing the energy difference between the minibands to increase and allowing for electrons to travel through the structure, tunnelling through the barriers.

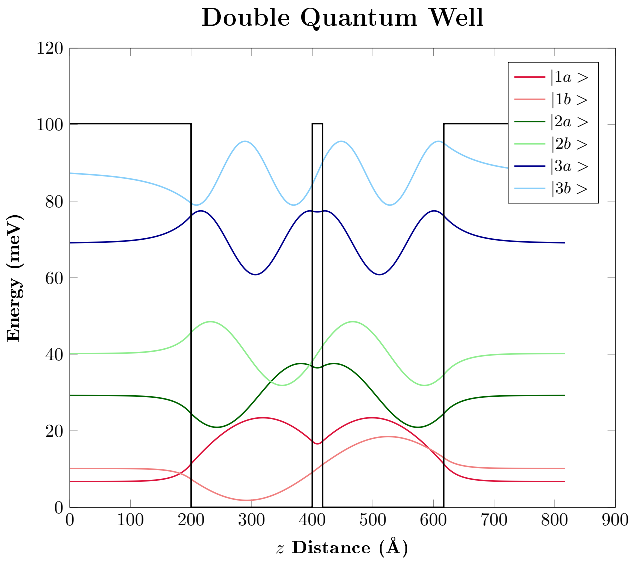

Figure 6.3: Diagram of system of two GaAs finite quantum wells, seperated by a 17 Å $\mathrm{Al_{0.12}Ga_{0.88}As}$ barrier, showing the first six wavefunctions. Simulated using QWWAD simulation tools [137].

Use of quantum well superlattice structures led to the development of diode lasers [140] and then later the QCL [141]. Unlike regular diode lasers where the frequency of the emitted photons is dependent on the bandgap of the material, the emission frequency can be engineered by adjusting the width of the wells and the bias applied to the device. As the photon emission occurs in solely the conduction band of the device in QCLs, the transition energy is much smaller (meV instead of eV), leading to lower frequency photons being emitted. This led to the development of QCLs capable of emission in the THz frequency range [142]. Figure 6.4 shows an example of the bandstructure of a QCL which has an output frequency of 3.3 THz. Quantum well superlattices can also be engineered to utilise intersubband absorption to allow for detecting radiation in both the IR [143] and THz [144, 145] regions of the EM spectrum with devices known as 'Quantum Well Photodetectors'. QCLs have also been shown to act as detectors through 'self-mixing' [146], allowing for the laser to act as both the emitter and detector within a system.

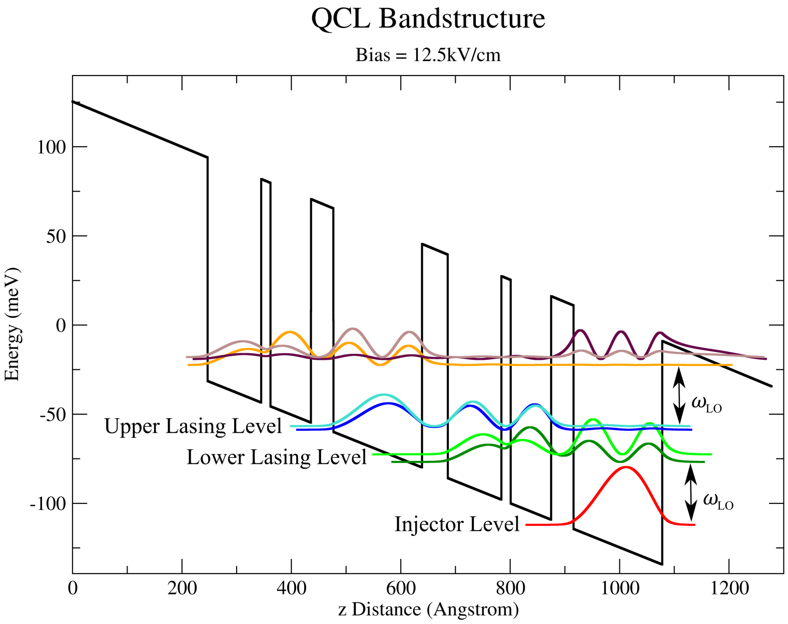

Figure 6.4: Bandstructure diagram of a resonant phonon QCL which emits radiation with a frequency of 3.3 THz. The structure in Å is as follows: **47**/98/**17**/74/**41**/54/<u>54</u>/54 ($Al_{0.15}Ga_{0.85}As$ barriers are in bold, Si doped layer (5×10^{16} cm^{-3}) is underlined, GaAs barriers otherwise). Two repeats of the structure are shown. Simulated using QWWAD simulation tools [137].

6.1.2 Rabi Oscillation

When a strong oscillating electric field interacts with a two-level system, such as two states in a semiconductor quantum well superlattice, it is possible for the population and polarisation of the system itself oscillate. This is known as a Rabi oscillation. The polarisation and population of the system can be obtained using the following equations [10]:

$$\Delta N(t) = \Delta N_0 \cos \Omega_{\mathrm{Rabi}} t, \tag{6.20}$$

$$P_1(t) = P_m \sin \Omega_{\mathrm{Rabi}} t, \tag{6.21}$$

where ΔN is the change in population, N_0 is the initial population, P_m is the maximum value of the polarisation and Ω_{Rabi} is the Rabi frequency, defined using the following equation:

$$\Omega_{\mathrm{Rabi}} = \frac{3\gamma_{\mathrm{rad}}\epsilon\lambda^3}{8\pi^2\hbar}E_1^2, \tag{6.22}$$

where γ_{rad} is the decay rate of the transition, ϵ is the dielectric permeability of the sample and λ is the wavelength of the excitation beam. A full derivation of these equations can be found in Appendix 8.2.

From the behaviour described above, a strong pulse with a duration T_p where $\omega_R T_p \equiv \pi$ entering a two-level system will cause a total population inversion which will decay to its initial state with a time constant of T_1. Pulses which cause this are known as 'π' pulses as they have a 'pulse area' ($\omega_R T_p$) of π [10]. A diagram showing the population and polarisation of a two-level system as a function of pulse area is shown in Figure 6.5.

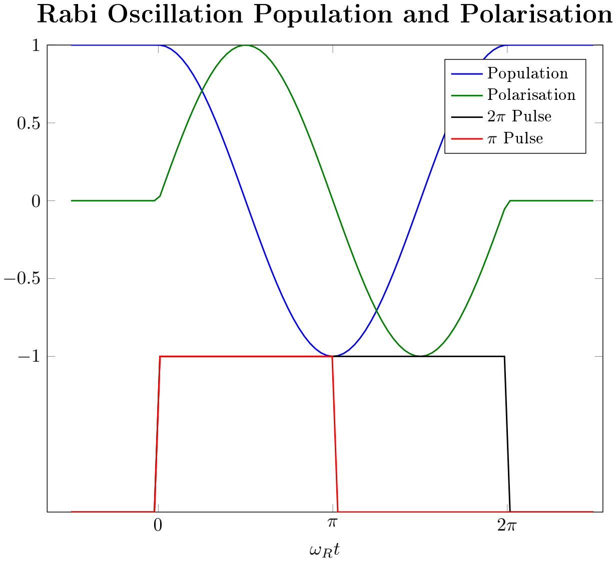

Figure 6.5: Diagram showing the population and polarisation of a two level system undergoing a Rabi oscillation as a function of pulse area.

6.1.3 Self-Induced Transparency Effect

In a two level system where a 2π pulse is applied, pulse is absorbed in the first half-cycle causing a population inversion and then the same energy is coherently emitted in the second half cycle, reverting the system back to its initial state, causing no energy to be absorbed in the system as it occurs over a period shorter than the relaxation times of the system (T_1 and T_2). This causes the system to appear transparent when compared to a lower energy pulse of the same frequency. This effect is known as SIT and was first described in 1967 [147]. It is dependent on the transition dipole moment, (d_{12}), the population relaxation time (T_1) and the dephasing time (T_2) of the two-level system, as well as the duration (τ) and area (S) of the slow envelope ($\varepsilon(t)$) of the pulse. If $\tau < T_2$ and $S = d_{12}/\hbar \int \varepsilon(t)dt = 2\pi$ the effect can occur [148, 149].

The SIT effect can be used to passively mode-lock (see Section 2.1.3), as 2π pulses have the lowest loss, thus other pulse shapes will be absorbed in the media, leading to only 2π pulses being present, thus the system acts as a saturable absorber. For passive mode-locking with other saturable absorbers, the pulse duration is limited by the inverse bandwidth of the gain medium $t = 1/T_2$, however, this does not apply to SIT media, as the pulse duration is inversely proportional to the incident optical power [150]. This is because the duration of the Rabi oscillations do not have a lower limit [151]. For mode-locking using SIT, it is also critical to have the laser gain medium have a dipole strength twice that of the SIT region [135, 150]. This causes the 2π pulse in the SIT region to act as a π pulse in the gain region (i.e. a half Rabi oscillation occurs, stimulating emission of all electrons in the upper lasing state to the lower lasing state). It is difficult to find material pairing that operate within these parameters, however, quantum well structures appear a promising candidate, as their material properties can be precisely engineered [135].

The following sections of this chapter describe an experimental investigation of a SIT structure using the system described in Section 4.2.

6.2 Sample Details

The SIT sample was designed by Dr. Muhammad Talukder, fabricated at the University of Leeds by Dr. Lianhe Li and has the following layer thicknesses in Å: 80/**20**/71/**20**/80/**20**/71/***28***/28/***36***/28/***28***. Values in a normal font are GaAs layers, values in **bold** font are $Al_{0.11}Ga_{0.89}As$ and values in ***bold italic*** font are $Al_{0.2}Ga_{0.8}As$ layers. Layers which are underlined are doped with a density of $2{\times}10^{16}\,\mathrm{cm}^{-3}$. The sample is 10 µm thick, containing multiple repeats of the aforementioned quantum well structure. A diagram of the bandstructure (simulated using QWWAD simulation tools [137]) is shown in Figure 6.6. The energy levels of the first four states in ascending order are 24.6 meV, 32.2 meV, 45.4 meV and 59.3 meV. The structure is designed so the SIT effect is seen when incident THz radiation is resonant with the $E_1 \rightarrow E_2$ transition ($\sim 1.85\,\mathrm{THz}$).

Using the wavefunctions obtained from the simulation shown in Figure 6.6, the excitation field to induce a full Rabi oscillation can be estimated using the following equation:

$$E_{\mathrm{THz}} = \frac{\Omega_{\mathrm{Rabi}}\hbar}{|d|}, \tag{6.23}$$

where Ω_{Rabi} is the Rabi frequency and d is the dipole moment of the transition which is obtained using:

$$d = q\int \psi_2^*(x)x\psi_1(x)\ dx, \tag{6.24}$$

where q is the charge of the particle transitioning, ψ_1 is the wavefunctions of the initial state and ψ_2^* is the complex conjugate of the excited state and x is the position of the particle. For this sample, $\Omega_{\mathrm{Rabi}} = 2\pi \times 1.85\,\mathrm{THz}$ and $d = q \times 55\,\mathrm{nm}$, giving an excitation field of $\approx 1.4\,\mathrm{kV\,cm^{-1}}$.

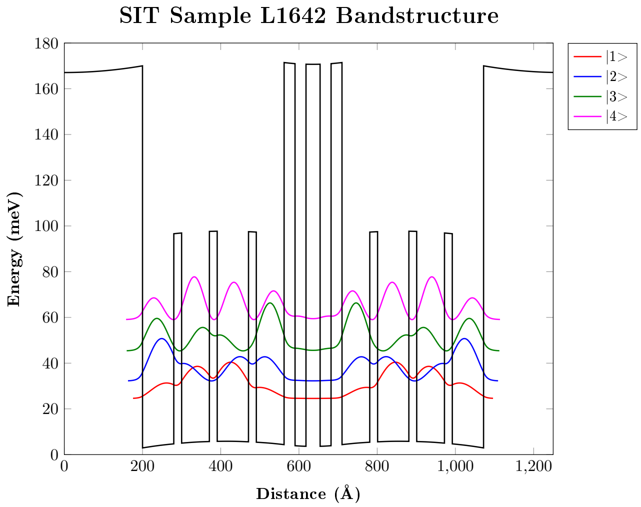

Figure 6.6: Bandstructure diagram of the measured SIT sample. The structure in Å is as follows: 80/**20**/71/**20**/80/**20**/71/***28***/28/***36***/28/***28***. Values in a normal font are GaAs layers, values in **bold** font are $Al_{0.11}Ga_{0.89}As$ and values in ***bold italic*** are $Al_{0.2}Ga_{0.8}As$ layers. Layers which are underlined are doped with a density of $2{\times}10^{16}\,\mathrm{cm}^{-3}$. Two repeats of the structure are shown. Simulated using QWWAD simulation tools [137].

6.3 Wedge Coupling

The first challenge considered with measuring the sample using TDS was how to couple the THz radiation in and out of the sample as the interactions with the quantum wells occur perpendicular to the growth direction of the sample because of dipole selection rules [152]. It is possible to do this by orienting the sample so that the edge of the structure is at the focus of the parabolic mirrors [22, 79], however, with the sample being ∼ 450 µm tall (including the substrate), much smaller than the spot size of the THz beam, most of the beam will be not couple into the sample, reducing the SNR. It was decided that the edges of the wafer would have a larger 45° face polished into both edges of the wafer, turning the shape into a right parallelogrammic prism (an extruded parallelogram). To polish the sample, the sample was attached to a steel block with an integrated 45° hole with ∼ 1 mm of the sample protruding from the block. The block containing the sample was then hand-polished to a mirror finish using fine glass paper. The shape would allow for the THz beam to be coupled into the sample in the growth direction at an edge, reflect internally off the 45° face, excite the quantum wells and the reflect at the opposite 45° face out of the sample (shown in Figure 6.7). As this geometry would cause a shift in the position of the beam coming out of the sample, the collection parabolic was also shifted the length of the sample (∼ 5 mm) to ensure that the THz beam was still collected and refocused onto the detector correctly.

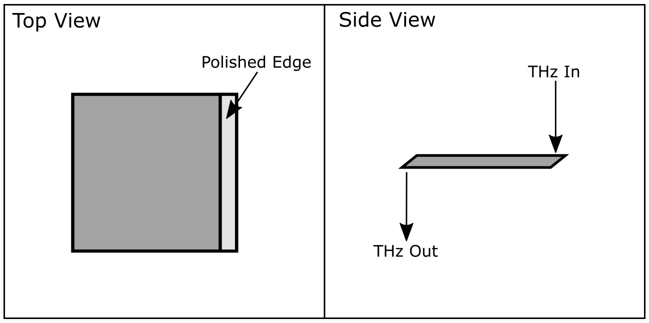

Figure 6.7: Diagram showing the SIT sample wafer after being polished to allow for coupling.

6.3.1 Linear Spectroscopy

To check if the sample had the expected absorption around 2 THz, linear spectroscopy was first performed on the sample using the low power TDS system described in Section 5.3. The sample was attached to a copper plate with a rectangular hole $\sim 1 \times 10\,\text{mm}$ using vacuum grease (see Figure 6.8) and then attached to cryostat's cold-finger (*Oxford Instruments Microstat*). Similar to the experiments discussed in Chapter 5, a 'sample' measurement was taken at a low temperature ($< 10\,\text{K}$) where the electrons in the sample have settled into the ground state and then a 'reference' measurement is taken of the same sample at a higher temperature, where the thermal distribution of the electrons will have reduced the population differences between the levels, to allow for the data to be normalised. For this measurement a temperature of 4 K was used for the sample measurement, whilst a temperature of 100 K was used for the reference measurement. The measurement was also performed in a dry air environment. To ensure that the optimal position to couple THz pulse into the sample and interact with the wells was obtained, the sample was stepped along the horizontal plane where the measurements were repeated.

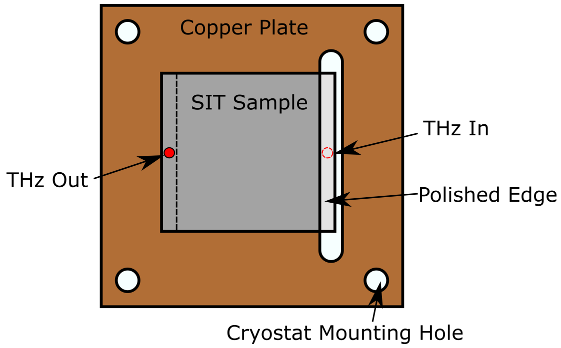

Figure 6.8: Diagram showing the SIT sample mounted to a copper plate, allowing it to be fixed to a cold-finger.

Figure 6.9 shows the time domain response and FFT for the sample and reference measurement, as well as the resulting normalised 'transmission' response (sample FFT / reference FFT) from a single sample position. A rectangular window has been applied to the time domain data to remove obvious reflections. Figure 6.10 shows the normalised transmission responses for each of the sample positions tested. From this data, no distinguishable features around the expected absorption frequency ($\sim 2\,\mathrm{THz}$) could be seen at any of the tested sample positions. The general increase in transmission above 2 THz is due to electron screening at the higher frequencies at the reference temperature. The oscillations seen in the transmission data across all sample positions is likely due to a reflection being present in the time domain data. Decreasing the width of the window in post-processing could not remove this however.

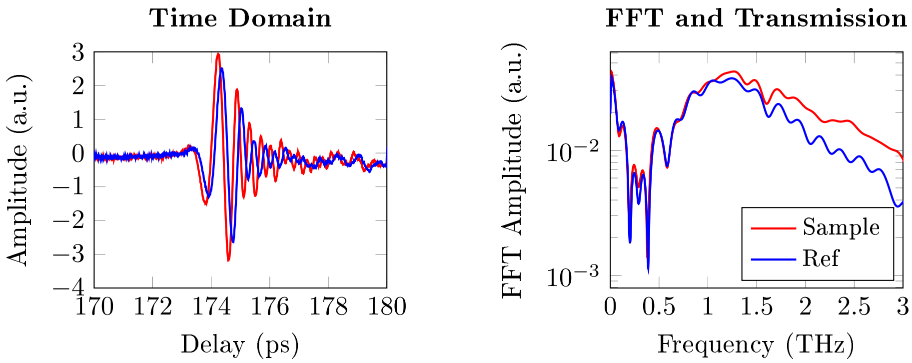

(a) (b)

Figure 6.9: Linear spectroscopy data of the wedge-polished sample. Red traces are the 'sample' measurement of the SIT wafer measured at 4 K whilst blue traces are the 'reference' measurement of the same wafer taken at 100 K. THz pulses are generated and detected using PCSes.

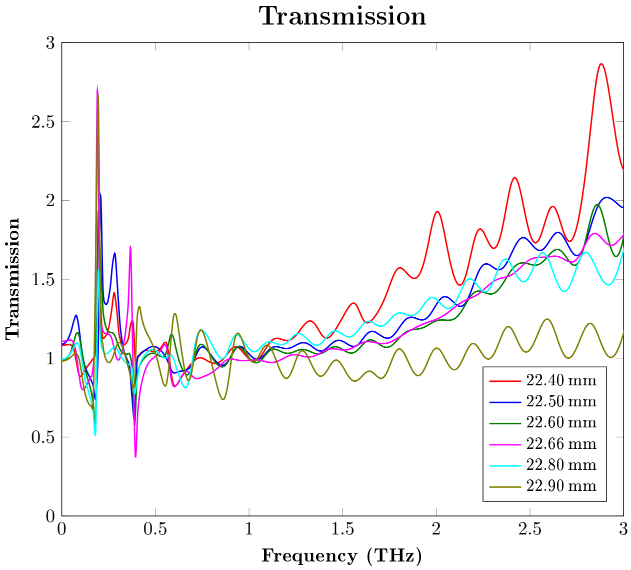

Figure 6.10: Transmission through the SIT wafer at low THz fields as a function of frequency through the wedge at multiple positions. Transmission values are obtained by dividing the spectrum obtained at low temperatures (4 K) by the spectrum obtained at higher temperatures 100 K.

To improve the confinement of the THz radiation into the sample and to hopefully allow for the transition to be observed, a layer of Au was added to the surface [153, 154] using a metal sputterer (performed by Nikollao Sulollari), leaving an unmetallised gap of ∼ 1 mm to still allow for coupling into the sample. Figure 6.11 shows a diagram of the sample after metallisation. The measurement using the low power TDS system was then repeated but this also did not yield any conclusive results due to a reduction of the strength of the detected signal.

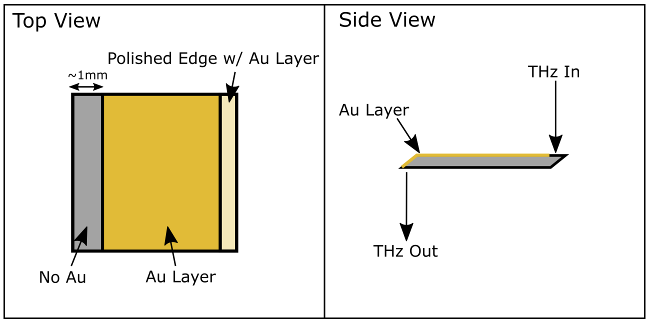

Figure 6.11: Diagram of the SIT sample after metallisation of one face was performed to increase the confinement of the THz pulse in the sample.

6.3.2 Saturation Measurement

Despite the lack of conclusive results from the linear spectroscopy measurements, a 'saturation' measurement was performed on the sample (see Section 5.4 for an explanation of the measurement technique).

For this measurement, a setup similar to the system shown in Figure 4.1 was used (using only one beam line). A 15×15 mm PCA was used as the emitter and excitation was performed using a ∼ 32 mm FWHM collimated 800 nm beam. The strength of the THz pulse incident on the sample was altered by changing the bias applied to the PCA. The peak field applied to the sample ranged between 6.25–50 $\mathrm{kV\,cm^{-1}}$ (measured at an earlier date). Expanded PTFE was placed between the emitter and the first parabolic mirror to block the excess IR pulse from interfering with the sample. A 1 mm thick ZnTe crystal was used for EO detection as the feature of interest was expected to be below the detection bandwidth of the crystal (∼ 3 THz) and detected signal was expected to be small. The sample was mounted with the same cryostat and mounting plate as described in Section 6.3.1. Temperatures of 7 K and 180 K were used as the sample and reference temperatures respectively. Similarly to the linear spectroscopy measurement of this sample (Section 6.3.1), the measurement was repeated at multiple horizontal positions in the sample space to ensure that the best coupling was achieved. All measurements were performed in a dry air environment.

The following analysis will only discuss the data acquired at the sample position where the strongest absorption was seen at the sample temperature for brevity. The time-domain traces were first windowed using a rectangular window and then Fourier transformed as seen in Figure 6.12. These graphs show the response from an applied field of $\sim 6.25\,\mathrm{kV\,cm^{-1}}$ because the absorption should be more obvious at lower excitation fields, where the transition is not saturated. In the FFT of the sample measurement, a clear, narrow absorption can be seen at $\sim 1.85\,\mathrm{THz}$ which does not appear in the reference data and is therefore likely to be the transition of interest. To then check is the strength of the absorption changes with the applied THz field, the FFT amplitude at each applied field is first compared (see Figure 6.13a). From this, it does initially appear that the strength of absorption seems to be affected by the strength of the applied field, but due to the differing overall amplitude of the spectrum, it is hard to acquire a conclusive answer. Figure 6.13c then shows the spectra in Figure 6.13a, divided by the maximum FFT amplitude of each scan. This normalises the data, allowing for the strength of the absorption to be compared for different applied fields. Comparing the strength of the absorption at the greatest field ($50\,\mathrm{kV\,cm^{-1}}$) to the other measurements, it can be seen that the absorption is much weaker, indicating that the transition may be saturating. To isolate that the peak field strength is affecting the transition and not that region of the spectrum, the self-normalisation was also performed on the reference data (Figure 6.13b shows the initial spectra and Figure 6.13d shows the normalised spectra). The normalised reference spectra does not appear to have much dependency with the strength of the applied field, adding credibility to saturation being observed in Figure 6.13c. The strong absorption seen in the reference data around 1 THz is unexpected and it is unclear where it has appeared from. It is possible that it could be due to misalignment of the sample as the cryostat finger has heated and expanded, causing a shift in the output beam, as the sample acts as a waveguide.

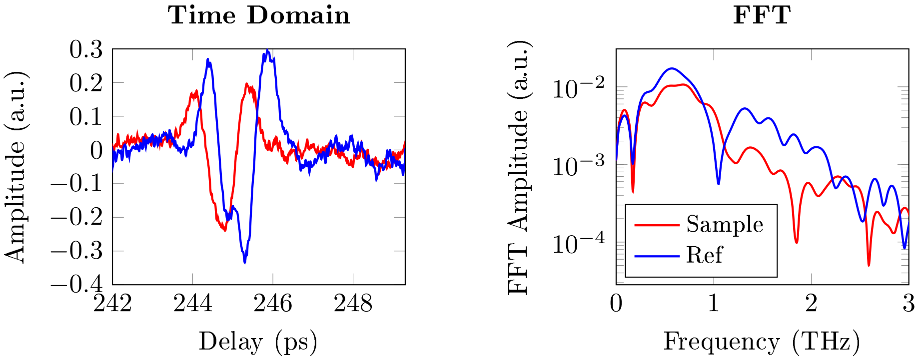

(a) (b)

Figure 6.12: Single scan from the saturation measurement of the SIT wafer with an applied THz field of $6.25\,\mathrm{kV\,cm^{-1}}$. Red traces are the 'sample' measurement of the SIT wafer measured at 7 K whilst blue traces are the 'reference' measurement of the same wafer taken at 180 K. THz pulses are generated and detected using PCSes. Signals were detected with a 1 mm thick ZnTe crystal.

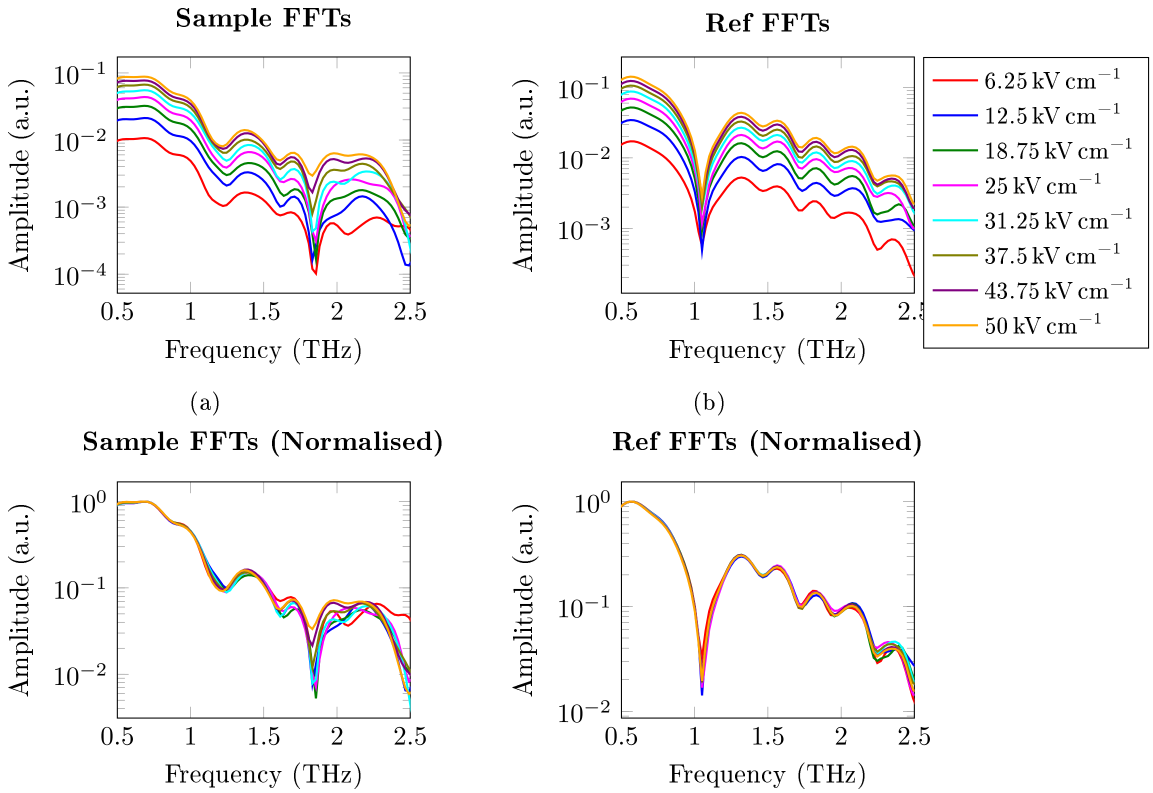

(a) (b)

(c) (d)

Figure 6.13: FFTs from the saturation measurement of the SIT wafer at varying applied THz fields. The different THz field strengths are obtained by changing the bias applied to the PCA emitter. A 1 mm ZnTe crystal was used for detection. ‘Sample’ measurements were taken at 7 K whilst ‘reference’ measurements were taken at 100 K.

Figure 6.14 shows the sample FFTs normalised using the reference FFTs. The subsequent analysis on the saturation of the transition seen at ~ 1.85 THz uses this metric of ‘transmission’ (Sample FFT / Reference FFT), as it should provide a more accurate normalisation than the self-normalisation shown in Figure 6.13c. The absorption minima shifts slightly between measurements, so the metric used to characterise the saturation will use the integral of the transmission at $\sim 1.85\,\text{THz} \pm 122\,\text{GHz}$. Figure 6.15 shows the result of this plotted as a function of peak, broadband applied field (measured without the sample present) and squared applied field (because Field$^2 \propto$ Intensity). The peak absorption at a given frequency can then be obtained using Equation 5.7 (also plotted on Figure 6.15). A typical absorption response of a saturated transition follows an exponential decay (see Figure 5.12), however it is immediately apparent that this is not the case for this data. At low fields ($< 30\,\mathrm{kV\,cm^{-1}}$), the absorption of the transition increases as a function of applied field, however, at higher fields ($> 30\,\mathrm{kV\,cm^{-1}}$), the absorption response switches to reduce as a function of applied field. Figure 6.16 shows this absorption response as a function of intensity (V_{Peak}^2), where the absorption at the greater applied fields appear to exponentially decay, as expected for a saturated transition. To estimate the field required to saturate the transition, these data points were fitted to an inhomogeneously and homogeneously broadened transition (Equations (5.8) and (5.9) respectively) using MATLAB. From fitting a homogeneously broadened response, a saturation field of $46.46 \pm 2.07\,\mathrm{kV\,cm^{-1}}$ was obtained giving a RMSE of 0.01335, whilst fitting an inhomogeneously broadened response, a saturation field of $27.85 \pm 0.91\,\mathrm{kV\,cm^{-1}}$ was obtained giving a RMSE of 0.00771. These saturation fields are much higher than the estimate from the Rabi oscillation calculation in Section 6.2 because the estimation was the field of a narrowband pulse, ignoring coupling losses. From this, it can be seen that it not conclusive if the transition is homogeneously or inhomogeneously broadened, as the data fits well to both, albeit with the inhomogeneously broadened transition having a lower RMSE and therefore, fitting better. In general, the transitions of semiconductor quantum well structures are homogeneously broadened [81, 155], however, inhomogeneities can arise from slight variations in the structure during wafer growth [155].

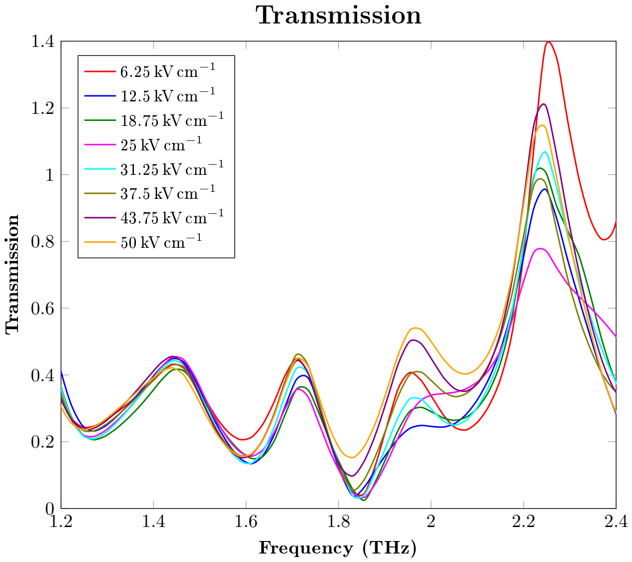

Figure 6.14: Normalised transmission from the saturation measurement of the SIT wafer, shown in Figure 6.13. The normalised transmission is obtained by dividing the frequency response of the 'sample' measurement (taken at 7 K) by the 'reference' measurement taken at 180 K. The SNR is much lower after 2 THz.

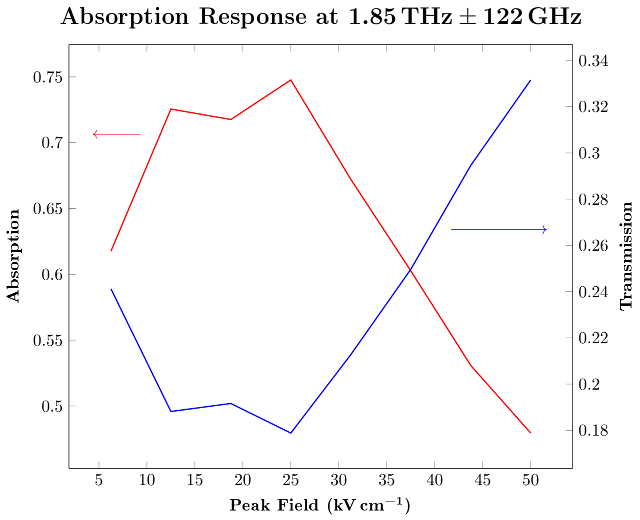

Figure 6.15: Absorption response of the SIT wafer at 1.85 THz ± 122 GHz. Blue traces are the transmission response (see Figure 6.14), red traces are the absorption response.

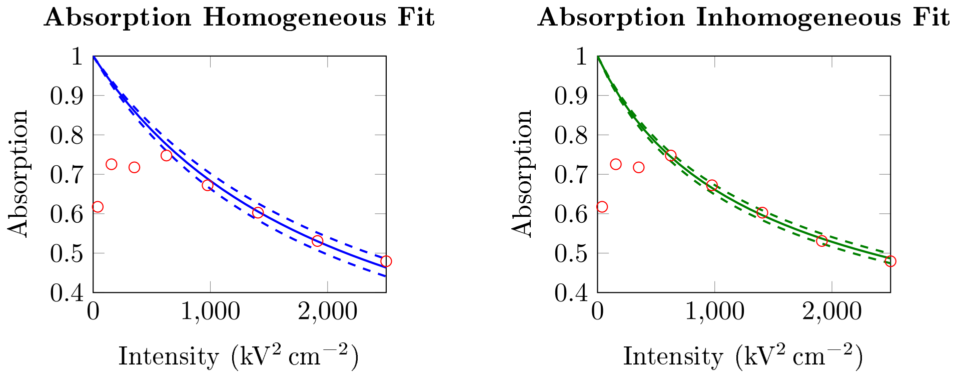

(a) Homogeneously broadened transition fit. $I_S = (46.46 \pm 2.07)$ kV cm^{-1}. RMSE = 0.01335

(b) Inhomogeneously broadened transition fit. $I_S = (27.85 \pm 0.91)$ kV cm^{-1}. RMSE = 0.00771

Figure 6.16: Absorption response of the SIT wafer (shown in Figure 6.15) as a function of intensity, fitted to a homogeneously and inhomogeneously broadened transition. Fitting performed using MATLAB.

6.4 Grating Coupling

An alternate coupling method was also tested where a metal grating structure is added to the surface of the wafer [84, 144, 156]. The metal grating allows for the incident THz pulses to be coupled into the quantum wells via diffraction, with the period of the grating determining the wavelength of the light to couple into the sample. The period can be designed using the grating equation:

$$m\lambda = nd(\sin\alpha + \sin\beta), \tag{6.25}$$

where m is the order of diffraction, λ is the wavelength of the light to be coupled, n is the refractive index of the sample, d is the grating period and α and β are the angles of the incident and diffracted light. For grating designs in general, λ is usually the cutoff wavelength of the grating, meaning that wavelengths shorter than λ will be diffracted, however, for near-field interactions such as for quantum well structures, it has been shown that longer wavelengths may also be coupled, and incident light with wavelengths equal to λ are coupled in most efficiently [144]. For the SIT sample under investigation, the grating is designed for $\lambda \approx 160\,\mu\text{m}$, $\alpha = 0°$, $\beta = 90°$ with $n \approx 3.2$, as the wafer is predominantly GaAs. Thus, Equation 6.25 can be simplified to:

$$d \approx 50\,\mu\text{m} \times m. \tag{6.26}$$

This equation is however a simplification and for a full understanding of how the incident pulses diffract into a multilayer structure such as a quantum well system, simulations must be performed [157], which is outside the scope of this thesis. For the SIT sample being tested, four gratings were designed and simulated by Dr. Paul Dean, with fabrication being performed by Dr. Mohammed Salih. The dimensions of each design is shown in Table 6.1. A diagram showing the layout of the gratings on the wafer are shown in Figure 6.17. The values of the grating periods in the table are lower than the estimation (Equation 6.26) as the dispersion effects between the multiple layers have been accounted for to optimise coupling at 1.85 THz.

Grating Number	Grating Period (µm)	Metal Width (µm)	Gap Width (µm)	Repeats	Diffraction Order
1	19.5	12	7.5	102	2
2	20.5	12.6	7.7	97	2
3	21.5	13.2	8.3	93	2
4	41	25.2	15.8	49	1

Table 6.1: Dimensions of the grating structures fabricated onto the SIT sample.

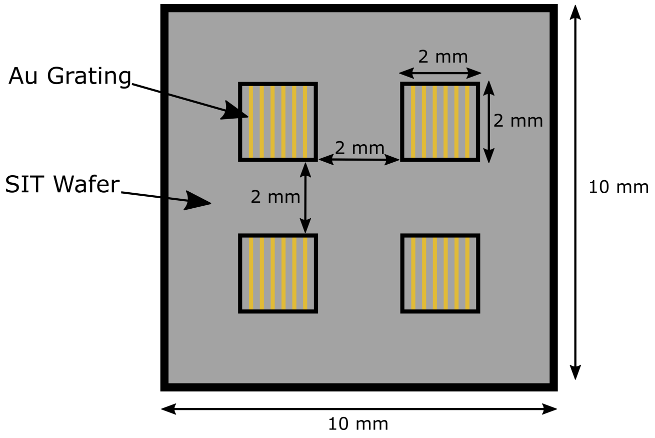

Figure 6.17: A diagram showing the placement of the grating structures fabricated onto the wafer. Each 2×2 mm grating region has a different spacing, found in Table 6.1. Diagram not to scale.

6.4.1 Linear Spectroscopy

The sample with the gratings were first tested using the lower power TDS system to ascertain which grating structure performed best. The measurement technique and system configuration was identical to that of the experiment described in Section 6.3.1, with two measurements being performed on the same sample at a low ‘sample’ temperature and a higher ‘reference’ temperature. 7 K and 290 K used for the sample and reference measurements respectively. The sample was clamped between two copper plates with four holes, allowing for the THz pulses to only be coupled into via the gratings. This also allowed for all four gratings to be tested within a single cooldown cycle of the cryostat to improve reliability of the comparison between the gratings.

Figures 6.18 to 6.21 show the time domain and FFT of each grating (after a window has been applied to the data). If the grating is working as intended, an absorption should be present around 1.85 THz at the sample temperature. Looking solely at the FFTs, a subtle, broad absorption is observed in all gratings. This is confirmed when a transmission response is obtained, normalising the sample data with their references, seen in Figure 6.22. Unfortunately, this normalisation is not perfect as there appears to be strong oscillations in the reference measurements of gratings one and two (see Figures 6.18b and 6.19b), possibly caused by water vapour being present in these scans owing to the system not being fully purged, as the absorption frequencies match with that of water [127]. An absorption can be seen with all the gratings tested, close to the expected frequency of 1.85 THz, however, grating four (the first order grating design) was chosen for further measurements, as the magnitude of the time domain signal was the greatest, whilst also having the strongest absorption at the 1.85 THz transition frequency (see Figure 6.23). The strong, narrow absorption at ~ 4 THz seen in all of the measurements is caused by an absorption in the quartz cryostat windows. This absorption is not normally present in measurements with the system, however, to match the polarisation of the THz pulses to the grating, the emitters were rotated, causing the pulses to interact with a different crystal axis of the quartz.

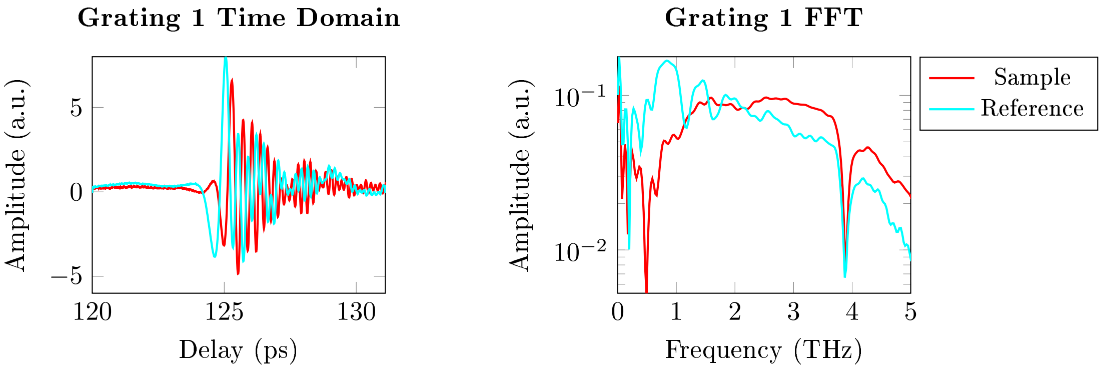

(a)

(b)

Figure 6.18: Grating 1 time and frequency domain response at the sample and reference measurement temperatures. Red traces are the 'sample' measurement of the SIT wafer measured at 7 K whilst cyan traces are the 'reference' measurement of the same wafer taken at 290 K. THz pulses are generated and detected using PCSes.

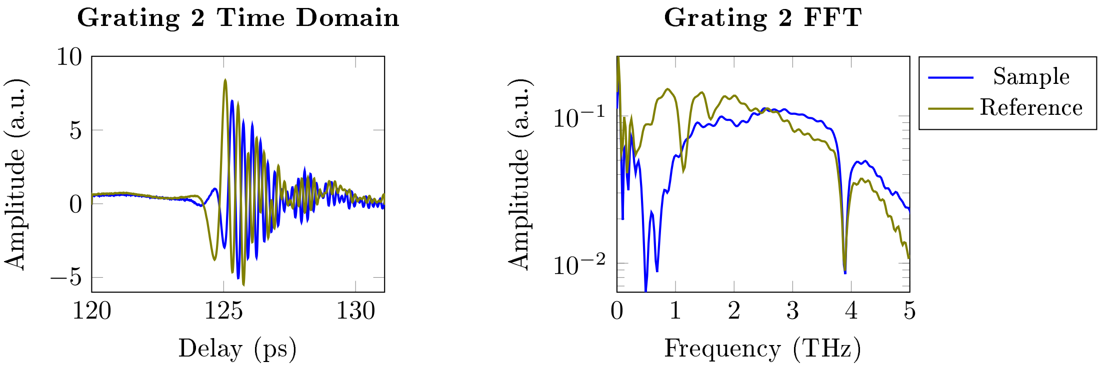

(a)

(b)

Figure 6.19: Grating 2 time and frequency domain response at the sample and reference measurement temperatures. Blue traces are the 'sample' measurement of the SIT wafer measured at 7 K whilst gold traces are the 'reference' measurement of the same wafer taken at 290 K. THz pulses are generated and detected using PCSes.

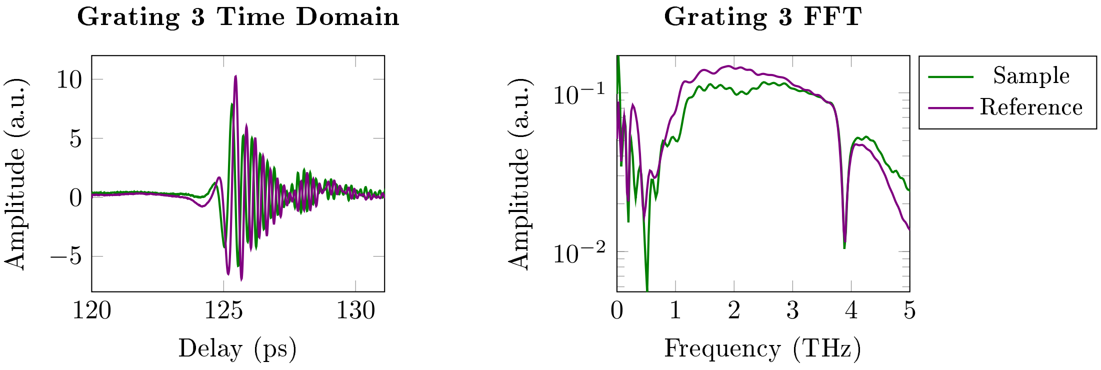

(a)

(b)

Figure 6.20: Grating 3 time and frequency domain response at the sample and reference measurement temperatures. Green traces are the 'sample' measurement of the SIT wafer measured at 7 K whilst purple traces are the 'reference' measurement of the same wafer taken at 290 K. THz pulses are generated and detected using PCSes.

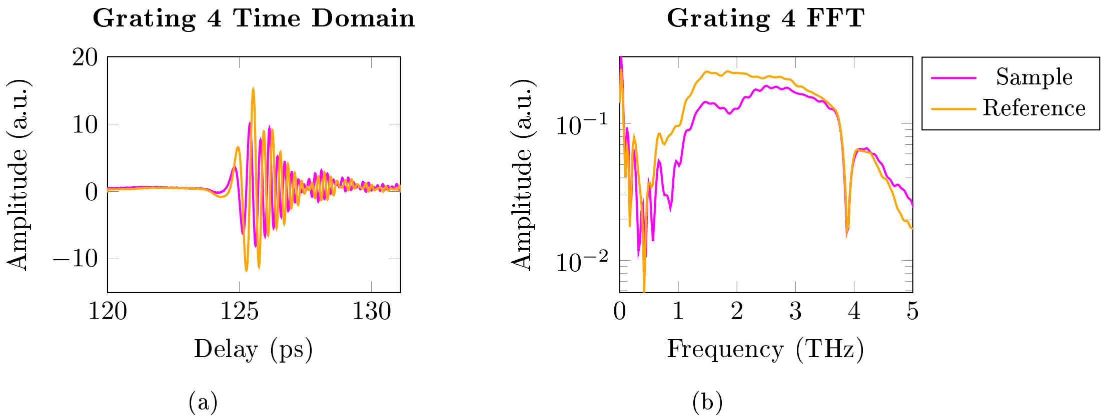

(a) (b)

Figure 6.21: Grating 4 time and frequency domain response at the sample and reference measurement temperatures. Magenta traces are the ‘sample’ measurement of the SIT wafer measured at 7 K whilst ornage traces are the ‘reference’ measurement of the same wafer taken at 290 K. THz pulses are generated and detected using PCSes.

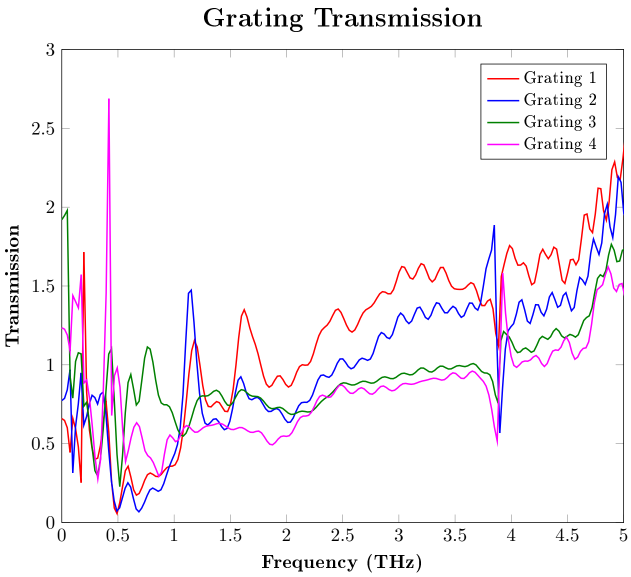

Figure 6.22: Transmission responses of the four gratings on the SIT wafer at low THz fields. Transmission response obtained by dividing the frequency response at low temperature (7 K), by that of a higher temperature reference (100 K).

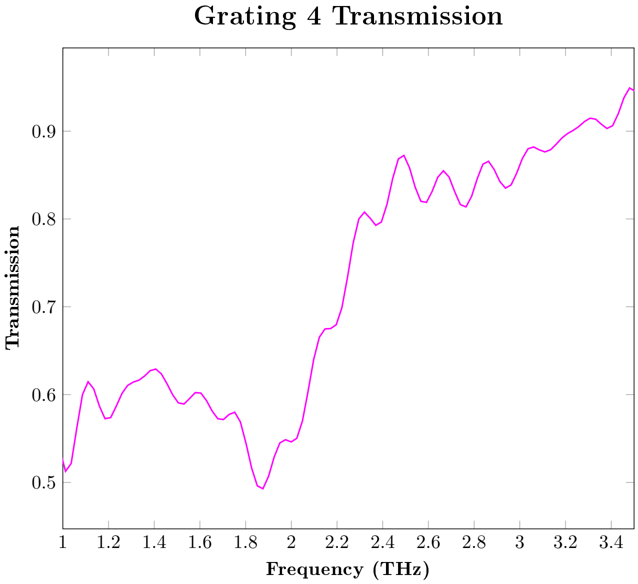

Figure 6.23: Zoomed low THz field transmission response of the SIT wafer, coupled using grating 4, shown in Figure 6.22.

6.4.2 Saturation Measurement

A saturation measurement was performed on the sample using a setup similar to the system shown in Figure 4.10, using only one beamline with a BNA crystal as the emitter. A BNA crystal was chosen over a PCA because the BNA was capable of generating greater peak fields (up to $\sim 230\,\mathrm{kV\,cm^{-1}}$), with greater spectral amplitude around the feature of interest at 2 THz (see Figure 4.13b). Excess IR was blocked using a 1 mm thick Si wafer. The strength of the emitter THz field was altered throughout the measurement between 23–$233\,\mathrm{kV\,cm^{-1}}$ by changing the incident optical power on the emitter using a series of ND filters. Owing to the slight difference in thickness of glass of the filters, the point in time that the peak field is found shifts with a range of $\sim 0.5\,\mathrm{ps}$, corresponding to a maximum difference in glass thickness of $\sim 100\,\mathrm{\mu m}$ (Borosilicate Glass (BK7) with $\eta = 1.51$). This small change in thickness will not significantly impact the pulse width of the excitation beam and should therefore not impact the generated THz pulse noticeably. A 1 mm ZnTe crystal was used as the detection crystal. The sample was mounted to the cryostat identically to as described in Section 6.4.1. ‘Sample’ measurements were taken at 6 K whilst ‘reference’ measurements were taken at 290 K.

Figures 6.24 to 6.26 show a subset of the spectra obtained at three different excitation fields for the sample and reference measurement and the resulting normalised transmission response. In all of the transmission responses, an absorption can be seen close to the expected frequency (1.85 THz) of varying strength. In the lower field measurements, it is more pronounced, whilst for the high field measurement, it appears less clearly, indicating that saturation may be occurring. The shift in absorption frequency is potentially caused by the grating and from a lack of frequency resolution to resolve any narrow absorptions.

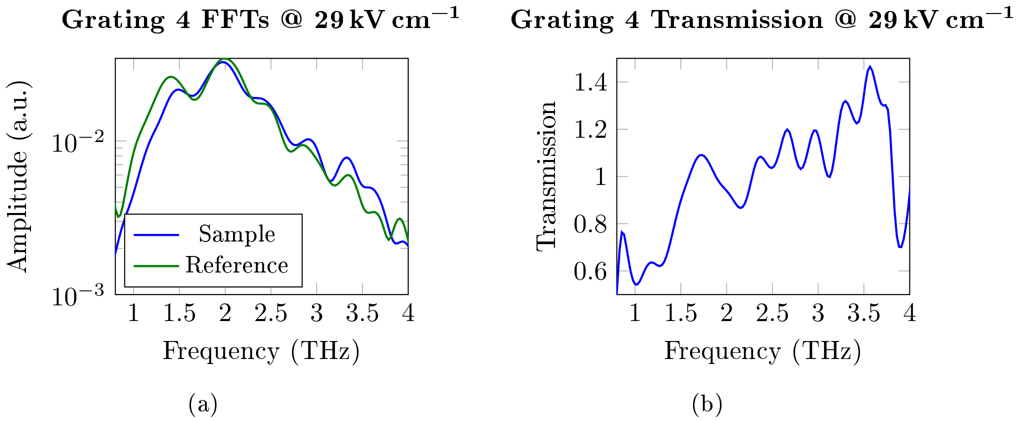

Figure 6.24: Response of the SIT wafer using grating four to couple a THz pulse with a peak field of 29 kV cm^{-1}. Blue traces are the 'sample' measurement of the SIT wafer measured at 6 K whilst green traces are the 'reference' measurement of the same wafer taken at 290 K. THz pulses are generated using a BNA crystal and are detected with a 1 mm ZnTe crystal.

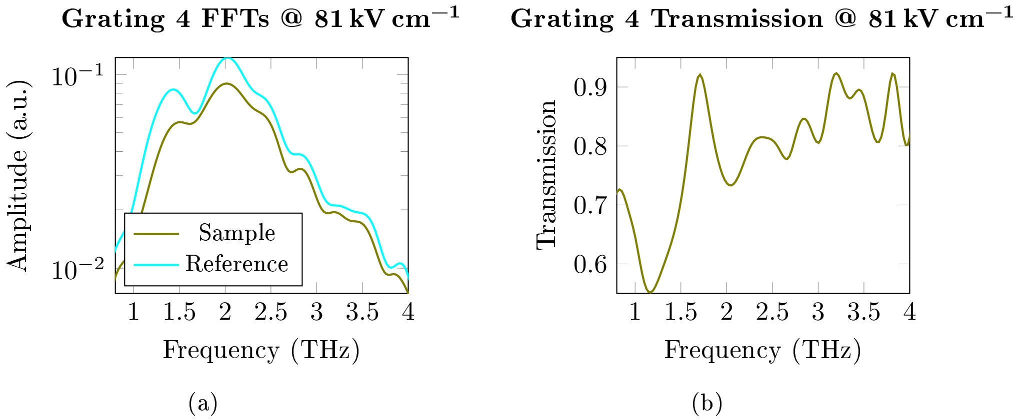

Figure 6.25: Response of the SIT wafer using grating four to couple a THz pulse with a peak field of 81 kV cm^{-1}. Gold traces are the 'sample' measurement of the SIT wafer measured at 6 K whilst cyan traces are the 'reference' measurement of the same wafer taken at 290 K. THz pulses are generated using a BNA crystal and are detected with a 1 mm ZnTe crystal.

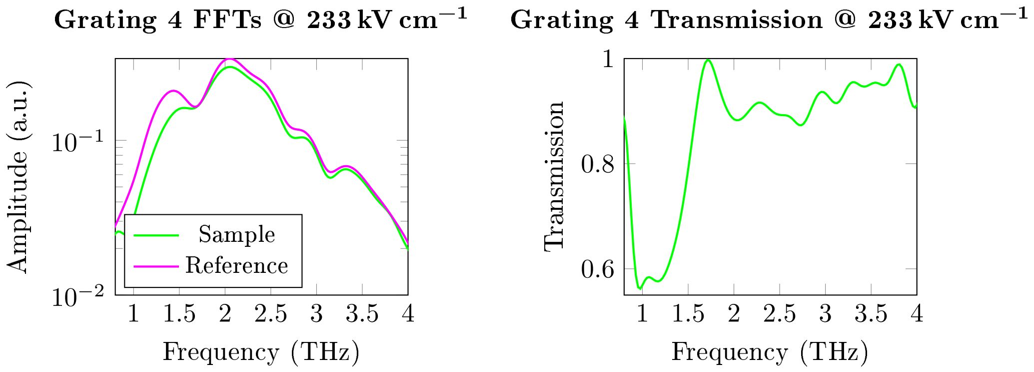

(a) (b)

Figure 6.26: Response of the SIT wafer using grating four to couple a THz pulse with a peak field of 233 kV cm^{-1}. Green traces are the 'sample' measurement of the SIT wafer measured at 6 K whilst magenta traces are the 'reference' measurement of the same wafer taken at 290 K. THz pulses are generated using a BNA crystal and are detected with a 1 mm ZnTe crystal.

To investigate this further, the normalised transmission response of all fields were compared (see Figure 6.27). From this it can be seen that similarly to the saturation measurement of the polished sample, the intensity of the THz field applied to the sample does seem to affect the strength of the absorption. Looking at the transmission response does however highlight that the reference used is not ideal, as there are lots of oscillations. This is likely owing to the sample changing thickness with temperature, but may also be from the cryostat windows being non-uniform, so when the coldfinger changes in length from the temperature change, the thickness of the window also changes. Some form of self referencing is required to remove the effects of the grating in the frequency domain, isolating the 1.85 THz absorption. Figure 6.28 shows the transmission of the feature at 2 THz ± 122 GHz as a function of peak THz field. The shape of the response appears similar to that seen with the polished sample (Figure 6.15), with there being a decrease in transmission as the field increases at low fields ($< 80\,\mathrm{kV\,cm^{-1}}$), then at higher fields, the transmission increases as a function of field, which when converted to an absorption response vs intensity (Figure 6.29), has an exponential decay as expected.

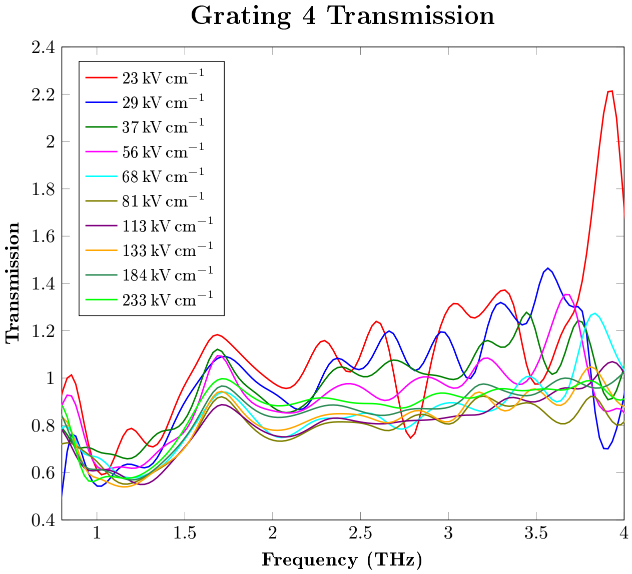

Figure 6.27: Normalised transmission response of the SIT structure using grating four to couple in the THz pulses. The normalised transmission is obtained by dividing the spectrum obtain at low temperatures (6 K) by the response at a higher temperature (290 K). Pulses of different THz field strengths are obtained by changing power of the 800 nm excitation beam incident on the BNA crystal. A 1 mm ZnTe crystal was used to detect the pulses.

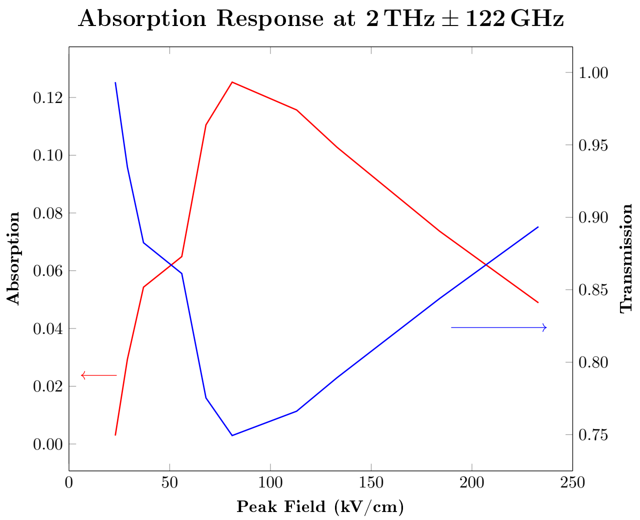

Figure 6.28: Absorption response of the SIT wafer at 2 THz ± 122 GHz. Blue traces are the transmission response (seen in Figure 6.27), red traces are the absorption response.

Fitting was again attempted on the exponentially decaying region of the data as both a homogeneously and inhomogeneously broadened transition using MATLAB. Neither of the curves provided a good fit for the data, however, the inhomogeneous fit provides a better fit than the homogeneous, with a saturating peak field of $11.89 \pm 2.19\,\mathrm{kV\,cm^{-1}}$ being obtained. The fitting parameters are displayed in Table 6.2.

Fit	Saturation Field (kV/cm)	RMSE
Homogeneous	36.35 ± 10.16	0.03644
Inhomogeneous	11.89 ± 2.19	0.0141

Table 6.2: Parameters used for the fits shown in Figure 6.29.

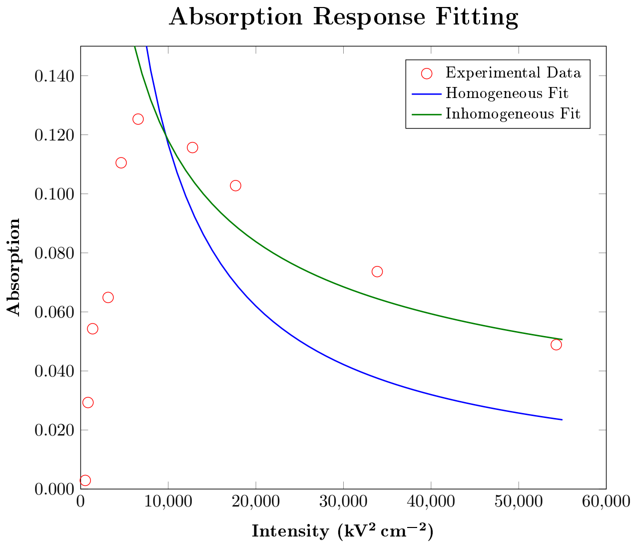

Figure 6.29: Fit of the absorption response of the SIT wafer at 2 THz as a function of THz pulse intensity. Fitting parameters can be found in Table 6.2. Fitting performed using MATLAB.

6.5 Two-Dimensional Spectroscopy

6.5.1 Experimental Information

The 2D-TDS setup used for the experiment was the same as described in Section 4.2, using a 15×15 mm PCA and a BNA crystal for THz generation, with the pulses being combined on a Si beamsplitter. Expanded PTFE filters were placed between each emitter and the Si beamsplitter to block the excess IR from exciting carriers in the wafer. With this configuration, the PCA was capable of generating peak fields of $\sim 60\,\mathrm{kV\,cm^{-1}}$, whilst the BNA was capable of generating peak fields of $\sim 130\,\mathrm{kV\,cm^{-1}}$. Both emitters were configured to emit at their peak field for this measurement. The pulses generated from the PCA will be referred to as 'A' pulses, whilst the pulses generated from the BNA will be referred to as 'B' pulses for the remainder of this section. A 1 mm ZnTe crystal was used for detection and the sample was mounted in a cryostat as described in the previous measurements (Sections 6.4.1 and 6.4.2). The sample was cooled to 6 K for the measurement. All measurements were performed in a dry air environment.

A sampling delay (t) range of 16 ps with a step size of 0.01 ps was used giving a FFT range and resolution of 100 THz and 63 GHz respectively. The delay range between E_A and E_B τ was -2.32–1.1 ps with a step size of 0.03 ps, giving a FFT range and resolution of 33 THz and 292 GHz respectively. Time constraints on performing the experiment prevented a larger τ range from being used. Similarly to the 2D TDS measurement detailed in Section 5.5, this dataset took ∼10 hours to obtain, and required the sample to be cooled using a continuous flow He dewar, making it impractical to perform longer scans as they would require unsupervised, overnight measurements. Time domain traces for all four signal states were acquired 100 times for each τ delay to improve the SNR.

6.5.2 Data Analysis

6.5.2.1 Initial Processing

Similarly to the 2D-TDS experiment discussed in Section 5.5, some initial corrections are performed on the dataset before further analysis is performed. Firstly, the τ correction is found using Equation 5.10 (which for this dataset is $-0.1\,\mathrm{ps}$) and applied to all scans. Next, the signals are averaged together to increase the SNR. This later is shown to be critical for this measurement because the nonlinear signal is incredibly small when compared with the detected excitation pulses, which are already relatively low due to losses through the sample. Finally, the detected signals are converted from arbitrary units into an estimated field using Equation 8.1 with $r_{41} = 3.9\,\mathrm{pm\,V^{-1}}$ [44], $L = 1\,\mathrm{mm}$ and $n_0 = 2.85$ [129] because a 1 mm ZnTe detection crystal was used.

6.5.2.2 Excitation Pulse Analysis

Figure 6.31 shows the time and frequency domain response of E_A and E_B after passing through the sample at $\tau \approx 1\,\mathrm{ps}$. Pulse E_B has a DC offset from the intense, unabsorbed IR excitation pulse scattering inside the system, creating a background level of light that was picked up by the photodiodes. In future experiments, this was fixed by adding baffling and opaque plastic sheeting around the photodiodes. The two broad absorption features around 1 and 2 THz, characteristic of the grating as seen in previous measurements (Figures 6.21b and 6.24b), can be seen clearly in the spectrum of E_A (Figure 6.30b), indicating that the pulses are passing through the grating as intended. Plotting E_A and E_B as a function of t and τ (Figure 6.31) show that both pulses appear as expected; E_A appears at a constant t for all values of τ, meanwhile E_B appears at $t = -\tau$. There are no obvious abnormalities which appear as τ changes, indicating that E_A and E_B stay relatively homogeneous throughout the measurement.

An analysis comparing E_AB to $E_\mathrm{A} + E_\mathrm{B}$ as performed for the 2D-TDS measurement discussed in Section 5.5.2.2 is not included here are the differences between the 2D signals are too minor to be seen within a simple 2D time plot.

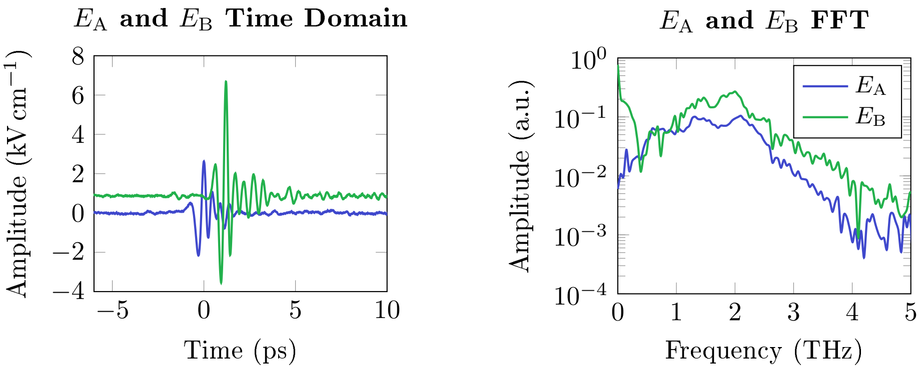

(a) (b)

Figure 6.30: Excitation pulses after passing through the SIT wafer at $\tau = -1.00$ ps. Pulses are coupled into the quantum wells using grating 4. E_A is generated using a PCA with a peak field of 60 kV cm^{-1}. E_B is generated using a BNA crystal with a peak field of 120 kV cm^{-1}. Pulses are detected using a 1 mm ZnTe crystal.

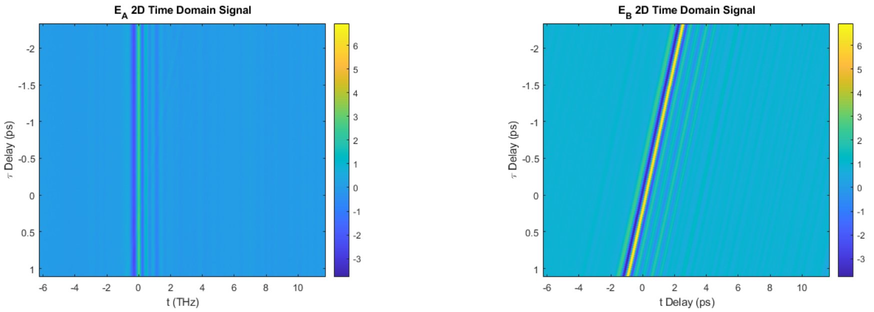

(a) 2D time domain response of E_A. (b) 2D time domain response of E_B.

Figure 6.31: 2D time domain response of the excitation pulses after passing through the SIT wafer. E_A is generated using a PCA with a peak field of 60 kV cm^{-1}. E_B is generated using a BNA crystal with a peak field of 120 kV cm^{-1}.

6.5.2.3 Nonlinear Signal Analysis

In the next stage of analysis, the nonlinear signal for each τ delay is acquired using Equation 4.1.3 to remove background artifacts. Figure 6.32 shows the time domain traces of all the signal states at $\tau \approx 0$ to highlight the difference in magnitude between the excitation pulses and the nonlinear signal, with the peak of E_B (with the DC offset removed) being around 70 times larger than E_{NL}. Figure 6.33 shows that E_{NL} is even obscured by the noise of the measurement when a single scan is performed, and even after averaging 100 scans, the SNR is still only ~5 dB (using the peak signal field and peak noise field).

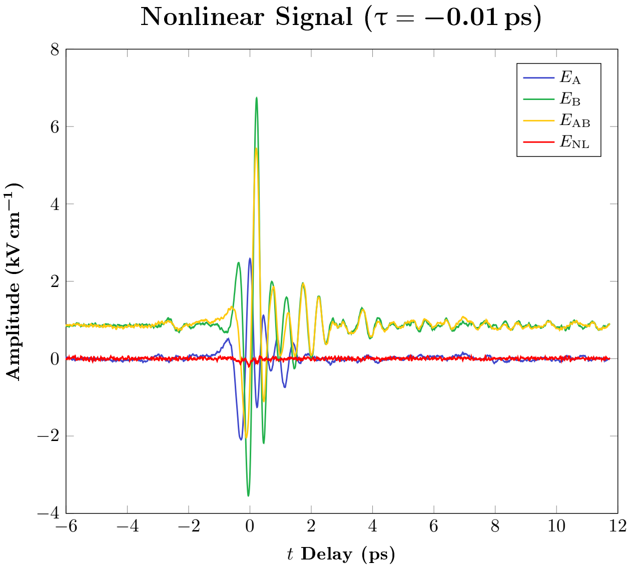

Figure 6.32: All signal states from the SIT wafer at $\tau = 0$ ps. E_A is generated using a PCA with a peak field of 60 kV cm^{-1}. E_B is generated using a BNA crystal with a peak field of 120 kV cm^{-1}. Pulses are detected using a 1 mm ZnTe crystal. Signals have been averaged using 100 repeats.

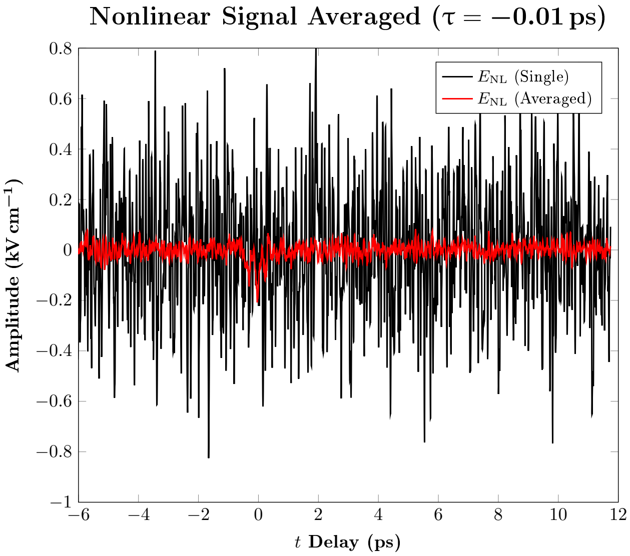

Figure 6.33: Comparison of the nonlinear signal at $\tau = 0\,\mathrm{ps}$ acquired from a single scan and after 100 repeated scans.

Figure 6.34 shows a subset of the calculated nonlinear signals where it can be seen that it becomes difficult to distinguish the nonlinear signal when $\tau \ll 0$. This is likely because for $\tau < 0$, the weaker pulse E_{A} is exciting the sample. Making an assumption that with the peak field of E_{A} being two times weaker than E_{B}, the resulting nonlinear signal would also be two times weaker, the peak field of the nonlinear signal when $\tau < 0$ would be obscured by the noise, which may explain why it cannot be seen. Plotting the nonlinear signal in the 2D time domain (Figure 6.36) allows for some features to be distinguished at $\tau < 0$. A nonlinear signal typical appears at $t = 0$ when $\tau > 0$ and then appears at $t = -\tau$ when $\tau < 0$, however here a response can be seen at $t = 0$ for all values of τ. This suggests that there may have been a phasing issue with the choppers, causing E_{A} to 'leak' into the background correction signal $E_{\oslash}$. Viewing the 2D FFT of the nonlinear signal (Figure 6.37), the frequency response at $f_{\tau} = 0\,\mathrm{THz}$ does also appear similar to that of E_{A} (see Figure 6.30b) also indicates that this is the case. This is confirmed when $E_{\oslash}$ is averaged (see black trace in Figure 6.35), where a response can be seen around $t = 0\,\mathrm{ps}$. It should be noted that the general skewed shape of $E_{\oslash}$ is caused by the detection electronics. To remove this unwanted contribution whilst still removing the skew caused by the detection electronics, the method of calculating E_{NL} (Equation 4.1.3) was adjusted slightly. Instead of adding raw $E_{\oslash}$ data, $E_{\oslash}$ is first passed through a 100 point moving average filter before being added. This corrects for the low frequency shape of the signal, whilst removing the higher frequency unwanted component without adding in artefacts caused by E_{A}. A 100 point filter was chosen (see blue trace in Figure 6.35) as using a lower number of points caused the unwanted features to still be present (see red trace in Figure 6.35), whilst using a greater number of points smoothed out the general shape, reducing the accuracy of the correction (see green trace in Figure 6.35).

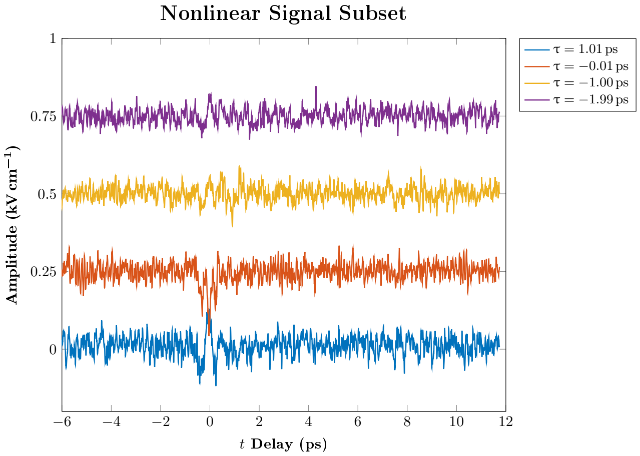

Figure 6.34: Subset of the nonlinear responses induced in the SIT wafer at different τ delays. Signals are offset to improve readability

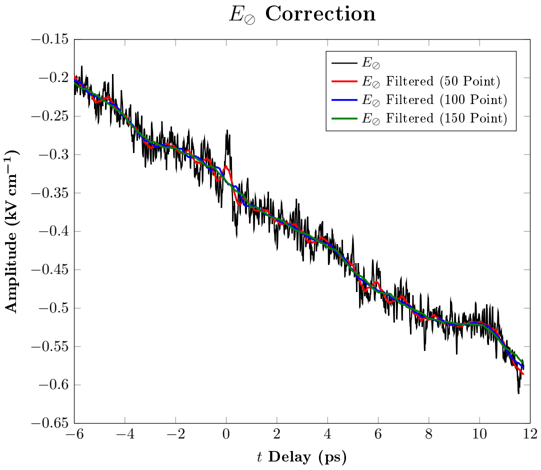

Figure 6.35: $E_{\oslash}$ (averaged) at $\tau = -0.01\,\text{ps}$ before and after being processed with a N point moving average filter. Here it can be seen that using a moving average filter with at least 100 point removes the signal embedded at $t = 0\,\text{ps}$ whilst still keeping the overall shape of the signal.

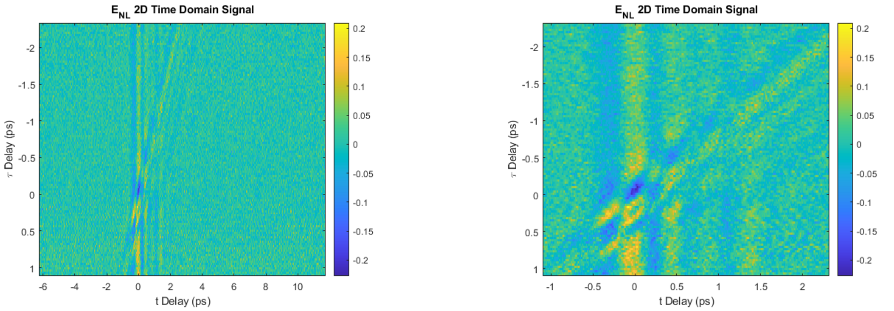

(a) Full 2D time domain response of E_{NL}.

(b) Zoomed 2D time domain response of E_{NL}.

Figure 6.36: 2D nonlinear time domain response (E_{NL}) of the SIT wafer cooled to 6 K. Nonlinear signal induced by two pump pulses, E_{A} and E_{B} and are coupled into the quantum wells using grating 4. E_{A} is generated using a PCA with a peak field of $60\,\mathrm{kV\,cm^{-1}}$. E_{B} is generated using a BNA crystal with a peak field of $120\,\mathrm{kV\,cm^{-1}}$.

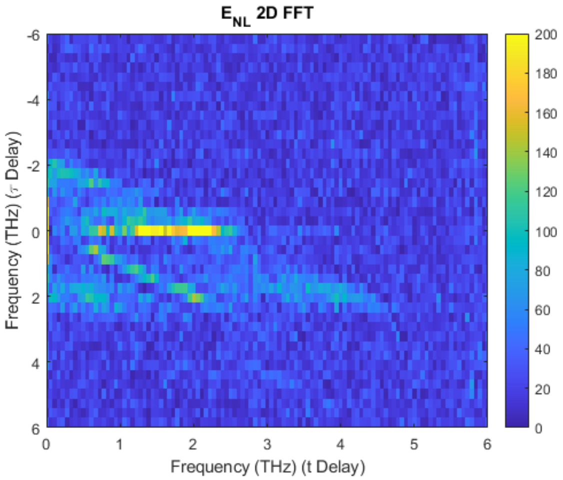

Figure 6.37: 2D FFT of E_{NL} in Figure 6.36a.

Figure 6.38 shows a subset of the re-calculated nonlinear signals which when compared with the original analysis (Figure 6.34), it appears that the unwanted response at $t = 0$ when $\tau < 0$ has been removed (purple and yellow traces) and this is confirmed when comparing the full 2D nonlinear time domain responses (Figures 6.36 and 6.39). The new 2D nonlinear FFT also shows that the residual response of E_{A} at $f_\tau = 0\,\mathrm{THz}$ has been removed, leaving only the response expected at $(f_t, f_\tau) = (2, 0)$ THz, corresponding to the $P_{\mathrm{B}}p_{\mathrm{A}}$ (P_x refers to the 'pump' pulse, whilst p_x refers to the probe pulse). The other regions of interest are $(2, 2)$ THz, corresponding to the $P_A p_B$ signal and $(4, 2)$ THz, possibly corresponding to the Sum-Frequency Generation (SFG) signal (the features around $(6, 0)$ THz are artefacts).

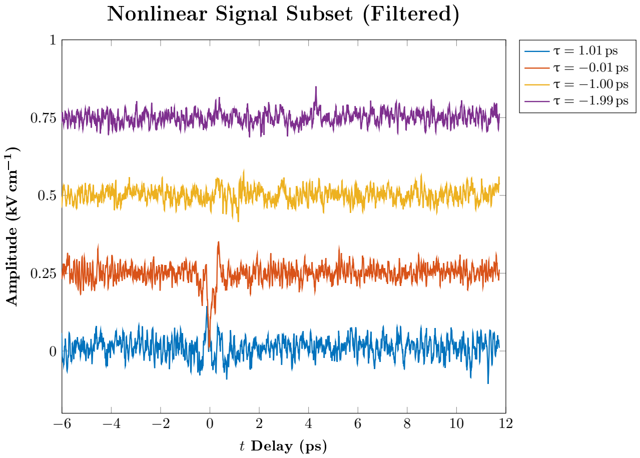

Figure 6.38: Same subset of the nonlinear signals shown in Figure 6.34, but using the filtered $E_{\oslash}$ for correction. Here it can be seen that the response present at $t = 0$ ps seen in $\tau = -1$ ps and $\tau = -1.99$ ps in Figure 6.34 is removed. Signals are offset to improve readability.

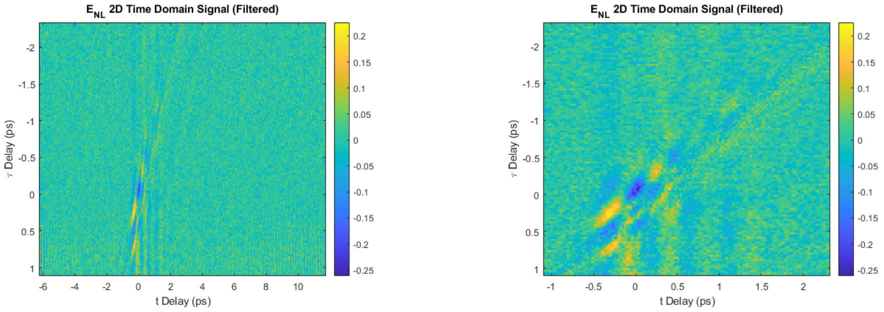

(a) Full 2D time domain response of E_{NL} using the filtered $E_{\oslash}$.

(b) Zoomed 2D time domain response of E_{NL} using the filtered $E_{\oslash}$.

Figure 6.39: 2D nonlinear time domain response of the SIT wafer, obtained using the filtered $E_{\oslash}$ shown in Figure 6.35 to remove residual signal present in $E_{\oslash}$.

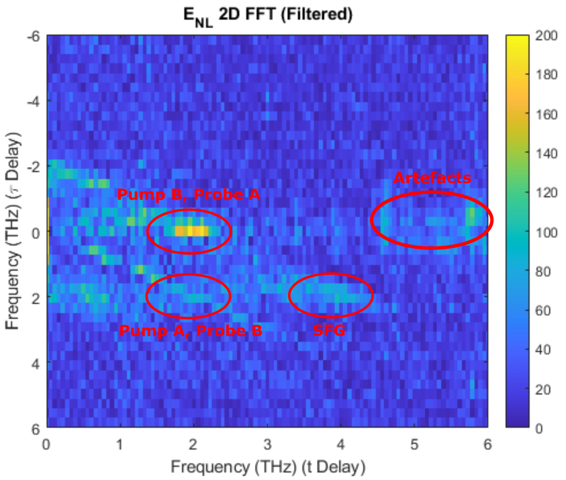

Figure 6.40: 2D FFT of E_{NL} in Figure 6.39a. The nonlinear responses present have been labelled. $P_{\mathrm{B}}p_{\mathrm{A}}$ found at $(2, 0)$ THz, $P_{\mathrm{A}}p_{\mathrm{B}}$ found at $(2, 2)$ THz and SFG found at $(4, 2)$ THz. The response seen at $(5, 0)$ THz is an artefact.

Performing an inverse 2D FFT on the three nonlinear response regions highlighted in Figure 6.40 acquires the time domain signals shown in Figure 6.41. In general, these signals appear at their expected regions in time, indicating that the signals are not artefacts; the $P_{\mathrm{B}}p_{\mathrm{A}}$ signal appears centred around $t = 0$, disappearing at $\tau < -t$; the $P_{\mathrm{A}}p_{\mathrm{B}}$ signal appears centred around $t = -\tau$; and the SFG signal appears where both pulses are strongly overlapped in time ($\sim t = \tau = 0$). In measurements of a similar sample (a Double Quantum Well (DQW) system), a second-order nonlinear effects was seen (a DFG response), however this was attributed to frequency mixing in the bulk GeAs semiconductor [82]. Performing a FFT as a function of τ on these nonlinear responses and then plotting the average response and selected frequency slices acquired the graphs shown in Figure 6.42. This data is difficult to interpret in this state, as the τ range is short, however an oscillation is observed in the $P_{\mathrm{A}}p_{\mathrm{B}}$ response (Figure 6.42b) at the expected frequency of 1.85 THz when $\tau < 0$, which is where the $P_{\mathrm{A}}p_{\mathrm{B}}$ response is expected to be seen. As this oscillation is not seen at the slightly higher frequency of 2 THz, it is likely an observation of the transition. The other graphs do not provide much insight into the sample, however this is somewhat expected, as the $P_{\mathrm{B}}p_{\mathrm{A}}$ signal (Figure 6.42a) would reside at $\tau > 0$, where we a limited by the range of the dataset.

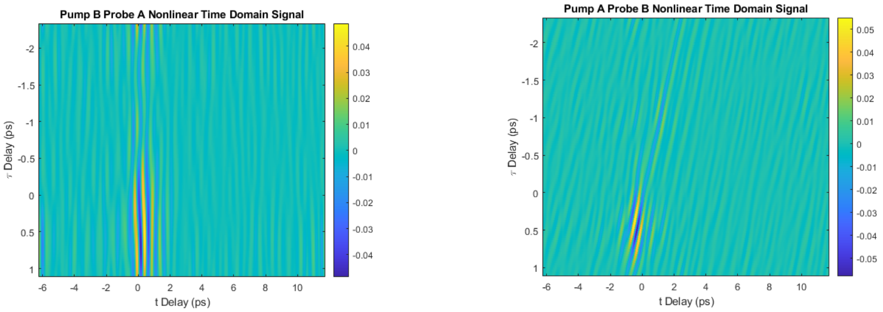

(a) $P_{\mathrm{B}}p_{\mathrm{A}}$ at $(2,0)$ THz.

(b) $P_{\mathrm{A}}p_{\mathrm{B}}$ at $(2,2)$ THz.

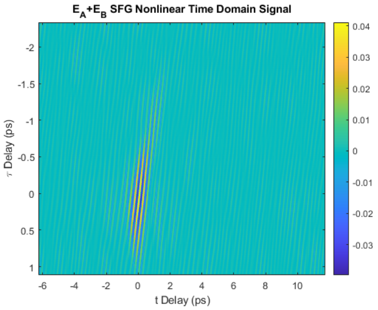

(c) SFG of E_{A} and E_{B} at $(4,2)$ THz.

Figure 6.41: Inverse 2D FFT of the nonlinear responses shown in Figure 6.40. The position of the responses in time appear as excepted, for example, the SFG signal appears where both pump pulses (E_{A} and E_{B}) are overlapped in time near $\tau \approx t \approx 0$.

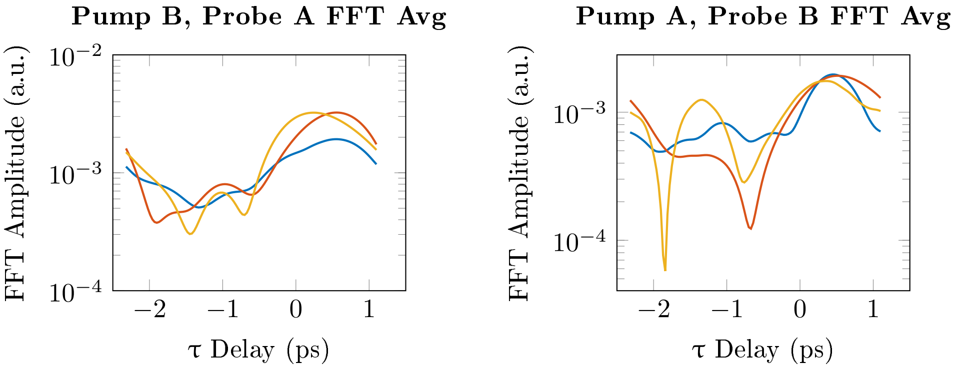

(a) Blue trace shows averaged response of the FFT of Figure 6.41a. Orange and yellow traces show the frequency response at 2.00 THz and 1.86 THz respectively.

(b) Blue trace shows averaged response of the FFT of Figure 6.41b. Orange and yellow traces show the frequency response at 2.00 THz and 1.86 THz respectively.

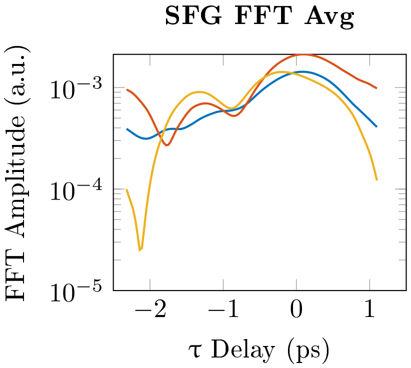

(c) Blue trace shows averaged response of the FFT of Figure 6.41c. Orange and yellow traces show the frequency response at 3.96 THz and 3.71 THz respectively.

Figure 6.42: Averaged FFT responses and single frequency slices of the nonlinear responses shown in Figure 6.41 as a function of τ delay. Owing to the limited τ range, it is difficult to interpret this data, however, an oscillation is seen at 1.85 THz in Figure 6.42b where $\tau < 0$ as expected.

As discussed in Section 5.5.2.3, it has been shown in a recent study of a similar sample [84] that the T_1 and T_2 values of the transition can be obtained by fitting a slice of the nonlinear 2D time domain signal at a set t delay to Equation 5.12. A region with greater intensity can be seen at $t \approx 0.4\,\mathrm{ps}$ in the 2D nonlinear signal (see Figure 6.39b) so a slice at this delay was chosen for fitting. To reduce the noise in the data to be fitted, the mean signal over a range of t delays (0.33–0.51 ps) was used instead of a single slice of t. Again, similarly to the fitting performed in Section 5.5.2.3, the T_1 component of the equation was replaced with a constant (A_1), as it proved difficult to obtain a good fit, likely owing to the small range of τ of the signal to be fitted. The data slice appeared to have the characteristic dampened oscillatory response beginning at $\tau < 0$ so a constant delay shift (τ_{Shift}) was applied to the fit to account for this. This shift arises from the change in which pulse is pumping the sample not occurring exactly at $\tau = 0$, but at some negative τ delay, likely because E_{B} is much more intense than E_{A}. As the transition of interest occurs at 2 THz, the equation used for fitting was the following:

$$E_{\mathrm{NL}}(\tau) = A_1 + A_2 \sin(2 \times 2\pi(\tau + \tau_{\mathrm{Shift}})) \exp(-\frac{(\tau + \tau_{\mathrm{Shift}})}{T_2}). \tag{6.27}$$

Using MATLAB's fitting toolbox, the data slice was fitted using Equation 6.27, producing the fit shown in Figure 6.43, acquiring ($T_2 = 1.064 \pm 0.996\,\mathrm{ps}$. This value seems reasonable, as slightly a larger value of $2.2 \pm 0.2\,\mathrm{ps}$ was found for a Multiple-Quantum-Well (MQW) saturable absorber [84], a sample similar to the SIT sample measured here. The fit however, is not perfect as the data is very noisy for $\tau > 0.5\,\mathrm{ps}$, reducing the reliability of the fit.

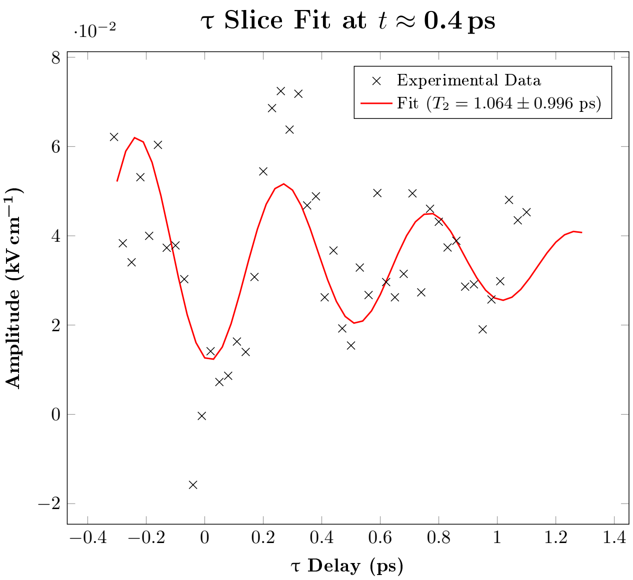

Figure 6.43: Fit of a slice of the nonlinear signal shown in Figure 6.39 to obtain the T_2 lifetime of the transition. Owing to the low SNR of the nonlinear signal, the data points between t =0.33–0.51 ps are averaged instead of taking a slice at a single t delay. A T_2 value of 1.064±0.996 ps is obtained for the transition of interest at 1.85 THz.

6.6 Experimental Conclusions

In conclusion a T_2 value of the transition of interest has been obtained of 1.064±0.996 ps and which seems reasonable given the number of barrier/well interfaces the wavefunctions interact with and hence an increase in interface roughness scattering compared to the 2 ps T_2 time measured in the double quantum well sample by Raab et al. [84]. The data used to obtain this value could be improved by repeating the measurement and using a larger τ range with more repeats per τ delay to improve the SNR of the nonlinear signal. Repeating the measurement for a number excitation fields would also allow for Rabi flopping of the transition to be investigated, allowing for the population inversion as a function of t and τ to be estimated, as well as the excitation field necessary to induce a 2π pulse within the sample [81, 84]. This information is critical for the future application of the sample of integrating the structure into a QCL to act as a saturable absorber. Performing the measurements at multiple fields may also give more insight into the odd saturation behaviour seen discussed in Sections 6.4.2 and 6.3.2, however as this response was present with two different coupling methods, it is likely not a measurement artifact. Simulating the measurements would also help verify the results and potentially identify the cause of the SFG signal found in the nonlinear 2D FFT (Figure 6.40).

Chapter 7

Conclusions and Further Work

7.1 Conclusions

Chapter 3 introduces large area, LT-GaAs on transparent substrate PCAs, designed for use with amplified laser systems, a progression from the single gap, LT-GaAs on quartz emitters [19] designed for use with low power, high-repetition rate mode-locked laser systems. Methods of characterising these devices have been discussed and results from this have shown that fields greater than $100\,\mathrm{kV\,cm^{-1}}$ over a broad bandwidth greater than 5 THz can be generated, with also having the benefit of suppressing pulse-to-pulse noise caused by using amplified lasers [94].

In Chapter 4, a two emitter, 2D THz TDS spectroscopy system has been demonstrated. Both emitters are interchangeable but have been tested with a large area PCA and an EO crystal (BNA), both of which are capable of generating the large fields required for nonlinear spectroscopy. In the current configuration, both emitters are optically chopped at 125 Hz ($1/8^{\mathrm{th}}$ of the 1 kHz repetition rate of the laser), with a 90° phase difference between the two choppers allowing for the four possible signal states to be acquired within eight laser pulses. The chopping frequency could however be sped up to 250 Hz to allow for the four signal states to be acquired every four pulses if a different optical chopper is used. The design of the system allows for the THz field at the sample space to be measured directly which has proved to be advantageous when aligning the system and estimating the field applied to a sample.

In Chapter 5, a doped semiconductor impurity centre (Ge:As) was measured, with the primary transition, $1s(A1) \rightarrow 2p_0$, at frequency of 2.28 THz being the main transition of interest. Performing a saturation measurement acquired that a broadband pulse with a peak field of $\sim 20\,\mathrm{kV\,cm^{-1}}$ is sufficient for the transition to become saturated, with the response following the expected trend of a inhomogeneously broadened transition. The 2D THz TDS measurement performed on the sample allowed for electrons excited from $1s(A1) \rightarrow 2p_0$ to become excited to a higher state, with a transition frequency of $\sim 0.78\,\text{THz}$, likely being either $2p_\pm$ or $3s(A1)$. This measurement allowed for a T_2 value of both of these transitions to be obtained being $\sim 5.83\,\text{ps}$ and $\sim 0.12\,\text{ps}$ for the $1s(A1) \rightarrow 2p_0$ and $2p_0 \rightarrow (2p_\pm/3s(A1))$ respectively.

In Chapter 6, a quantum well structure, designed to exhibit the SIT effect with incident pulses at a frequency of 1.85 THz. Two methods of coupling broadband THz pulses into the quantum wells were tested, polishing 45° incident facets into the wafer and diffraction gratings fabricated on the wafer surface. Both coupling methods allowed for a response to be observed at the expected frequency when the system was cryogenically cooled, however owing to its ease of use, coupling using gratings is preferred. Saturation measurements performed on the sample using both coupling methods acquired an unexpected response, where the absorption of the transition as a function of applied field increases until a threshold field, where the response changed to a more expected response (the absorption reduces with applied field). The field where this change in response occurs is dependent on the method of coupling used, as the coupling efficiency differs between the two methods. A 2D THz TDS measurement was perform on the sample using the diffraction grating coupling method where a T_2 value of the transition was acquired as $\sim 1\,\text{ps}$. This measurement also showed that a SFG signal was being induced within the sample.

7.2 Further Work

The PCAs developed by Dr. David Bacon for this work show lots of promise as broadband emitters for high power systems such as the one developed. Devices with larger area active region and with other device optimisations (e.g. unequal anode to cathode width [37] or anti-reflective coatings [94]) would allow for even greater fields to be obtained. The other major improvement which could be implemented is to use thicker substrates to increase the spectral resolution of the measurements, as the reflection in the substrate would be pushed back in time, however, this would likely require the current device recipe to be altered to account for this.

The experimental system could be improved further by investigating methods to improve the SNR and to reduce the time taken to acquire a TDS trace, as this would allow for smaller strength nonlinear signals to be detected and allow for larger datasets to be obtained. The scan times could be improved by adding a fast, frictionless delay line (referred to as a ‘shaker’) [158], or by using Echelon mirrors which split the sampling beam into an array of beamlets delayed in time, which are then captured by a CCD array, allowing for the THz pulse to be acquired in the time domain every laser pulse [159]. Adding more parabolic mirrors of different focal lengths before the sample space to reduce the THz spot size would also allow for the field strength to be increased at the cost of increased complexity of the system. With the system uses two emitters simultaneously, measurements with a narrowband pump and a broadband probe should be relatively straightforward to perform and may be preferable to be implemented when only a single transition is being investigated, for example. Use of an Optical Parametric Amplifier (OPA) and certain EO emission crystals (e.g. GaSe) would allow for controllable narrowband pulse generation.

Regarding both of the measured samples (Ge:As and the SIT sample), repeating the 2D THz TDS measurements with a larger τ delay range and more repeats per τ delay would allow for the T_2 values of the transitions to be obtained with more accuracy then in the data shown in this work and for the SIT sample, this may allow for a value of T_1 to also be obtained. Performing the measurements at multiple field strengths may potentially allow for Rabi oscillations to be observed which is important for both samples. For the Ge:As, observation of a Rabi oscillation and knowledge of T_1 and T_2 would allow for coherent control measurements to be performed on the sample, whilst for the SIT sample, it would allow for the suitability of the structure as a saturable absorber for a QCL to be assessed.

Chapter 8

Appendix

8.1 Electro-Optic Detection Field Estimate

The following equation is used to provide a more accurate field estimation of a THz pulse detected using EO detection and was provided by Dr Joshua Freeman:

$$\begin{aligned} E_{\mathrm{THz}} &= V_{\mathrm{P}} \frac{\lambda \mathrm{LIF}}{V_0 2\pi L n_0^3 d_{41} \mathrm{D_R} \mathrm{T_C}}, \\ \mathrm{T_C} &= \frac{2}{1+n_T}, \\ \mathrm{LIF} &= \frac{\pi}{2\sqrt{2}\sin(\pi \mathrm{D})}, \end{aligned} \tag{8.1}$$

where E_{THz} is the estimated THz field, V_{P} is the voltage received from the balanced photodiodes, λ is the wavelength of the detection beam, V_0 is the voltage received from the photodiodes when there is no THz present, L is the thickness of the detection crystal, n_0 is the optical refractive index of the crystal, d_{41} is the EO coefficient of the crystal, $\mathrm{D_R}$ is the response of the EO crystal, $\mathrm{T_C}$ is the transmission of the THz pulse at the air-crystal interface, n_T is the THz refractive index of the crystal, LIF is a factor accounting for the square nature of the signal detected by the LIA and D is the duty cycle of the detected signal.

The parameters used with the crystals used in this project can be found in Table 8.1.

Crystal	L	d_{41}	n_O	n_T	$\mathrm{D_R}$
ZnTe	1×10^{-3}	4×10^{-12}	2.85	3.12	0.72
GaP	150×10^{-6}	0.97×10^{-12}	3.57	3.34	0.9

Table 8.1: Parameters used in Equation 8.1 for the crystals used througout this project.

8.2 Rabi Oscillation Derivation

To derive a Rabi oscillation, we first consider the transition as a dipole in resonance using the following equation [10]:

$$\frac{d^2p(t)}{dt^2} + \Delta\omega_a \frac{dp(t)}{dt} + \omega_a^2 p(t) = K\Delta N(t)\varepsilon(t) \tag{8.2}$$

where $p(t)$ is the polarisation of the transition, $\Delta\omega_a$ is the linewidth of the transition, ω_a the frequency of the transition, $N(t)$ is the population of the transition, $\varepsilon(t)$ is the electric field of the excitation field and K is defined by the following equation:

$$K \equiv \frac{3\omega_a \epsilon \lambda^3 \gamma_{\mathrm{rad}}}{4\pi^2}, \tag{8.3}$$

where ϵ is the dielectric permeability of the sample, γ_{rad} is the decay rate of the transition and λ is the wavelength of the excitation beam. A resonant applied field can be written as $\varepsilon(t) = E_1(t)\exp(j\omega_a t)$ and the polarisation can be written as $p(t) = -jP_1(t)\exp(j\omega_a t)$ as there is a phase difference of -90° between $\varepsilon(t)$ and $p(t)$. Substituting this into Equation 8.2 gives:

$$\frac{d^2P_1(t)}{dt^2} + (2j\omega_a + \Delta\omega_a)\frac{dP_1(t)}{dt} + j\omega_a\Delta\omega_a P_1(t) = jKE_1(t)\Delta N(t). \tag{8.4}$$

This can be simplified further by using the Slow Varying Envolope Approximation (SVEA): the envelope of a pulse changes slowly when compared to its wavelength. This allows for the second-derivative term to be ignored as it will be small compared with the first-derivative term. As $\Delta\omega_a \ll \omega_a$, the $\Delta\omega_a$ in front of the first-derivative may also be ignored, giving the following equation:

$$\frac{dP_1(t)}{dt} + \frac{\Delta\omega_a}{2}P_1(t) \approx \frac{K}{2\omega_a}E_1(t)\Delta N(t), \tag{8.5}$$

We then consider the population of a two-level system which is defined by the following equation:

$$\frac{d\Delta N(t)}{dt} + \frac{\Delta N(t) - \Delta N_0}{T_1} = -(\frac{2}{\hbar\omega_a})\varepsilon(t) \cdot \frac{dp(t)}{dt} \tag{8.6}$$

where T_1 is the carrier lifetime and N_0 is initial population. Presuming that $\varepsilon(t) \cdot p(t)$ is averaged over time, Equation 8.6 can be simplified to:

$$\frac{dN(t)}{dt} + \frac{\Delta N(t) - \Delta N_0}{T_1} \approx -\frac{1}{\hbar}E_1(t)P_1(t). \tag{8.7}$$

Next we substitute Equation 8.7 into Equation 8.5 acquiring:

$$\frac{d^2\Delta N(t)}{dt^2} + (\frac{\Delta\omega_a}{2} + \frac{1}{T_1})\frac{d\Delta N(t)}{dt} + (\frac{\Delta\omega_a}{2T_1} + \frac{KE_1^2}{2\hbar\omega_a})\Delta N(t) = \frac{\Delta\omega_a}{2T_1}\Delta N_0. \tag{8.8}$$

The Rabi frequency (Ω_{Rabi}) is then defined as:

$$\Omega^2_{\text{Rabi}} \equiv \frac{KE_1^2}{2\hbar\omega_a} \equiv \frac{3\gamma_{\text{rad}}\epsilon\lambda^3}{8\pi^2\hbar}E_1^2. \tag{8.9}$$

This allows for Equation 8.8 to be rewritten using Ω_{Rabi} in terms of $\Delta N(t)$ or $P_1(t)$:

$$[\frac{d^2}{dt^2} + (\frac{\omega_a}{2} + \frac{1}{T_1})\frac{d}{dt} + (\frac{\Delta\omega_a}{2T_1})]\Delta N(t) = \frac{\Delta\omega_a}{2T_1}\ \Delta N_0, \tag{8.10}$$

$$[\frac{d^2}{dt^2} + (\frac{\omega_a}{2} + \frac{1}{T_1})\frac{d}{dt} + (\frac{\Delta\omega_a}{2T_1})]\ P_1(t) = \frac{KE_1}{2T_1\omega_a}\Delta N_0. \tag{8.11}$$

Finally, assuming that E_1 is strong and $\Omega_{\text{Rabi}} \gg \Delta\omega_a$ and $\Omega_{\text{Rabi}} \gg 1/T_1$, $P_1(t)$ and $\Delta N(t)$ can be found by substituting Ω_{Rabi} into the above equations:

$$\frac{d^2\Delta N}{dt^2} + \Omega^2_{\text{Rabi}}\Delta N \approx 0 \ \Rightarrow \ \Delta N(t) = \Delta N_0 \cos\Omega_{\text{Rabi}}t, \tag{8.12}$$

$$\frac{d^2P_1}{dt^2} + \Omega^2_{\text{Rabi}}P_1 \approx 0 \ \Rightarrow \ P_1(t) = P_m \sin\Omega_{\text{Rabi}}t, \tag{8.13}$$

where P_m is the maximum value of the polarisation oscillation and equals $\sqrt{K\hbar/2\omega_a}\Delta N_0$ [10].

Chapter 9

Bibliography

[1] Y. S. Lee, *Principles of terahertz science and technology.* Boston, MA: Springer US, 2009.

[2] J. Raab, F. P. Mezzapesa, L. Viti, N. Dessmann, L. K. Diebel, L. Li, A. G. Davies, E. H. Linfield, C. Lange, R. Huber, and M. S. Vitiello, "Ultrafast terahertz saturable absorbers using tailored intersubband polaritons," *Nature Communications*, vol. 11, pp. 1–8, aug 2020.

[3] S. Winnerl, F. Göttfert, M. Mittendorff, H. Schneider, M. Helm, T. Winzer, E. Malic, A. Knorr, M. Orlita, M. Potemski, M. Sprinkle, C. Berger, and W. A. De Heer, "Time-resolved spectroscopy on epitaxial graphene in the infrared spectral range: Relaxation dynamics and saturation behavior," *Journal of Physics Condensed Matter*, vol. 25, p. 054202, feb 2013.

[4] A. Dienst, E. Casandruc, D. Fausti, L. Zhang, M. Eckstein, M. Hoffmann, V. Khanna, N. Dean, M. Gensch, S. Winnerl, W. Seidel, S. Pyon, T. Takayama, H. Takagi, and A. Cavalleri, "Optical excitation of Josephson plasma solitons in a cuprate superconductor," *Nature Materials*, vol. 12, pp. 535–541, jun 2013.

[5] J. Heberle and T. Gensch, "When FT-IR spectroscopy meets X-ray crystallography," *Nature Structural Biology*, vol. 8, pp. 195–197, mar 2001.

[6] J. D. Steill, J. Szczepanski, J. Oomens, J. R. Eyler, and A. Brajter-Toth, "Structural characterization by infrared multiple photon dissociation spectroscopy of protonated gas-phase ions obtained by electrospray ionization of cysteine and dopamine," *Analytical and Bioanalytical Chemistry*, vol. 399, pp. 2463–2473, mar 2011.

[7] P. T. Greenland, S. A. Lynch, A. F. G. Van Der Meer, B. N. Murdin, C. R. Pidgeon, B. Redlich, N. Q. Vinh, and G. Aeppli, "Coherent control of Rydberg states in silicon," *Nature*, vol. 465, no. 7301, pp. 1057–1061, 2010.

[8] D. Strickland and G. Mourou, “Compression of amplified chirped optical pulses,” *Optics Communications*, vol. 56, pp. 219–221, dec 1985.

[9] Spectra-Physics, “Spitfire ® Ace ™ PA,” 2019.

[10] A. E. Siegman, *Lasers*. University Science Books, 1986.

[11] S. Kasap, “Principles of Electronic Materials and Devices,” 2006.

[12] T. H. Maiman, “Stimulated optical radiation in Ruby,” *Nature*, vol. 187, no. 4736, pp. 493–494, 1960.

[13] O. Svelto, *Principles of lasers*. 2010.

[14] F. J. McClung and R. W. Hellwarth, “Giant optical pulsations from ruby,” *Journal of Applied Physics*, vol. 33, pp. 828–829, jun 1962.

[15] P. Rudawski, “Second-generation High-Order Harmonic Sources From CPA to OPCPA,” 2014.

[16] T. Nagy, M. Kretschmar, and A. Rouzée, “High-energy sub-5 fs pulses from a Ti:sapphire laser,” in *Optics InfoBase Conference Papers*, p. HTh3B.5, The Optical Society, nov 2020.

[17] A. Dunn, *Developing terahertz sources for characterising GaN semiconductor structures*. PhD thesis, 2018.

[18] D. H. Auston, K. P. Cheung, and P. R. Smith, “Picosecond photoconducting Hertzian dipoles,” *Applied Physics Letters*, vol. 45, pp. 284–286, aug 1984.

[19] D. R. Bacon, A. D. Burnett, M. Swithenbank, C. Russell, L. Li, C. D. Wood, J. Cunningham, E. H. Linfield, A. G. Davies, P. Dean, and J. R. Freeman, “Investigation into free-space terahertz radiation from a LT-GaAs-on-quartz photoconductive emitter,” *International Conference on Infrared, Millimeter, and Terahertz Waves, IRMMW-THz*, vol. 24, p. 26986, nov 2017.

[20] C. D. Wood, O. Hatem, J. E. Cunningham, E. H. Linfield, A. G. Davies, P. J. Cannard, M. J. Robertson, and D. G. Moodie, “Terahertz emission from metal-organic chemical vapor deposition grown Fe:InGaAs using 830 nm to 1.55 μm excitation,” *Applied Physics Letters*, vol. 96, p. 194104, may 2010.

[21] L. Hou and W. Shi, “An LT-GaAs terahertz photoconductive antenna with high emission power, low noise, and good stability,” *IEEE Transactions on Electron Devices*, vol. 60, no. 5, pp. 1619–1624, 2013.

[22] D. R. Bacon, “Time-Resolved Pump-Probe Investigation of the Terahertz Quantum Cascade Laser,” 2017.

[23] N. M. Burford and M. O. El-Shenawee, “Review of terahertz photoconductive antenna technology,” *Optical Engineering*, vol. 56, no. 1, p. 010901, 2017.

[24] K.-E. Peiponen, A. Zeitler, and M. Kuwata-Gonokami, eds., *Terahertz Spectroscopy and Imaging*, vol. 171 of *Springer Series in Optical Sciences*. Berlin, Heidelberg: Springer Berlin Heidelberg, 2013.

[25] S. Gupta, J. F. Whitaker, and G. A. Mourou, “Ultrafast Carrier Dynamics in Iii-V Semiconductors Grown by Molecular-Beam Epitaxy At Very Low Substrate Temperatures,” *IEEE Journal of Quantum Electronics*, vol. 28, no. 10, pp. 2464–2472, 1992.

[26] M. Tani, S. Matsuura, K. Sakai, and S.-i. Nakashima, “Emission characteristics of photoconductive antennas based on low-temperature-grown GaAs and semi-insulating GaAs,” *Applied Optics*, vol. 36, p. 7853, oct 1997.

[27] R. A. Höpfel, J. Shah, D. Block, and A. C. Gossard, “Picosecond time-of-flight measurements of minority electrons in GaAs/AlGaAs quantum well structures,” *Applied Physics Letters*, vol. 48, pp. 148–150, jan 1986.

[28] J. S. Weiner and P. Y. Yu, “Free carrier lifetime in semi-insulating GaAs from time-resolved band-to-band photoluminescence,” *Journal of Applied Physics*, vol. 55, pp. 3889–3891, aug 1984.

[29] M. R. Stone, M. Naftaly, R. E. Miles, J. R. Fletcher, and D. P. Steenson, “Electrical and radiation characteristics of semilarge photoconductive terahertz emitters,” *IEEE Transactions on Microwave Theory and Techniques*, vol. 52, pp. 2420–2429, oct 2004.

[30] B. B. Hu, X. C. Zhang, and D. H. Auston, “Temperature dependence of femtosecond electromagnetic radiation from semiconductor surfaces,” *Applied Physics Letters*, vol. 57, pp. 2629–2631, jun 1990.

[31] M. Tani, M. Herrmann, and K. Sakai, “Generation and detection of terahertz pulsed radiation with photoconductive antennas and its application to imaging,” Tech. Rep. 11, oct 2002.

[32] H. M. Heiliger, M. Vossebürger, H. G. Roskos, H. Kurz, R. Hey, and K. Ploog, “Application of liftoff low-temperature-grown GaAs on transparent substrates for THz signal generation,” *Applied Physics Letters*, vol. 69, pp. 2903–2905, nov 1996.

[33] M. Naftaly and R. E. Miles, “Terahertz time-domain spectroscopy for material characterization,” *Proceedings of the IEEE*, vol. 95, pp. 1658–1665, aug 2007.

[34] D. Grischkowsky, S. Keiding, M. van Exter, and C. Fattinger, "Far-infrared time-domain spectroscopy with terahertz beams of dielectrics and semiconductors," *Journal of the Optical Society of America B*, vol. 7, p. 2006, oct 1990.

[35] D. Bacon, M. Rosamond, T. Gill, A. Burnett, L. Li, J. Cunningham, E. Linfield, A. Davies, P. Dean, and J. Freeman, "Photoconductive Arrays for High-Field Terahertz Generation," (Paris), IEEE, sep 2019.

[36] A. Singh, S. Winnerl, J. C. König-Otto, D. R. Stephan, M. Helm, and H. Schneider, "Plasmonic efficiency enhancement at the anode of strip line photoconductive terahertz emitters," *Optics Express*, vol. 24, p. 22628, oct 2016.

[37] A. Singh, M. Welsch, S. Winnerl, M. Helm, and H. Schneider, "Improved electrode design for interdigitated large-area photoconductive terahertz emitters," *Optics Express*, vol. 27, p. 13108, apr 2019.

[38] S. L. Dexheimer, "Terahertz spectroscopy: principles and applications," *The Journal of Physical ...*, p. 358, 2008.

[39] X. Mu, Y. J. Ding, and I. B. Zotova, "Investigation of relations among matrix elements of second-order nonlinear susceptibility tensor of GaSe crystal," in *Conference on Quantum Electronics and Laser Science (QELS) - Technical Digest Series*, 2008.

[40] J. Hebling, K. L. Yeh, M. C. Hoffmann, and K. A. Nelson, "High-power THz generation, THz nonlinear optics, and THz nonlinear spectroscopy," *IEEE Journal on Selected Topics in Quantum Electronics*, vol. 14, no. 2, pp. 345–353, 2008.

[41] K. A. Niessen, "Optimization of THz Microscopy Imaging," *Spie*, pp. 3–4, jul 2015.

[42] N. B. Singh, T. Henningsen, V. Balakrishna, D. R. Suhre, N. Fernelius, F. K. Hopkins, and D. E. Zelmon, "Growth and characterization of gallium selenide crystals for far-infrared conversion applications," *Journal of Crystal Growth*, vol. 163, pp. 398–402, jun 1996.

[43] H. Lin, B. M. Fischer, and D. Abbott, "Comparative simulation study of ZnTe heating effects in focused THz radiation generation," in *IRMMW-THz 2010 - 35th International Conference on Infrared, Millimeter, and Terahertz Waves, Conference Guide*, pp. 1–2, IEEE, sep 2010.

[44] Q. Wu and X. C. Zhang, "Ultrafast electro-optic field sensors," *Applied Physics Letters*, vol. 68, pp. 1604–1606, mar 1996.

[45] M. Schall, M. Walther, and P. Uhd Jepsen, "Fundamental and second-order phonon processes in CdTe and ZnTe," *Physical Review B - Condensed Matter and Materials Physics*, vol. 64, p. 094301, aug 2001.

[46] A. Leitenstorfer, S. Hunsche, J. Shah, M. C. Nuss, and W. H. Knox, "Detectors and sources for ultrabroadband electro-optic sampling: Experiment and theory," *Applied Physics Letters*, vol. 74, pp. 1516–1518, mar 1999.

[47] B. Wu, L. Cao, Q. Fu, P. Tan, Y. Xiong, and T. Hust, "Comparison of the detection performance of three nonlinear crystals for the electro-optica sampling of a FEL-THz source," 2014.

[48] N. Kuroda, O. Ueno, and Y. Nishina, "Lattice-dynamical and photoelastic properties of GaSe under high pressures studied by Raman scattering and electronic susceptibility," *Physical Review B*, vol. 35, pp. 3860–3870, mar 1987.

[49] K. Nassau, *Handbook of non-linear optical crystals*, vol. 27 of *Springer Series in Optical Sciences*. Berlin, Heidelberg: Springer Berlin Heidelberg, 1992.

[50] K. Liu, J. Xu, and X.-C. Zhang, "GaSe crystals for broadband terahertz wave detection," *Applied Physics Letters*, vol. 85, pp. 863–865, aug 2004.

[51] R. Huber, A. Brodschelm, F. Tauser, and A. Leitenstorfer, "Generation and field-resolved detection of femtosecond electromagnetic pulses tunable up to 41 THz," *Applied Physics Letters*, vol. 76, pp. 3191–3193, may 2000.

[52] W. Shi, Y. J. Ding, N. Fernelius, and K. Vodopyanov, "Efficient, tunable, and coherent 018–527-THz source based on GaSe crystal: erratum," *Optics Letters*, vol. 28, p. 136, aug 2003.

[53] L. Palfalvi, J. Hebling, J. Kuhl, A. Pter, and K. Polgar, "Temperature dependence of the absorption and refraction of Mg-doped congruent and stoichiometric $\mathrm{LiNbO_3}$ in the THz range," *Journal of Applied Physics*, vol. 97, p. 123505, jun 2005.

[54] S. R. Marder, J. W. Perry, and W. P. Schaefer, "Synthesis of organic salts with large second-order optical nonlinearities," *Science*, vol. 245, pp. 626–628, aug 1989.

[55] A. Schneider, M. Neis, M. Stillhart, B. Ruiz, R. U. A. Khan, and P. Gunter, "Generation of terahertz pulses through optical rectification in organic DAST crystals: theory and experiment," *Journal of the Optical Society of America B*, vol. 23, p. 1822, sep 2006.

[56] H. Hashimoto, Y. Okada, H. Fujimura, M. Morioka, O. Sugihara, N. Okamoto, and R. Matsushima, "Second-harmonic generation from single crystals of N-substituted 4-nitroanilines," *Japanese Journal of Applied Physics, Part 1: Regular Papers and Short Notes and Review Papers*, vol. 36, pp. 6754–6760, nov 1997.

[57] H. Hashimoto, H. Takahashi, T. Yamada, K. Kuroyanagi, and T. Kobayashi, "Characteristics of the terahertz radiation from single crystals of N-substituted 2-methyl-4-nitroaniline," *Journal of Physics Condensed Matter*, vol. 13, p. L529, jun 2001.

[58] K. Miyamoto, H. Minamide, M. Fujiwara, H. Hashimoto, and H. Ito, "Widely tunable terahertz-wave generation using an N-benzyl-2-methyl-4-nitroaniline crystal," *Optics Letters*, vol. 33, p. 252, feb 2008.

[59] H. Hamster, A. Sullivan, S. Gordon, W. White, and R. W. Falcone, "Subpicosecond, electromagnetic pulses from intense laser-plasma interaction," *Physical Review Letters*, vol. 71, pp. 2725–2728, oct 1993.

[60] D. J. Cook and R. M. Hochstrasser, "Intense terahertz pulses by four-wave rectification in air," *Optics Letters*, vol. 25, p. 1210, aug 2000.

[61] T. Löffler, F. Jacob, and H. G. Roskos, "Generation of terahertz pulses by photoionization of electrically biased air," *Applied Physics Letters*, vol. 77, pp. 453–455, jul 2000.

[62] T. P. Bartel and P. Gaal, "Generation of single-cycle THz transients with high electric-field amplitudes Coherent multidimensional terahertz spectroscopy View project magnetoacoustics View project," *Osapublishing.Org*, vol. 30, pp. 2805–2807, oct 2005.

[63] T. Löffler and H. G. Roskos, "Gas-pressure dependence of terahertz-pulse generation in a laser-generated nitrogen plasma," *Journal of Applied Physics*, vol. 91, pp. 2611–2614, feb 2002.

[64] S. Winnerl, F. Peter, S. Nitsche, A. Dreyhaupt, B. Zimmermann, M. Wagner, H. Schneider, M. Helm, and K. Köhler, "Generation and detection of THz radiation with scalable antennas based on GaAs substrates with different carrier lifetimes," *IEEE Journal on Selected Topics in Quantum Electronics*, vol. 14, no. 2, pp. 449–457, 2008.

[65] J. H. Scofield, "Frequency-domain description of a lock-in amplifier," *American Journal of Physics*, vol. 62, pp. 129–133, feb 1994.

[66] Signal Recovery, "What is a Boxcar Averager?," tech. rep., Oak Ridge, 2004.

[67] M. Theuer, S. S. Harsha, D. Molter, G. Torosyan, and R. Beigang, "Terahertz time-domain spectroscopy of gases, liquids, and solids," *ChemPhysChem*, vol. 12, pp. 2695–2705, oct 2011.

[68] J. Kroll, J. Darmo, and K. Unterrainer, "High-performance terahertz electro-optic detector," *Electronics Letters*, vol. 40, pp. 763–764, jun 2004.

[69] K. Maussang, A. Brewer, J. Palomo, J. M. Manceau, R. Colombelli, I. Sagnes, J. Mangeney, J. Tignon, and S. S. Dhillon, "Echo-Less Photoconductive Antenna Sources for High-Resolution Terahertz Time-Domain Spectroscopy," *IEEE Transactions on Terahertz Science and Technology*, vol. 6, pp. 20–25, jan 2016.

[70] W. Withayachumnankul, B. Ferguson, T. Rainsford, S. P. Mickan, and D. Abbott, "Simple material parameter estimation via terahertz time-domain spectroscopy," *Electronics Letters*, vol. 41, pp. 800–801, jul 2005.

[71] S. C. Howells and L. A. Schlie, "Transient terahertz reflection spectroscopy of undoped InSb from 0.1 to 1.1 THz," *Applied Physics Letters*, vol. 69, pp. 550–552, jun 1996.

[72] T. I. Jeon and D. Grischkowsky, "Characterization of optically dense, doped semiconductors by reflection THz time domain spectroscopy," *Applied Physics Letters*, vol. 72, pp. 3032–3034, jun 1998.

[73] W. F. Sun, X. K. Wang, and Y. Zhang, "Measurement of refractive index for high reflectance materials with terahertz time domain reflection spectroscopy," *Chinese Physics Letters*, vol. 26, p. 114210, nov 2009.

[74] P. N. Saeta, J. F. Federici, B. I. Greene, and D. R. Dykaar, "Intervalley scattering in GaAs and InP probed by pulsed far-infrared transmission spectroscopy," *Applied Physics Letters*, vol. 60, pp. 1477–1479, aug 1992.

[75] M. C. Beard, G. M. Turner, and C. A. Schmuttenmaer, "Transient photoconductivity in GaAs as measured by time-resolved terahertz spectroscopy,"

[76] R. L. Milot, G. F. Moore, R. H. Crabtree, G. W. Brudvig, and C. A. Schmuttenmaer, "Electron injection dynamics from photoexcited porphyrin dyes into SnO 2 and TiO2 nanoparticles," *Journal of Physical Chemistry C*, vol. 117, no. 42, pp. 21662–21670, 2013.

[77] G. Haran, W. D. Sun, K. Wynne, and R. M. Hochstrasser, "Femtosecond far-infrared pump-probe spectroscopy: A new tool for studying low-frequency vibrational dynamics in molecular condensed phases," *Chemical Physics Letters*, vol. 274, pp. 365–371, aug 1997.

[78] R. McElroy and K. Wynne, "Time-resolved terahertz spectroscopy of condensed phase reactions," *Laser Chemistry*, vol. 19, no. 1-4, pp. 145–148, 1999.

[79] D. R. Bacon, J. R. Freeman, R. A. Mohandas, L. Li, E. H. Linfield, A. G. Davies, and P. Dean, "Gain recovery time in a terahertz quantum cascade laser," *Applied Physics Letters*, 2016.

[80] P. Hamm and M. Zanni, *Concepts and methods of 2D infrared spectroscopy.* 2011.

[81] W. Kuehn, K. Reimann, M. Woerner, and T. Elsaesser, "Phase-resolved two-dimensional spectroscopy based on collinear n-wave mixing in the ultrafast time domain," *The Journal of Chemical Physics*, vol. 130, p. 164503, apr 2009.

[82] M. Woerner, W. Kuehn, P. Bowlan, K. Reimann, and T. Elsaesser, "Ultrafast two-dimensional terahertz spectroscopy of elementary excitations in solids," *New Journal of Physics*, vol. 15, 2013.

[83] E. L. Hahn, "Spin echoes," *Physical Review*, vol. 80, pp. 580–594, nov 1950.

[84] J. Raab, C. Lange, J. L. Boland, I. Laepple, M. Furthmeier, E. Dardanis, N. Dessmann, L. Li, E. H. Linfield, A. G. Davies, M. S. Vitiello, and R. Huber, "Ultrafast two-dimensional field spectroscopy of terahertz intersubband saturable absorbers," *Optics Express*, vol. 27, p. 2248, feb 2019.

[85] H. Y. Hwang, S. Fleischer, N. C. Brandt, B. G. Perkins, M. Liu, K. Fan, A. Sternbach, X. Zhang, R. D. Averitt, and K. A. Nelson, "A review of non-linear terahertz spectroscopy with ultrashort tabletop-laser pulses," *Journal of Modern Optics*, vol. 62, pp. 1447–1479, oct 2015.

[86] S. Markmann, M. Franckié, S. Pal, D. Stark, M. Beck, M. Fiebig, G. Scalari, and J. Faist, "Two-dimensional spectroscopy on a THz quantum cascade structure," *Nanophotonics*, vol. 10, pp. 171–180, jan 2021.

[87] T. Maag, A. Bayer, S. Baierl, M. Hohenleutner, T. Korn, C. Schüller, D. Schuh, D. Bougeard, C. Lange, R. Huber, M. Mootz, J. E. Sipe, S. W. Koch, and M. Kira, "Coherent cyclotron motion beyond Kohn's theorem," *Nature Physics*, vol. 12, pp. 119–123, nov 2016.

[88] J. Lu, Y. Zhang, H. Y. Hwang, B. K. Ofori-Okai, S. Fleischer, and K. A. Nelson, "Two-dimensional terahertz photon echo and rotational spectroscopy in the gas phase," *Optics InfoBase Conference Papers*, vol. 113, pp. 11800–11805, oct 2016.

[89] C. Somma, G. Folpini, K. Reimann, M. Woerner, and T. Elsaesser, "Two-phonon quantum coherences in InSb studied by two-dimensional terahertz spectroscopy," *Optics InfoBase Conference Papers*, vol. 116, p. 177401, apr 2016.

[90] C. Somma, G. Folpini, K. Reimann, M. Woerner, and T. Elsaesser, "Phase-resolved two-dimensional terahertz spectroscopy including off-resonant interactions beyond the $\chi(3)$ limit," *Journal of Chemical Physics*, vol. 144, p. 184202, may 2016.

[91] H. Hirori, A. Doi, F. Blanchard, and K. Tanaka, "Single-cycle terahertz pulses with amplitudes exceeding 1 MV/cm generated by optical rectification in $LiNbO_3$," *Applied Physics Letters*, vol. 98, p. 091106, mar 2011.

[92] A. Dreyhaupt, S. Winnerl, T. Dekorsy, and M. Helm, “High-intensity terahertz radiation from a microstructured large-area photoconductor,” *Applied Physics Letters*, vol. 86, pp. 1–3, mar 2005.

[93] M. Awad, M. Nagel, H. Kurz, J. Herfort, and K. Ploog, “Characterization of low temperature GaAs antenna array terahertz emitters,” *Applied Physics Letters*, vol. 91, p. 181124, oct 2007.

[94] D. R. Bacon, T. B. Gill, M. Rosamond, A. D. Burnett, A. Dunn, L. Li, E. H. Linfield, A. G. Davies, P. Dean, and J. R. Freeman, “Photoconductive arrays on insulating substrates for high-field terahertz generation,” *Optics Express*, vol. 28, p. 17219, jun 2020.

[95] C. D. Mosley, M. Staniforth, A. I. Serrano, E. Pickwell-Macpherson, and J. Lloyd-Hughes, “Scalable interdigitated photoconductive emitters for the electrical modulation of terahertz beams with arbitrary linear polarization,” *AIP Advances*, vol. 9, p. 045323, apr 2019.

[96] K. Maussang, J. Palomo, J. Mangeney, S. S. Dhillon, and J. Tignon, “Large-area photoconductive switches as emitters of terahertz pulses with fully electrically controlled linear polarization,” *Optics Express*, vol. 27, p. 14784, may 2019.

[97] I. S. Gregory, C. Baker, W. R. Tribe, M. J. Evans, H. E. Beere, E. H. Linfield, A. G. Davies, and M. Missous, “High resistivity annealed low-temperature GaAs with 100 fs lifetimes,” *Applied Physics Letters*, vol. 83, pp. 4199–4201, nov 2003.

[98] F. Niklaus, R. J. Kumar, J. J. McMahon, J. Yu, J.-Q. Lu, T. S. Cale, and R. J. Gutmann, “Adhesive Wafer Bonding Using Partially Cured Benzocyclobutene for Three-Dimensional Integration,” *Journal of The Electrochemical Society*, vol. 153, no. 4, p. G291, 2006.

[99] B. B. Hu, J. T. Darrow, X. C. Zhang, D. H. Auston, and P. R. Smith, “Optically steerable photoconducting antennas,” *Applied Physics Letters*, vol. 56, pp. 886–888, jun 1990.

[100] J. L. Carthy, P. C. Gow, S. A. Berry, B. Mills, and V. Apostolopoulos, “Terahertz Focusing and Polarization Control in Large-Area Bias-Free Semiconductor Emitters,” *Journal of Infrared, Millimeter, and Terahertz Waves*, vol. 39, pp. 223–235, mar 2018.

[101] S. V. Alekseev, N. G. Ivanov, M. V. Ivanov, V. F. Losev, and Y. N. Panchenko, “Broadening of the spectra of femtosecond laser pulses upon passing through optical materials,” *Bulletin of the Russian Academy of Sciences: Physics*, vol. 79, pp. 242–245, mar 2015.

[102] D. S. Kim and D. S. Citrin, “Coulomb and radiation screening in photoconductive terahertz sources,” *Applied Physics Letters*, vol. 88, p. 161117, apr 2006.

[103] X. Ropagnol, X. Chai, S. M. Raeis-Zadeh, S. Safavi-Naeini, M. Kirouac-Turmel, M. Bouvier, C. Y. Cote, M. Reid, M. A. Gauthier, and T. Ozaki, "Influence of gap size on intense THz generation from ZnSe interdigitated large aperture photoconductive antennas (October 2016)," *IEEE Journal of Selected Topics in Quantum Electronics*, vol. 23, jul 2017.

[104] J. Ma, P. Yuan, J. Wang, Y. Wang, G. Xie, H. Zhu, and L. Qian, "Spatiotemporal noise characterization for chirped-pulse amplification systems," *Nature Communications*, vol. 6, pp. 1–8, feb 2015.

[105] C. Ungureanu and L. M. Nemțoi, "Peak Voltage Measurements Using Standard Sphere Gap Method," *Advances in Electrical Engineering*, vol. 2014, pp. 1–5, oct 2014.

[106] Y. Suzaki and A. Tachibana, "Measurement of the μm sized radius of Gaussian laser beam using the scanning knife-edge," *Applied Optics*, vol. 14, p. 2809, dec 1975.

[107] S. Kimura and C. Munakata, "Measurement of a Gaussian laser beam spot size using a boundary diffraction wave," *Applied Optics*, vol. 27, p. 84, jan 1988.

[108] V. K. Mag-usara, S. Funkner, G. Niehues, E. A. Prieto, M. H. Balgos, A. Somintac, E. Estacio, A. Salvador, K. Yamamoto, M. Hase, and M. Tani, "Low temperature-grown GaAs carrier lifetime evaluation by double optical pump terahertz time-domain emission spectroscopy," *Optics Express*, vol. 24, p. 26175, nov 2016.

[109] Z. B. Zaccardi, I. C. Tangen, G. A. Valdivia-Berroeta, C. B. Bahr, K. C. Kenney, C. Rader, M. J. Lutz, B. P. Hunter, D. J. Michaelis, and J. A. Johnson, "Enabling High-Power, Broadband THz Generation with 800-nm Pump Wavelength," oct 2020.

[110] M. Shalaby, C. Vicario, K. Thirupugalmani, S. Brahadeeswaran, and C. P. Hauri, "Intense THz source based on BNA organic crystal pumped at Ti:sapphire wavelength," *Optics Letters*, vol. 41, p. 1777, apr 2016.

[111] H. W. Hübers, S. G. Pavlov, and V. N. Shastin, "Terahertz lasers based on germanium and silicon," *Semiconductor Science and Technology*, vol. 20, pp. S211–S221, jul 2005.

[112] S. Kamiya, M. Shirahata, S. Matsuura, Y. Sawayama, Y. Doi, M. Kawada, T. Nakagawa, Y. Creten, B. Okcan, and W. Raab, "Development of a far-infrared Ge:Ga monolithic array detector for SPICA (space infrared telescope for cosmology and astrophysics)," in *IRMMW-THz 2010 - 35th International Conference on Infrared, Millimeter, and Terahertz Waves, Conference Guide*, pp. 1–2, IEEE, sep 2010.

[113] J. J. Morton, D. R. McCamey, M. A. Eriksson, and S. A. Lyon, "Embracing the quantum limit in silicon computing," *Nature*, vol. 479, pp. 345–353, nov 2011.

[114] M. T. Mądzik, S. Asaad, A. Youssry, B. Joecker, K. M. Rudinger, E. Nielsen, K. C. Young, T. J. Proctor, A. D. Baczewski, A. Laucht, V. Schmitt, F. E. Hudson, K. M. Itoh, A. M. Jakob, B. C. Johnson, D. N. Jamieson, A. S. Dzurak, C. Ferrie, R. Blume-Kohout, and A. Morello, "Precision tomography of a three-qubit donor quantum processor in silicon," *Nature*, vol. 601, no. 7893, pp. 348–353, 2022.

[115] R. K. Zhukavin, K. A. Kovalevskii, Y. Y. Choporova, V. V. Tsyplenkov, V. V. Gerasimov, P. A. Bushuikin, B. A. Knyazev, N. V. Abrosimov, S. G. Pavlov, H. W. Hübers, and V. N. Shastin, "Relaxation Times and Population Inversion of Excited States of Arsenic Donors in Germanium," *JETP Letters*, vol. 110, pp. 677–682, nov 2019.

[116] R. J. Bell, W. T. Bousman, G. M. Goldman, and D. G. Rathbun, "Surface and bulk impurity eigenvalues in the shallow donor impurity theory," *Surface Science*, vol. 7, pp. 293–301, jul 1967.

[117] A. K. Ramdas and S. Rodriguez, "Spectroscopy of the solid-state analogues of the hydrogen atom: donors and acceptors in semiconductors," *Reports on Progress in Physics*, vol. 44, pp. 1297–1387, dec 1981.

[118] G. Dodel, J. Heppner, E. Holzhauer, and E. Gornik, "Wideband heterodyne detection in the far infrared with extrinsic Ge photoconductors," *Journal of Applied Physics*, vol. 54, pp. 4254–4259, aug 1983.

[119] O. D. Dubon, I. Wilke, J. W. Beeman, and E. E. Haller, "Dependence of the hole lifetime on uniaxial stress in Ga-doped Ge," *Physical Review B*, vol. 51, pp. 7349–7352, mar 1995.

[120] T. Theiler, H. Navarro, R. Till, and F. Keilmann, "Saturation of ionization edge absorption by donors in germanium," *Applied Physics A Solids and Surfaces*, vol. 56, pp. 22–28, jan 1993.

[121] G. Jungwirt and W. Prettl, "Nonlinear far-infrared photoionization of shallow acceptors in Germanium," *Infrared Physics*, vol. 32, pp. 191–194, jan 1991.

[122] F. A. Hegmann, J. B. Williams, B. Cole, M. S. Sherwin, J. W. Beeman, and E. E. Haller, "Time-resolved photoresponse of a gallium-doped germanium photoconductor using a variable pulse-width terahertz source," *Applied Physics Letters*, vol. 76, pp. 262–264, jan 2000.

[123] N. Deßmann, S. G. Pavlov, A. Pohl, N. V. Abrosimov, S. Winnerl, M. Mittendorff, R. K. Zhukavin, V. V. Tsyplenkov, D. V. Shengurov, V. N. Shastin, and H. W. Hübers, "Lifetime-limited, subnanosecond terahertz

germanium photoconductive detectors," *Applied Physics Letters*, vol. 106, p. 171109, apr 2015.

[124] N. Deßmann, S. G. Pavlov, V. V. Tsyplenkov, E. E. Orlova, A. Pohl, V. N. Shastin, R. K. Zhukavin, S. Winnerl, M. Mittendorff, J. M. Klopf, N. V. Abrosimov, H. Schneider, and H. W. Hübers, "Dynamics of non-equilibrium charge carriers in p-germanium doped by gallium," *Physica Status Solidi (B) Basic Research*, vol. 254, p. 1600803, jun 2017.

[125] N. Deßmann, S. G. Pavlov, V. N. Shastin, R. K. Zhukavin, V. V. Tsyplenkov, S. Winnerl, M. Mittendorff, N. V. Abrosimov, H. Riemann, and H. W. Hübers, "Time-resolved electronic capture in n -type germanium doped with antimony," *Physical Review B - Condensed Matter and Materials Physics*, vol. 89, p. 035205, jan 2014.

[126] N. Greenall, "Parameter Extraction and Uncertainty in Terahertz Time-Domain Spectroscopic Measurements," no. September, pp. 1–278, 2017.

[127] D. M. Slocum, E. J. Slingerland, R. H. Giles, and T. M. Goyette, "Atmospheric absorption of terahertz radiation and water vapor continuum effects," *Journal of Quantitative Spectroscopy and Radiative Transfer*, vol. 127, pp. 49–63, sep 2013.

[128] H. W. Icenogle, B. C. Platt, and W. L. Wolfe, "Refractive Indexes and Temperature Coefficients of Germanium and Silicon.," *Applied Optics*, vol. 15, pp. 2348–2351, oct 1976.

[129] H. H. Li, "Refractive Index of ZnS, ZnSe, and ZnTe and Its Wavelength and Temperature Derivatives," *Journal of Physical and Chemical Reference Data*, vol. 13, pp. 103–150, oct 1984.

[130] N. Dessmann, S. G. Pavlov, V. N. Shastin, R. K. Zhukavin, S. Winnerl, M. Mittendorff, and H. W. Hubers, "Time-resolved electronic capture in germanium doped with hydrogen-like impurity centers," in *International Conference on Infrared, Millimeter, and Terahertz Waves, IRMMW-THz*, pp. 1–2, IEEE, sep 2012.

[131] S. Barbieri, M. Ravaro, P. Gellie, G. Santarelli, C. Manquest, C. Sirtori, S. P. Khanna, E. H. Linfield, and A. G. Davies, "Coherent sampling of active mode-locked terahertz quantum cascade lasers and frequency synthesis," *Nature Photonics*, vol. 5, pp. 306–313, apr 2011.

[132] C. Y. Wang, L. Kuznetsova, V. M. Gkortsas, L. Diehl, F. X. Kärtner, M. A. Belkin, A. Belyanin, X. Li, D. Ham, H. Schneider, P. Grant, C. Y. Song, S. Haffouz, Z. R. Wasilewski, H. Liu, and F. Capasso, "Mode-locked pulses from mid-infrared Quantum Cascade Lasers," *Optics Express*, vol. 17, p. 12929, jul 2009.

[133] F. Wang, V. Pistore, M. Riesch, H. Nong, P. B. Vigneron, R. Colombelli, O. Parillaud, J. Mangeney, J. Tignon, C. Jirauschek, and S. S. Dhillon, "Ultrafast response of harmonic modelocked THz lasers," *Light: Science and Applications*, vol. 9, pp. 1–8, apr 2020.

[134] A. Mottaghizadeh, D. Gacemi, P. Laffaille, H. Li, M. Amanti, C. Sirtori, G. Santarelli, W. Hänsel, R. Holzwart, L. H. Li, E. H. Linfield, and S. Barbieri, "5-Ps-Long Terahertz Pulses From an Active-Mode-Locked Quantum Cascade Laser," *Optica*, vol. 4, p. 168, jan 2017.

[135] C. R. Menyuk and M. A. Talukder, "Self-induced transparency modelocking of quantum cascade lasers," *Physical Review Letters*, vol. 102, p. 023903, jan 2009.

[136] E. Schrödinger, "An undulatory theory of the mechanics of atoms and molecules," *Physical Review*, vol. 28, pp. 1049–1070, dec 1926.

[137] P. Harrison, "Quantum Wells, Wires and Dots: Theoretical and Computational Physics of Semiconductor Nanostructures: Second Edition," *Quantum Wells, Wires and Dots: Theoretical and Computational Physics of Semiconductor Nanostructures: Second Edition*, pp. 1–482, jan 2006.

[138] "Springer Handbook of Electronic and Photonic Materials," *Springer Handbook of Electronic and Photonic Materials*, 2007.

[139] G. Bastard and J. Schulman, "Wave Mechanics Applied to Semiconductor Heterostructures," *Physics Today*, vol. 45, pp. 103–105, feb 1992.

[140] K. F. Renk, *Basics of Laser Physics*, vol. 33 of *Graduate Texts in Physics*. Berlin, Heidelberg: Springer Berlin Heidelberg, 2012.

[141] J. Faist, F. Capasso, D. L. Sivco, C. Sirtori, A. L. Hutchinson, and A. Y. Cho, "Quantum cascade laser," *Science*, vol. 264, pp. 553–556, apr 1994.

[142] R. Köhler, A. Tredicucci, F. Beltram, H. E. Beere, E. H. Linfield, A. G. Davies, D. A. Ritchie, R. C. Iotti, and F. Rossi, "Terahertz semiconductor-heterostructure laser," *Nature*, vol. 417, no. 6885, pp. 156–159, 2002.

[143] B. F. Levine, "Quantum-well infrared photodetectors," *Journal of Applied Physics*, vol. 74, p. R1, jun 1993.

[144] R. Zhang, X. G. Guo, C. Y. Song, M. Buchanan, Z. R. Wasilewski, J. C. Cao, and H. C. Liu, "Metal-grating-coupled terahertz quantum-well photodetectors," *IEEE Electron Device Letters*, vol. 32, pp. 659–661, may 2011.

[145] D. Shao, Z. Fu, Z. Tan, C. Wang, F. Qiu, L. Gu, W. Wan, and J. Cao, "Research Progress on Terahertz Quantum-Well Photodetector and Its Application," *Frontiers in Physics*, vol. 9, p. 581, nov 2021.

[146] P. Dean, Y. Leng Lim, A. Valavanis, R. Kliese, M. Nikolić, S. P. Khanna, M. Lachab, D. Indjin, Z. Ikonić, P. Harrison, A. D. Rakić, E. H. Linfield, and A. G. Davies, "Terahertz imaging through self-mixing in a quantum cascade laser," *Optics Letters*, vol. 36, p. 2587, jul 2011.

[147] S. L. McCall and E. L. Hahn, "Self-induced transparency by pulsed coherent light," *Physical Review Letters*, vol. 18, pp. 908–911, may 1967.

[148] S. L. McCall and E. L. Hahn, "Self-Induced Transparency," *Physical Review*, vol. 183, pp. 457–485, jul 1969.

[149] M. V. Arkhipov, A. A. Shimko, N. N. Rosanov, I. Babushkin, and R. M. Arkhipov, "Self-induced-transparency mode locking in a Ti:sapphire laser with an intracavity rubidium cell," *Physical Review A*, vol. 101, p. 013803, jan 2020.

[150] R. M. Arkhipov, M. V. Arkhipov, I. Babushkin, and N. N. Rosanov, "Self-induced transparency mode locking, and area theorem," *Optics Letters*, vol. 41, p. 737, feb 2016.

[151] V. V. Kozlov, N. N. Rosanov, and S. Wabnitz, "Obtaining single-cycle pulses from a mode-locked laser," *Physical Review A - Atomic, Molecular, and Optical Physics*, vol. 84, p. 053810, nov 2011.

[152] J. Faist, *Quantum cascade lasers.* Oxford University Press, 2013.

[153] Q. Hu, B. S. Williams, S. Kumar, H. Callebaut, S. Kohen, and J. L. Reno, "Resonant-phonon-assisted THz quantum-cascade lasers with metal-metal waveguides," *Semiconductor Science and Technology*, vol. 20, pp. S228–S236, jul 2005.

[154] B. S. Williams, "Terahertz quantum-cascade lasers," *Nature Photonics*, vol. 1, pp. 517–525, sep 2007.

[155] Z. J. Xin and H. N. Rutt, "Inhomogenous broadening in quantum well lasers," *Infrared Physics and Technology*, vol. 40, pp. 37–40, feb 1999.

[156] T. Suhara and H. Nishihara, "Integrated Optics Components and Devices Using Periodic Structures," *IEEE Journal of Quantum Electronics*, vol. 22, no. 6, pp. 845–867, 1986.

[157] Y. Todorov and C. Minot, "Modal method for conical diffraction on a rectangular slit metallic grating in a multilayer structure," *Journal of the Optical Society of America A*, vol. 24, p. 3100, oct 2007.

[158] C. Hoberg, P. Balzerowski, and M. Havenith, "Integration of a rapid scanning technique into THz time-domain spectrometers for nonlinear THz spectroscopy measurements," *AIP Advances*, vol. 9, p. 035348, mar 2019.

[159] Y. Minami, Y. Hayashi, J. Takeda, and I. Katayama, “Single-shot measurement of a terahertz electric-field waveform using a reflective echelon mirror,” *Applied Physics Letters*, vol. 103, p. 051103, jul 2013.